

BRNO UNIVERSITY OF TECHNOLOGY

VYSOKÉ UČENÍ TECHNICKÉ V BRNĚ

CENTRAL EUROPEAN INSTITUTE OF TECHNOLOGY BUT

STŘEDOEVROPSKÝ TECHNOLOGICKÝ INSTITUT VUT

MAGNETISM IN CURVED GEOMETRIES

MAGNETISMUS V ZAKŘIVENÝCH STRUKTURÁCH

DOCTORAL THESIS

DIZERTAČNÍ PRÁCE

AUTHOR Ing. Igor Turčan

AUTOR PRÁCE

Ing. Michal Urbánek, Ph.D.

SUPERVISOR VEDOUCÍ PRÁCE

BRNO 2021

Summary

In the field of magnonics, which is a novel research topic utilizing the physics of spin waves, there is an increasing interest in developing functional spin-wave devices with unique properties. These devices allow us to control the spin-wave flow and are needed for future spin-wave-based information processing. However, their technical realization is highly challenging with conventional approaches. They rely on planar magnonic structures, where the magnetic properties are exclusively given by the intrinsic parameters of used materials. Thus, properties like uniaxial magnetic anisotropy cannot be directly controlled. The presented thesis exploits a novel approach of inducing the effective magnetic interaction by the curvature of the system. The corrugation-induced uniaxial magnetic anisotropy is studied in structures with modulated surfaces prepared by focused electron beam-induced deposition and electron beam lithography. The potential of the local control over the magnetization direction using the 3D nanofabrication approach is universal and can be used with any commonly used magnetic material. Furthermore, the spinwave propagation in the Damon-Eshbach geometry without an external magnetic field is demonstrated in corrugated magnetic waveguides by means of Brillouin light scattering microscopy. The broadening of the ferromagnetic resonance peak and extraction of the damping parameter is presented for the planar and corrugated structures. Finally, the comparison of the spin-wave propagation length measurement in corrugated waveguides with the total damping measurements, and with analytical calculations is shown. The decrease of the propagation length for the waveguides with larger modulation amplitude is associated to the increase of the damping parameter α .

Abstrakt

V oblasti magnoniky, nového výzkumného oboru využívajícího fyziku spinových vln, roste zájem o vývoj funkčních zařízení s unikátními vlastnostmi . Hlavní překážkou pro budoucí generace výpočetní techniky založené na spinových vlnách je řízení toku spinových vln. Technická realizace je však u konvenčních přístupů velmi náročná, jelikož spoléhají na rovinné magnetické struktury, kde jsou magnetické vlastnosti dány výlučně vlastnostmi použitých materiálů. Vlastnosti jako jednoosá magnetická anizotropie tedy nelze přímo ovládat. Předkládaná dizertační práce využívá nový přístup k indukci efektivní magnetické interakce zakřivením systému. Jednoosá magnetická anizotropie, která je způsobena vlnitostí systému, je studována ve strukturách s modulovanými povrchy připravenými depozicí indukovanou elektronovým svazkem a elektronovou litografií. Potenciál lokální kontroly směru magnetizace pomocí přístupu 3D nanofabrikace je univerzální a lze jej použít s jakýmkoli běžně používaným magnetickým materiálem. Kromě toho je demonstrováno šíření spinových vln v Damonově-Eshbachově geometrii bez aplikace vnějšího magnetického pole ve vlnitých magnetických vlnovodech pomocí mikroskopie Brillouinova rozptylu světla. Rozšíření šířky píku feromagnetické rezonance a získání parametru tlumení je uvedeno pro rovinné a vlnité struktury. V poslední části práce je srovnáno měření délky šíření spinových vln ve vlnitých strukturách s měřením parametru tlumení a s analytickými výpočty. Snížení délky šíření spinových vln u vlnovodů s větší amplitudou modulace je spojeno se zvýšení parametru tlumení α .

Keywords

spin waves, magnonics, 3D nanostructures, corrugated-induced anisotropy



	Place and date	Ing. Igor Turčan
and	d using the technical literature and o	the thesis supervisor, Ing. Michal Urbánek, Ph.D other sources of information which are all properly e list of literature at the end of the thesis.
		ny thesis entitled Magnetism in curved geometrie

ACKNOWLEDGMENT

At this place, I would like to express my sincere gratitude to all of those who helped and supported me throughout the years of my PhD studies. I want to begin by thanking my supervisor Dr. Michal Urbánek. I am grateful for the opportunity to do my PhD in his group. His guidance and expertise helped me become a better scientist with a deeper understanding of the exciting topic of magnonics. I want to thank prof. Tomáš Šikola and the whole collective of the Institute of Physical Engineering and CEITEC for the inspiring atmosphere, conversations in "kafárna" and constantly positive environment. I will always be grateful for the life lessons of prof. Jiří Spousta. His wisdom and motto: "Hlavní je se z toho nepo...!" will further accompany me in my journey through life. I would also like to thank Dr. Lukáš Flajšman. Without him, I would not be the person I am today. His scientific thinking and patience have shown me how an outstanding scientist should look like. I also thank him for the detailed thesis proofreading and all the comments he provided me. I am grateful to my friends from CEITEC (Mára, Ondra, Kuba, Kristýna, Tesi, Káta, and others) for their friendship and all the help and fun they introduced into my scientific and personal life. Many thanks go to my boys Kuba, Martin, Ondra, Rado, Tomáš, and Tonda. Without our constant mocking and laughter, life would be too sad. And naturally, my biggest thanks goes to my family and mainly to my wife Míša for her everlasting love, support, and patience.

Ing. Igor Turčan

Financial support from the Brno Ph.D. talent program financed by city of Brno and South Moravian Region is gratefully acknowledged.

CzechNanoLab project LM2018110 funded by MEYS CR is gratefully acknowledged for the financial support of the measurements/sample fabrication at CEITEC Nano Research Infrastructure.

Contents

In	Introduction 1				
1.	The	oretica	l background		
	1.1.		tization and magnetic materials		
	1.2.	_	nagnetic energies		
		1.2.1.	Zeeman energy		
		1.2.2.	Dipolar energy		
		1.2.3.	Exchange energy		
		1.2.4.	Anisotropy Energy		
			Magnetocrystalline anisotropy		
		1.2.5.	Total energy		
	1.3.	Geome	try-induced anisotropy		
		1.3.1.	Aharoni model of rectangular prism		
		1.3.2.	Curvature-induced anisotropy		
		1.3.3.	Mixed anisotropies		
	1.4.	Stoner-	-Wohlfarth model		
	1.5.		tization dynamics		
			Dynamic susceptibility		
		1.5.2.	Ferromagnetic resonance		
			Influence of a uniaxial magnetic anisotropy		
	1.6.	Dampi	ng		
	1.7.	Spin W	Vaves		
		1.7.1.	Spin-wave dispersion in magnetic thin film		
		1.7.2.	Spin waves in magnonic waveguides		
2.	Sam	ıple fal	orication methods 33		
	2.1.	Focuse	d Electron Beam-Induced Deposition		
		2.1.1.	Experimental Apparatus		
	2.2.	Electro	on beam lithography		
3.	Cha	racteri	zation methods 4		
	3.1.	Atomic	e Force Microscopy		
	3.2.		to-Optical Kerr effect		
		3.2.1.	Kerr Microscopy		
	3.3.	Spin W	Vave Excitation		
	3.4.	Brillou	in Light Scattering Spectroscopy		
		3.4.1.	Brillouin light scattering – experimental setup		
		3.4.2.	Phase-resolved Brillouin light scattering microscopy 5		

	3.5.	Vector	network analyzer		54
		3.5.1.	Vector network analyzer architecture		56
		3.5.2.	Calibration of VNA		57
		3.5.3.	Vector network analyzer ferromagnetic resonance technique	•	58
4.	Exp	erimer	ntal results		62
	4.1.	The su	ubstrate modulation		62
		4.1.1.	Focused ion beam		62
		4.1.2.	Focused electron beam-induced deposition		66
	4.2.	Magne	stostatic study of corrugated structures		70
		4.2.1.	Sample fabrication		70
		4.2.2.	Kerr microscopy		72
	4.3.	Spin w	vave propagation in corrugated waveguides		78
	4.4.	Ferron	nagnetic resonance of corrugated structures	•	87
Co	onclu	sion			95
Re	efere	nces			97
Lis	st of	abbrev	viations	1	13
Α.	Vib	rating	sample magnetometry		i
В.	List	of san	nples		ii

Introduction

The search for truth begins with belief.

– Star Wars: Clone Wars, Episode: A Distant Echo

Today's computing electronics and integrated logic circuits are based on complementary metal-oxide-semiconductor (CMOS) transistors because of their low power consumption, high density, and low fabrication cost [1]. The information in current computing systems is represented by electric charge or voltage, and the charge movements provide the computation. However, the further development of the CMOS technology is expected to decelerate [2] because of the unsustainable power densities or economic inefficiency [3]. Despite the slowdown, the International Roadmap for Devices and Systems (IRDS), which summarizes the roadmap for future developments, does not expect the CMOS scaling to end in the next decade or beyond [4].

Magnonic circuits, utilizing magnons (also called spin waves), i.e., collective oscillations of magnetic moments in magnetically ordered material, are increasingly attracting interest for their possible applications in low-power wave-based computing technology and information processing [5, 6]. Owing to their potential, they are considered as a complementary technology to CMOS, or even a candidate for beyond CMOS generation of logic circuits [7–10]. That is because no Joule heat is produced during operation as there are no moving charges involved, and a non-linear regime is easily accessible, allowing for manipulation of one signal by another [11].

Thanks to recent advances in nanofabrication technology, many spin wave-based devices, such as all-magnon transistor [11], frequency filter [12] or a majority gate [13] have already been demonstrated. Nevertheless, conventionally used approaches rely on planar magnonic structures with very well-defined dimensions. The magnetic properties are exclusively given by the intrinsic parameters of used materials and by the shape of desired structures. In general, the control of the demagnetizing field in such structures is challenging.

In order to overcome the strong effect of the demagnetizing field, an external magnetic field must be applied. However, one of the elementary premises of complex magnonic circuits is a need for operation in the absence of an external magnetic field. Additionally, suppose an external magnetic field is used to stabilize the magnetic ordering in a nanostructure. In that case, even a simple circuit element such as a spin-wave turn will be affected due to the mismatch of the orientation of the external magnetic field to the regions before and after the turn, which will lead to a mismatch in dispersion. Therefore, it is essential to locally control the effective field and stabilize the magnetization of different parts of the magnonic circuit in the desired direction to prevent the dispersion mismatch.

In our work, we exploit the recently presented approach of inducing the effective magnetic interaction by adding the curvature to the system [14]. The curvature-induced effects [15] can be used to adjust the static and dynamic response of a magnetic system.

The applicability of the surface curvature can be found, e.g., in control of the direction and the magnitude of the magnetic anisotropy [16]. The introduction of the curvature-induced uniaxial magnetic anisotropy has been previously observed in various experiments using ion beam induced erosion [14, 17–19]. However, in these experiments the whole sample area was irradiated by the broad ion beam. Similarly, the forming and the control of the uniaxial magnetic anisotropy has been demonstrated via field sputtering or field annealing [20–22]. Using these types of induced anisotropies, it is difficult to locally control the magnetic anisotropy direction and magnitude on small scales.

Recent advances in 3D nanofabrication introduce the methods of structure preparation with shapes and properties unobtainable by standard lithography approaches [23–27]. In this work, we study corrugated magnonic waveguides prepared by the novel combination of the focused electron beam-induced deposition (FEBID) and the electron beam lithography. The magnonic waveguides are deposited on a sinusoidally modulated substrate prepared by FEBID. We can locally control the magnitude and the direction of the uniaxial magnetic anisotropy just by changing the parameters of the surface modulation. We are utilizing curvature-induced effects to achieve unprecedented spin-wave propagation in narrow waveguides in the Damon-Eshbach geometry in the absence of an external magnetic field.

The thesis is organized as follows: Chapter 1 provides a brief introduction to the theoretical background needed for the understanding of the experimental part of the thesis. We first outline the basic concepts of magnetostatics. We continue with micromagnetic theory and description of different magnetic energies governing the behavior of the magnetic system. Then we introduce additional energy contributions describing mesoscopic magnetic effects not fully covered by the micromagnetic theory. Further, the Stoner-Wohlfarth model of magnetic anisotropy is discussed. The following sections are devoted to the magnetization dynamics. We introduce the Landau-Lifshitz equation, and then we apply it in finding the analytical solution of the collective oscillations. We continue with the description of the ferromagnetic resonance and especially the influence of a uniaxial magnetic anisotropy. The last part of the chapter introduces the concept of spin waves and discusses spin-wave dispersion in magnetic thin film and magnonic waveguides.

Chapter 2 deals with the experimental methods needed for the sample fabrication. The nanofabrication methods of focused electron beam-induced deposition and electron beam lithography are discussed. The chapter ends with a brief description of the e-beam evaporation technique used for the deposition of materials within the presented thesis.

In chapter 3, we focus on the characterization methods employed in the thesis. The chapter starts with a concise description of the atomic force microscopy (AFM) technique. It is followed by the basic theory of the magneto-optical Kerr effect (MOKE) and the description of the essential components for the Kerr microscopy. In the next small section, the spin-wave excitation using a microstrip antenna is discussed. The following section is devoted to the Brillouin light scattering (BLS) as it is the fundamental technique used to study spin-wave propagation. The chapter ends with presenting the vector network analyzer (VNA) measuring principles and the description of vector network analyzer ferromagnetic resonance (VNA-FMR) experimental setup.

Chapter 4 is dedicated to the experimental results. In the first part, we show how it is possible to fabricate curved geometries before the deposition of the magnetic material. We present the FEBID technique and prove that the modulation period can be tuned down to 40 nm while the sinusoidal shape of the modulation is preserved. We use atomic force microscopy to analyze the overall shape of the grown modulation and the relation

between the number of e-beam scans per line and the modulation amplitude. In the next part of the chapter, we investigate the prepared magnetic structures with curved geometries using Kerr microscopy. We study the magnetization reversal processes and quantify the corrugation-induced uniaxial magnetic anisotropy depending on the corrugation parameters. Moreover, we design and experimentally test a system for spin-wave propagation in Damon-Eshbach geometry in the absence of an external magnetic field. For that, we use corrugated magnonic waveguides with the aspect ratio of 1:10, where the corrugation-induced anisotropy is used to overcome the shape anisotropy. We study the influence of modulation amplitude on the spin-wave propagation length. In the final part of the chapter, we use the VNA-FMR method to extract the damping of the planar and corrugated magnetic structures and analyze if there is any dependence of the damping on the modulation amplitude.

The final chapter gives a conclusion which also contains a summary of the most important results and an outlook for future studies.

1. Theoretical background

A lesson learned is a lesson earned.

– Star Wars: Clone Wars, Episode: Holocron Heist

This chapter provides a brief introduction to the theory of magnetism. It is crucial for the understanding of the methods employed in the experimental parts of the thesis. It provides the theoretical background to both magnetization statics and dynamics. The theoretical topics covering the magnetostatic regime are magnetic energies and the Stoner-Wohlfarth model. This part follows well-established textbooks on magnetism and solid-state physics [28–33]. The magnetodynamic part, together with the physics of spin waves, is based on the books by Hillebrands & Ounadjela [34], Stancil & Prabhakar [35], and Demokritov & Slavin [36].

1.1. Magnetization and magnetic materials

Magnetized materials are characterized by the magnetization \mathbf{M} , which is the effective contribution of all the atomic magnetic moments $\boldsymbol{\mu}$ of a sample averaged over a given volume V. The essential task in magnetism is to find the magnetization \mathbf{M} and the magnetic field \mathbf{H} . The connection between \mathbf{M} and \mathbf{H} is provided by the magnetic susceptibility $\hat{\boldsymbol{\chi}}$. It is a dimensionless tensor of the material. The relation is given by

$$\mathbf{M} = \hat{\mathbf{\chi}} \cdot \mathbf{H} \,. \tag{1.1}$$

For the isotropic material and $\mathbf{M} \parallel \mathbf{H}$, the tensor $\hat{\chi}$ is replaced with scalar χ . Moreover, when an alternating field is applied, the susceptibility can have both real (χ') and imaginary (χ'') parts. The real component reflects the in-phase contribution, and the imaginary component corresponds to the out-of-phase or loss contributions. The susceptibility classifies magnetic materials into distinct magnetic categories. The sign and amplitude of susceptibility allow us to roughly define the following classes of magnetic materials.

• Diamagnets $(\chi \leq -10^{-5})$ – small negative χ : Au, Si, water, ... Due to orbital magnetic moments of electrons, these materials create a magnetic field which counteracts the external magnetic field \boldsymbol{H} , which leads to the repulsion of the material from the magnetic field. The special class of diamagnets is ideal superconducting materials, where $\chi \sim -1$, i.e., no magnetic field can penetrate superconductor. In general, all materials are diamagnetic. This effect is feeble, and in most cases, it is dominated by the atomic magnetic moments' response to the applied field, which is much stronger.

- Paramagnets ($\chi \sim 10^{-5} 10^{-3}$) small positive χ : Al, Pt, Mg, ... When no field is applied the net magnetization is zero. After applying the external magnetic field \boldsymbol{H} , uncompensated spins of electrons align parallel to the magnetic field, which results in a small net magnetization and positive susceptibility. Paramagnetic materials are attracted by the external magnetic field.
- Ferromagnets $(\chi \sim 10-10^4) \chi$ is large and strongly depends on the magnetic field \boldsymbol{H} : Fe, Co, Ni, Fe₃O₄, ... These materials show spontaneous magnetization, i.e. the finite magnetization is retained even after the external magnetic field \boldsymbol{H} is removed. When the external magnetic field \boldsymbol{H} is strong enough, the material is fully magnetized along the applied field direction (saturated). The maximal limiting value of magnetization is called the saturation magnetization, M_s .

The alignment of individual atomic spins causes the spontaneous magnetization of ferromagnetic materials. However, parallel alignment is not the only type of magnetic ordering. In an antiferromagnet, two equal but oppositely oriented magnetic sublattices are formed. It is sometimes possible to switch an antiferromagnet into a ferromagnet with a sufficiently large external magnetic field. This change of magnetic order is commonly known as a metamagnetic transition. On the other hand, two nonequivalent sublattices with magnetizations $M_A \neq M_B$ can be found in a ferrimagnet, resulting in a net spontaneous magnetization. The above-described classes of magnetism are schematically illustrated in Figure 1.1.

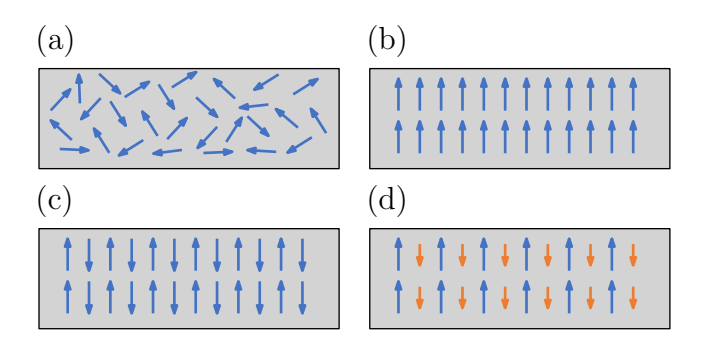


Figure 1.1: Illustration of classes of magnetism: (a) paramagnetism, (b) ferromagnetism, (c) antiferromagnetism, (d) ferrimagnetism. Each arrow represents one atomic magnetic dipole moment.

The alignment of the atomic magnetic dipole moments does not necessarily need to be collinear. E.g., in manganese and some of its alloys, helical or spiral magnetic structures can be found.

The next sections are further devoted to the exceptional phenomenon of ferromagnetism because the presented thesis deals with spin waves in ferromagnets.

1.2. Micromagnetic energies

For the rigorous treatment of ferromagnetism, the quantum mechanical approach must be used. In certain cases, the purely quantum mechanical problem can be generalized in a continuum approximation [37] described by well-developed micromagnetic theory. The major fundamental energy contributions are Zeeman, demagnetizing field, exchange, and anisotropy energies. The following section discusses the various magnetic energy contributions occurring in a magnetic system, emphasizing the dipolar and exchange energies.

1.2.1. Zeeman energy

The Zeeman energy is at play when the external magnetic field $\boldsymbol{H}_{\mathrm{ext}}$ is present and describes an interaction of the magnetization \boldsymbol{M} with the external magnetic field $\boldsymbol{H}_{\mathrm{ext}}$. The energy density is given by

$$\epsilon_{\rm Z} = -\frac{\mu_0}{V} \iiint_{\Omega} \mathbf{M} \cdot \mathbf{H}_{\rm ext} dV, \qquad (1.2)$$

where μ_0 is the permeability of vacuum $(\mu_0 = 4\pi \cdot 10^{-7} \,\mathrm{H/m})^1$, and V is the volume. The minus sign indicates the minimum energy found for the magnetization aligned along the external magnetic field.

1.2.2. Dipolar energy

Dipolar energy describes Zeeman-like mutual self-interaction of all magnetic moments in a ferromagnet. It is a long-range interaction between magnetic moments. Imagine the magnetization \boldsymbol{M} inside a finite ferromagnetic material. In the presence of the interface, it abruptly vanishes, and thus a divergence of \boldsymbol{M} emerges. For $\boldsymbol{H}_{\text{ext}}=0$ we can write

$$\mathbf{B} = \mu_0 \left(\mathbf{M} + \mathbf{H} \right) \,, \tag{1.3}$$

where \mathbf{B} is the magnetic induction. It is another quantity used for the description of magnetic fields. With the help of one of Maxwell's equations $\nabla \cdot \mathbf{B} = 0$, we obtain

$$\nabla \cdot \mathbf{H} = -\nabla \cdot \mathbf{M} \,. \tag{1.4}$$

The situation is similar when the gradient of the magnetization is established inside the material. In this case, in analogy with electrostatics, we define magnetic volume charges inside the magnetic medium. When the gradient is found on the interface, we define surface charges. Generally, the self-fields are opposite to the magnetization direction; therefore, they are known as demagnetizing fields. The demagnetizing field largely determines the formation of magnetic domains inside the magnetic sample. The situation is depicted in Figure 1.2. As a result of the distribution of the surface charges, the demagnetizing field \mathbf{H}_{dem} is formed throughout the material's interior.

In general the task of calculating \mathbf{H}_{dem} from nontrivial spatial distribution of \mathbf{M} is complicated and only few cases can be solved analytically. Doing so for a special case of a uniformly magnetized ellipsoid

$$\mathbf{H}_{\text{dem}} = -\hat{\mathbf{N}} \cdot \mathbf{M}, \quad \text{with} \quad \hat{\mathbf{N}} = \begin{pmatrix} N_x & 0 & 0 \\ 0 & N_y & 0 \\ 0 & 0 & N_z \end{pmatrix}.$$
 (1.5)

 \hat{N} is a geometry dependent demagnetizing field tensor. It is given by both the shape of the sample and the orientation of the magnetization. The trace of this tensor is

$$\operatorname{Tr} \hat{\mathbf{N}} = N_x + N_y + N_z = 1. \tag{1.6}$$

¹In the revised SI system, which has gone into force in 2019, the ampere redefinition led to the permeability of vacuum becoming a measurable quantity. The experimental value of μ_0 is now based on the dimensionless experimental fine structure constant α, the fixed reduced Planck constant \hbar , fixed speed of light in vacuum c, and fixed elementary charge e, $\mu_0 = 4\pi\alpha\hbar/(e^2c) = 1.256\,637\,062\,12(19)\cdot 10^{-6}\,\text{H/m}$. The uncertainty of μ_0 comes from the uncertainty in α and the CODATA (Committee on Data for Science and Technology) truncation of \hbar and e [38].

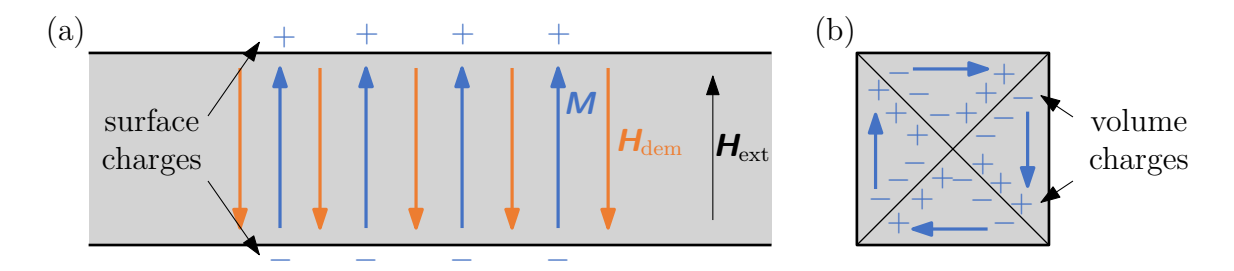


Figure 1.2: Schematic illustration of the origin of the demagnetizing field. It is generated by magnetization and points in the opposite direction. (a) the surface charges are present due to the magnetization gradient M on the interface. (b) volume charges are present due to the gradient of magnetization inside the material. The illustration shows the formation of magnetic domains. In this special case, we speak about the so-called "Landau" state.

For the simple geometries of sphere, cylinder and infinite layer, the demagnetization tensor can be found analytically [29, page 31]

$$\hat{\boldsymbol{N}}_{s} = \begin{pmatrix} 1/3 & 0 & 0 \\ 0 & 1/3 & 0 \\ 0 & 0 & 1/3 \end{pmatrix}, \quad \hat{\boldsymbol{N}}_{c} = \begin{pmatrix} 1/2 & 0 & 0 \\ 0 & 1/2 & 0 \\ 0 & 0 & 0 \end{pmatrix}, \quad \hat{\boldsymbol{N}}_{l} = \begin{pmatrix} 0 & 0 & 0 \\ 0 & 0 & 0 \\ 0 & 0 & 1 \end{pmatrix},$$

where \hat{N}_s , \hat{N}_c and \hat{N}_l are demagnetization tensors for sphere, cylinder and infinite layer respectively. In the continuum model [39], the dipolar energy density is described by

$$\epsilon_{\rm dip} = -\frac{\mu_0}{2V} \iiint_{\Omega} \mathbf{M} \cdot \mathbf{H}_{\rm dem} dV$$
 (1.7)

The integral goes over all the magnetic volume; therefore, to prevent double-counting of the demagnetizing field energy from the individual dipoles, the factor $\frac{1}{2}$ must be included.

It is clearly visible, that by combining (1.5) and (1.7), the dipolar energy is always positive. Therefore, any stray field will increase the total energy of the system. This results in the rather general **charge avoidance principle** [28, page 238] as the ferromagnetic systems minimize the total energy to arrive at a stable configuration, the magnetic charges have to be avoided.

1.2.3. Exchange energy

Any classical theory cannot explain the phenomena of ferromagnetic ordering at room temperature. Despite some initial rather phenomenological models, it was the introduction of the quantum mechanics and exchange energy terms that finally explained ferromagnetism. It is a direct consequence of Coulomb's interaction and Pauli's exclusion law. The Pauli exclusion principle states that two electrons (fermions) with the same quantum number cannot occupy the same quantum mechanical state. If the spins of these two electrons are parallel, they cannot share a common orbit. This forces the electrons to form separate orbits and hence reduces the Coulomb interaction. However, if they are antiparallel, the electrons will share a common orbit, thus increasing the electrostatic Coulomb energy.

The exchange interaction Hamiltonian of such a system can be written as

$$\mathcal{H}_{\text{ex}} = -\sum_{i,j}^{N} J_{ij} \mathbf{S}_i \cdot \mathbf{S}_j = -2 \cdot \sum_{i>j}^{N} J_{ij} \mathbf{S}_i \cdot \mathbf{S}_j, \qquad (1.8)$$

where J_{ij} is the exchange integral describing the coupling between the neighboring spin moment vectors \mathbf{S}_i and \mathbf{S}_j . Based on the sign of the exchange integral, the ground state of the magnetic order is determined. If $J_{ij} > 0$, the lowest energy state occurs for the spins aligned parallelly. This applies to ferromagnetic ordering. When $J_{ij} < 0$, the spins favor the antiparallel alignment, and the ordering is antiferromagnetic. The exchange integral highly varies with the spin-spin distance. Therefore, the exchange interaction is of a very short-range character.

In the continuum limit, the exchange energy density is given by

$$\epsilon_{\rm ex} = A_{\rm ex} \iiint_{\Omega} \left(\nabla \cdot \frac{\mathbf{M}}{M_{\rm s}} \right)^2 \mathrm{d}V,$$
(1.9)

where $A_{\rm ex}$ is the exchange stiffness constant. The exchange stiffness constant is positive in ferromagnetic materials. Therefore, the exchange energy is minimal when the magnetization is uniform. In antiferromagnetic materials, the exchange constant is negative. Hence, when two spins are antiparallel, the energy is minimal.

The competition between the exchange energy $E_{\rm ex}$ and the dipolar energy $E_{\rm dip}$ is characterized by the exchange length $l_{\rm ex}$, which is typically a few nm. The exchange interaction is dominant at length scales below the exchange length $l_{\rm ex}$ forcing the magnetization to be locally homogeneous. On the other hand, the dipolar interaction dominates at larger length scales, and domains with different orientations of \boldsymbol{M} can be formed.

The exchange field is given by

$$\mathbf{H}_{\mathrm{ex}} = \frac{2A_{\mathrm{ex}}}{\mu_0 M_{\mathrm{s}}^2} \Delta \mathbf{M} = l_{\mathrm{ex}}^2 \Delta \mathbf{M} \equiv \lambda_{\mathrm{ex}} \Delta \mathbf{M},$$
 (1.10)

where Δ is the Laplace operator and $\lambda_{\rm ex}$ is the exchange constant.

If $E_{\rm ex}$ were the only term to consider, there would be no incentive for the orientation of \mathbf{M} to vary, and the magnetization would remain uniform. However, $E_{\rm dem}$ is ever-present, and it tends to reduce the net moment of an isotropic sample to zero.

1.2.4. Anisotropy Energy

Magnetocrystalline anisotropy

In oriented crystalline substances, a ferromagnetic sample's magnetization usually lies along some energetically preferred direction(s) due to the spin-orbit interaction. This property is called magnetic anisotropy. In the description of anisotropies, symmetry plays a major role. Therefore, expansions in terms of spherical harmonics are often used to describe the most important contributions. The simplest case is the uniaxial anisotropy, where the energy density depends only on the angle ϑ , which is the angle between magnetization and the uniaxial anisotropy axis. Generally, the tendency for magnetization to lie along an easy axis is represented by the energy density term

$$\epsilon_{\text{uni}} = K_{\text{u1}} \sin^2 \vartheta + K_{\text{u2}} \sin^4 \vartheta + \dots , \qquad (1.11)$$

where $K_{\rm u1}$ and $K_{\rm u2}$ are anisotropy constants. For magnetic particles with uniaxial magnetic anisotropy, as described by the Stoner-Wohlfarth model later in section 1.4, the $K_{\rm u2}$ constant is usually negligible, therefore does not need to be considered. For the sake of simplicity, the constant $K_{\rm u1}$, being the only constant left, is denoted as $K_{\rm u}$. There are even cases where no term is considered, e.g., in NiFe (Permalloy) films, where the random orientation of grains (crystallites) results in no net in-plane anisotropy.

1.2.5. Total energy

To conclude the description using the micromagnetic theory, the total energy density ϵ_{tot} of the system is sum of all the individual contributions

$$\epsilon_{\text{tot}} = \epsilon_{\text{Z}} + \epsilon_{\text{ex}} + \epsilon_{\text{dip}} + \epsilon_{\text{anj}}$$
 (1.12)

The magnetic ground state of the magnetization might be determined by finding the minima in (1.12). Now we can introduce the total effective magnetic field \mathbf{H}_{eff} . It is defined as the functional derivative of ϵ_{tot} with respect to magnetization \mathbf{M} as

$$\mathbf{H}_{\text{eff}} = -\frac{1}{\mu_0} \nabla_{\mathbf{M}} \epsilon_{\text{tot}} = -\frac{1}{\mu_0} \left(\frac{\partial \epsilon_{\text{tot}}}{\partial M_x} \mathbf{e}_x + \frac{\partial \epsilon_{\text{tot}}}{\partial M_y} \mathbf{e}_y + \frac{\partial \epsilon_{\text{tot}}}{\partial M_z} \mathbf{e}_z \right). \tag{1.13}$$

For equilibrium, \boldsymbol{M} is parallel to $\boldsymbol{H}_{\text{eff}}$. In the dynamic case, the magnetization \boldsymbol{M} does not lie in the direction of $\boldsymbol{H}_{\text{eff}}$, yet $\boldsymbol{H}_{\text{eff}}$ defines the precessional axis of the magnetization.

1.3. Geometry-induced anisotropy

The system that we need to describe is far from trivial. Therefore, the following section addresses the simplification needed to get the contribution of shape and topography individually. The effective anisotropy comprises all contributions to the anisotropy energy into one resulting anisotropy.

1.3.1. Aharoni model of rectangular prism

If the geometry of the sample is to be considered, the combination of (1.5) and (1.7) gives

$$\epsilon_{\text{dem}} = \frac{\mu_0}{2} \left(N_x M_x^2 + N_y M_y^2 + N_z M_z^2 \right) . \tag{1.14}$$

Here, depending on the demagnetizing factors, the energy will differ for different magnetization orientations. This leads to an effective anisotropy of the system called shape anisotropy. The role of the shape anisotropy is non-negligible and starts to play an important part when dealing with mesoscopic magnetic structures. In such structures, the magnetization prefers to lay in the direction parallel to the longer axis of the rectangle. The analytic treatment of the demagnetizing field problem in a magnetic thin film structure of rectangular cross-section is not at all easy task. Nevertheless, it has already been done by Aharoni[40]. He provided the solution for the demagnetizing factor in the z-direction of a magnetic rectangular prism as

$$\pi N_z = \frac{b^2 - c^2}{2bc} \ln \left(\frac{\sqrt{a^2 + b^2 + c^2} - a}{\sqrt{a^2 + b^2 + c^2} + a} \right) + \frac{a^2 - c^2}{2ac} \ln \left(\frac{\sqrt{a^2 + b^2 + c^2} - b}{\sqrt{a^2 + b^2 + c^2} + b} \right)$$

$$+ \frac{b}{2c} \ln \left(\frac{\sqrt{a^2 + b^2} + a}{\sqrt{a^2 + b^2} - a} \right) + \frac{a}{2c} \ln \left(\frac{\sqrt{a^2 + b^2} + b}{\sqrt{a^2 + b^2} - b} \right) + \frac{c}{2a} \ln \left(\frac{\sqrt{b^2 + c^2} + b}{\sqrt{b^2 + c^2} + b} \right)$$

$$+ \frac{c}{2b} \ln \left(\frac{\sqrt{a^2 + c^2} + a}{\sqrt{a^2 + c^2} - a} \right) + 2 \arctan \left(\frac{ab}{c\sqrt{a^2 + b^2} + c^2} \right) + \frac{a^3 + b^3 - 2c^3}{3abc}$$

$$+ \frac{c}{ab} \left(\sqrt{a^2 + c^2} + \sqrt{b^2 + c^2} \right) + \frac{(a^2 + b^2 - 2c^2)\sqrt{a^2 + b^2 + c^2}}{3abc}$$

$$- \frac{(a^2 + b^2)^{\frac{3}{2}} + (b^2 + c^2)^{\frac{3}{2}} + (c^2 + a^2)^{\frac{3}{2}}}{3abc}.$$

$$(1.15)$$

In his assumptions, he considered the total length of 2a, the total width of 2c, and the total thickness of 2b. The other two demagnetizing factors N_x and N_y can be derived by applying twice cyclic permutation $c \to a \to b \to c$. The demagnetizing field calculated for rectangular prism using (1.15) is depicted in Figure 1.3. However, later in the experimental section, the demagnetizing field calculated using the Aharoni model and demagnetizing field measured by Kerr magnetometry will be compared with a poor agreement. The strong assumption of the homogeneously magnetized body employed in the model by Aharoni is not valid for micron-sized structures. Nevertheless, it provides great insight into the problem and serves as an important starting point in the experiment's design. This model must be employed with great care, and one cannot expect a quantitative match of the model and the experiment. On the other hand, the model qualitatively describes the overall trend for rectangular prisms with various aspect ratios. The Aharoni model gives the magnetic field needed to rotate the magnetization in the energetically unpreferred direction (in the case of a rectangular prism, the direction perpendicular to the longer edge).

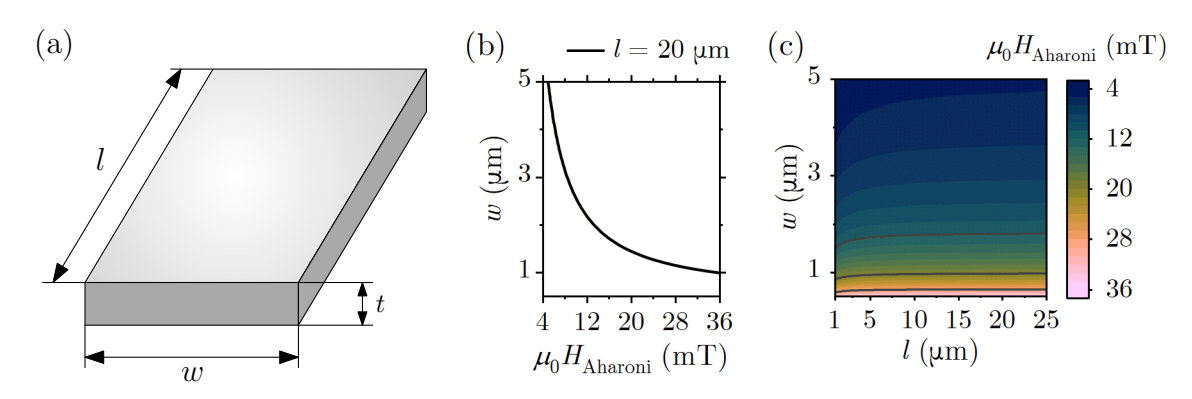


Figure 1.3: (a) Geometry of a rectangular prism, l=2a, w=2b, t=2b. (b) Demagnetizing field, calculated using Aharoni model (1.15) for the following parameters: length $l=20\,\mu\mathrm{m}$, thickness $t=10\,\mathrm{nm}$ and $M_\mathrm{s}=800\,\mathrm{kA/m}$. (c) Variation of both width and length for the thickness $t=10\,\mathrm{nm}$.

1.3.2. Curvature-induced anisotropy

As we mentioned above, due to the complex shape of our structures, we are not able to analytically obtain the demagnetizing tensor. We can only measure the total effective anisotropy and then simplify it as the anisotropy from two individual contributors – shape and topography. This paragraph is devoted to the latter category.

The shape anisotropy has a significant effect on the ground-state magnetization direction. Nevertheless, even in the case of strong anisotropy, the magnetization might not be strictly tangential. For example, in the case of a helical nanowire, which has strong anisotropy pointing along the wire, the ground state is tilted with an angle, dependent on the curvature product and the torsion [41, 42]. In the Magnetism in curved geometries review by Streubel et al. [15], 2D geometries with nontrivial topology are discussed. Bruno [43] theoretically showed that the surface roughness gives rise to an effective dipolar perpendicular anisotropy whose order of magnitude is evaluated as a function of the parameters characterizing the roughness. However, further studies show that in magnetic nanostructures with large-scale varying curvature, the magnetization prefers to stay in a plane tangential to the surface [44–46]. Bisio et al. [47] utilized ion beam erosion to

induce uniaxial magnetic anisotropy in Fe thin films on a flat Ag(001) substrate. The selection of an induced in-plane uniaxial magnetic anisotropy direction in a thin film of Fe grown epitaxially on ripple patterned MgO(001) was reported by Liedke et al. [48]. Vayalil et al. [49] tailored the uniaxial magnetic anisotropy of Permalloy thin films deposited on nano rippled Si substrates. Tretiakov et al. [16] summarized it and introduced the method of surface engineering of an ultrathin magnetic film. Their method uses the effect of large periodic curvature on the shape anisotropy forming perpendicular or any other given direction of magnetic anisotropy. The method is solely related to the interplay of surface curvature and dipolar interactions in the film and, therefore, does not require any spin-orbit coupling. Basically, using their approach, it is possible to engineer perpendicular magnetic anisotropy or in-plane magnetic anisotropy of any particular orientation in thin films with periodic curvature just by choosing the surface shape appropriately.

1.3.3. Mixed anisotropies

Now, we further describe the used simplification of individual anisotropy terms, describing shape and curvature of our complex structure. We consider the case of a rectangular-shaped polycrystalline NiFe structure with curvature-induced uniaxial anisotropy perpendicular to the longer edge of the rectangle. The shape anisotropy energy density is analogous to the form of the uniaxial anisotropy discussed in equation (1.11). The rectangular waveguide is magnetized at some arbitary angle, as shown in Figure 1.4. Therefore the total energy density with the assumption of zero applied field is

$$\epsilon_{\rm T} = \epsilon_{\rm s} + \epsilon_{\rm c} = K_0 + K_{\rm s} \sin^2 \vartheta + K_{\rm c} \sin^2 (\pi/2 - \vartheta) = K_0 + (K_{\rm s} - K_{\rm c}) \sin^2 \vartheta + K_{\rm c},$$
 (1.16)

where ϵ_s is the energy density of the shape anisotropy contribution, ϵ_c is the energy density of the curvature-induced anisotropy contribution and K_s , K_c are corresponding anisotropy constants. To find the resulting anisotropy, the first and second derivatives must be found. They are given by

$$\frac{\partial \epsilon_{\rm T}}{\partial \vartheta} = 2 \left(K_{\rm s} - K_{\rm c} \right) \sin \vartheta \cos \vartheta \,, \tag{1.17}$$

$$\frac{\partial^2 \epsilon_{\rm T}}{\partial \vartheta^2} = 2 \left(K_{\rm s} - K_{\rm c} \right) \cos 2\vartheta \,. \tag{1.18}$$

In the trivial case of $K_s = K_c$, there is no anisotropy or angular dependence, and the magnetization can point in any arbitrary direction. Nevertheless, if $K_s > K_c$ we can study two cases. For $\vartheta = 0$, $\frac{\partial \epsilon_T}{\partial \vartheta} = 0$, $\frac{\partial^2 \epsilon_T}{\partial \vartheta^2} > 0$ and the easy axis given by the shape anisotropy is a direction of minimum energy. For $\vartheta = \pi/2$, $\frac{\partial \epsilon_T}{\partial \vartheta} = 0$, $\frac{\partial^2 \epsilon_T}{\partial \vartheta^2} < 0$ and the easy axis given by the curvature-induced anisotropy is a direction of maximum energy. On the other hand, if $K_s < K_c$ the situation is completely reversed for $\vartheta = 0$ and $\vartheta = \pi/2$. Finally, suppose a structure under study has anisotropies arising from different phenomena, and their respective easy axes are perpendicular to one another. In that case, the resulting easy direction is not given (as someone might intuitively think) by some intermediate direction. It is one of the two easy directions, depending on the magnitude of anisotropy energies.

In summary, when the system has, e.g., two contributing uniaxial anisotropies, two general rules can be found. First, when the anisotropies have their axes parallel to each other, the total energy adds up to form an even stronger anisotropy. When the axes of the contributing anisotropies are perpendicular to each other, the resulting easy axis is in

the stronger anisotropy direction. The difference between the two contributions gives the energy.

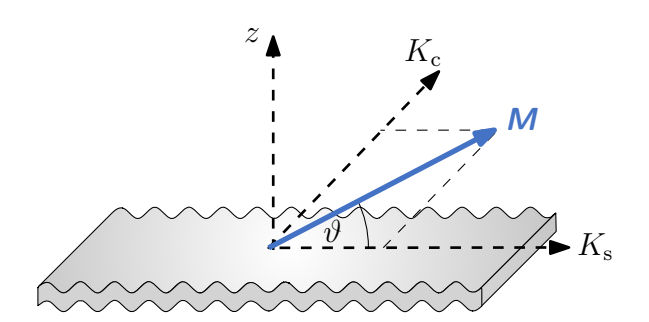


Figure 1.4: Schematic representation of a rectangular waveguide with curvature-induced anisotropy magnetized in-plane at the arbitary angle ϑ . $K_{\rm s}$ is the shape anisotropy constant and $K_{\rm c}$ is the curvature-induced anisotropy constant.

1.4. Stoner-Wohlfarth model

In magnetic materials, the magnetization M response to the applied magnetic field H is in general nonlinear and irreversible. Its value depends both on the history of the applied magnetic field and the magnetization orientation. Such behavior is captured in a well-known M(H) hysteresis loop, sketched in Figure 1.5 where the component of M in the direction of the applied field H is plotted. From the shape of a loop, one can already analyze the magnetic system. The curve starting at the origin is known as a *virgin*

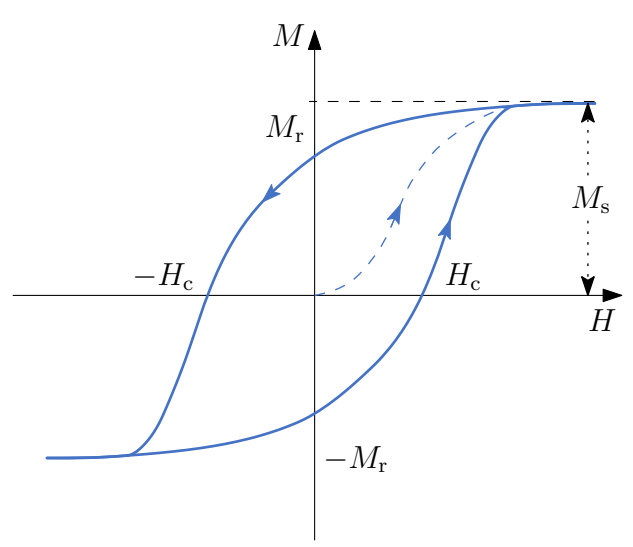


Figure 1.5: Schematic representation of a hysteresis curve of a typical ferromagnetic material. The virgin curve is represented by the dashed curve. Saturation magnetization $M_{\rm s}$, remanence $M_{\rm r}$ and coercivity $H_{\rm c}$ are shown. Adapted from [29].

magnetization curve. It can be measured only for the case of a sample never exposed to the magnetic field or for a fully demagnetized sample. When H is high enough, all magnetic moments are aligned with the direction of the external magnetic field H, and the component of magnetization reaches the saturation value $M_{\rm s}$. Lowering the applied magnetic field H will result in the decrease of the magnetization component in the arrow's direction (see Figure 1.5). The remanent magnetization or remanence $M_{\rm r}$ is the remaining magnetization projection when the applied magnetic field reaches zero. In order to reduce the magnetization to zero, the coercive field $H_{\rm c}$ must be applied.

The modeling of the hysteretic behavior has historically been performed by empirical models where Stoner and Wohlfarth have used a newly developed micromagnetic theory as a first to do so. Their model is called the coherent rotation model and it is a simple, nevertheless compelling micromagnetic model. It considers magnetization processes

governed by the magnetization vector's rotations or switching and is essentially based on micromagnetic energies [50, 51]. A detailed description of many micromagnetic models is given in the book [52]. This model's main assumption is that the material is made up of magnetized elliptical nanoparticles with a uniaxial anisotropy constant $K_{\rm u}$, sufficiently separated from each other so that interactions between them are negligible. A key prediction for the Stoner-Wohlfarth model is that the coercive field is equal to the anisotropy field. That is very strong assumption, and generally, the coercive field is overestimated by a lot. If a magnetic field is applied at an angle φ to the anisotropy axis, the total energy density is the sum of the uniaxial anisotropy energy density $\epsilon_{\rm uni}$ and the Zeeman energy density $\epsilon_{\rm Z}$

$$\epsilon = \epsilon_{\text{uni}} + \epsilon_{\text{Z}} = K_{\text{u}} \sin^2 \vartheta - \mu_0 M_{\text{s}} H \cos (\varphi - \vartheta).$$
 (1.19)

The magnetization M will always align in the direction of minimal total energy either by rotation or by switching. The geometry of the elliptical magnetic nanoparticle is shown in Figure 1.6.

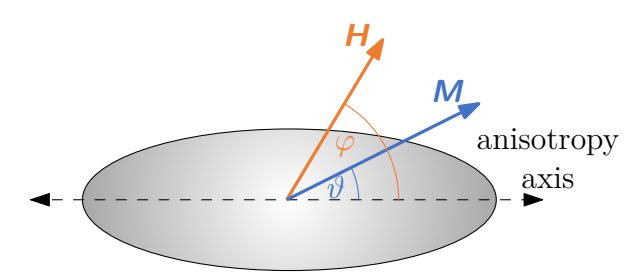


Figure 1.6: A Stoner-Wohlfarth elliptical nanoparticle with magnetization \boldsymbol{M} in an external magnetic field \boldsymbol{H} . Corresponding angles φ and ϑ are shown with respect to the anisotropy axis.

In order to find the M(H) loop, the numerical methods solving the minimization of energy by changing the the angle θ must be employed. However, for the simple case of $\varphi = 0$ and $\varphi = \pi/2$ it can be solved analytically using the first and second derivative of ϵ .

$$\frac{\partial \epsilon}{\partial \vartheta} = 2K_{\rm u} \sin \vartheta \cos \vartheta - \mu_0 M_{\rm s} H \sin(\varphi - \vartheta) = 0, \qquad (1.20)$$

$$\frac{\partial^2 \epsilon}{\partial \vartheta^2} = 2K_{\rm u} \cos 2\vartheta + \mu_0 M_{\rm s} H \cos(\varphi - \vartheta) \ge 0. \tag{1.21}$$

When the magnetic field is applied in the direction of the anisotropy axis $(\varphi = 0)$, the energy density (1.19) has two minima. The first minimum is at $\vartheta = 0$ (\rightarrow) and the second at $\vartheta = \pi$ (\leftarrow). By changing the magnitude of the external field so that the magnetization goes from the first minimum (\rightarrow) to the second (\leftarrow), we can find the value of the coercive field, where the magnetization flips as

$$H_{\text{ext}} = -H_{\text{c}} = \frac{2K_{\text{u}}}{\mu_0 M_{\text{s}}}.$$
 (1.22)

Increasing field back to the original value will lead again in the magnetization switch at the external field $H_{\rm ext}=H_{\rm c}$. The resulting loop, called the easy-axis loop, is a perfect square loop, see Figure 1.7. For $\varphi=\pi/2$ the loop degenerates into a piecewise linear function. Even though the assumption of a coercive field being equal to an anisotropy field does not apply in real materials, the anisotropy field can be derived using this model with a good precision. The anisotropy field $H_{\rm ani}$ is defined as the field needed to reach the saturation. For fields lower than the anisotropy field, a linear function with slope $\frac{{\rm d}M}{{\rm d}H}=\frac{2K_{\rm u}}{\mu_0 M_{\rm s}^2}$ is obtained. This hysteresis loop is called a hard-axis loop. The anisotropy field is then

$$H_{\rm ani} = \frac{2K_{\rm u}}{\mu_0 M_{\rm s}}.\tag{1.23}$$

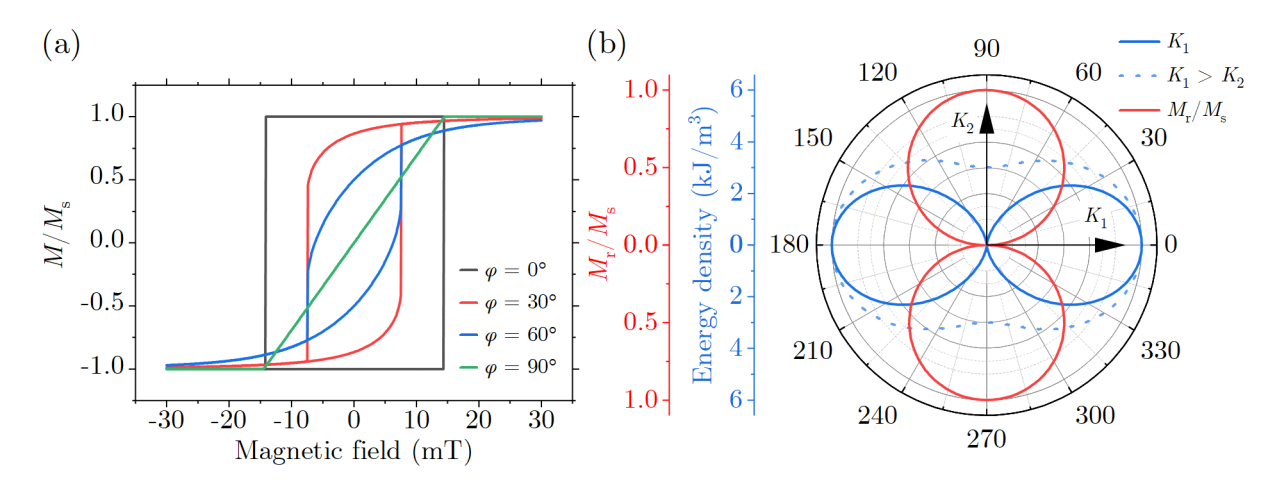


Figure 1.7: (a) Numerical modeling of hysteresis loops using Stoner-Wohlfarth model² for the uniaxial magnetic anisotropy case considering K_u = 6 kJ/m³, M_s = 800 kA/m for the four representative angles from the interval φ ∈ [0,π/2]. (b) The blue solid polar plot shows the total energy density when no external magnetic field is applied for the case when only one anisotropy axis is present; K₁ = 6 kJ/m³. The dotted blue polar plot, on the other hand, depicts the case where there are two anisotropy axis perpendicular to each other; K₁ = 6 kJ/m³ and K₂ = 3 kJ/m³. The dependence is depicted for the energy density on the angle between the easy axis and the magnetization − ϑ. The red solid polar plot shows the relative remanence extracted at the zero external magnetic field from graph (a). The easy and hard axis directions are clearly visible. Note the difference between the shape of blue and red plots.

1.5. Magnetization dynamics

This section gives a brief introduction to the theory of magnetization dynamics. It describes what happens with the magnetization when the time-varying external magnetic field is applied. The Landau-Lifschitz-Gilbert equation of motion will be introduced, and the complex dynamic susceptibility tensor will be derived.

When magnetization \mathbf{M} and effective magnetic field \mathbf{H}_{eff} are non-collinear, the magnetization will experience non-zero restoring torque. The torque causes the magnetization \mathbf{M} to move according to Newton's classical equation of motion [33, page 85]. This yields the well-known Landau-Lifshitz equation [28, 33]

$$\frac{\mathrm{d}\mathbf{M}}{\mathrm{d}t} = -\gamma \mathbf{M} \times \mu_0 \mathbf{H}_{\mathrm{eff}} \,, \tag{1.24}$$

where γ is a gyromagnetic ratio. This leads to the Larmor precession of \mathbf{M} around the magnetic field \mathbf{H}_{eff} with the angular frequency $\omega = \mu_0 \gamma H_{\text{eff}}$ with a constant cone angle ϑ .

However, equation (1.24) describes an idealized case and does not comprise the dissipation of energy. To account this, a second torque term is added into the Landau-Lifshitz equation introducing a phenomenological damping torque [53]

$$\frac{\mathrm{d}\mathbf{M}}{\mathrm{d}t} = -\gamma \mathbf{M} \times \mu_0 \mathbf{H}_{\mathrm{eff}} - \frac{\gamma \lambda}{M_{\mathrm{s}}^2} \mathbf{M} \times (\mathbf{M} \times \mu_0 \mathbf{H}_{\mathrm{eff}}). \tag{1.25}$$

²The numerical modeling was done in Python, adapting the code from https://github.com/tgwoodcock/Stoner-Wohlfarth-Tutorial.

Here, λ is a phenomenological damping parameter. The damping term derived by T. Gilbert transforms equation (1.25) to the famous Landau-Lifshitz-Gilbert (LLG) equation [54]

$$\frac{\partial \mathbf{M}}{\partial t} = \underbrace{-\gamma \mathbf{M} \times \mu_0 \mathbf{H}_{\text{eff}}}_{\text{precession term}} + \underbrace{\frac{\alpha}{M_s} \left(\mathbf{M} \times \frac{\partial \mathbf{M}}{\partial t} \right)}_{\text{damping term}},$$
(1.26)

where α is the Gilbert damping parameter. The first term in equation (1.26) is a precessional term and the second term (damping term) corresponds to a torque which forces M to align parallel to H_{eff} . It represents the energy dissipation channels, e.g. the interactions between spin system and the electrons as well as the lattice (phonons). All these effects are incorporated in the phenomenological Gilbert damping constant α . Thus, the combined effect of both terms results in a damped spiral motion of the magnetization around the effective magnetic field toward the equilibrium state, as graphically illustrated in Figure 1.8.

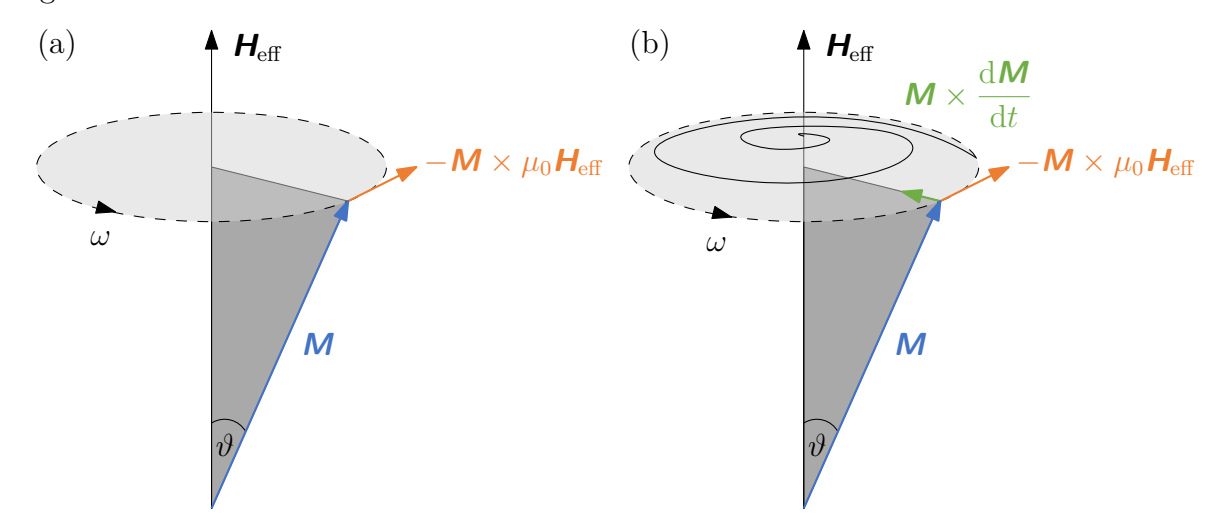


Figure 1.8: Precessional motion of the magnetization \mathbf{M} in effective field $\mu_0 \mathbf{H}_{\text{eff}}$ according to the LLG equation (1.26). (a) The precession of \mathbf{M} around \mathbf{H}_{eff} at the angular frequency ω . (b) The precession of \mathbf{M} in combination with the damping torque term which leads to the overall spiral motion around \mathbf{H}_{eff} .

1.5.1. Dynamic susceptibility

Finding an analytical solution for the general form of the Landau-Lifshitz-Gilbert equation (1.26) is impossible, and it is usually solved numerically. However, the analytical solution of the collective oscillations in a linear regime is possible. It is done by solving the Landau-Lifshitz equation (1.24) for the ferromagnetic system under the following assumptions.

- The ferromagnetic system is under the effect of the magnetic field, which consists of a static part $\mathbf{H}_0 = H_0 \mathbf{e}_z$ applied along the z-axis and of a small harmonic (microwave) excitation field $|\mathbf{h}(t)| \ll H_0$ oriented in the xy plane. Vector \mathbf{e}_z is a unit vector pointing along the z-axis.
- The total magnetic field is then $\mathbf{H}_{\text{eff}} = \mathbf{H}_0 + \mathbf{h}(t)$.
- The equilibrium magnetization \mathbf{M}_0 is oriented parallel to the static part of the magnetic field \mathbf{H}_0 .

- The dynamic component $\mathbf{m}(t)$ of the magnetization is assumed to be small compared to the saturation magnetization $|\mathbf{m}| \ll M_{\rm s}$
- m(t) depends harmonically on time t and the precession occurs around the z-axis.
- The total magnetization is then $\mathbf{M} = \mathbf{M}_0 + \mathbf{m}(t)$.

Inserting this into equation (1.24) gives

$$\frac{\partial \mathbf{m}}{\partial t} = -\gamma \mu_0 \left(\underbrace{\mathbf{M}_0 \times \mathbf{H}_0}_{0} + \mathbf{M}_0 \times \mathbf{h} + \mathbf{m} \times \mathbf{H}_0 + \underbrace{\mathbf{m} \times \mathbf{h}}_{\text{neglected}} \right). \tag{1.27}$$

The first term vanishes because the equilibrium magnetization \mathbf{M}_0 is parallel to the static part of applied field \mathbf{H}_0 . The last term can be neglected due to the assumption of \mathbf{h} and \mathbf{m} being small compared to the magnitude of static components. The result gives linearized LL equation

$$\frac{\partial \mathbf{m}}{\partial t} = -\gamma \mu_0 \left[\mathbf{M}_0 \times \mathbf{h} + \mathbf{m} \times \mathbf{H}_0 \right]. \tag{1.28}$$

Assuming the harmonic time dependence in the form $e^{i\omega t}$

$$i\omega \mathbf{m} = -\gamma \mu_0 \left[M_s \mathbf{e}_z \times \mathbf{h} + \mathbf{m} \times H_0 \mathbf{e}_z \right] , \qquad (1.29)$$

$$i\omega \mathbf{m} = -\mathbf{e}_z \times [\omega_M \mathbf{h} - \omega_H \mathbf{m}] , \qquad (1.30)$$

where $\omega_M = \gamma \mu_0 M_s$ and $\omega_H = \gamma \mu_0 H_0$. Projecting along the axes of the coordinate system leads to a set of equations.

$$i\omega m_x = \omega_M h_y - \omega_H m_y \,, \tag{1.31}$$

$$i\omega m_y = -\omega_M h_x + \omega_H m_x \,, \tag{1.32}$$

$$i\omega m_z = 0. ag{1.33}$$

Rewriting the equations (1.31) - (1.33) in a matrix form gives

$$\begin{pmatrix} \omega_H & -\mathrm{i}\omega \\ \mathrm{i}\omega & \omega_H \end{pmatrix} \begin{pmatrix} m_x \\ m_y \end{pmatrix} = \omega_M \begin{pmatrix} h_x \\ h_y \end{pmatrix}. \tag{1.34}$$

To extract the susceptibility tensor $\hat{\chi}$ after Polder [55], an inverse matrix needs to be found

$$\begin{pmatrix} m_x \\ m_y \end{pmatrix} = \mathbf{m} = \hat{\boldsymbol{\chi}} \cdot \mathbf{h} = \begin{pmatrix} \chi & \mathrm{i}\kappa \\ -\mathrm{i}\kappa & \chi \end{pmatrix} \begin{pmatrix} h_x \\ h_y \end{pmatrix} , \qquad (1.35)$$

where

$$\chi = \frac{\omega_H \omega_M}{\omega_H^2 - \omega^2} \quad \text{and} \quad \kappa = \frac{\omega \omega_M}{\omega_H^2 - \omega^2}.$$
(1.36)

The Polder tensor is a non-diagonal non-symmetric tensor describing the gyrotropic behavior of the ferromagnetic medium. The microwave magnetic field $(h_x$ and $h_y)$ creates not only the dynamical magnetization parallel to it $(m_x, m_y, \text{respectively})$ but also a perpendicular components with a $\pi/2$ phase shift corresponding to the imaginary unit i in (1.35). This response to the microwave magnetic field excitation confirms the precessional motion of \mathbf{M} .

1.5.2. Ferromagnetic resonance

The Polder susceptibility tensor $\hat{\chi}$ described in the previous section is derived under the assumption of the known field at a given point. However, this is an oversimplification because the demagnetizing field \mathbf{H}_{dem} depends on the magnetization \mathbf{M} inside the sample. Therefore, the LL equation solution in an ellipsoidal geometry, where the magnetization is uniformly distributed, will be provided in this section. The ellipsoid's principal axes are parallel to the x, y, and z axes. The ellipsoid is depicted in Figure 1.9.

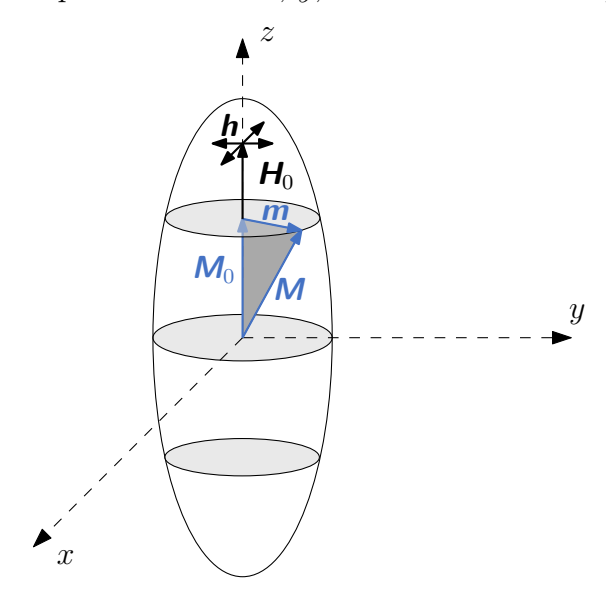


Figure 1.9: The uniform oscillation of magnetization M in an ellipsoid.

A static magnetic field $\mathbf{H}_0 = H_0 \mathbf{e}_z$ is applied along the z-axis and a small oscillating field \mathbf{h} is applied in the xy plane. Considering the demagnetizing field (1.5) the effective field is defined as

$$\mathbf{H}_{\text{eff}} = \mathbf{H}_0 + \mathbf{H}_{\text{dem}} \,. \tag{1.37}$$

Rewriting equation (1.37) in a vector form leads to

$$\mathbf{H}_{\text{eff}} = \begin{pmatrix} h_x - N_x m_x \\ h_y - N_y m_y \\ H_0 - N_z M_s \end{pmatrix} . \tag{1.38}$$

Solving the LL equation following the section 1.5.1, the Kittel susceptibility tensor is derived

$$\mathbf{h} = \hat{\mathbf{\chi}}_{K}^{-1} \mathbf{m} = \begin{pmatrix} h_{x} \\ h_{y} \end{pmatrix} = \frac{1}{\omega_{M}} \begin{pmatrix} \omega_{x} & -i\omega \\ i\omega & \omega_{y} \end{pmatrix} \begin{pmatrix} m_{x} \\ m_{y} \end{pmatrix}, \tag{1.39}$$

where $\omega_x = \omega_H + (N_x - N_z)\omega_M$ and $\omega_y = \omega_H + (N_y - N_z)\omega_M$.

The resonance frequency can be derived by solving $\det \left(\hat{\boldsymbol{\chi}}_{K}^{-1} \right) = 0$ which yields the famous Kittel formula

$$\omega_{\text{res}} = \sqrt{\omega_x \omega_y} = \gamma \mu_0 \sqrt{\left[H_0 + (N_x - N_z) M_s\right] \left[H_0 + (N_y - N_z) M_s\right]}$$
 (1.40)

It is clearly visible that the resonance frequency strongly depends on the sample geometry. For the simplest spherical geometry where the demagnetizing factors are $N_x = N_y = N_z = 1/3$ the resonant frequency is $\omega_{\rm res} = \gamma \mu_0 H_0$. For the in-plane magnetized ferromagnetic thin film where $N_x = N_z = 0$ and $N_y = 1$ the resonant frequency is given by

$$\omega_{\rm res} = \gamma \mu_0 \left[H_0 \left(H_0 + M_{\rm s} \right) \right]^{1/2}.$$
 (1.41)

The magnetization's oscillations are unquestionably accompanied by dissipation of the energy. To account for the dissipation of energy, equation (1.26) must be solved. It results in the correction of the tensor $\hat{\chi}$ components. It is sufficient to replace the real frequency ω in (1.36) by the complex quantity $\omega' + i\omega''$. Thus, the χ_{yy} component of the susceptibility tensor $\hat{\chi}$ is given by

$$\chi_{yy} = \frac{\omega_M \left(\omega_H + \omega_M - i\omega\right)}{\omega_{res}^2 - \omega^2 - i\alpha\omega \left(2\omega_H + \omega_M\right)}.$$
 (1.42)

It can be split into the real and imaginary parts $\chi_{yy} = \chi'_{yy} + i\chi''_{yy}$

$$\operatorname{Re}(\chi_{yy}) = \chi'_{yy} = \frac{\omega_M (\omega_H + \omega_M) (\omega_{\text{res}}^2 - \omega^2)}{(\omega_{\text{res}}^2 - \omega^2)^2 + \alpha^2 \omega^2 (2\omega_H + \omega_M)^2}, \tag{1.43}$$

$$\operatorname{Im}(\chi_{yy}) = \chi_{yy}'' = \frac{\alpha \omega \omega_M \left[\omega^2 + (\omega_M + \omega_H)^2\right]}{(\omega_{\text{res}}^2 - \omega^2)^2 + \alpha^2 \omega^2 \left(2\omega_H + \omega_M\right)^2}.$$
 (1.44)

The imaginary part can be approximated by an assymetric Lorentzian function and its maximum is found for $\omega = \omega_{\rm res}$. The linewidth $\Delta \omega$ of the Lorentzian peak is connected with the damping parameter α . In the assumption of $\Delta \omega \ll \omega_{\rm res}$, a full width at half maximum (FWHM) of ω yields

$$\Delta\omega = \alpha \left(2\omega_H + \omega_M\right) \,. \tag{1.45}$$

The connection of the linewidth $\Delta\omega$ and the linewidth ΔH is also observed. It is often interpreted in terms combining the inhomogeneous broadening ΔH_0 , representing the extrinsic contributions to the damping, and Landau-Lifshitz or Gilbert damping model [56]. Therefore

$$\mu_0 \Delta H = \frac{4\pi \alpha f_{\text{res}}}{\gamma} + \mu_0 \Delta H_0. \tag{1.46}$$

Influence of a uniaxial magnetic anisotropy

The energy of the magnetic anisotropy is also affecting the total effective field. In the case of the uniaxial anisotropy, the first term of energy density (1.11) can be rewritten as

$$\epsilon_{\rm ani} = K_{\rm u} \sin^2 \vartheta = K_{\rm u} \left(1 - \frac{M_i^2}{M_{\rm s}^2} \right) \,, \tag{1.47}$$

where M_i is the component of **M** along the anisotropy axis.

The effective field gives

$$\mathbf{H}_{\rm ani} = -\frac{1}{\mu_0} \frac{\partial \epsilon_{\rm ani}}{\partial \mathbf{M}} = \frac{2K_{\rm u}M_i}{\mu_0 M_{\rm s}^2} \mathbf{e}_i \,.$$
 (1.48)

In a general ellipsoid case, the uniaxial anisotropy axis \mathbf{e}_i can point in any direction. For simplicity, let us limit our calculations to two cases. The external magnetic field \mathbf{H}_0 points along the z-axis, and it is either perpendicular or parallel to the anisotropy axis. The expression for the anisotropy field can be written in a similar form to the demagnetizing field $\mathbf{H}_{\rm ani} = -\hat{\mathbf{N}}_{\rm ani} \cdot \mathbf{M}$. As we mentioned above, the structure's complex

shape (demagnetizing tensor) can be simplified by including the shape and curvature individually

$$\mathbf{H}'_{\text{ani}} = -\left(\hat{\mathbf{N}} + \hat{\mathbf{N}}_{\text{ani}}\right) \cdot \mathbf{M} = -\begin{pmatrix} N_x + N_{\text{ani},x} & 0 & 0\\ 0 & N_y + N_{\text{ani},y} & 0\\ 0 & 0 & N_z + N_{\text{ani},z} \end{pmatrix} \begin{pmatrix} m_x\\ m_y\\ M_s \end{pmatrix}. (1.49)$$

The demagnetizing factors N_x , N_y , N_z in equation (1.40) can be replaced by new factors $N'_x = N_x + N_{\text{ani},x}$, $N'_y = N_y + N_{\text{ani},y}$, $N'_z = N_z + N_{\text{ani},z}$, respectively. The effect of uniaxial anisotropy is thoroughly studied in [57, pages 44-45] and [58, pages 22-26]. Here, they transform the coordinates and perform substitution to express the effect of uniaxial anisotropy on the ferromagnetic resonance, which gives

$$\omega_{\rm r} = \gamma \mu_0 \left\{ \left[H_0 \cos(\vartheta - \varphi) + \frac{2K_{\rm u}}{\mu_0 M_{\rm s}} \cos^2 \vartheta + (N_x - N_z) M_{\rm s} \right] \times \left[H_0 \cos(\vartheta - \varphi) + \frac{2K_{\rm u}}{\mu_0 M_{\rm s}} \cos 2\vartheta + (N_y - N_z) M_{\rm s} \right] \right\}^{1/2}.$$

$$(1.50)$$

For the case of in-plane magnetized ferromagnetic thin film $(N_x = N_z = 0, N_y = 1)$ with uniaxial anisotropy parallel to the direction of the applied field $(\vartheta = \varphi = 0)$, the resonant frequency, employing (1.50), can be then written as

$$\omega_{\rm res} = \gamma \mu_0 \left[\left(H_0 + \frac{2K_{\rm u}}{\mu_0 M_{\rm s}} \right) \left(H_0 + M_{\rm s} + \frac{2K_{\rm u}}{\mu_0 M_{\rm s}} \right) \right]^{1/2}, \tag{1.51}$$

and for the external magnetic field perpendicular to the direction of the uniaxial anisotropy $(\vartheta = \varphi = \pi/2)$

$$\omega_{\rm res} = \gamma \mu_0 \left[H_0 \left(H_0 + M_{\rm s} - \frac{2K_{\rm u}}{\mu_0 M_{\rm s}} \right) \right]^{1/2} .$$
 (1.52)

It is clearly seen that the term representing the effect of anisotropy shifts the resonant frequency to either lower or higher magnetic fields, depending on the orientation of the external magnetic field. If the external magnetic field is collinear with the anisotropy axis, the resonant frequency is increased. One can look at it as if the effective anisotropy field $H_{\rm ani}$ is added to the external magnetic field. However, when the magnetic field is perpendicular to the anisotropy axis, the resonant frequency is lowered because, effectively, the demagnetizing factor N_y is lowered. The dependence of the resonant frequency on the magnetic field for various geometries is depicted in Figure 1.10. In this figure, the resonant frequency of the sphere, out-of-plane magnetized ferromagnetic film, and in-plane magnetized thin film with no anisotropy and for two cases of uniaxial anisotropy can be found. The sphere and out-of-plane magnetized ferromagnetic thin film are depicted to give the full overview of possible geometries. Further, the case of an in-plane magnetized ferromagnetic film with and without anisotropy will be discussed.

For the external magnetic field being collinear with the uniaxial anisotropy direction, the most significant difference compared to the thin film without anisotropy is the non-zero FMR frequency without any external magnetic field. That is possible only due to the uniaxial magnetic anisotropy. When the field is perpendicular to the direction of the uniaxial anisotropy, for the fields $\mu_0 H_{\rm ext} < \mu_0 H_{\rm ani}$ the frequency goes down due to the realignment of magnetization from the uniaxial anisotropy direction to the direction of

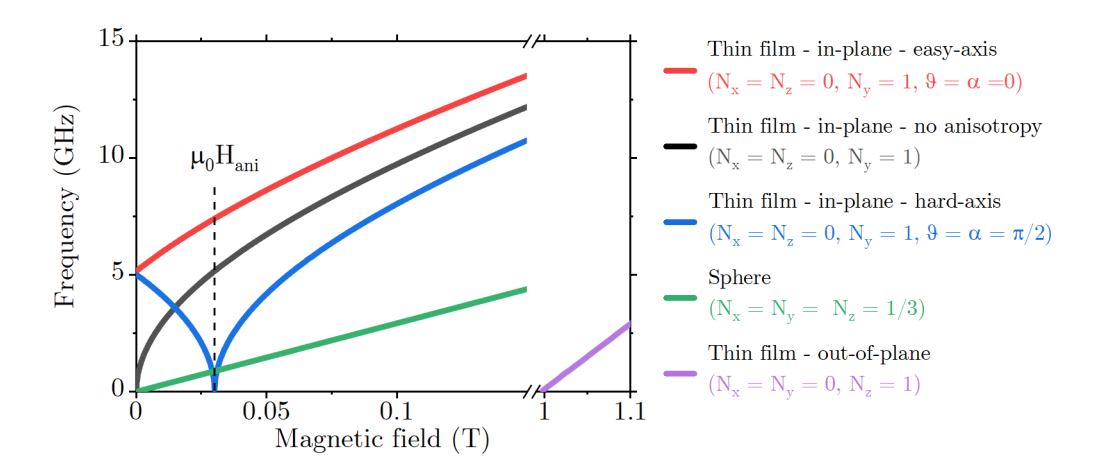


Figure 1.10: Ferromagnetic resonance calculated for various geometries. The red line represents the case where the magnetic field is collinear with the uniaxial anisotropy axis. Therefore, the resonant frequency is increased. The black line is the resonant frequency for the in-plane magnetized ferromagnetic thin film calculated using (1.41). The blue line shows the case of the magnetic field oriented perpendicular to the uniaxial anisotropy axis. The green line represents the simplest case of spherical geometry, and the violet line corresponds to the out-of-plane magnetized ferromagnetic thin film. The calculation was done for NiFe. Parameters of the calculation are: $M_{\rm s} = 800\,{\rm kA/m},~K_{\rm u} = 12\,{\rm kJ/m^3},~{\rm and}~\gamma/(2\pi) = 29.3\,{\rm GHz/T}.$

the external magnetic field. When $\mu_0 H_{\rm ext} = \mu_0 H_{\rm ani}$, the thin film is fully saturated in the direction of the external magnetic field, and the FMR frequency is zero as the applied magnetic field completely compensates the uniaxial magnetic anisotropy and thus fully cancels the restoring force acting on the magnetization. Finally, for $\mu_0 H_{\rm ext} > \mu_0 H_{\rm ani}$, the frequency increases with the magnetic field, and the behavior is similar to the easy axis or the thin film without anisotropy cases, but it is shifted to the higher magnetic fields.

1.6. Damping

In this section, the effects incorporated in the most common sources of damping will be briefly reviewed. In this context, damping represents the dimensionless parameter α from equation (1.26) usually referred to as the Gilbert damping constant. For those who have a taste for deeper understanding, Gurevich and Melkov [57], Stancil [59], and Azzawi et al. [60] deal with this topic thoroughly. The routes for the loss of energy in magnetic systems can be mediated in many ways. They are commonly described as intrinsic and extrinsic processes. These damping processes represent two broadly defined classes of mechanisms. The intrinsic processes are inherent to the system's fundamental physical state. They are defined as the Gilbert-type relaxation represented by the damping term in equation (1.26). Extrinsic damping is the non-Gilbert type of relaxation. It is linked to defects or other non-uniformities in the magnetic material. The different pathways for the dissipation of energy end in microscopic thermal motion.

Overall in calculations, the LLG equation application in micromagnetic simulations utilizes the single value of the Gilbert damping parameter α , which rather empirically combines all damping contributions.

Intrinsic damping

Intrinsic relaxation in the ferromagnetic layer originates in spin-orbit coupling (SOC). Without the SOC, which links the magnon and phonon lattices, there would be no damping of the uniform mode (k=0) [61–63]. Kamberský [64–66] explained the mechanism of intrinsic damping in bulk metallic materials expressing the phenomenological damping parameter λ from equation (1.25). In his model, he used a torque originating from spin-orbit interaction to derive the Hamiltonian using the one-electron model. Overall, the bulk material's primary intrinsic source of damping is the SOC and the dissipation of the energy to the lattice caused by the electron-hole recombination.

If an impurity is present, the mechanism comes from modifying the electron-magnon interaction [67, 68]. It enables the otherwise-forbidden violation of conservation of the momentum resulting in the dissipation of the energy from the uniform magnon mode (k=0) directly to the lattice.

In multilayered thin films, sharp interfaces lead to the higher localization of the interaction between the conduction electrons and magnons [69]. This may lead to an increase of the damping due to the difference in momentum between spin "up" and "down" states at the Fermi level. At the interface, due to the spin-flip process, allowing electrons to cross the momentum gap between spin-up and spin-down states, the Gilbert damping parameter is modified [69, 70].

Extrinsic damping

Extrinsic damping processes are connected to the ferromagnetic system's inhomogeneities such as defects, impurities, non-uniformity of the sample surface, local anisotropies, local magnetization orientation, etc. **Two magnon scattering** describes the interaction between uniform (k = 0) and non-uniform $(k \neq 0)$ resonance modes. The uniform spin waves can be scattered at scattering centers to non-uniform states and dissipate energy into the lattice [17, 71]. The occurrence of two magnon scattering highly depends on the structure defects, grain and grain boundaries [72, 73]. The exchange interaction forces magnetization in the system to align parallel. In contrast, over longer distances, magnetic moments interact through dipolar interaction. The combination of these interactions leads to the formation of magnetic domains, separated by domain walls. In the multi-domain state, the uniform resonant mode of each domain affects the precession and excites additional magnon modes. Through these modes, the energy is lost via a two-magnon mechanism³. The extrinsic relaxation is affected due to grains being the scattering centers for the two magnon scattering, but grains also increase the damping parameter itself [76].

Another extrinsic contribution to the damping comes from the interaction of the high-frequency magnetic field associated with the propagation of spin waves with the metallic nature of the magnetic films used in this thesis. The combination of the high-frequency magnetic field and conductive layers results in the formation of eddy currents formation and thus forms another damping channel for the magnetic excitations. The **eddy-current damping** has been recognized since the 1960s [77, 78]. It is a contribution to the relaxation caused by the screening of the electromagnetic microwave field by the conduction electrons [79]. According to Faradays's law, an AC voltage is induced when a conducting

³Two magnon scattering can be suppressed by applying the out-of-plane DC field [74, 75], because no degenerate modes are available for the out-of-plane geometry. Hence, to eliminate the two magnon scattering contribution and get the intrinsic Gilbert damping parameter, out-of-plane measurements are preferable.

material passes through the time-varying magnetic flux created by a microwave magnetic field and a precessing magnetic moment. Energy dissipation caused by the induced eddy currents is the so-called eddy-current damping [80]. It highly depends on the thickness of the material. It is negligible when the film is thin enough; however, thick films have a higher contribution to this type of damping [81].

Radiative damping is closely connected to the eddy-currents damping because it similarly comes from the inductive coupling of the excitation antenna and the measured thin film [80]. However, the radiative damping is caused by eddy-currents induced in the excitation antenna due to the precessing spin waves and not the film itself. For very thin films or films with low saturation magnetization, the radiative damping can typically be ignored [82].

The damping parameter is also enhanced in multilayer systems consisting of ferromagnetic and adjacent nonmagnetic metallic layers. Owing to magnetization's precession, spin currents are generated at the interface between the ferromagnetic and nonmagnetic layers. The spin angular momentum injected into the neighboring nonmagnetic layer relaxes in this layer and thus further contributes to the damping [74, 83]. This thickness-dependent phenomenon is called **spin-pumping damping**. If the nonmagnetic layer's thickness is lower than the spin diffusion length, it is negligible [84].

Overall, what historically started as a phenomenological addition to account the dissipation of energy developed into the whole field of study. Furthermore, the damping is not constant yet depends on many intrinsic and extrinsic factors (e.g. precession frequency). All of the above described damping mechanisms contribute to the total damping

$$\alpha_{\text{total}}(f) = \alpha_{\text{int}} + \alpha_{\text{TMS}} + \alpha_{\text{eddy}} + \alpha_{\text{radiative}} + \alpha_{\text{spin-pumping}} + \alpha_{\text{other}}.$$
 (1.53)

In the broadband experiment, such as VNA-FMR discussed later in the text, the measured value is the α_{total} . Based on the experience and the system properties, the individual damping channels can be identified, and after that, the measured value can be compared with the theoretical predictions.

1.7. Spin Waves

Spin waves (SW) are collective excitations of magnetic moments in magnetically ordered material. The spin-wave quasi-particle, the magnon, is a boson that carries a quantum of energy $\hbar\omega$ and posses a spin \hbar . In a magnetically ordered system with a temperature above absolute zero, there is a non-zero population of incoherent thermal magnons. However, this thesis is mainly interested is in the externally excited spin-wave signals, i.e., spin waves that propagate in ferromagnets over distances that are large compared to their characteristic wavelengths [85]. Unlike a uniform excitation (ferromagnetic resonance), where all the magnetic moments precess in phase, SW has a phase delay between neighboring magnetic moments so they can carry information. The spin-wave propagation is depicted in Figure 1.11. The behavior of SW is fully characterized by its dispersion relation, i.e the dependence of the angular frequency ω on wave vector \mathbf{k} . The modes of the fully saturated homogeneous media were derived by Walker where his approach relies on finding of the magnetostatic scalar potential [86]

$$(1+\chi)\left[\frac{\partial^2 \psi}{\partial x^2} + \frac{\partial^2 \psi}{\partial y^2}\right] + \frac{\partial^2 \psi}{\partial z^2} = 0, \qquad (1.54)$$

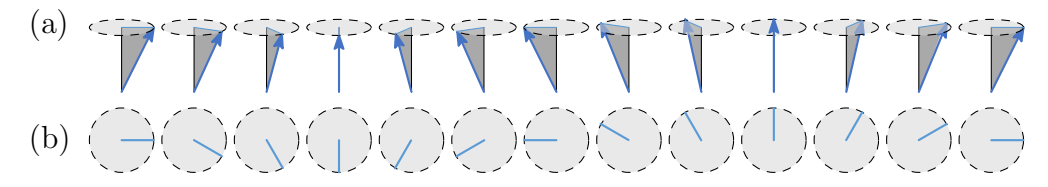


Figure 1.11: Scheme of the propagation of spin waves in one dimension. (a) tilted view, (b) top view.

where χ is the susceptibility and ψ is the magnetostatic scalar potential. Solutions of Walker's equation (1.54) are commonly referred to as magnetostatic modes [87, 88]. In the special case of a uniform plane wave propagating in an infinite medium and assuming the spatial evolution of the scalar potential as $\psi \propto \exp(i\mathbf{k} \cdot \mathbf{r})$, equation (1.54) becomes

$$(1+\chi)(k_x^2+k_y^2)+k_z^2=0. (1.55)$$

If the angle between the direction of the static bias field and the propagation direction is φ , then

$$k_x^2 + k_y^2 = k^2 \sin^2 \varphi \,, \tag{1.56}$$

$$k_z^2 = k^2 \cos^2 \varphi \,. \tag{1.57}$$

1.7.1. Spin-wave dispersion in magnetic thin film

In order to further develop the theory of spin waves, the total wave vector needs to be discussed first. The total wave vector \mathbf{k} consists of an in-plane component \mathbf{k}_{ζ} and an out-of-plane component \mathbf{k}_{p} . The in-plane component \mathbf{k}_{ζ} is decomposed in a component parallel to the in-plane magnetization \mathbf{M} , i.e., \mathbf{k}_{\parallel} , and a component perpendicular to the magnetization, k_{\perp} , by

$$k_{\zeta}^{2} = k_{\parallel}^{2} + k_{\perp}^{2} \,. \tag{1.58}$$

The out of plane component k_p is quantized due to the finite thickness in the perpendicular direction

$$k_p = \frac{p\pi}{t} \tag{1.59}$$

where $p = 0, 1, 2, \ldots$ stands for the number of the thickness mode. The magnitude of the total wave vector k can be calculated from

$$k = \sqrt{k_{\zeta}^2 + \left(\frac{p\pi}{t}\right)^2} \,. \tag{1.60}$$

In general, two major geometries for an in-plane magnetized system can be distinguished. The so-called Damon-Eshbach~(DE) geometry where \mathbf{M} is perpendicular to the \mathbf{k}_{ζ} and the backward~volume~(BV) geometry, where \mathbf{M} and \mathbf{k}_{ζ} are co-linear. The derivations of dispersions of both modes can be found in [35].

The dispersion relation for the Damon-Eshbach spin waves is given by

$$\omega_{\rm DE}^2 = \omega_H(\omega_H + \omega_M) + \frac{\omega_M^2}{4} \left[1 - \exp(-2k_{\perp}t) \right],$$
 (1.61)

where $\omega_H = \mu_0 \gamma H_{\text{eff}}$, $\omega_M = \mu_0 \gamma M_{\text{s}}$ and t is the thickness of the magnetic film. The name of the backward volume geometry mode is related to the fact that group and phase velocities have opposite sign. The dispersion relation is then

$$\omega_{\rm BV}^2 = \omega_H \left[\omega_H + \omega_M \left(\frac{1 - \exp(-k_{\parallel}t)}{k_{\parallel}t} \right) \right]. \tag{1.62}$$

When the magnetization M is perpendicular to the sample plane, the configuration is referred to as forward volume (FV) geometry. The dispersion relation is given by

$$\omega_{\text{FV}}^2 = \omega_H \left[\omega_H + \omega_M \left(1 - \frac{1 - \exp(-k_\zeta t)}{k_\zeta t} \right) \right]. \tag{1.63}$$

These three geometries are shown in Figure 1.12.

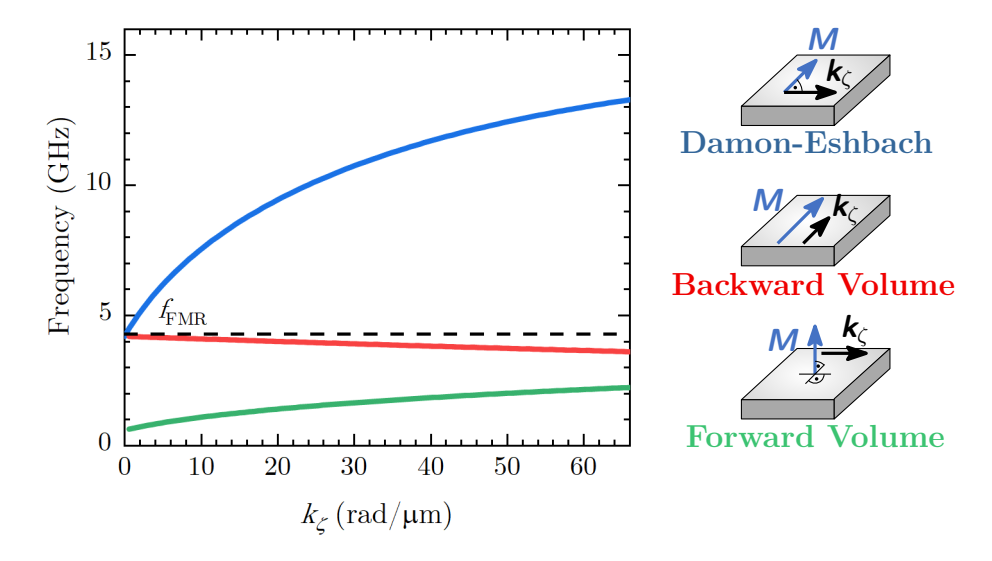


Figure 1.12: Calculated dispersion relations using (1.61), (1.62), and (1.63) in the dipolar regime for three magnetostatic modes, two in-plane and one out-of-plane. These modes differ in the orientations of the magnetization vector \mathbf{M} with respect to inplane component of the wave vector \mathbf{k}_{ζ} . In the Damon-Eshbach geometry, \mathbf{M} and \mathbf{k}_{ζ} are in-plane of the thin magnetic film and $\mathbf{M} \perp \mathbf{k}_{\zeta}$. In the backward volume mode $\mathbf{M} \parallel \mathbf{k}_{\zeta}$, and in the forward volume geometry \mathbf{M} is normal to the surface. Parameters of calculations are: $\mu_0 H_{\text{eff}} = 20 \,\text{mT}$, $M_{\text{s}} = 800 \,\text{kA/m}$, $t = 10 \,\text{nm}$, $\gamma/(2\pi) = 29.3 \,\text{GHz/T}$.

When the wave vector \mathbf{k} lies out-of-plane of the magnetic thin film, the modes are called *perpendicular standing spin waves* (PSSW) due to reflections at the top and bottom surfaces which cause standing spin waves and spin wave resonances. As a result of the geometrical constrain in the perpendicular direction, the out-of-plane component of the wave vector is quantized, see (1.59). The resonance frequencies are given by the Herrings-Kittel [89] formula

$$\omega_{\text{PSSW}}^2 = \left[\omega_H + \omega_M + \gamma \frac{2A_{\text{ex}}}{M_{\text{s}}} \left(\frac{p\pi}{t}\right)^2\right] \left[\omega_H + \gamma \frac{2A_{\text{ex}}}{M_{\text{s}}} \left(\frac{p\pi}{t}\right)^2\right]. \tag{1.64}$$

Dispersion relations (1.61), (1.62) and (1.63) take only dipolar interaction into account. The more general approach which also considers the exchange interaction was derived by Kalinikos and Slavin using classical perturbation theory for the approximate solution of the system [90]. Using their approach, it is possible to calculate any dispersion relation independently of the orientation between magnetization \mathbf{M} and in-plane wave vector \mathbf{k}_{ζ}

$$\omega^2 = \left(\omega_H + \omega_M \lambda_{\rm ex} k^2\right) \left(\omega_H + \omega_M \lambda_{\rm ex} k^2 + \omega_M F_p\right), \qquad (1.65)$$

where

$$F_p = P_p + \sin^2 \vartheta \left[1 - P_p \left(1 + \cos^2 \varphi \right) + \frac{\omega_M P_p (1 - P_p) \sin^2 \varphi}{\omega_H + \omega_M \lambda_{\text{ex}} k^2} \right]. \tag{1.66}$$

The geometry of the coordinate system is depicted in Figure 1.13. The P_p is called the propagation factor, ϑ is the angle between the magnetization and the normal of the film, and φ is the in-plane angle between the magnetization and the wave vector, and $\lambda_{\rm ex}$ is the exchange length.

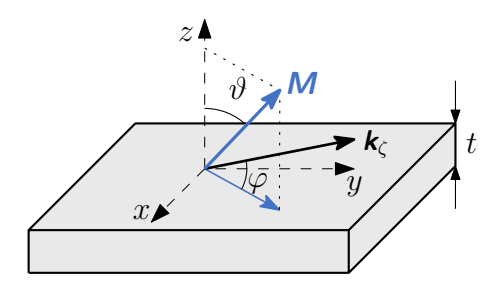


Figure 1.13: Schematic illustration of the coordinate systems used to describe spin wave propagation in a thin film

In the case of totally unpinned surface spins, where the spins near the surfaces of magnetic thin films can freely precess

$$P_p = \frac{k_{\zeta}^2}{k^2} - \frac{1}{1 + \delta_{0p}} \frac{k_{\zeta}^4}{k^4} \frac{2}{k_{\zeta}t} \left[1 - (-1)^p \exp(-k_{\zeta}t) \right] , \qquad (1.67)$$

where δ is the Kronecker delta, i.e. $\delta_{0p} = 1$ for p = 0, and $\delta_{0p} = 0$ for $p \neq 0$. For the case of totally pinned surface spins, the spins near the magnetic thin film surfaces are not allowed to precess

$$P_p = \frac{k_{\zeta}^2}{k^2} + \frac{k_{\zeta}^2}{k^4} \left(\frac{p\pi}{t}\right)^2 \frac{2}{k_{\zeta}t} \left[1 - (-1)^p \exp\left(-k_{\zeta}t\right)\right], \qquad (1.68)$$

where p > 0. The difference between totally unpinned and pinned surface spins is often insignificant. Only when some confinement is present, the boundary conditions differ [91]. Moreover, the surface pinning can be even more generally described by the pinning parameter d. For the totally unpinned surface spins d = 0 and for the totally pinned surface $d = \infty$. For any value of the pinning parameter from the interval $(0,\infty)$ the partially pinned boundary conditions must be used. Interested reader can find more information in [90, 92, 93].

Further, spin waves are characterized by the group \pmb{v}_g and phase \pmb{v}_{ph} velocities defined as

$$\mathbf{v}_{\mathrm{g}} = \frac{\partial \omega(\mathbf{k})}{\partial \mathbf{k}}, \qquad \mathbf{v}_{ph} = \frac{\omega(\mathbf{k})}{\mathbf{k}}.$$
 (1.69)

The calculated dispersion relations of the in-plane magnetostatic modes for $\varphi \in \langle 0; \pi/2 \rangle$ are shown in Figure 1.14(a). The dipolar and exchange interactions by which the spins are coupled differ in strength and the length scales over which they act. The dipolar interaction is weak but long-range, and the exchange interaction is strong but relatively short-range. This difference leads to three characteristic regimes of spin-wave propagation. For the lower k values (long wavelengths), $k < 1 \text{ rad/}\mu\text{m}$, the dominant interaction is the dipolar one and the dispersion relation is given by $\omega_{\text{dip}}^2 = \omega_H(\omega_H + \omega_M F_p)$. As can be seen from equation (1.66), the factor F_p depends on magnetization orientation; therefore, the spin-wave properties in the dipolar regime will be anisotropic. In the limit of spin waves

with k = 0 (infinite wavelengths), the frequency approaches the ferromagnetic resonance. The modes in this regime are called **dipolar spin waves**. By contrast, it is clearly visible that for the higher k values (short wavelengths), $k > 10 \,\mathrm{rad/\mu m}$, the dispersion relation shows a quadratic behavior, because the $\omega_M \lambda_{\mathrm{ex}} k^2$ term from equation (1.65) will become dominant. Therefore, the dispersion will be governed by this exchange term, and the modes are called the **exchange spin waves**. In an intermediate region, where both dipolar and exchange interactions play a role, we speak about the **dipole-exchange spin waves** [6].

Corresponding calculated group velocities are depicted in Figure 1.14(b). For lower k values, the Damon-Eshbach mode demonstrates high group velocity due to the dispersion relation's high slope. On the other hand, the backward volume mode shows negative group velocity for the dipolar regime [see the inset in Figure 1.14(b)]. Therefore, phase and group velocities are pointing in the opposite direction, and the spin waves propagating in this mode are called backward waves. For higher k values, the limiting cases of spin-wave propagation (DE and BV waves) have similar group velocities in the exchange regime.

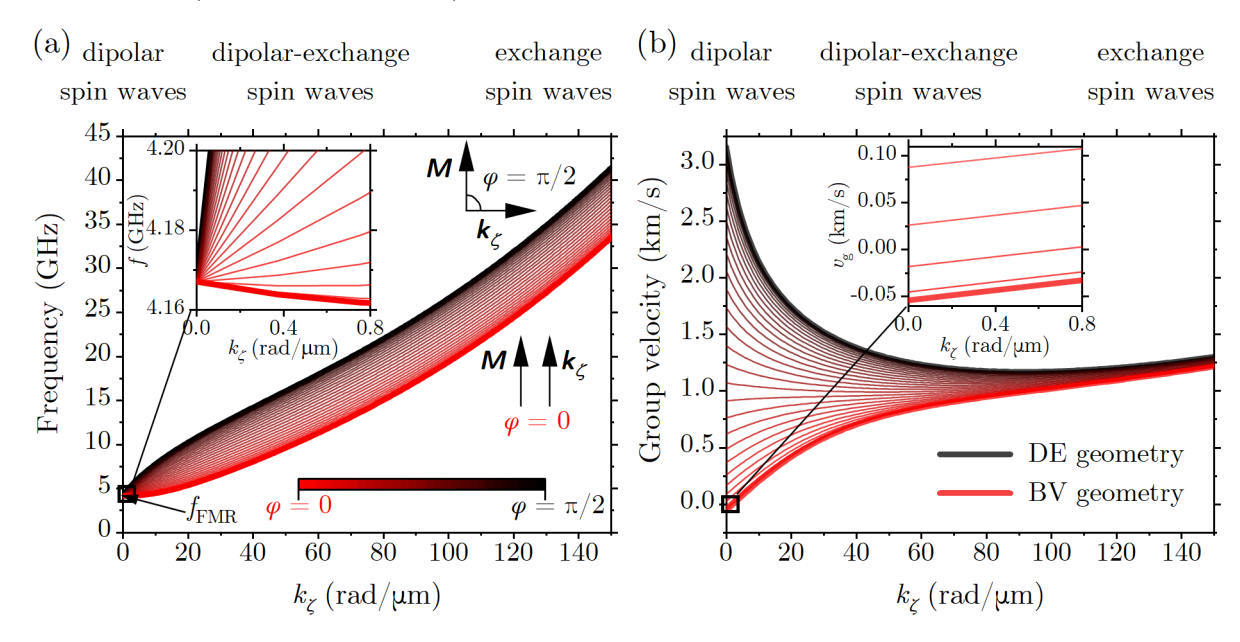


Figure 1.14: Calculated dispersion relations (a) and group velocities (b) for thin NiFe film using equation (1.65). In the Damon-Eshbach (DE) geometry (blue line), $\mathbf{M} \perp \mathbf{k}_{\zeta} \rightarrow \varphi = \pi/2$ and in the backward volume (BV) mode (red line) $\mathbf{M} \parallel \mathbf{k}_{\zeta} \rightarrow \varphi = 0$. The angles, where $\varphi \in (0; \pi/2)$ are represented by the lines between these two geometries. The inset of (a) stresses the negativity of the slope for the BV geometry. The inset of (b) shows the negative group velocity $v_{\rm g}$ for the BV mode, hence the name of the mode. Parameters of calculations are: $\mu_0 H_{\rm eff} = 20\,\mathrm{mT}$, $M_{\rm s} = 800\,\mathrm{kA/m}$, $t = 10\,\mathrm{nm}$, $\gamma/2\pi = 29.1\,\mathrm{GHz/T}$ and $A_{\rm ex} = 16\,\mathrm{pJ/m}$.

As denoted in section 1.5.1, the temporal evolution of the dynamic component of magnetization $\mathbf{m}(t)$ is described by

$$\mathbf{m}(t) = \mathbf{m} \exp(\mathrm{i}\omega t). \tag{1.70}$$

In the simplest case, the spin-wave lifetime τ is inversely proportional to the spin-wave angular frequency $\tau \propto \frac{1}{\omega}$ [35]. Nevertheless, if we consider both dipolar and exchange interactions, the dependence is not so trivial anymore. The main parameter defining the

lifetime τ is the Gilbert damping α . In section 1.5.2 we discussed that the damping can be accounted for by replacing the real precession frequency ω in equation (1.36) with the complex quantity $\omega' + i\omega''$. Thus, the dynamic component of magnetization is

$$\mathbf{m}(t) = \mathbf{m}(0) \exp(t\omega\alpha). \tag{1.71}$$

In an infinite medium, the lifetime of the uniform circular precession is

$$\frac{1}{\tau_0} = \alpha \omega \,. \tag{1.72}$$

The magnetization precession in thin film is, however, usually elliptic due to the shape anisotropy. Therefore, following the phenomenological loss theory, the lifetime is [35, page 172][94, page 256]

$$\frac{1}{\tau} = \frac{1}{\tau_0} \frac{\partial \omega}{\partial \omega_H} = \alpha \omega \frac{\partial \omega}{\partial \omega_H} \,. \tag{1.73}$$

The distance, where the spin-wave amplitude falls to the 1/e of its original amplitude is called the decay length Λ and is calculated as

$$\Lambda = \tau v_{\rm g} \,. \tag{1.74}$$

The spin waves are usually studied in magnetic thin films, and the choice of magnetic material is crucial not only in fundamental but also in applied magnonics. There are many requirements for magnetic materials [6]:

- 1. In order to have high propagation length Λ , low Gilbert damping α is essential.
- 2. For high group velocities v_g , large saturation magnetization M_s is needed. The high saturation magnetization is also vital for magneto-optical or electrical experiments.
- 3. To provide thermal stability, a high Curie temperature is favorable.
- 4. To assure repeatability of procedures, simplicity in the fabrication of magnetic films and the patterning processes is necessary.

There are some magnetic materials, which fulfill those demands. The most commonly used materials for spin-wave research, together with their selected magnetic properties and estimated spin-wave characteristics, are shown in Table 1.1. These characteristics are the saturation magnetization M_s , the Gilbert damping parameter α , the exchange length $l_{\rm ex}$, the group velocity $v_{\rm g}$, which, together with the lifetime τ , defines the propagation length Λ . The listed materials are Co, CoFeB, Fe, NiFe, and YIG.

The Co and Fe are representative ferromagnetic materials. Nowadays, the attention of the magnonic community is focused on the new promising material, $Co_{40}Fe_{40}B_{20}$ [95]. It is an amorphous material with higher saturation magnetization and smaller Gilbert damping parameter values than other ferromagnetic materials listed in the table. Therefore, it is very suitable for the purposes of magnonics.

The material used within this thesis is NiFe, a polycrystalline magnetic alloy of nickel and iron. In our case, it refers to an alloy with about 20% iron and 80% nickel content. The composition of the permalloy alloy is tailored to minimize the magnetic anisotropy efficiently, and thus this material is considered a very soft magnetic compound with low coercivity and anisotropies. The Gilbert damping is reasonably low, considering it is a metal,

Material	$M_{\rm s}$ (MA/m	$\alpha \times 10^{-3}$	$l_{\rm ex}$) (nm)	$v_{ m g} = (\mu { m m/ns})$	τ s) (ns)	$\begin{array}{c} \Lambda \\ (\mu m) \end{array}$	References
Со	1.4	5	4.8	4.6	1.2	5.5	[82, 97–100]
$\mathrm{Co}_{40}\mathrm{Fe}_{40}\mathrm{B}_{20}$	1.3	4	3.9	3.9	1.7	6.6	[74, 95, 101]
Fe	1.7	60	3.4	5.8	0.08	0.5	[102–106]
$Ni_{80}Fe_{20}$ (Permalloy)	0.8	7	6.3	2.2	1.4	3.2	[56, 107, 108]
YIG (µm films)	0.14	0.05	17	42	600	25000	[109–113]
YIG (nm films)	0.14	0.2	17	0.3	150	44	[114-120]

Table 1.1: Material properties of selected ferromagnetic materials. Inspired by [91, 94, 96]

and the typical propagation length is in the units of micrometers. It was chosen mainly to meet the requirement of its substantial simpleness of the fabrication of nanostructures.

The last material listed in the table is Yttrium Iron Garnet (Y₃Fe₅O₁₂). Table 1.1 shows two rows related to YIG values, one corresponding to the µm films and the other to nm films. YIG has been an important material for a number of years due to its extremely narrow ferromagnetic resonance linewidth. The most common way of growing high quality single crystal YIG films is the liquid phase epitaxy (LPE) [116, 121]. With the recent development of technologies, it became possible to grow high-quality nm-thick YIG films by pulsed-laser deposition and, recently, by magnetron sputtering [122] only within the last years. It is a monocrystalline ferrimagnet insulator with the smallest known Gilbert damping parameter and a long spin-wave lifetime and propagation lengths. However, the fabrication of nanostructures might still be cumbersome due to the elevated temperatures needed for crystalline growth or post-growth annealing.

1.7.2. Spin waves in magnonic waveguides

Moving from the infinite magnetic system to spatially confined structures logically affects the dispersion of spin waves mainly due to the modification of the internal magnetic field related to the confinement. Patterned magnetic elements are usually approximated by ellipsoidal elements with corresponding demagnetizing factors [123] because there is an analytical solution of the spin-wave spectrum ellipsoidal elements [86, 124]. However, it has been shown that the dynamic properties of the finite, non-ellipsoidal magnetic elements are drastically affected by the highly inhomogeneous internal magnetic field within the element [125].

The problem in confined magnetic structures is selecting the magnetization boundary conditions for the edges of the waveguide. As mentioned above, there are three possibilities for the spins at the surface: they are either totally unpinned, partially pinned, or totally pinned. Additionally, the introduction of the "effective" pinning boundary conditions by rigorous calculation of the demagnetizing tensors in rectangular magnetic elements lead to the redefinition of the boundary conditions [126] in longitudinally magnetized waveguides.

In order to calculate spin-wave dispersion relations in a transversally magnetized spin-wave waveguide of a finite width w, which is much larger than the thickness t, the total k vector must be redefined. The term describing the confinement in one direction should be considered. The total in-plane k vector is then defined as

$$k = \sqrt{k_{\vdash}^2 + k_n^2} \,, \tag{1.75}$$

where k_{\vdash} is the spin-wave wavenumber along the waveguide and $k_n = \frac{n\pi}{w}$ is the perpendicular quantized wavenumber with $n = 0, 1, 2, \ldots$ being the transversal quantization number in the case of the magnetic waveguide. The parameter w is the width of the waveguide. The schematic illustration of the coordinate systems used to describe spin-wave propagation in the magnonic waveguide is depicted in Figure 1.15(a). The quantization of the total k-vector and the transverse profile of the dynamic magnetization is shown in Figure 1.15(b).

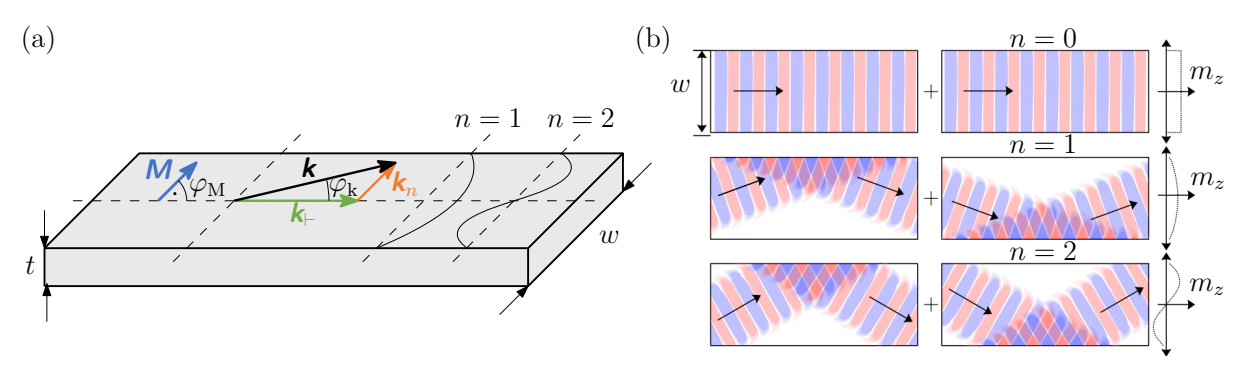


Figure 1.15: (a) Schematic illustration of the coordinate systems used to describe spin wave propagation in magnonic waveguide. It shows the special case for $\vartheta=0,\ \varphi_{\rm M}=\pi/2$ and $\varphi_{\rm k}=\arctan\frac{k_n}{k_{\rm L}}$. The transverse profile of the m_z component of the dynamic magnetization is schematically shown for n=1,2. (b) Representative sketch of the modes of spin waves in narrow magnonic waveguide. The blue and red colors represent the m_z component of the magnetization \mathbf{M} . Due to the confinement of the spin waves, the propagation vector k_n is quantized, therefore the direction of the propagation of the total k vector changes. It is represented by the black arrow . The modes with n=0,1,2 are depicted. With kind permission, adapted from [58].

As discussed above, the behavior and specifically the dispersion relation of spin waves in waveguides with dimensions comparable or smaller to the wavelength are strongly affected by waveguide boundaries and lateral confinement effects [127]. Due to these strong effects, the spin-wave dispersion of a waveguide with finite width $w \gg t$ and with a rectangular cross section given by equation (1.65) will be slightly different. More precisely, in equation (1.66) the $\varphi_k - \varphi_M$ will be used instead of φ . This will help with the better description of the total k-vector because in the confined direction it can have only certain valued components. The thickness of the magnetic layer used withing the thesis is low, therefore the higher thickness modes with p > 0 are not taken into account. Then, the factor P from equation (1.67) describing the totally unpinned spins at the surface is redefined. F is given by

$$F = P + \sin^2 \vartheta \left[1 - P \left(1 + \cos^2(\varphi_k - \varphi_M) \right) + \frac{\omega_M P (1 - P) \sin^2(\varphi_k - \varphi_M)}{\omega_H + \omega_M \lambda_{ex} k^2} \right]$$
(1.76)

and

$$P = 1 - \frac{1 - \exp(-kt)}{kt} \,. \tag{1.77}$$

Here k is the total k vector from equation (1.75), $\varphi_k = \arctan\left(\frac{k_n}{k_{\vdash}}\right)$ is the angle between the spin-wave wave vector \mathbf{k}_{\vdash} along the waveguide and the long axis of the waveguide, and φ_{M} is the angle between the magnetization \mathbf{M} and the long axis of the waveguide.

The dispersion relations and propagation lengths calculated for the waveguides are depicted in Figure 1.16. The confinement is most significant for the small k_{\vdash} , see (1.75), and the dispersion is most influenced by the quantized transverse component k_n . Therefore, for small k_{\vdash} in Figure 1.16(a) the plateau resembling a BV mode is formed. The dispersions are calculated in the Damon-Eshbach geometry using eqs. (1.65) and (1.75) to (1.77) while varying the waveguide width from $w = 200 \,\mathrm{nm}$ to $w = 10 \,\mathrm{\mu m}$. The plateau is even more visible in Figure 1.16(b), which shows the dispersion for the waveguide width $w = 2 \,\mathrm{\mu m}$ for modes with n = 1, n = 2 and the thin film case for comparison (n = 0). For higher k_{\vdash} , the dispersions for the waveguide modes come back to the Damon-Eshbach dispersion for the thin film.

Figure 1.16(c) shows the calculation of the propagation length from dispersion using eqs. (1.69) to (1.74). The same variation of the waveguide width w was employed. Here,

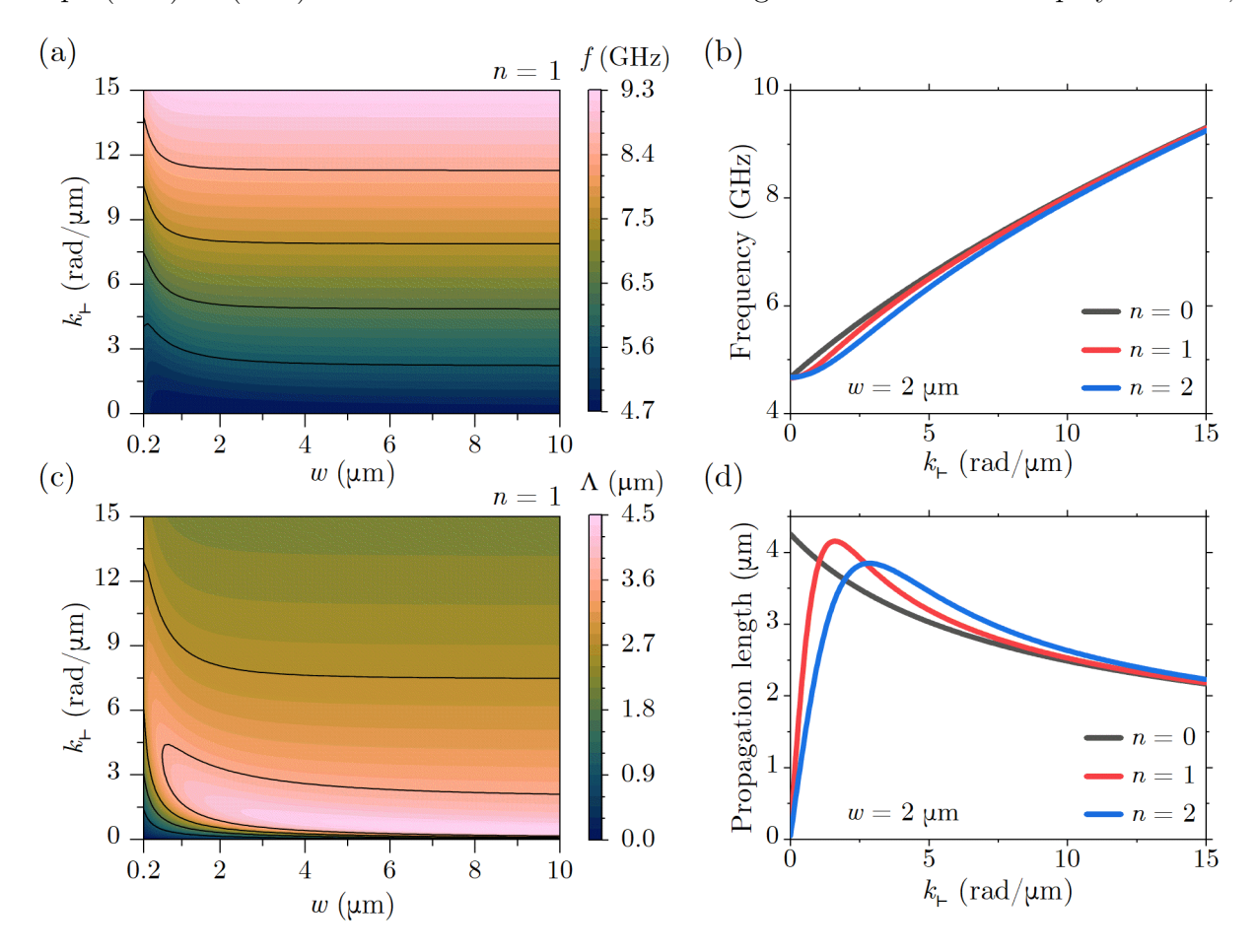


Figure 1.16: Dispersions (a) and propagation lengths (c) calculated for the Damon-Eshbach mode using eqs. (1.65) and (1.69) to (1.77) for the variation of the spin-wave wavevector along the waveguide k_{\vdash} and the waveguide width w for the first transversal mode (n=1). Dispersions (b) and propagaion lengths (d) calculated for the waveguide width $w=2\,\mu\mathrm{m}$. The two different waveguide modes are characterized by the different n. The dispersion and the propagation lengths for the uniform zeroth transversal mode (n=0) are shown for the reference. Calculation is performed for NiFe waveguide. Calculation parameters are: $\mu_0 H_{\mathrm{eff}} = 20\,\mathrm{mT}$, $M_{\mathrm{s}} = 800\,\mathrm{kA/m}$, $t=10\,\mathrm{nm}$, $\gamma/2\pi = 29.1\,\mathrm{GHz/T}$ and $A_{\mathrm{ex}} = 16\,\mathrm{pJ/m}$.

we can see that the combination of the BV and DE modes for small k_{\vdash} ensue the maximal propagation length for certain value of k_{\vdash} . Again, Figure 1.16(d) shows the propagation

length for the waveguide width $w = 2 \mu m$. When compared with the thin film case, it is clear that the confinement results in higher propagation length.

For thin waveguides with thickness-to-width aspect ratio $a_r = t/w \ll 1$, the effect of "dipolar pinning" is demonstrated at the lateral edges. For the theoretical description, the thin strip approximation, valid for the uniformly magnetized waveguide along the lateral direction (BV geometry), was developed [87, 126, 128, 129]. A semianalytical theory has recently been developed for the waveguides with thickness-to-width aspect ratio $a_r = t/w \to 1$ because the thin strip model of effective pinning is not sufficient [130]. However, waveguides studied within the thesis range are wide enough, and the description using the equations presented above is adequate.

From eqs. (1.73, 1.74) it is evident, that the propagation length is linearly dependent on parameter $1/\alpha$, where α is the Gilbert damping. Figure 1.17(a) shows the calculation of the propagation length for the variation of the spin-wave wavevector along the waveguide k_{\vdash} and the damping parameter α for the first transversal mode (n = 1) in waveguide with the width $w = 2 \,\mu\text{m}$. Figure 1.17(b) shows the comparison of the propagation length in the thin film and in the waveguide for modes with n = 1, n = 2 for selected $k_{\vdash} = 3.1 \,\text{rad/}\mu\text{m}$.

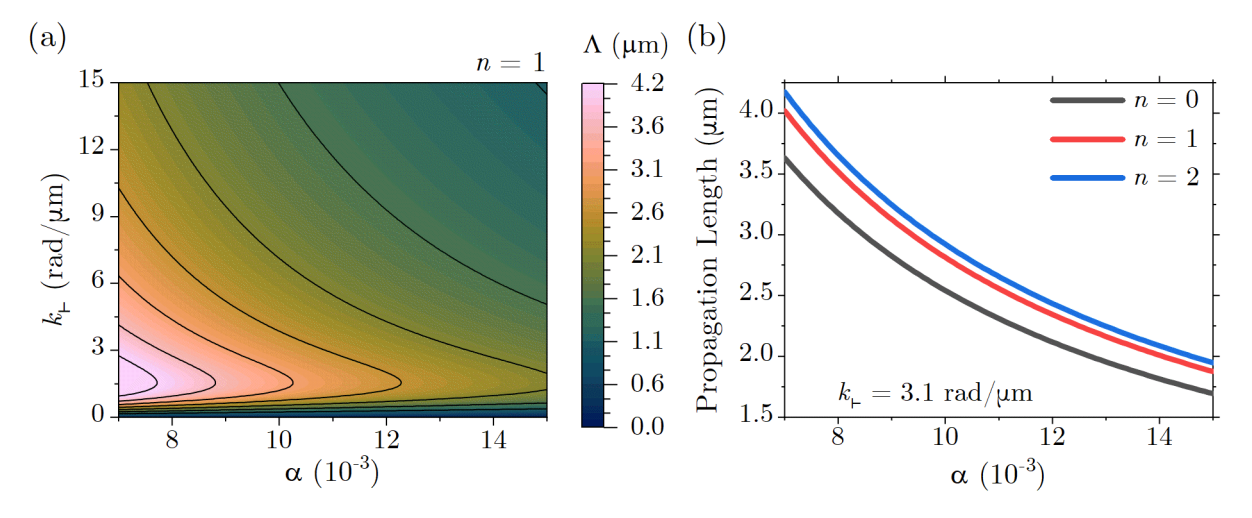


Figure 1.17: (a) Propagation lengths calculated in the Damon-Eshbach geometry for the variation of the spin-wave wavevector along the waveguide k_{\vdash} and the damping parameter α for the first transversal mode (n=1) in waveguide with the width $w=2\,\mu\mathrm{m}$. (b) Dependence of the propagation lengths on the damping parameter α for the $k_{\vdash}=3.1\,\mathrm{rad}/\mu\mathrm{m}$. The first (n=1) and second (n=2) transversal mode is compared against the thin film (n=0). Calculation is performed for NiFe waveguide. Calculation parameters are: $\mu_0 H_{\mathrm{eff}}=20\,\mathrm{mT},\,M_{\mathrm{s}}=800\,\mathrm{kA/m},\,t=10\,\mathrm{nm},\,\gamma/2\pi=29.1\,\mathrm{GHz/T}$ and $A_{\mathrm{ex}}=16\,\mathrm{pJ/m}$.

Figure 1.18(a) shows the calculation of the propagation length in the waveguide with the width $w = 2 \,\mu\text{m}$ dependent on the external magnetic field and damping for the fixed $k_{\vdash} = 3.1 \,\text{rad/\mu m}$ and the first transversal mode n = 1. When increasing the external magnetic field, the propagation length is decreased. This is more visible for the fixed damping $\alpha = 7 \times 10^{-3}$, depicted in Figure 1.18(b), where also the comparison of the thin film and the first and second transversal modes is made.

To conclude this chapter, we have introduced the basic principles of static magnetism and magnetization dynamics. Then we moved to the ferromagnetic resonance and dispersion of spin waves in thin film and in a waveguide. The spin-wave propagation length in magnonic waveguides will be under investigation in the experimental section. Therefore,

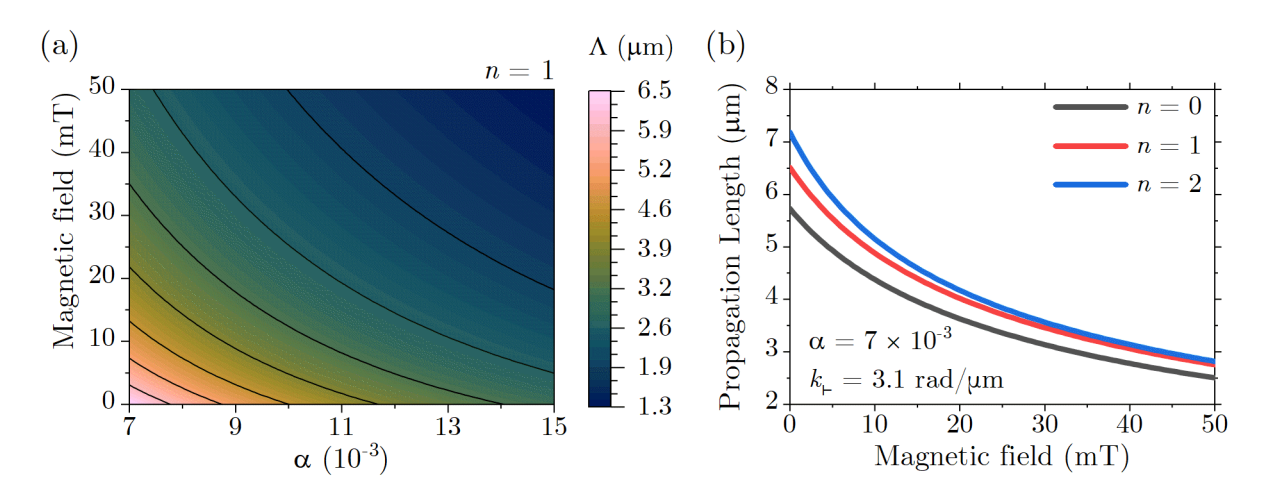


Figure 1.18: (a) Propagation lengths calculated in the waveguide with the width $w=2\,\mu\mathrm{m}$ in the Damon-Eshbach geometry for the variation of the the damping parameter α and the external magnetic field for the fixed $k_{\vdash}=3.1\,\mathrm{rad}/\mu\mathrm{m}$ and the first transversal mode (n=1). (b) Dependence of the propagation lengths on the external magnetic field for the $\alpha=7\times10^{-3}$ and $k_{\vdash}=3.1\,\mathrm{rad}/\mu\mathrm{m}$. The comparison of the thin film (n=0), the first (n=1) and the second (n=2) transversal mode is shown. Material parameters used for the calculation are: $\mu_0H_{\mathrm{eff}}=20\,\mathrm{mT}$, $M_{\mathrm{s}}=800\,\mathrm{kA/m}$, $t=10\,\mathrm{nm}$, $\gamma/2\pi=29.1\,\mathrm{GHz/T}$ and $A_{\mathrm{ex}}=16\,\mathrm{pJ/m}$.

the parameters influencing the propagation length, such as waveguide width w, damping parameter α , external magnetic field $\mu_0 H_{\rm ext}$ or the spin-wave wave vector along the waveguide k_{\vdash} were discussed.

2. Sample fabrication methods

The best confidence builder is experience.

– Star Wars: Clone Wars, Episode: Rookies

This chapter deals with the experimental methods essential for preparing magnetic samples with curved geometries. In the scope of the thesis, we deposited magnetic layers on a sinusoidally modulated substrate and created different structures. The chapter introduces nanofabrication methods of focused electron beam-induced deposition and electron beam lithography used within the thesis.

2.1. Focused Electron Beam-Induced Deposition

Nanofabrication techniques, which do not require any mask to create a desired pattern on the substrate, are called direct-write processes. Masks are conventionally in the form of patterned electron or photon-sensitive resists. Focused electron beam-induced deposition (FEBID) is a direct-write patterning technique by which a solid material can be locally deposited onto a solid substrate utilizing an electron-mediated decomposition of a precursor molecule [131]. Another examples of a direct-write patterning technique are, e.g., focused ion beam (FIB) milling or focused ion beam-induced deposition (FIBID).

Although the FEBID process is relatively well-developed, the technique has gained attention and significant recognition in the field only recently. The driving force behind the increased interest in the technique is the resolution limit of conventional lithography methods (deep-UV photolithography, electron beam lithography) and the possibility of fabricating 3D nanostructures with shapes unobtainable by standard lithography approaches [23, 24, 132–134]. The main advantage of FEBID (compared to the other lithography techniques) is the possibility to prepare nanostructures in a rapid single-step, single-machine maskless lithography technique from a wide range of materials. Another advantage is the adjustability of the surface. The structure can be defined on the flat as well as patterned topographical surfaces. Nevertheless, the substantial drawback hindering the method's applicability to real-world applications is the low growth rate, restricting FEBID to single-sample, sometimes even single-structure fabrication. Also, the final deposit composition is far from ideal. The typical structure created using metal-organic precursors grows in a matrix of amorphous carbon with embedded metal nanocrystals.

The first report on the successful application of FEBID was in 1934 by Stewart [135]. He observed the formation of insulating films on the substrate surface after the electron irradiation. He concluded that the insulation layer was carbonaceous, and the polymerization of residual organic vapors caused the deposition in the vacuum chamber by the electron beam. At that time, it was considered the bane of electron microscopy because the contamination was ever-present in most vacuum systems. Thankfully, the technology

has developed, and it nowadays is possible to considerably minimize the residual hydrocarbon vapors in the vacuum system. However, the issue of contamination remained in all forms of scanning electron microscopy (SEM).

First studies that exploited FEBID potentiality as a valuable technique for the intentional deposition of micro and nanostructures were done in the 1960s. Christy [136] studied the influence of the deposition parameters on the growth rate, and Baker and Morris [137] were the first who studied the metallic films demonstrating the possibility of the preparation of conducting materials. In the following decades, the steady increase in experimental FEBID investigations led to the development of a wide range of usable materials, resulting in the confirmation of EBID being the promising technique for maskless nanofabrication.

Despite the long history of using the FEBID as a direct-write technique, detailed knowledge of the process is still a bit clouded. While the excessive number of materials has been studied and a vast amount of publications on the focused electron beam-induced processes published [131, 138], a high level of control over the geometry of the deposit has been elusive. The helplessness of the situation is most significantly illustrated in confusion around the many names of this technique: FEBID, e-beam induced resist, e-beam induced metal formation, e-beam assisted deposition, e-beam induced selective deposition, e-beam induced chemical vapor deposition, e-beam stimulated deposition, e-beam induced surface reaction, e-beam writing, environmental e-beam deposition, e-beam assisted direct-write nanolithography, contamination lithography, additive lithography, or 3D deposition lithography [138].

In the process itself, artificially injected precursor molecules (most commonly metalorganic molecules) interact with the substrate and adsorb on the sample surface. The highly focused electron beam locally exposes the region with adsorbed precursor molecules. The electrons from the primary beam are scattered upon impact and subsequently participate in a dissociation reaction resulting in a solid deposit and a volatile by-product, which afterward desorbs from the surface and is pumped away. A diagram of a process is shown in Figure 2.1. The primary beam properties have a real effect on the deposition rate and the resulting chemical composition of deposits. Furthermore, the combination of the precursor's chemical properties and the environmental effects, such as the sample temperature or the ambient pressure, significantly influence the deposition process. However, when the parameters are optimized with care, the method allows the fabrication of individual 3D nanostructures with nanometer resolution in a single step.

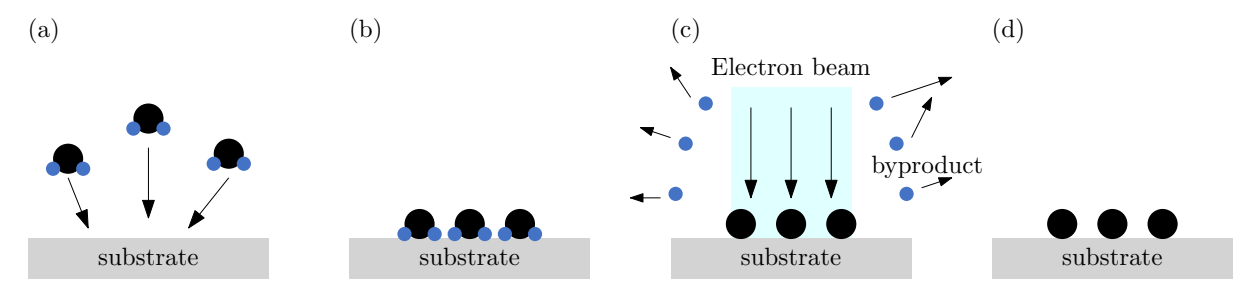


Figure 2.1: Visualization of the FEBID process. (a) Precursor molecules are introduced to the chamber and (b) adsorb to the sample surface. (c) The interaction with the focused electron beam leads to the dissociation of adsorbed molecules resulting in a solid deposit and a volatile by-product. (d) The final deposit. Adapted from [131]

As the FEBID method relies on processes stimulated by a focused electron beam, it is essential to address the many different interactions between the electron beam and the sample's surface. When the precursor molecules are involved, their dissociation, ionization, adsorption, desorption, and diffusion are the interactions that occur.

In the initial phase of the FEBID process, the beam of primary electrons (PE) is focused on the sample. Those electrons collide with the solid substrate and are scattered, i.e., their original trajectory deviates. In the case of inelastic scattering, part of the PE's energy is transferred to other electrons in the solid. When the electron is weakly bound in the electron shell, it can be either excited to a higher energy level or emitted from a solid as a secondary electron (SE). If the electron's energy after leaving the sample is higher than 50 eV, we speak about backscattered electrons (BSE) by convention. The energy spectrum for secondary and backscattered electrons is shown in Figure 2.2(a). If the electron comes from the inner shell, its position is subsequently filled by an electron from a higher energy level. The quantum of excess energy is then either radiated in the form of electromagnetic energy in the X-ray part of the spectrum or transmitted to an electron from the outer shell, emitted as a so-called Auger electron (AE). Besides, due to the gradual deceleration, the primary electron emits continuous x-rays called bremsstrahlung. All these generated signals then form a so-called interaction volume in the solid below the irradiated spot, the schematic representation shown in Figure 2.2(b). The shape and size of the interaction volume highly depend on PE's energy and the substrate. SE and BSE can escape from the substrate and enter the vacuum resulting in the precursor molecule dissociation.

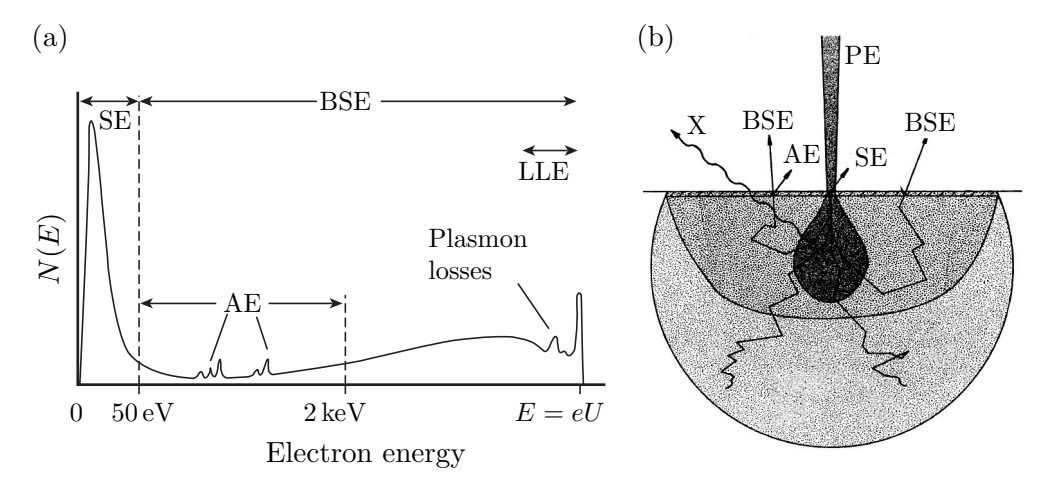


Figure 2.2: (a) Schematic energy spectrum of electrons emitted from the solid after the impact of the beam of primary electrons (PE) with energy E = eU. It consists of secondary electrons (SE) and backscattered electrons (BSE). By convention, the limit value when distinguishing them is 50 eV. Other significant peaks correspond to Auger electrons (AE), plasmon excitations, and elastically scattered electrons, so-called low-loss electrons (LLE). Adapted from [139, page 18]. (b) A simple representation of a primary electron (PE) beam's interaction volume in a solid flat sample. The various signals representing secondary electrons (SE), backscattered electrons (BSE), Auger electrons (AE), and X-ray quanta (X) are illustrated. Reprinted from [140, page 5].

The effective cross-section $\sigma(E)$ generally expresses the probability that an electron will cause the chemical decomposition. In a simplified picture, the larger the effective cross-section, the greater the likelihood of the molecule decomposition. Nevertheless,

determining a cross-section for the adsorbed precursor molecules is complicated as the cross-section depends on many parameters. It is necessary to think, for instance, about the energy of bonds within the given molecule, the influence of the environment in which the reaction takes place, or the specific geometry in which the molecule is adsorbed. As a result, complete data sets of effective cross-sections for chemical compounds are barely available, especially for the FEBID method.

Generally, it can be said that the secondary electrons play a crucial role in the deposition. The emission of secondary electrons significantly affects the smallest possible size of deposited structures. Depending on the energy, the interaction volume changes, which leads to the increased emission of secondary electrons over a large area. As a result, the deposition will occur even in places where the primary beam did not impinge on a solid surface. Therefore, in a conventional FEBID experiment, it is almost impossible to prepare a deposit with dimensions comparable to the electron beam spot size. This phenomenon is all the more significant in the deposition of tall nanopillars. Once the deposit begins to form, it becomes a source of secondary electrons; therefore, due to the higher surface area to volume ratio, there is a deposition on the pillar's entire surface, which expands the lower base of such a structure (base-broadening) [141].

2.1.1. Experimental Apparatus

An elementary premise for the FEBID method is a controlled vacuum environment limiting the electron scattering. Usually, the FEBID setup utilizes a scanning electron microscope (SEM); however, other possibilities include a transmission electron microscope [142, 143] or scanning tunneling microscope [144]. In the scanning electron microscope, the energies of the primary beam electrons are usually in the range of $1 \, \text{keV} - 30 \, \text{keV}$, the used current is in the range from pA to nA, and the spot size ranges from units of nm to hundreds of nm.

Within the thesis range, the FEBID experiments were done using Tescan LYRA3 electron microscope. The microscope is equipped with an electron column with a Schottky cathode and an ion column with a gallium liquid metal ion source (LMIS). The primary electron beam energy can be tuned from 200 eV to 30 keV, and the smallest spot size is in units of nanometers. In particular, the microscope is equipped with a gas injection system (GIS) that allows precursors to flow to the close vicinity of the sample. It is possible to store five precursors independently, whether for etching or deposition.

By using various precursors, it is possible to prepare not only metallic but also semiconducting or dielectric structures. The choice of material plays a crucial role when selecting a desirable chemical precursor. When approaching new material, a list of precursors suitable for chemical vapor deposition (CVD) or atomic layer deposition (ALD) methods is usually the first choice. Throughout the work with chemical precursors, it is necessary to follow the chemical safety requirements. The main requirement is chemical stability. When the GIS is not being used, precursor reservoirs are still part of the vacuum system. Hence, the chemical compound used as a precursor for the FEBID technique must be stable independently of the precursor state (solid, liquid, gaseous). Besides, contamination of the vacuum system should not occur. An equally important requirement is the precursor molecules' behavior during the decomposition of the molecule by an electron beam. It is necessary that the decomposition results in a solid deposit and a volatile byproduct, which is easily removed from the microscope chamber by a vacuum pump system. Another requirement is chemical purity. The chemical composition of the deposits is influ-

enced by multiple parameters of both the intrinsic and extrinsic nature. Since this thesis utilizes the FEBID solely to modify the substrate topography, we will not further discuss the chemical composition of nanostructures prepared using this technique. Selected precursors available in the CEITEC Nano research infrastructure in the Tescan LYRA3 are listed in Table 2.1.

Deposit	Precursor	Application		
Tungsten	$W(CO)_6$	• TEM lamella protection		
Platinum	$\mathrm{MeCpPt}(\mathrm{Me}_3)^1$	• Electrical connections, nanostructures		
Silicon	PMCPS ²	• Electrical insulation		
Carbon	Phenanthrene	NanostructuresTEM lamella protection		

Magnetic nanostructures

Table 2.1: The table shows precursors for deposition available in the Tescan LYRA3 SEM.

The flow rate of the FEBID process highly depends on the amount of precursor in the reservoir. Besides, the flow rate influences the growth rate of prepared nanostructures. Therefore, it is sometimes necessary to refill the precursor reservoir with an additional liquid, solid, or gas compound. For this case, it is better to consult the manufacturer of the available SEM setup. However, if the nanofabrication facility has a chemical glove box with the possibility of an inert atmosphere, it is possible to do it in-house. The chemical glove box must be used because most of the chemical compounds suitable for FEBID use are highly toxic or carcinogenic. It is advised to look up the safety information before any manipulation with the precursor reservoir and always use personal protective equipment in the form of a type P3 respirator, face shield, and at least two pairs of rubber gloves.

2.2. Electron beam lithography

 $Co_2(CO)_8$

Cobalt

All samples and structures discussed in the thesis's experimental section are prepared using FEBID and electron beam lithography (EBL). This section serves as a brief description of the EBL technique. Interested reader may consult special chapters devoted to this technique in books by Utke *et al.* [139, chapter 27], or Gatzen *et al.* [145, chapter 6] dedicated to nanofabrication.

EBL is a versatile technique for fabricating nanostructures in most cases complemented by layer deposition using sputtering or evaporation. Individual steps of the lithographic process are schematically depicted in Figure 2.3. Even though the EBL is a serial process (the desired design is exposed point by point), it is much faster than direct writing using FEBID. That is mainly due to the slow deposition rate of the FEBID technique. As we are interested in the rapid prototyping and fabrication of different patterns, both techniques have the requisite qualities to meet a task. However, the efficiency when exposing large sample areas is complemented by a relatively high time consumption. For mass production, none of the techniques mentioned above (EBL, FEBID) is ideal. The ultimate techniques

¹Trimethylmethylcyclopentadienyl platinum, Me – methyl, Cp – cyclopentadiene

²2,4,6,8,10-Pentamethylcyclopentasiloxane

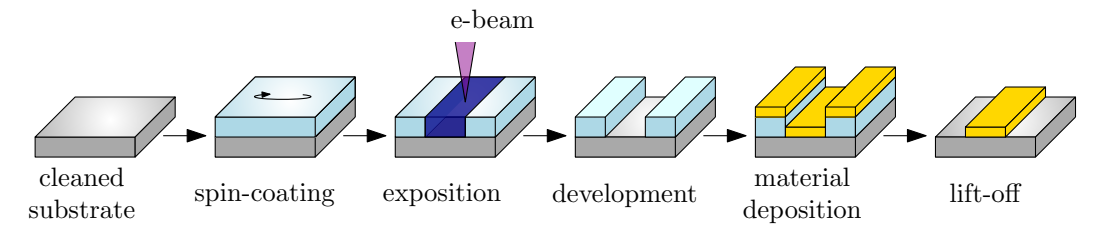


Figure 2.3: Schematical illustration of electron beam lithography using the positive resist processing steps. First, a thin layer of resist is spin-coated on a clean substrate. A local exposition by a focused electron beam is then done using a scanning electron microscope (SEM). The sample is then developed using appropriate chemical processing. Depending on the type of spin-coated resist, the process is either positive or negative. In the next step, the sample is covered by the metallic layer using a physical vapor deposition (PVD) process, such as e-beam evaporation or magnetron sputtering. The resist which protected the selected parts of the substrate is later dissolved using a resist remover, and the deposited material is washed away along with it. Thus, only the desired metallic structures remain on the substrate in the end.

for batch production to fabricate identical samples in a large production facility are an optical lithography or a multi-beam mask writer.

Both optical and electron beam lithography rely on the use of a so-called resist. Most commonly, the resist is a polymeric chemical compound dissolved in a liquid solvent (usually anisole, ethyl lactate, etc.). For good reproducibility of the subsequent process, it is necessary to achieve its uniform distribution on the substrate's surface without the presence of defects. Besides the quality of the resist layer, the repeatability of its preparation is also essential. Spin-coating is one of the most commonly used techniques for applying electron- (photon-) sensitive resist layers to substrates before the electron (photon) patterning in the e-beam and optical lithography.

The droplet of the resist is dropped on the substrate surface. Then, the sample is spun, usually at the spin speed of thousands of rpm. During this rotational movement, the centrifugal force spreads the resist homogeneously over the substrate surface. The thickness of the resist layer depends mainly on the spin speed and the used resist viscosity. The centrifugal process is usually preceded by heating the substrate to the desired temperature to prevent water on the substrate surface and promote the resist layer's adhesion. The solvent must be removed from the resist layer in the so-called soft-bake process, preserving the resist layer in a solid-state suitable for further manipulation.

The next step after the formation of a homogeneous resist layer is the e-beam exposition. The electrons interact with the resist and change its structure on the molecular level. Depending on the resist properties after the e-beam exposure, two resist types are recognized – positive and negative. In a positive e-beam resist, the polymeric chain cleavage after the e-beam exposure leads to molecular weight reduction. Hence, the solubility of the irradiated parts of the resist is increased. On the other hand, the opposite phenomenon (polymeric chains crosslink) can be found in the negative resist.

The fundamental parameter controlling the resist exposure parameters is the dose of electrons, usually given in units of $\mu C/cm^2$. For each combination of resist and substrate, the dose needed to successfully remove (preserve) the whole layer of positive (negative) resist is different. Exposure of the desired structure is followed by resist development. In this step, the exposed (unexposed) parts of the positive (negative) resist layer are

selectively dissolved in a suitable solvent – developer. If the electron dose is insufficient (underexposure), the positive resist's exposed part does not dissolve completely. Similarly, when the electron dose is too high (overexposure), the structures in the positive resist are deformed and expanded. In the case of negative resists, underexposure causes disruption or complete dissolution of the exposed part. Conversely, overexposure leads to enlargement or the interconnection of adjacent structures. The final structure's quality depends not only on the exposition parameters but also on the developer and the conditions during the development (time, temperature, . . .). The development process's termination is completed by rinsing with a suitable stopper solution [IPA, de-ionized water (DI water), etc.]. Simply blowing with compressed nitrogen or air is sufficient to dry.

The next steps in the lithographic process are usually done using the lift-off technique. In this technique, the material of interest is deposited onto the sample with the resist layer containing the desired pattern. The technique of choice in the presented thesis is the electron beam evaporation. It was chosen due to its simplicity of operation and also the preferable geometry of the sample inside the vacuum chamber for the lift-off process, as the sample is located directly above the crucible with molten source material.

In contrast with the lift-off technique is the etching technique where the material of interest deposition is followed by the spin-coating of the polymeric resist layer. After the resist pattering using a lithographic technique, the remaining resist layer serves as a mask for an etching process as it protects fabricated structures while the non-protected material is removed. In the final step, the residuals of the resist are removed using a suitable solvent.

E-beam evaporation is one of the most common physical vapor deposition (PVD) processes. It is based on the local heating of the desired material above the evaporation point and subsequent transfer to the substrate. The schematic representation of this process is depicted in Figure 2.4. The electrons emitted from the electron gun are accelerated

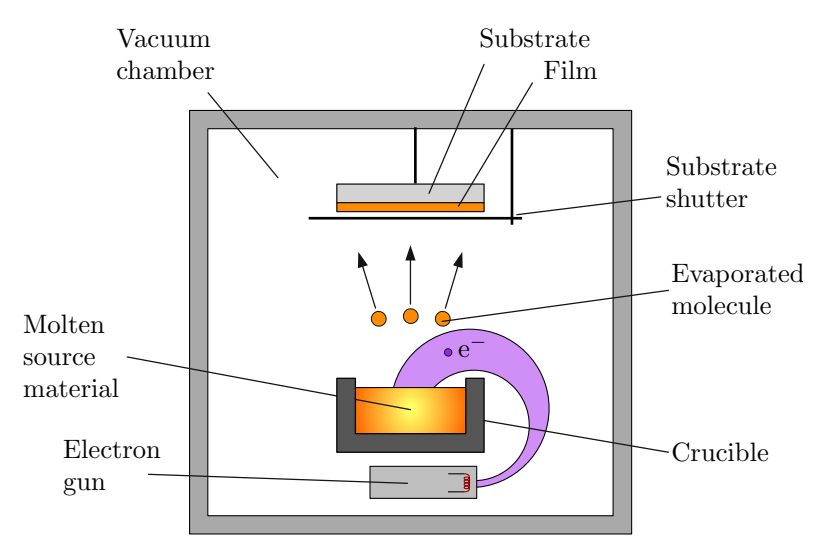


Figure 2.4: Schematics of a simplified e-beam evaporation system. An electron beam is focused on the desired material in the crucible to heat it locally. The molecules start to evaporate. When they reach the substrate, the homogeneous layer of the film is formed.

by the potential difference applied between the cathode and grounded anode. A transverse magnetic field deflects the e-beam towards the top opening of the crucible. The focused electron beam locally heats and melts the target material leading to well-controlled evaporation of the material, which further condensates on the sample substrate, forming

2.2. ELECTRON BEAM LITHOGRAPHY

a new layer. The deposition rate is controlled by the electron beam spot's size and the current formed by the e-beam. Usually, there are several crucibles containing different materials available in the dedicated vacuum chamber, and thus the multilayer deposition is readily possible. In our case, the layer thickness is controlled by in situ quartz crystal microbalance-based thickness meter mounted in the chamber. Compared to other deposition techniques, the main advantage is the high deposition rate of up to $\approx 10\,\text{Å/s}$.

3. Characterization methods

Easy isn't always simple.

– Star Wars: Clone Wars, Episode: Lightsaber Lost

In the previous chapter, we have discussed the tools and techniques used to fabricate the magnetic samples with curved geometries. The following chapter introduces the characterization methods used in the scope of the thesis. Since we study the effect of the substrate's topography on the static and dynamic properties of magnetic thin films, suitable techniques for analyzing the sample topography and its magnetic properties are needed. It starts with a brief description of the atomic force microscopy (AFM) technique, followed by the basic theory needed to understand the Magneto-optical Kerr effect (MOKE). The spin-wave excitation is discussed in the next section. It continues with the explanation of the Brillouin light scattering (BLS) technique. The chapter ends with a description of the vector network analyzer-based (VNA) techniques.

3.1. Atomic Force Microscopy

In atomic force microscopy (AFM), a very sharp tip (in an ideal case atomically sharp) mounted on a cantilever is used to raster over a sample. The chips where the cantilevers are mounted are usually manufactured from Si, or Si₃N₄. The force between the tip and the sample causes a deflection of the cantilever. Most commonly, optical detection is utilized to detect such a small movement variation of the cantilever. A laser beam shines on the cantilever's backside and is reflected towards the photodiode with four quadrants (QPD). Due to the laser's optical path being much larger than the deflection. the cantilever's minute deflection is effectively magnified on the QPD. For the scanning of the tip, a piezoelectric tube is implemented. A voltage applied to the x and y electrodes on the piezoelectric tube result in the horizontal deflection producing a precise raster scan over the sample surface. The vertical height of the tip is controlled by the voltage applied to the z electrodes. The main advantage of using a piezoelectric tube is the possibility to attach several electrodes and scan in x, y, and z directions independently. The stepper motor, on the other hand, is used for the rough positioning of the sample. A simplified scheme is given in Figure 3.1(a). The typical probes used for measuring AFM are depicted in Figure 3.1(b)-(d).

During the measurement, the system's mechanical stability is ensured by the active damping suspension system and the acoustic hood, preventing airflow, temperature variation, and other possible sources of noise.

The main advantage of using AFM compared to SEM is the possibility of precisely map the topography. The lateral resolution of the AFM reaches down to $0.1 \,\mathrm{nm}$, and the vertical resolution as low as $0.5 \,\mathrm{\mathring{A}}$ [146].

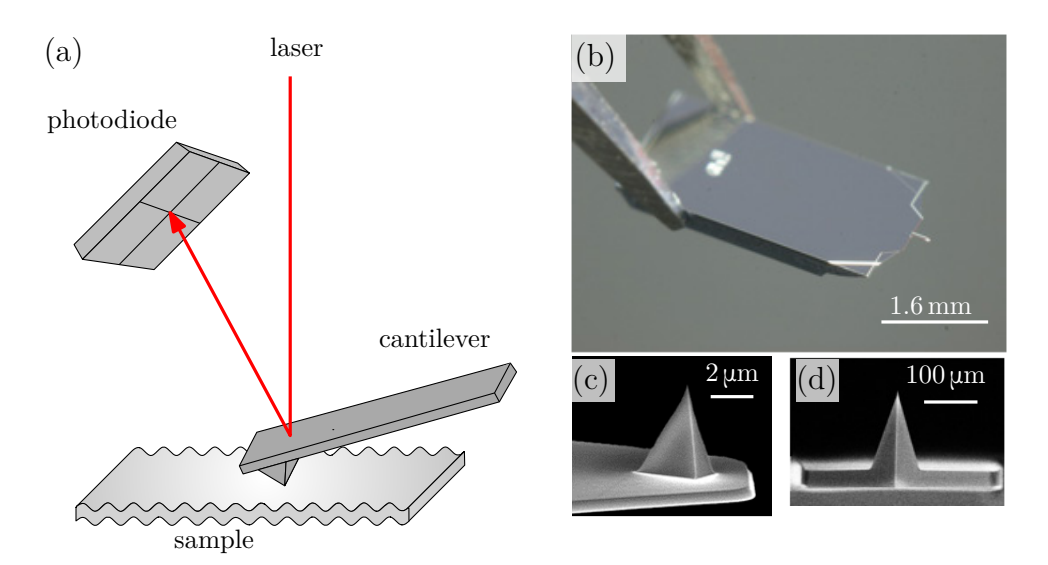


Figure 3.1: (a) Scheme of the principle of the AFM. Laser light shines on the backside of the cantilever and is being reflected towards the segmented photodiode. This principle is used to detect small changes in the tip position. (b) Olympus AC240TS chip [147] used for the Tapping mode, (c) side view of the ScanAsyst-air tip used for the ScanAsyst mode [148], (d) front side of the Olympus AC240TS tip [147]. These two chips mainly differ in the cantilever geometry and the tip position on the cantilever. In the Olympus AC240TS chip, the cantilever is rectangular, and the tip is located at the very end of the cantilever. In contrast, in the ScanAsyst-air, the geometry is triangular, and the tip location is approximate 20 µm from the cantilever end.

All of the AFM measurements in the thesis were done on the Bruker Dimension Icon instrument in the Tapping or ScanAsyst modes. Tapping mode works with a probe oscillating near its resonant frequency. Therefore, the reflected laser beam deflects in a regular pattern over a photodiode array. When the tip deflects after its interaction with the surface, the pattern on a photodiode array changes. Thus, the reflected laser beam reveals information about the sample. With tapping mode, topography and phase images are acquired simultaneously. In ScanAsyst mode, the image quality is monitored continuously and the image optimization is done automatically, including adjusting scan parameters such as setpoint, scan rates or feedback gains. In this mode, the cantilever does not resonate; therefore, cantilever tuning is not required. The ScanAsyst mode is useful for faster imaging because no adjusting is necessary. This mode is based on Peak Force Tapping mode in which force curves are collected at every pixel of the image. The possibility of operation at very low forces compared to the Tapping Mode [149] is possible due to the direct force control provided by the peak force of each of the force curves being used as the imaging feedback signal.

The lateral resolution is highly dependent on the tip shape and its apex's curvature because the final AFM image is the convolution of the probe geometry with the sample topography. In general, the tip's high aspect ratio determines the reliability of imaging the high aspect ratio structures. If the probe cannot reach the bottom of a hole or track the particle sides, the image will be distorted (see Figure 3.2). Quantitative imaging is possible if the tip's dimensions and shape, including the tip apex, are known. It is done using deconvolution in the post-processing.

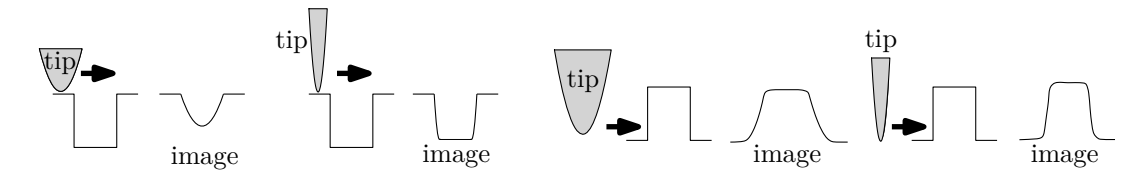


Figure 3.2: Schematic illustration of the tip-shape influence on the resulting image. A dull AFM tip will lead to a distorted image with features appearing larger than in reality. The holes imaged with the blunt probe will appear shallower than when imaged with a sharp probe.

3.2. Magneto-Optical Kerr effect

Historically, the magneto-optical (MO) effect's first manifestation was demonstrated in 1845 by Michael Faraday [150]. He inserted a glass rod into the magnetic field and found an exciting change in the light's polarization plane's rotation after it passed through the rod. The phenomenon is named after its discoverer and is nowadays known as Faraday rotation. After few years, in 1877 [151], John Kerr observed the change in the light polarization after the reflection of polarized light from the polished pole of a magnet. This effect is today known as the magneto-optical Kerr effect (MOKE). The Kerr and Faraday effects are linearly proportional to magnetization. There is also the Voigt effect [152], which is quadratic in magnetization. Generally, the MO effects are based on a small change of the light's polarization state interacting with the magnetic medium. The detected alteration is utilized to create the magnetic image.

The physical origin of the MOKE dwells in the Zeeman exchange splitting together with spin-orbit interaction [153]. Phenomenologically, it can be treated as magnetic circular birefringence and dichroism. The magnetic circular birefringence describes the polarization plane's rotation of linearly polarized light arising from the different refractive indices of circularly polarized components of light. On the other hand, the magnetic circular dichroism treats the change in an ellipticity due to different absorption coefficients of left- and right-handed circularly polarized light in the medium. Therefore the linearly polarized light will become elliptical after the reflection on the magnetic sample, and the parameters of the ellipse (rotation, ellipticity) are proportional to the magnetization.

On the whole, the MOKE's change in the polarization of light can be described by the dielectric tensor accounting for the effect of magnetic medium. For an isotropic or cubic materials, it is described by the dielectric law [154]

$$\mathbf{D} = \hat{\boldsymbol{\varepsilon}} \cdot \mathbf{E} \,, \tag{3.1}$$

where \boldsymbol{D} is the electric displacement vector, $\hat{\boldsymbol{\varepsilon}}$ is the dielectric permittivity tensor and \boldsymbol{E} is the electric field vector. The generalized dielectric permittivity tensor is accordingly described by [153]

$$\hat{\boldsymbol{\varepsilon}} = \varepsilon \begin{pmatrix} 1 & -iQm_z & iQm_y \\ iQm_z & 1 & -iQm_x \\ -iQm_y & iQm_x & 1 \end{pmatrix} + \begin{pmatrix} B_1m_x^2 & B_2m_xm_y & B_2m_xm_z \\ B_2m_xm_y & B_1m_y^2 & B_2m_ym_z \\ B_2m_xm_z & B_2m_ym_z & B_1m_z^2 \end{pmatrix}, \quad (3.2)$$

where ε is the scalar relative permittivity, and Q is the complex Voigt constant that is to the first order directly proportional to the sample's magnetization. By the Voigt constant, the gyration vector is coupled to the magnetization vector [155]. B_1 and B_2 are MO constants describing the quadratic effect (Voigt effect), and m_i are the components of

the unit vector of magnetization ($|\mathbf{m}|^2 = 1$). The sign convention used in (3.2) represents the positive rotation and ellipticity of Faraday and Kerr effects for a clockwise rotation of the polarization ellipse.

For the Kerr effect, the equation (3.1) can be rewritten using the relation from (3.2) in the form

$$\mathbf{D} = \varepsilon \left(\mathbf{E} + iQ\mathbf{m} \times \mathbf{E} \right) \,, \tag{3.3}$$

where vector \boldsymbol{D} represents the secondary light amplitude rising from the magneto-optical interaction of \boldsymbol{E} with the magnetization vector \boldsymbol{m} in the sample. The cross product from eq. 3.3 can be explained using the Lorentz force theory. It also proves the gyroelectric nature of the Kerr effect.

The three main magneto-optical Kerr effect configurations can be understood. The polar Kerr effect, where the magnetization points in the direction perpendicular to the surface normal, the longitudinal Kerr effect, where the magnetization lies in the direction parallel to the surface and along the plane of incidence, and the transverse Kerr effect, where the magnetization is parallel to the surface and perpendicular to the plane of incidence. All geometries are shown in Figure 3.3.

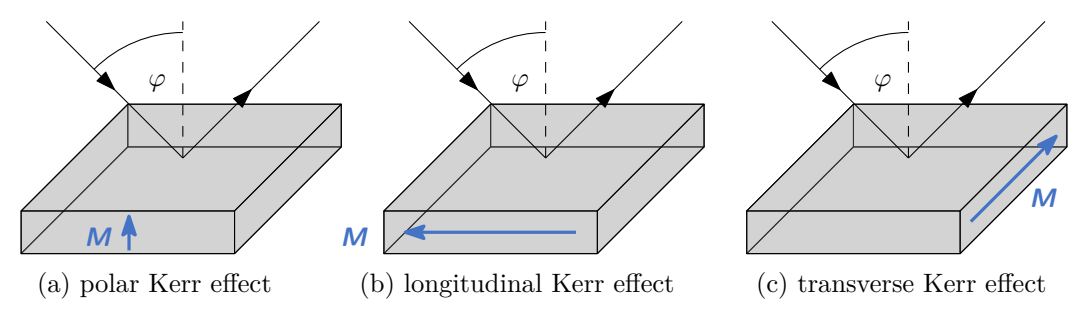


Figure 3.3: Schematic to show the three different configurations when measuring Kerr effect. (a) polar Kerr effect, (b) longitudinal Kerr effect, (c) transversal Kerr effect.

Most commonly, the polar and longitudinal Kerr effects are used. A schematic sketch of the longitudinal Kerr effect with an oblique plane of incidence and s-polarization is depicted in Figure 3.4. For the longitudinal configuration, the magneto-optical rotation can be seen for both perpendicular s-polarization and parallel p-polarization (concerning the plane of incidence).

As the magnetization direction is collinear with one of the coordinate axis, the dielectric permittivity tensor from (3.2) can be reduced. For the configuration shown in Figure 3.4, where $m_y = \pm 1$, $m_x = m_z = 0$ it gives

$$\hat{\boldsymbol{\varepsilon}} = \boldsymbol{\varepsilon} \begin{pmatrix} 1 & 0 & iQm_y \\ 0 & 1 & 0 \\ -iQm_y & 0 & 1 \end{pmatrix} . \tag{3.4}$$

When the s-polarized light is used for the illumination of the magnetic sample, in general, the reflected light consist of two orthogonal components, the identical s-polarized and orthogonal p-component. Then, a Fresnel coefficient r_{ss} describing the reflected s-polarized wave and a Fresnel coefficient r_{ps} accounting for the orthogonal component polarized along the p-direction can be defined. The Jones matrix [156] describing the polarization state for the reflected light is then defined as [157]

$$\begin{pmatrix} E_p^{\text{refl}} \\ E_s^{\text{refl}} \end{pmatrix} = \begin{pmatrix} r_{pp} & r_{ps} \\ r_{sp} & r_{ss} \end{pmatrix} \begin{pmatrix} E_p^{\text{inc}} \\ E_s^{\text{inc}} \end{pmatrix} ,$$
(3.5)

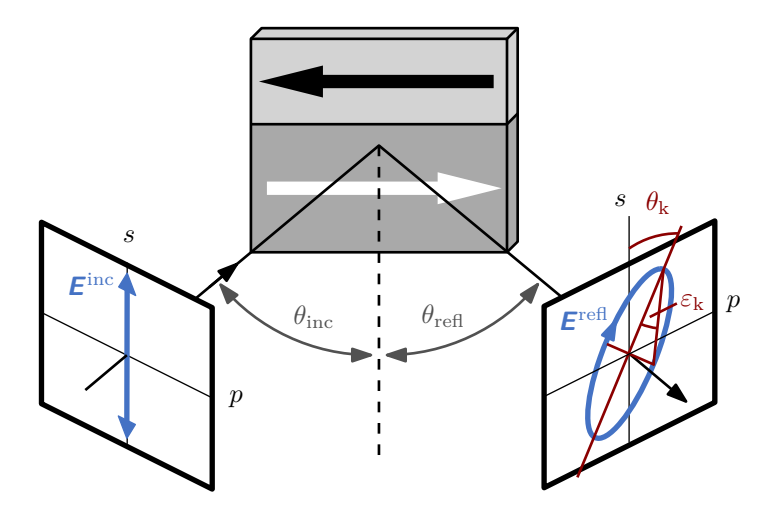


Figure 3.4: Illustration of the longitudinal Kerr effect. The interaction of the originally s-polarized light with MO active structure is shown. The incoming linearly polarized light $\boldsymbol{E}^{\text{inc}}$ changes its polarization to the elliptically polarized light $\boldsymbol{E}^{\text{ref}}$ after the reflection from the magnetic medium. The resulting Kerr rotation θ_k and ellipticity ε_k are the parameters of the elliptical polarization. Adapted from [153].

where $E_{p,s}^{\rm inc}$ and $E_{p,s}^{\rm refl}$ are the electric field vectors of incident and reflected light, respectively. Then, the complex Kerr angle $\Phi_{\rm k}$ is a sum of the Kerr rotation $\theta_{\rm k}$ and Kerr ellipticity $\varepsilon_{\rm k}$. For s- and p-polarized light it is

$$\Phi_{\mathbf{k},s} = \theta_{\mathbf{k},s} + i\varepsilon_{\mathbf{k},s} = \frac{r_{ps}}{r_{ss}} \quad \text{and} \quad \Phi_{\mathbf{k},p} = \theta_{\mathbf{k},p} + i\varepsilon_{\mathbf{k},p} = \frac{r_{sp}}{r_{pp}}.$$
(3.6)

3.2.1. Kerr Microscopy

In recent years, there has been a significant advancement in magnetic structures imaging using visible light. However, the classical Kerr microscopy technique has many unvanquishable advantages. The method is based on the magneto-optical Kerr effect (MOKE). It uses nearly crossed polarizers. The polarizer polarizes the light, which then travels to the sample and is reflected from it. The local magnetization-induced light polarization changes are converted to intensity changes on the second polarizer (analyzer) that are further detected by the sensitive camera. The main advantage when using this technique is that no specific surface treatment of the sample is required. Also, using the additional electromagnet, an external field up to hundreds of mT can be applied in an arbitrary direction, which makes the observation of magnetization reversal processes possible. The Kerr microscopy information depth depends on the penetration depth of the used light and studied material. For the visible light reflected on the metallic surface it is around 50 nm [158, page 220]. The field of view depends on the microscope objective. Therefore, by changing the objective, the view field's variation is achievable from several centimeters down to the detailed study of micrometer-sized structures. The significant drawback is the lateral resolution which is limited by the Rayleigh criterion. For the visible light, it is about 300 nm, which is restricting the study of sub-micrometer patterned structures like magnetic vortices or stripe domains in very thin films.

In the Kerr microscopy, the sample's whole image is obtained directly using a single objective lens and a digital camera. The ray diagram showing the illumination and image-formation light paths is shown in Figure 3.5.

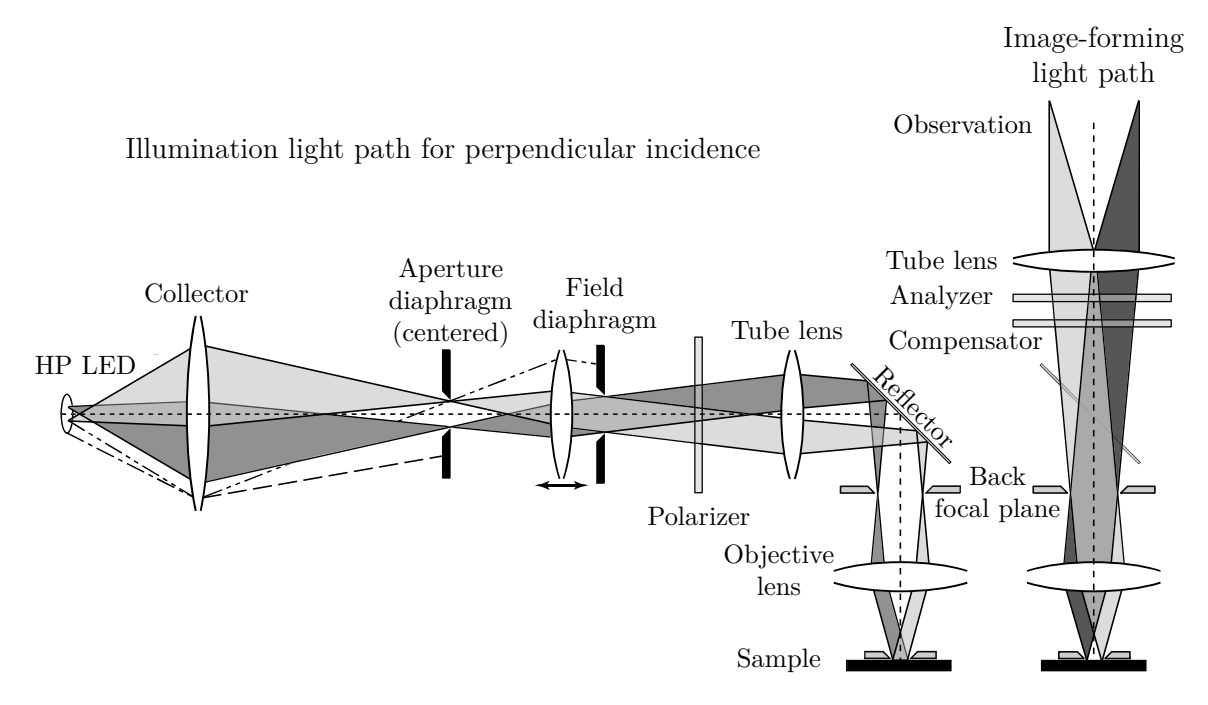


Figure 3.5: The essential components and ray diagram for the wide-field Kerr microscopy. The light from the high-power LED, coming from the left, is focused on the aperture diaphragm plane by the collector lens. Then it passes through the field diaphragm and is polarized on the polarizer. After it passes through the objective lens, it is reflected from the sample and passes through the infinity-corrected objective. Then it is polarized on the analyzer and finally imaged on the camera. After [154].

In this thesis, the Kerr microscopy experiments were measured using the setup from Evico magnetics GmbH. For the illumination, eight light-emitting diodes (LED) are used in this setup. It is possible to control them individually using the computer, which allows us to probe individual orthogonal components of the magnetization simply by switching on/off the individual LEDs. The sample is placed on the stage with the 3D positioning capabilities and also rotation. Additionally, the external magnetic field is provided by the rotatable electromagnet.

3.3. Spin Wave Excitation

In section 1.5.1, the discussion of the dynamic response of the magnetic system $\mathbf{m}(t)$ on the harmonic microwave excitation magnetic field $\mathbf{h}(t)$ is provided. Accompanying, in section 1.7, the corresponding dispersion relations are summarized. Having this established, the following section presents the methods used to generate the dynamic magnetic fields.

In general, the approach presented in the thesis relies on the dynamic magnetic field (Oersted field) created by a microwave current flowing through a wire. The spin waves are excited only if the excitation source matches both the spin-wave dispersion's temporal and spatial frequency. The temporal frequencies of the spin waves are in the GHz range, which is usually referred to as the Radio-Frequency (RF) range¹. Hence, the microwave current must also be in this frequency range, and it is called RF current. If the RF current flows through a single wire, the radiation losses are enormous. Therefore, such a conductor is also denoted as a microwave antenna or a microstrip antenna.

¹The radio spectrum is in the frequency range from 30 kHz to 300 GHz.

The spatial distribution of the oscillating magnetic field depends on the shape and dimensions of the antenna. The microwave field inductively couples to the magnetization of the ferromagnetic layer beneath, leading to the excitation of spin waves. The excited spin waves then propagate in both directions $(+\mathbf{k} \text{ and } -\mathbf{k})$ with wavelengths defined by the spatial distribution of the magnetic field from the antenna. Due to the microwave magnetic field's inductive coupling to the magnetization of the ferromagnetic layer beneath, the excited SWs have the same frequency ω . The dominant wavenumber corresponds to the width of the microwave antenna. The excitation spectrum of the antenna and the wave vector distribution can be calculated using Fourier transform of the spatial profile of the excitation field [159]. This requires the knowledge of the magnetic field's spatial distribution, which must be calculated. Typically it is done using finite element analysis. However, the excitation efficiency J_{exc} can also be approximately calculated from the spatial current density distribution.

For the simple rectangular geometry of the microstrip antenna, the excitation efficiency J_{exc} can be calculated as [160]

$$J_{\rm exc}(k) = \left(\frac{\sin\frac{kw_{\rm a}}{2}}{\frac{kw_{\rm a}}{2}}\right)^2,\tag{3.7}$$

where w_a is the width of the microstrip antenna. Figure 3.6(a) shows a schematic geometry of the microstrip antenna used for the spin waves excitation. The spatial distribution of the dynamic magnetic field created by the RF current in a distance of 100 nm above a 1 µm wide and 100 nm thick microstrip antenna calculated numerically using FEMM² software is depicted in Figure 3.6(b). The red line represents the in-plane component of the dynamic magnetic field \boldsymbol{h} , which is maximal below the antenna (schematically shown by the yellow rectangle). The black line corresponds to the oscillating magnetic field's out-of-plane component \boldsymbol{h} with the amplitude maximal at the antenna's edges. Figure 3.6(c) shows the comparison of the normalized Fourier transform of the spatial profile of the excitation field, and the excitation efficiency $J_{\rm exc}$. The first excitation minimum is formed in $k = 2\pi/w_a$ and the second excitation maxima efficiency is always below ten % of the maximal value. Hence, the first minimum is often regarded as a cut-off, and the excitation is considered only for $k < 2\pi/w_a$. This reciprocal dependence shows that the limiting factor for the high k-vector regime (exchange-dominated regime) is the fabrication limit. Therefore, for better k-vector selectivity and higher excitation efficiency, different types of excitation antennas must be prepared. Usually, combinations of many strip lines or coplanar waveguides in the form of a meander [159, 161] or a ladder [162] are used [92, 160]. The excitation of spin waves utilized in the presented thesis was done via stripline antennas, and the attempt for the k-vector selectivity was not pursued.

Most of the experimental part of the thesis is done on microstructures, namely spin-wave waveguides. Due to the experiment's geometry, where the microstrip antenna is perpendicular to the spin-wave waveguide, the maximal amplitude of the dynamic magnetic field \boldsymbol{h} in the spin-wave waveguide is under the excitation antenna. From section 1.5.1, equation 1.28, we already know, that the term $\boldsymbol{M}_0 \times \boldsymbol{h}$ is the main responsible for the excitation of the magnetization dynamics. Thus, the maximal excitation efficiency is when $\boldsymbol{M}_0 \perp \boldsymbol{h}$, i.e., DE geometry, and the \boldsymbol{M}_0 is perpendicular to the long axis of the spin-wave waveguide. By contrast, in the BV geometry, where \boldsymbol{M}_0 is parallel to the long axis of the

²Finite Element Method Magnetics http://www.femm.info.

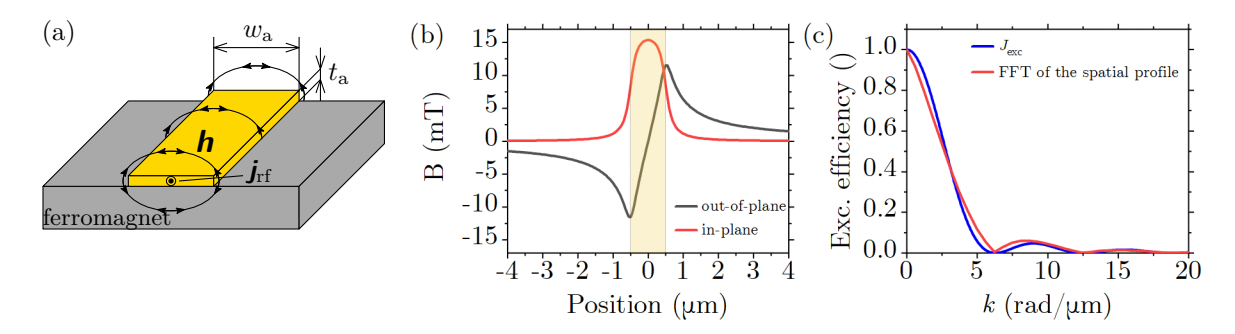


Figure 3.6: (a) Schematic of the microwave antenna for the excitation of spin waves. The width of the microstrip antenna is w_a , the thickness is t_a . The microwave field h, generated by the microwave current $j_{\rm rf}$ flowing through the antenna, is approximately uniform and parallel to the conductor surface. (b) Micromagnetic simulation of the magnetic field distribution and the magnetic vector field orientation and magnitude calculated using Finite Element Method Magnetics (FEMM). The red line represents the in-plane component of the dynamic magnetic field, while the black line corresponds to the out-of-plane component of the oscillating magnetic field. The yellow rectangle symbolized the microstrip antenna. The parameters of simulation are: $w_a = 1 \,\mu\text{m}$ and $t_a = 100 \,\text{nm}$. (c) Absolute value of the normalized excitation efficiency (red line) and the excitation efficiency $J_{\rm exc}$ of the microstrip antenna, calculated approximately using (3.7) (blue line).

waveguide, the in-plane component of the dynamic magnetic field \boldsymbol{h} does not excite spin waves, and only the out-of-plane component contributes to the excitation which results in the excitation efficiency decrease.

The excitation of spin waves in the DE mode is strongly nonreciprocal [163, 164]. As discussed above, in DE mode, both in-plane and out-of-plane components of the dynamic magnetic field contribute to the excitation of spin waves. Contributions of these components are efficiently intermixed by the dynamic susceptibility tensor with non-trivial result [165]. Together with the implicit non-reciprocity [166] the outcome is the significant difference of spin-wave amplitudes propagating in the positive and negative direction from the microstrip antenna. By reversing the applied external magnetic field's direction, the non-reciprocity in the spin-wave excitation can be switched.

3.4. Brillouin Light Scattering Spectroscopy

This section is devoted to the Brillouin Light Scattering (BLS) technique, which allows us to probe the magnetization dynamics in the range of GHz. The method's versatility, with many possible studies to be performed, and a wide variety of magnetic information obtainable (frequency-, space-, phase-, and time resolution), has rendered BLS one of the most fundamental techniques for observing spin dynamics [167]. A detailed description of the technique is provided in the review [108]. The more in-depth description of the Brillouin light scattering can be found in references [58, 91].

BLS process can be described by the inelastic scattering of incident photons with magnons (quasi-particle of spin-wave excitation). In this process, both energy and momentum conservations are taken into account, described by

$$hf_{\text{out}} = hf_{\text{in}} \mp hf_{\text{SW}}, \qquad (3.8)$$

$$\hbar \mathbf{k}_{\text{out}} = \hbar \mathbf{k}_{\text{in}} \mp \hbar \mathbf{k}_{\text{SW}}, \qquad (3.9)$$

where h is the Planck constant³, and \hbar is the reduced Planck constant. f_{out} is the frequency of the outcoming scattered photon, f_{in} is the frequency of the incoming photon before scattering, and f_{SW} is the frequency of the generated magnon. For wave vector \mathbf{k} , the same notation as for the frequencies applies. The negative sign on the right-hand side of equations (3.8) and (3.9) represents Stokes process where the photon generates a magnon; hence, the scattered light's frequency is lower. Correspondingly, the positive sign represents the anti-Stokes process where the incident light annihilates the magnon. In this case, the energy of the scattered light is increased, and the frequency of the scattered light is higher. A sketch of the scattering process is schematically shown in Figure 3.7(a).

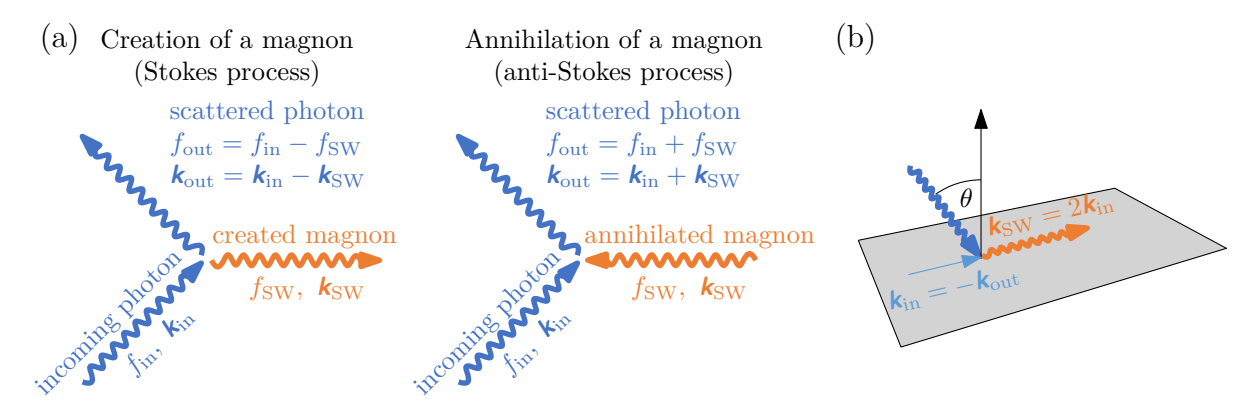


Figure 3.7: (a) Scheme of the BLS process. The incoming light with frequency $f_{\rm in}$ and wave vector $\mathbf{k}_{\rm in}$ is scattered on the magnon with frequency $f_{\rm SW}$ and wave vector $\mathbf{k}_{\rm SW}$. The Stokes process describes the creation of a magnon, and the anti-Stokes process describes the annihilation of a magnon. The system's energy and momentum are conserved; therefore, the scattered photon carries the information about the wave vector and the spin wave frequency. (b) Illustration of the BLS process in the back-scattering geometry.

The BLS can also be approached classically. The process is then based on a periodic modulation of the dielectric tensor of light induced by the traveling spin wave in a magnetic medium due to spin-orbit coupling. Because of the magnons' wave nature, the periodicity in time represents the spin-wave frequency. Correspondingly, the periodicity in space represents the spin wave's wavelength. Therefore, the scattering can be understood as the scattering from a moving Bragg grating [168]. The scattered light's frequency shift is then treated as a Doppler-shifted with a spin wave frequency.

Both the magnons and phonons can cause the periodic modulation of the dielectric tensor. To distinguish between the scattering processes caused by phonons and magnons, the analysis of the polarization direction of the scattered light is employed. The light

³The Planck constant is one of the fundamental constants in quantum mechanics. In the revised SI system, the Planck constant has the exact value $h = 6.626\,070\,15 \cdot 10^{-34}\,\mathrm{Js}$. It is a key value in the redefinition of the kilogram.

scattered on magnons, in contrast to phonons, has its light polarization rotated by $\pi/2$, which can be easily distinguished.

The conservation of momentum (3.9) can be applied only for the infinite medium. In thin film, only the in-plane component of the k-vector is conserved due to the broken translation invariance by the surface of the film. Thus, only the in-plane component of the wave vector is conserved. The in-plane component of the wave vector can be calculated from the Figure 3.7(b) as

$$k_{\parallel} = |\mathbf{k}_{\rm in}| \sin \theta \,, \tag{3.10}$$

where θ is the angle of incidence. By changing this angle, it is possible to select the desired wave-vector of the spin wave. In the back-scattering geometry, shown in Figure 3.7(b), the spin-wave k-vector is maximal, because the k-vector of the scattered photon is opposite to the k-vector of the incoming photon. The maximal probed k-vector using green laser light is

$$k_{\rm SW}^{\rm max} = 2|\mathbf{k}_{\rm in}|\sin\theta = 2\frac{2\pi}{\lambda_{\rm 532\,nm}} = 23.6\,{\rm rad/\mu m}$$
. (3.11)

Hence, the minimal wavelength of the spin wave that can be detected using the green light is $\lambda_{\rm SW}^{\rm min} = 266\,{\rm nm}$.

The inelastically scattered photons carry information about the energy (frequency) and momentum (wave vector) of the corresponding spin-wave mode and phase information. The phases of the scattered and detected photons are connected using a well-defined relation. This phase relation will be used for a phase-resolved BLS investigation later in the text.

Due to the energy conservation, the shift in the frequency of scattered light directly corresponds to the frequency of the investigated spin-wave mode; hence, the scattered light's energy analysis is crucial for the BLS measurement. In order to distinguish the inelastically scattered photons from all the elastically Rayleigh scattered photons, extreme sensitivity and high-contrast are needed. Also, when compared to the photon energy, the photon frequency shift due to the magnon generation/annihilation are 10⁶ smaller. Therefore, an essential tool for a BLS spectroscope is a high-contrast frequency analysis[169] device as well as a monochromatic source of light.

3.4.1. Brillouin light scattering – experimental setup

As discussed above, a light source with a narrow frequency distribution is a crucial tool to determine the inelastically scattered light's frequency shift. In the BLS setup used in the presented thesis, two easily changeable continuous laser sources are used, Laser Quantum Torus and Cobolt Samba 05.01. The interchangeability of light sources is useful when one of the lasers is under maintenance. The operation wavelength for both lasers is $\lambda = 532\,\mathrm{nm}$. The laser's key specification is the single-mode operation, i.e., the higher laser modes must be suppressed. If the higher modes are not sufficiently suppressed, they appear as an additional signal in the measured spectrum.

The spin-wave frequencies are usually in the Gigahertz range, leading to the spectrometer's resolution's requirement to be better than $0.05\,\mathrm{cm}^{-1}$. This condition is fully satisfied by the tandem Fabry-Pérot interferometer (TFPI). In the presented thesis's experimental setup, the frequency shift was analyzed using a multi-path TFPI. It was designed by John. R. Sandercock [170] and uses a set of two Fabry-Pérot interferometers. In an FPI, the multiple reflections of a light beam between two parallel highly reflective mirroring plates

cause a path difference compared to a directly transmitted beam. For the transmission through the TFPI, the transmission criteria of both FPIs must be fulfilled simultaneously. Transmission of the FPI is periodic with respect to the mirror distance and can be described by the Airy function. The free spectral range (FSR) defines this periodicity in the frequency space. Thus, the TFPI determines the frequency resolution and the maximal accessible frequency range (FSR).

In the measurement, the wavelength (frequency) is analyzed from the detected transmitted light intensity during the scanning of the interferometer mirrors distance. Therefore, the precise alignment of the mirror spacings is essential. As can be seen from the TFPI scheme in Figure 3.8(a), one of each FPI mirrors is mounted on the scanning stage. The first FPI is mounted in the piezo-stage scanning direction, while the second is tilted by an angle α . Thus, the scanning stage movement results in the mirror spacing change, which for FPI₁ is Δd , while for FPI₂ is $\Delta d \cos \alpha$. The frequency shift is then determined from the comparison of the reference beam directly from the light source with light scattered from the sample. The result of a typical BLS measurement showing the central reference laser peak, marking the zero position in a BLS spectrum, together with Stokes and anti-Stokes signal, is depicted in Figure 3.8(b). The interferometer used in the BLS setup at CEITEC is the TFP-2 HC from Table Stable LTD, providing the contrast better than 10^{15} .

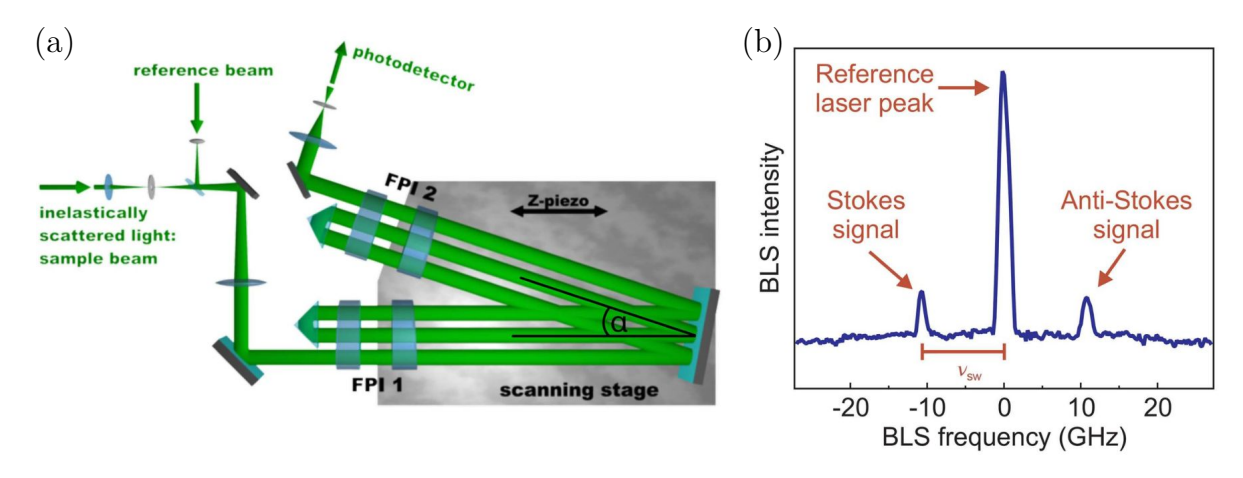


Figure 3.8: (a) Principle of the Tandem Fabry-Pérot interferometer (TFPI). It is an essential tool for frequency shift analysis of inelastically scattered light. TFPI comprises two FPIs that are aligned under an angle α . One mirror of each FPI is mounted on the scanning stage to control the mirror spacing. (b) Typical BLS measurement, where the central peak corresponds to the reference light and the lower peaks correspond to the Stokes and anti-Stokes signals. After [108].

The BLS setup comprises fundamental components like the laser, an electromagnet, and the interferometer. In addition to it, the setup also includes an appropriate optical microscope objective with a high numerical aperture (NA) together with a CCD camera and a positioning system. The setup with the microscope objective strongly increases the spatial resolution and is commonly known as micro-focused BLS (µBLS). Furthermore, to excite spin waves at precise frequencies, a microwave generator is utilized. It is connected via an SMA cable to a microwave probe, which is placed on the sample. The setup used in the range of the thesis is based on the commercial scanning optical microscope from THATec Innovation GmbH and further developed by Lukáš Flajšman [58] in his dissertation thesis, and Ondřej Wojewoda [91] in his master's thesis. It uses a precise 3D piezo

stage. The setup is controlled by a sophisticated PC software package Tandem Fabry-Pérot Data Acquisition System (TFPDAS), which was developed in 1999 [171] and the further development is realized by THATec Innovation⁴ under the platform thaTEC:OS. The software also offers an active stabilization of the sample during the measurement, hence, compensating for any thermal drifts.

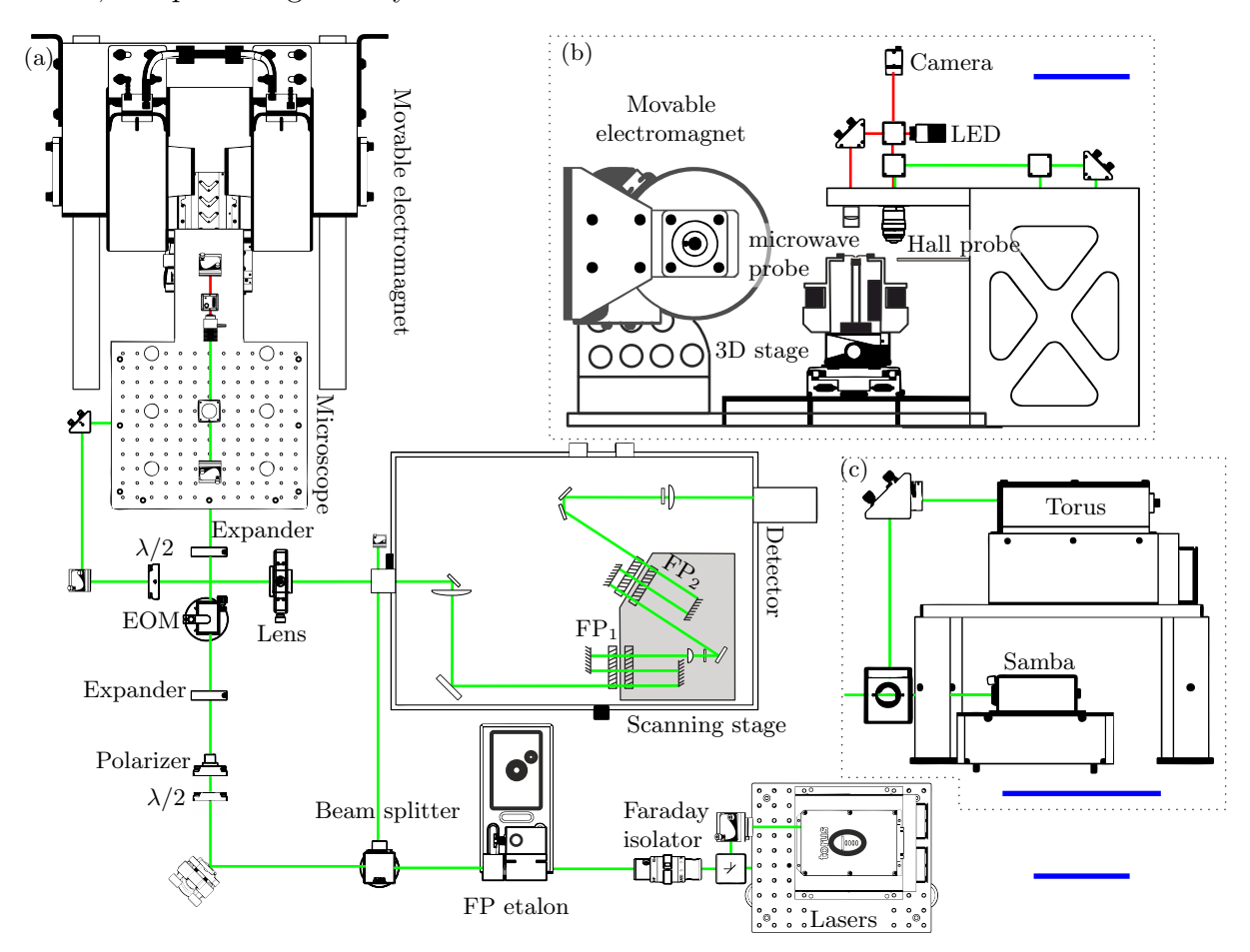


Figure 3.9: (a) Schematic of the μBLS setup. Green and red lines represent the laser paths.
(b) The commercial scanning optical microscope with a movable electromagnet is illustrated in the side-view. (c) Configuration employing interchangeability of two laser sources, Laser Quantum Torus and Cobolt Samba 05.01. Blue lines (scale bars) are 250 mm. Adapted from [91].

The optical setup is schematically shown in Figure 3.9. First, the laser beam from the laser source passes through a Faraday isolator to prevent the reflection of any light back to the solid-state laser. Then, the light passes through a filter (Fabry-Pérot etalon), which suppresses the higher laser modes and eventually improves the obtained BLS signal. After that, the light passes through a 90:10 beamsplitter, 10% of the laser intensity goes to the reference input of the TFPI, and 90% of the intensity continues to the measurement arm. In order to control the laser power, the beam then passes through the $\lambda/2$ plate and the polarizer. After the modification of the laser power, the beam passes through the first lens of an expander. Then it goes through the electro-optic modulator (EOM), and the expansion of the beam is finished via the second lens of the telescope. Subsequently, two mirrors in the periscope configuration are used to direct laser light to the top part

⁴http://thatec-innovation.com

of the optical stage, where the beam passes through the beamsplitter. Then, the light goes through the coupling dichroic mirror, where the green light from the laser source is overlapped with the red laser light from the LED source utilized for the imaging.

As discussed before in the text, the scanning optical microscope is a commercial solution purchased from THATec Innovation GmbH. In their microscope, it is possible to contact the sample utilizing the integrated micro-positioning probe station. For the purposes of contacting, the 3D stage can be moved to the so-called contacting position, and the microscope with low magnification is employed. For the measurement, the sample stage and contacted micro-probes are moved under the high-resolution objective lens (LD EC Epiplan-Neofluar 100x/0.75 BD). Figure 3.9(b) shows that both low magnification microscope and high-resolution objective share the same illumination and camera.

After the scattering, the laser beam is guided by the beamsplitter and mirrors from the top part of the optical stage back to the table level. Here it passes through the $\lambda/2$ plate, which adjusts the polarization angle before the final focus to the input pinhole of the TFPI. The size of the pinhole is variable. After it passes through the TFPI, the signal is detected using a highly efficient single-photon counter Hamamatsu C11202-060.

The numerical aperture of the objective $NA = n \sin \theta$ determines the spatial resolution of the μ BLS setup. Here, the medium between the objective and the sample was air, so $n \approx 1$. Following (3.11), the maximum wave detector, which can be detected, is given by

$$k_{\rm SW}^{\rm max} = 2|\mathbf{k}_{\rm in}|\sin\theta = 2\frac{2\pi}{\lambda_{\rm 532\,nm}}NA \approx 17.7\,{\rm rad/\mu m}$$
. (3.12)

In the μ BLS, the detected signal comes from many spin-wave modes with different \mathbf{k} -vectors. In general, using μ BLS, it is not possible to distinguish them.

3.4.2. Phase-resolved Brillouin light scattering microscopy

In the previous section, the possibility of a phase sensitivity and a k-selectivity was suppressed in order to have the highest spatial resolution. However, the BLS process is phase-sensitive, and the scattered photon carries the phase information of the spin wave. This phase information can be extracted using the interference of the sample beam with the reference beam. It is essential that the phase of the reference beam is well-defined relative to the sample beam. Furthermore, the reference beam's frequency must be the same as the sample beam, thus, ensuring the temporal coherence of the two beams. When these requirements are fulfilled, the interference patterns can be observed, and the spin-wave phase can be investigated. This phase-resolved measurement technique was developed in the group of prof. Hillebrands [163, 172].

The reference signal is generated by the electro-optical modulator (EOM) implemented in the beam path. The EOM and the antenna that excites the spin waves are connected to the same RF source. A minor part of the light beam is modulated in the EOM, and the major part remains with unchanged frequency. To match the intensity of the modulated and unmodulated parts of the light beam, it is necessary to place a tunable attenuator between the EOM and the RF source. When the photons from the laser beam interact with the spin waves, the part of the light's frequency is shifted to the same frequency as the EOM light. Additionally, the EOM light phase is constant, so only the photons

scattered from spin waves carry the spin waves' phase information. These two signals interfere, and the interference signal intensity can be expressed as

$$I = I_{SW} + I_{EOM} + \sqrt{2I_{SW}I_{EOM}}\cos\Delta\Phi, \qquad (3.13)$$

where I_{SW} is the intensity of photons scattered from spin waves, I_{EOM} is the intensity of the EOM light⁵. Due to the temporal coherence, the relative phase of the reference and sample beams depends on the probing laser beam's position. When the probing laser position changes, the spin waves phase also changes with $\Phi_{\text{SW}} = \Phi_0 + k_{\text{SW}}x$. Therefore, any time dependence can be neglected, and the relative phase of the reference and the sample beams is

$$\Delta\Phi = \Delta\Phi_0 + k_{\rm SW}x. \tag{3.14}$$

To illustrate the extraction of the spin-wave wavelength, the phase-resolved BLS is utilized for the simplest case of the 1D spin-wave propagation in spin-wave waveguide. The RF current running through a microstrip antenna excites spin waves that are locally probed by the μ BLS. The BLS intensity is mapped while increasing distance (x) from the excitation antenna. As discussed above, the spin-wave phase $\Phi_{\rm SW}$ is evolving depending on the position of the probing laser. The spin-wave intensity is assumed as an exponentially decaying function $I_{\rm SW} = I_0 \exp(-x/l_{\rm att})$, where I_0 is the maximal spin-wave intensity and $l_{\rm att}$ is the propagation length known from (1.74). For homogeneous samples, $I_{\rm EOM}$ can be assumed as a constant. Then, equation (3.13) becomes

$$I = I_0 \exp\left(-\frac{x}{l_{\text{att}}}\right) + I_{\text{EOM}} + 2\sqrt{I_0 I_{\text{EOM}} \exp\left(-\frac{x}{l_{\text{att}}}\right)} \cos\left(\Delta\Phi_0 + \frac{2\pi}{\lambda}x\right), \quad (3.15)$$

where λ is the wavelength of the spin waves. The modeled phase and intensity of the spin waves are schematically shown in Figure 3.10.

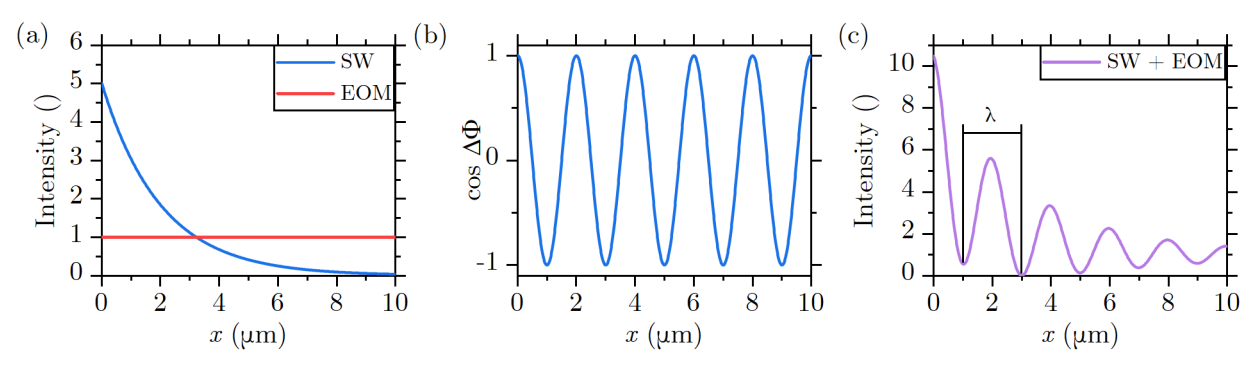


Figure 3.10: (a) Analytically modeled intensity of spin waves and EOM, and (b) phase profiles as functions of distance x from the excitation antenna. (c) The interference signal modeled using (3.15). The wavelength of spin waves can be extracted from two neighboring minima.

3.5. Vector network analyzer

This section provides the essential introduction to the measurements with a vector network analyzer (VNA). This device allows for the generation and detection of high-frequency signal waves. Utilizing ground-signal-ground (GSG) microwave probes and high-frequency

⁵The full phase reconstruction is calculated in [91].

coaxial cables connected to the VNA ports make it possible to study the sample's characteristics. Usually, the sample is referred to as a device under test (DUT). In general, any RF component such as coupler, filter, attenuator, antenna, amplifier, etc., can be characterized by VNA.

To understand the physics behind the measurement procedure with VNA, it is essential to briefly address two-port networks because the spin-wave devices can electrically be described as two-port networks. The practical problem arises when we want to measure high-frequency current and voltage because the direct, measurable quantities are usually only the magnitude and the phase of a traveling or standing wave. The best representation in accord with direct measurement is given by scattering matrix $\hat{\boldsymbol{S}}$, which describes the idea of an incident, reflected, and transmitted wave [173]. Figure 3.11 depicts the illustration of a two-port network.

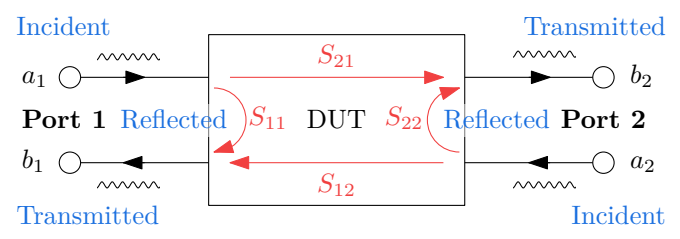


Figure 3.11: Schematics of the two-port S-parameter model with device under test. This model uses complex normalized waves a_i , b_i at a port i.

The scattering parameters (S-parameters) describe the relation of the outgoing and incoming waves. The complex normalized wave a_i generated at port i characterizes the incident wave. It travels to the DUT, where either reflection, absorption, or transmission occurs. The result of either one of the processes is the complex normalized wave b_j detected at port j. For the two-port network, i, j represent port numbers 1 and 2. In an n-port device, n^2 S-parameters are needed. Thus, in our case, the two-port device, there are four S-parameters connecting the incoming and outgoing waves by

$$\begin{pmatrix} b_1 \\ b_2 \end{pmatrix} = \hat{\boldsymbol{S}} \begin{pmatrix} a_1 \\ a_2 \end{pmatrix} = \begin{pmatrix} S_{11} & S_{12} \\ S_{21} & S_{22} \end{pmatrix} \begin{pmatrix} a_1 \\ a_2 \end{pmatrix} . \tag{3.16}$$

Every S_{ij} parameter gives the ratio between the outgoing complex normalized wave b_i at port i to the incident complex normalized wave a_j at port j

$$S_{ij} = \left. \frac{b_i}{a_j} \right|_{a_k = 0 \text{ for } k \neq j} . \tag{3.17}$$

Therefore S-parameters on the main diagonal $(S_{11} \text{ and } S_{22})$ describe reflections of the waves from the DUT back to the port where they were generated. For the case of a two-port network, the off-diagonal elements $(S_{12} \text{ and } S_{21})$ are linked with the microwave transmission, i.e., the parameter S_{21} is the transmission coefficient from port 1 to port 2 and correspondingly parameter S_{12} describes the transmission from port 2 to port 1. A full set of four S-parameters completely describes any linear DUT [79]. Besides, equation (3.17) says that the incident waves on all ports are zero, except for the port j. Thus, only one port is active during the measurement, and all other ports should be terminated in matched loads to avoid reflections.

The VNA ports must be matched; otherwise, the connections themselves will create reflections, and the S-parameters measured on a DUT will not be reliable, i.e., the reflection coefficient looking into port i is not equal to S_{ii} . Similarly, transmission from

port i to port j is not equal to S_{ji} . The S-parameters of the network are defined only if all ports are matched [173]. To correctly work with the VNA and eliminate the error, it is necessary to calibrate the VNA before any measurement. The calibration of the VNA is described later in the text.

Important characteristics of the DUT are reciprocity and symmetry. If the DUT is reciprocal, the transmission does not depend on the propagation direction, and the scattering matrix $\hat{\mathbf{S}}$ is symmetric $(S_{12} = S_{21})$. The DUT is called symmetric when $S_{11} = S_{22}$.

3.5.1. Vector network analyzer architecture

A primary advantage of using a vector network analyzer compared to a scalar network analyzer or spectrum analyzer is the capability of measuring vector information about the signal (magnitude and phase). The scattering matrix $\hat{\mathbf{S}}$ is the complex matrix, and each S-parameter is a dimensionless complex number. In operation, the signal generator sweeps the frequency over a specified bandwidth at a given power, and a switch allows for the connection to one of the two ports of the DUT. The VNA measures the reference signal utilizing a directional coupler, which taps off a small part of the signal. The rest of the signal continues to the DUT and is either reflected on the same port or transmitted to the second port. The switch is then flipped to the other port of the DUT, and corresponding signals are measured reversely. The magnitude and phase of all four scattering parameters are calculated in the internal processing unit. The simplified scheme of the VNA architecture is depicted in Figure 3.12.

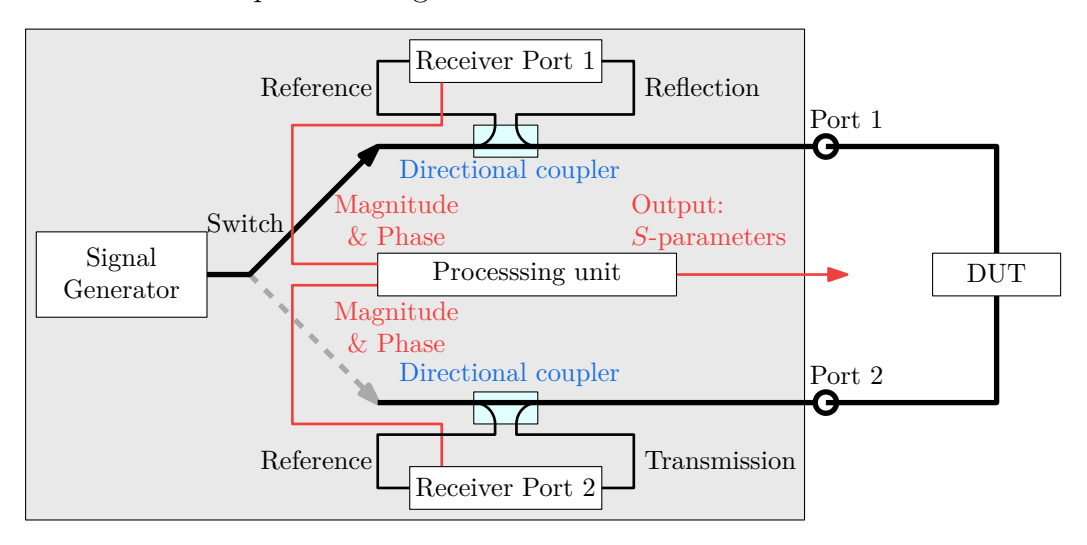


Figure 3.12: Schematics of the architecture of the two-port VNA. The signal generator generates the signal, and depending on the switch's connection, it is directed to one of the two ports. In this scheme, it is connected to port 1. The receivers measure reference, reflected, and transmitted signals, and the phase and magnitude of the signal are sent to the internal processing unit, which calculates all four scattering parameters.

The magnitude of the S-parameters is often measured in the dB units. It is a relative unit used to express the ratio of two power values. Then

$$S_{ij}(dB) = 10 \log_{10} \frac{P_{in,i}}{P_{out,j}} = 10 \log_{10} \frac{|b_i|^2}{|a_j|^2} = 20 \log_{10} \frac{|b_i|}{|a_j|} = 20 \log_{10} |S_{ij}|,$$
 (3.18)

where $P_{\rm in}$, $P_{\rm out}$ is the power of the incoming and outgoing waves, respectively. $S_{ij}({\rm dB})$ is always negative due to the nature of experiment as we do not consider active devices such as transistors or amplifiers, thus, $b_i < a_j$. The power generated by the VNA is in the unit of dBm (decibelmiliwatt). It is a power ratio of the signal generator to the reference power of 1 mW, expressed in dB. The power conversion between the power in dBm and the power in miliwatts is given by

$$P(dBm) = 10 \cdot \log_{10} \frac{P(mW)}{1 \text{ mW}}.$$
 (3.19)

Table 3.1 shows examples of the conversion between the power in dBm and the power in mW for $50\,\Omega$ systems. The characteristic impedance of most coaxial cables and connectors is usually $50\,\Omega$. Exceptionally, $75\,\Omega$ cables are used in television systems. The reason is that the minimal attenuation of an air-filled coaxial line is for a characteristic impedance of about $77\,\Omega$ while the maximal power capacity passes for a characteristic impedance of $30\,\Omega$. Therefore, by convention, a $50\,\Omega$ characteristic impedance is a compromise between a minimum attenuation and a maximum power capacity. As mentioned above, to prevent any unwanted reflection from every interface, all elements used in the VNA's internal structure must be matched for the characteristic impedance $Z_{\rm c} = 50\,\Omega$. A better understanding of the concept of characteristic impedance is given in [173, 174].

Table 3.1: The conversion between the power dBm and the power in mW.

P (dBm)	-30	-20	-10	0	2	5	10	20
P (mW)	0.001	0.01	0.1	1	1.5849	3.1628	10	100

3.5.2. Calibration of VNA

Considerable improvement in accuracy when using VNA is possible with error-correcting software. Errors caused by the imperfections of the internal architecture such as directional coupler mismatch, low directivity, loss, and variations in the analyzer system's frequency response are accounted for by using a 12-term error model, and a calibration procedure [173]. As the presented thesis does not aim to describe further the hardware components inside the VNA, a more in-depth description of the microwave engineering and the internal architecture of the VNA is provided in [173, 175].

In our experiments, the VNA connection to DUT is realized by the pair of coaxial cables and high-frequency microwave probes. The contributions of the connecting cables and probes are always present in the measurement, but can be removed using a proper calibration. The calibration procedure aims to move the measurement's high-frequency reference planes from the VNA's port to the microwave probes' tips providing the connection to the DUT. The calibration procedure ideally removes the contributions of the connection between the VNA port and the DUT and the systematic errors caused by the imperfection of the hardware used in the VNA.

A vast number of calibration methods exist. We used the so-called SOLT method within the thesis, abbreviating Short, Open, Load, and Through. In some literature, it is also known by the name TOSM, abbreviating Through, Open, Short, and Match. For the use of high-frequency microwave probes, the calibration kit is in the coplanar geometry. As the name suggests, it consists of four calibration standards – a short-circuit,

where the signal port is connected directly to the ground; an open-circuit, where the signal and ground ports are not connected; a precise $50\,\Omega$ matching standard, where the signal port is connected to the ground through a $50\,\Omega$ load; and the through standard where the connection between two ports is provided by a short section of the coplanar waveguide. The calibration using the calibration standard must be done for both ports and the frequencies and power used later in actual measurement. Figure 3.13. schematically depicts the calibration standards for using high-frequency microwave probes. For the full correction of the 12 error terms, the calibration standard's measurement is not sufficient. Additionally, knowledge of the parameters of probes and the calibration substrate is needed. Therefore, for successful calibration, the same manufacturer should provide both the calibration substrate and high-frequency microwave probes.

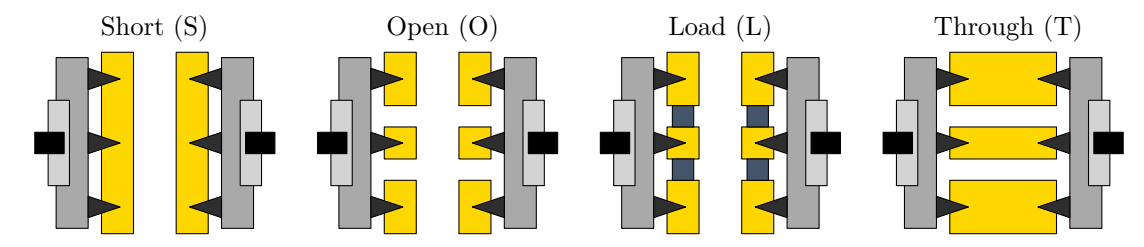


Figure 3.13: Schematics of the SOLT calibration standard for the use with high-frequency microwave probes in the coplanar geometry.

When the VNA and DUT are connected directly with coaxial cables without microwave probes, the VNA is calibrated using a special calibration kit. There are kits both for automatic or manual calibration. When using the automatic calibration, the calibration unit is connected to both ports of the VNA. Additionally, it is also plugged into the VNA's USB port, and the calibration is done automatically without the need for reconnecting through the calibration standards. The manual calibration kit consists of four calibration standards, three one-port fixtures for the single, open, and load calibration, and a two-port fixture for through calibration. These calibration kits are available with separate male and female versions of connectors. Calibration standards are directly mounted to the coaxial cables, so the physical compatibility between the calibration standard and the used coaxial cable is of the essence. The list of relevant connectors with intermateable capabilities is provided in Table 3.2. The calibration kit used for the direct cable connection is depicted in Figure 3.14.

In general, opinions about the necessity of calibration differ. Bilzer [79] suggests that the calibration should be successively repeated multiple times to improve the error terms. He also states that the calibration degrades with time, mainly due to the temperature variations. He proposes to do the calibration at least twice a day in the absence of air conditioning. On the other hand, Vaňatka [92] advises that the calibration should be done regularly, approximately once a week. He then continues with the suggestion that it is ideal to do the calibration before each measurement. In some groups, [177], the VNA is not calibrated as they are using high-quality coaxial cables with almost no attenuation. Besides, their interest is not quantitative but lies in the difference from known references. Nevertheless, even in such a case, calibration is effective..

3.5.3. Vector network analyzer ferromagnetic resonance technique

The broadband vector network analyzer ferromagnetic resonance (VNA-FMR) technique uses the vector network analyzer to measure the ferromagnetic resonance. In the VNA-

Table 3.2:	Commonly used connectors in high-frequency applications. Table entries based on
	the HUBER+SUHNER RF Coaxial connectors general catalogue [176].

Connector	Coupling mechanism	Frequency range	Intermateable with
BNC	bayonet	Up to 4 GHz.	
N	screw-on	Up to 18 GHz, depending on	
		the connector and cable type.	
SMA	screw-on	Up to 18 GHz, extended	PC 3.5 and SK $(2.92 \mathrm{mm})$
		frequency version up to	
		$26.5\mathrm{GHz}.$	
PC 3.5	screw-on	Up to $26.5\mathrm{GHz}$.	SMA and SK $(2.92 \mathrm{mm})$
$SK (2.92 \mathrm{mm})$	screw-on	Up to 40 GHz.	SMA and PC 3.5
PC 2.4	screw-on	Up to $50\mathrm{GHz}$.	PC 1.85
PC 1.85	screw-on	Up to 67 GHz.	PC 2.4
PC 1	screw-on	Up to 110 GHz.	



Figure 3.14: Rohde & Schwarz[®] ZV-Z235 calibration kit with the 3.5 mm connector type and both male and female version of calibration standards. Reprinted from [92].

FMR experiment, a stripline or a coplanar waveguide (CPW) are used for the creation of a small oscillating field \boldsymbol{h} , and the studied magnetic sample is either directly lithographically prepared on the same substrate as the CPW or just placed magnetic film side downwards over the CPW in the so-called flip-chip technique. Figure 3.15 shows a scheme of a typical VNA-FMR experiment using high-frequency microwave probes. Additionally, the sample is located in the gap of a rotatable electromagnet with an in-plane magnetic field.

The connection between the VNA's ports and the CPW is provided by the coaxial cables connected to the high-frequency microwave probes of the brand Picoprobe by GGB industries [178]. These probes connect the planar sample utilizing three individual legs in a Ground-Signal-Ground (GSG) geometry with the VNA via the female SK (2.92 mm standard) type of precision connector. As visible from Table 3.2, these connectors are suitable for use in the frequency range up to 40 GHz. For this experiment, the microwave probes must be completely non-magnetic to prevent unwanted movement when applying the external magnetic field.

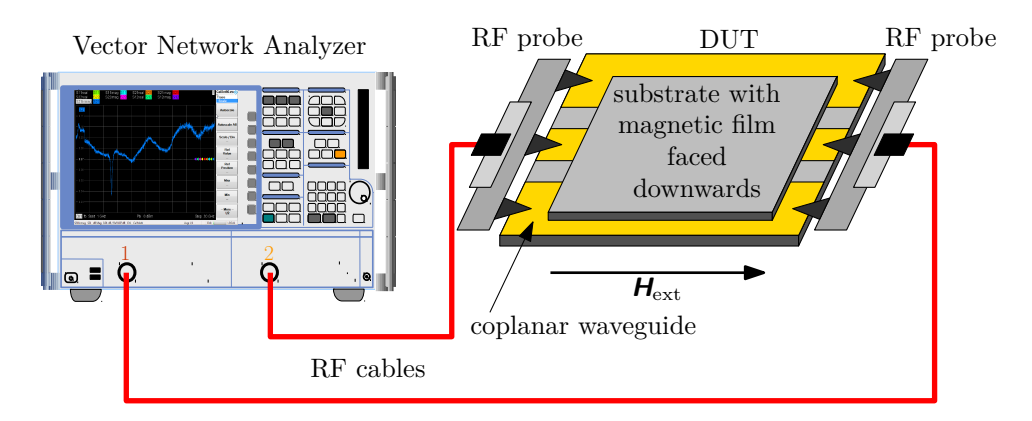


Figure 3.15: Schematics of the VNA-FMR experimental setup. The magnetic sample is either placed facing downwards over the coplanar waveguide in the so-called flip-chip technique or directly lithographically prepared on the same substrate as the CPW. The VNA is connected to the CPW via coaxial cables and high-frequency microwave probes with an SK connector. The external magnetic field is provided by the rotatable electromagnet so that the magnetic field direction is parallel to the CPW.

The VNA-FMR experimental setup's skeleton is the mechanical probe station TS200 from the MPI corporation [179] (see Figure 3.16). It provides a platen lift possibility controllable via the lever on the probe station's left side. There are three discrete positions of the lever: the contacting position, $300\,\mu\text{m}$ above the sample, so-called separation position, and 3 mm above the sample for the safe loading. The probe platen supports opposing positionable x,y,z micromanipulators with the mounted high-frequency probe. The micromanipulator allows for precise manipulation of the probe during the contacting of the planar sample. Furthermore, it is possible to tilt the mounted probe to ensure the contact of all three legs.

When contacting the sample, the lever is carefully moved from the safety position to the contacting position. The contact between the planar sample and the high-frequency microwave probe is fine-tuned by changing the z-position of the probe with a micromanipulator. The optical microscope allowing for the inspection of the established connection is located above the lever-movable probe plate. The movement in the x and y axes of the microscope stage is ensured via independently controlled manipulators with locking screws. The mechanical stability of the probe station is ensured by the adjustable air damping suspension. The rotatable electromagnet with the sample stage is located in the center of the lower part of the probe station. The rotation of the electromagnet is independent of the sample rotation. It is ensured by the stepper motor, and it can be turned 360° applying the magnetic field in any in-plane direction. The magnetic field can be monitored using a Hall probe between the pole pieces. The Hall probe is connected to the gaussmeter Hirst Magnetic Instruments GM08. The highest possible magnetic field at the sample position is up to $400 \, \text{mT}$.

The Rohde & Schwarz ZVA50 vector network analyzer is placed on the upper fixed shelf behind the optical microscope. The whole experimental setup is controllable via computer using thaTEC:OS software and modules compiled in the LabView. It is described in detail in the bachelor thesis of Václav Roučka [180].

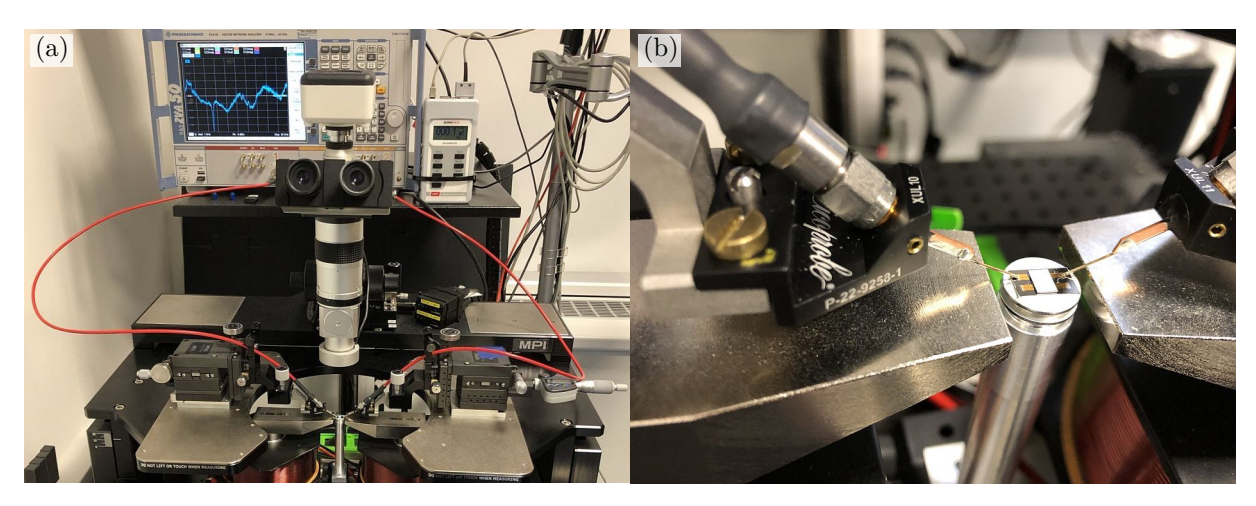


Figure 3.16: (a) Photograph of the experimental VNA-FMR setup built on the mechanical probe station. The Rohde & Schwarz ZVA50 vector network analyzer is connected via coaxial cables to high-frequency microwave probes. These probes provide the electrical connection from the planar coplanar waveguide to VNA's ports. The sample is placed between the rotatable electromagnet's pole pieces with the possibility of an in-plane magnetic field up to 400 mT. An optical microscope is used for precise navigation. (b) Detail of the high-frequency probe of the brand Picoprobe by GGB industries connected to the coplanar waveguide. The sample is placed magnetic film side downwards over the CPW in the so-called flip-chip technique.

4. Experimental results

It is a rough road that leads to the heights of greatness.

— Star Wars: Clone Wars, Episode: Storm over Ryloth

Up to now, we have focused on the theoretical parts of the presented thesis. We discussed the theoretical background of both magnetization statics and dynamics in chapter 1, dealt with the sample fabrication methods in chapter 2 and presented the characterization methods in chapter 3. Ultimately, the following chapter brings all of the acquired knowledge together. The achieved results are presented, analyzed, and discussed.

4.1. The substrate modulation

The presented thesis's title implies that the main goal is to study magnetism in curved geometries. The curvature-induced effects [15] allow us to tailor the static and dynamic response of the structures with a high degree of freedom. We decided to exploit further the influence of the surface curvature leading to effective uniaxial magnetic anisotropy. The magnitude and direction of the induced anisotropy can be finely tuned by shaping the shape of the magnetic layer [16]. The curvature-induced uniaxial magnetic anisotropy has been previously introduced to the magnetic system in several experiments using ion beam-induced erosion [14, 17–19]. Similarly, the magnetocrystalline anisotropy can be controlled via field sputtering [21] or field annealing [22]. The formation of magnetic anisotropy can also be controlled lithographically [20]. However, the aforementioned methods are hardly applicable in truly local control of the uniaxial magnetic anisotropy. The broad beam ion approach, same as field-induced processes or lithography approach, relies on the large-scale control of the magnetic anisotropy. Recently, studies have shown local control of the magnetic anisotropy in thin films by focused ion beam irradiation exploiting either structural phase transformation [181, 182] or induced chemical disorder [183]. Nevertheless, these approaches utilize unconventional material systems and, thus, cannot be universally applied.

4.1.1. Focused ion beam

The modification of the substrate is the crucial step preceding the deposition of the magnetic material. Mainly, two materials are used as a substrate in semiconductor technologies: silicon (Si) and gallium arsenide (GaAs). Silicon is most often used due to its affordability and its low-frequency noise. When compared to Si, the GaAs is a more suitable substrate for high-frequency circuits as it offers higher operating frequencies. The drawback is its higher price.

Two straightforwards approaches in local modification of the substrate are the subtractive approach, where the substrate is milled to achieve the desired shape, or the additive,

where the material is deposited on the existing substrate to form a shaped substrate. The first idea of how it would be possible to modify the substrate surface locally was to use focused ion beam (FIB) milling. The goal was to prepare a sinusoidal modulation of the substrate topography with varying peak-to-peak amplitude and varying periodicity. The ion dose per area defines the pattern written by FIB

$$D = \frac{It_{\rm DW}N}{ed_{\rm p}^2},\tag{4.1}$$

where I is a probe current, t_{DW} is a dwell time, i.e., the time that the beam stays at each spot, N is the number of scans over the area, e is the elementary charge, and d_{p} is the pitch, i.e., the distance between the two pixels.

The first pioneering experiments using FIB milling of the Si substrate are depicted in Figure 4.1. The patterns were created in the TESCAN DrawBeamTM software. The structure in Figure 4.1(a) was prepared using a stair pattern, and structures in Figure 4.1(b)-(d) were made by multiple overlaid rectangles with different aspect ratios but the same center position. All structures were prepared using the so-called zig-zag scanning type. In the final perfected structure, see Figure 4.1(c), the combination of 21 rectangles per period was used. In the design, the width of each rectangle changed with the step of 200 nm. The energy of Ga⁺ ions was 30 keV, and the current was 2 nA. The ion dose differed based on each rectangle's position to reach the sinusoidal modulation of the substrate's topography. The doses used for this experiment were in the range of $15 \cdot 10^{15}$ ions/cm²- $25 \cdot 10^{15}$ ions/cm². The milling was conducted at the normal incidence angle.

To induce the measurable uniaxial magnetic anisotropy in a magnetic material deposited on top of the sinusoidal modulation, we must decrease the periodicity of prepared modulations at least ten times [184, 185] to reach dimensions of hundreds of nanometers. Therefore, the milled pattern has been modified. Due to the ultimate resolution of the method, the patterning of rectangular patterns on such length scales can be easily replaced by patterning a line pattern. We performed the resolution test (see Figure 4.2), revealing the lowest periodicity of sinusoidal modulations that can be prepared using this approach by changing the distance between lines. The test was done for the ion energy of 30 keV and for two probe currents: $I_1 = 600 \,\mathrm{pA}$, $I_2 = 60 \,\mathrm{pA}$. Each line was written with N ==2000 scans providing a good contrast with the GaAs substrate. Further in the text, the number of scans is used instead of the ion dose due to the simplicity during preparation as the number of scans is directly controllable with the TESCAN DrawBeam[™] software employed in the definition of milled patterns. As is evident from the resolution test shown in Figure 4.2, lines are still distinguishable when a pitch is higher than 200 nm. If the probe current were lower, each line would be narrower, and the pitch could be further reduced.

It has been previously recognized that Ga FIB milling of III-V compound materials causes the formation of nanodots or "droplets" distributed randomly on the milled surface [186–188]. The mechanism is the preferential sputtering of the group V elements, leading to an excess of group III elements to form the group-III rich nanodots [189]. We observed the same effect of forming Ga rich droplets in Figure 4.2(a). When the probe current was lowered from 600 pA to 60 pA [see Figure 4.2(b)] the Ga rich droplets are formed only for the lowest pitch, i.e., for 20 nm. That is caused by the beam's overlapping when scanning neighboring lines, hence, the higher total dosage.

We fixed the pitch between individual lines to 200 nm and varied the ion beam's number of scans from 1000 to 14000 scans for the control over the peak-to-peak height.

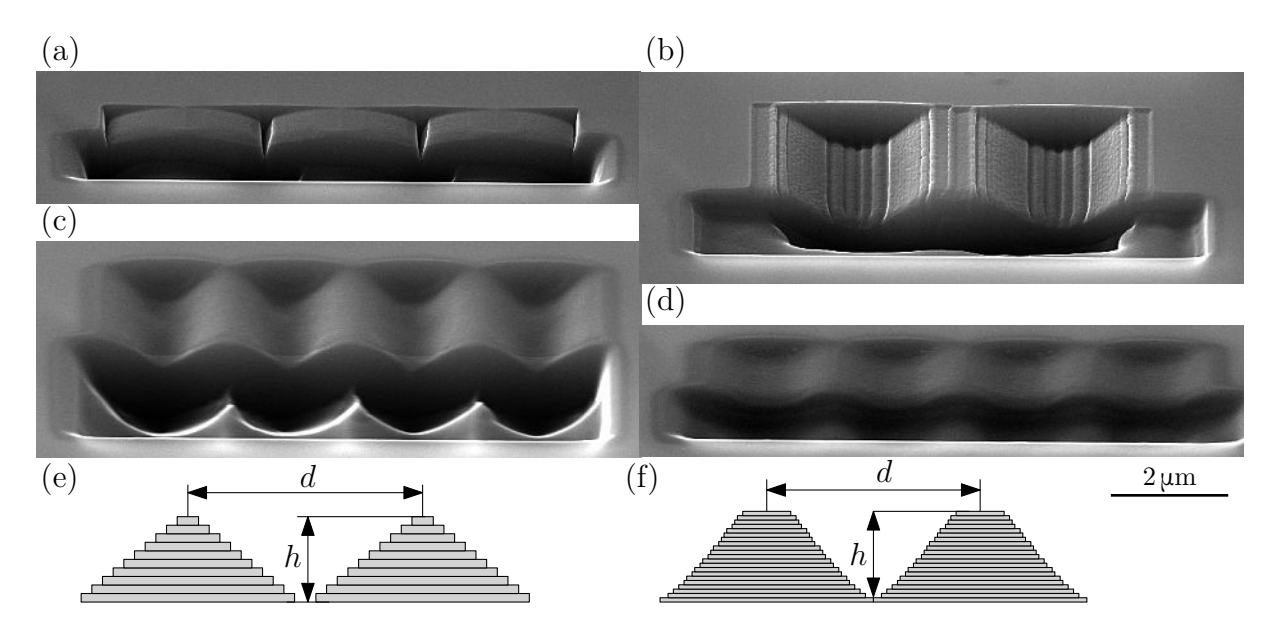


Figure 4.1: First successful attempts of modifying the Si substrate surface using focused ion beam milling. The energy of Ga⁺ ions was 30 keV, and the probe current was 2 nA. (a) The stair pattern used to mill the substrate locally. (b) Roughly milled structure showing first signs of sinusoidal pattern. The structure was created using a combination of multiple overlaid rectangles with different sizes. The change in the rectangle's width was too high, and the steps between the used rectangles are visible, showing a stair-like pattern. (c) A perfected structure created using the same approach as (b) but with a smaller width change between the overlaying rectangles. (d) Final structure with a different amplitude of modulation than (c). All images were taken under tilt 55°. The scale bar applies to all images. (e) The design cross-section used in (b). (f) The perfected design uses smaller width changes between the overlaying rectangles.

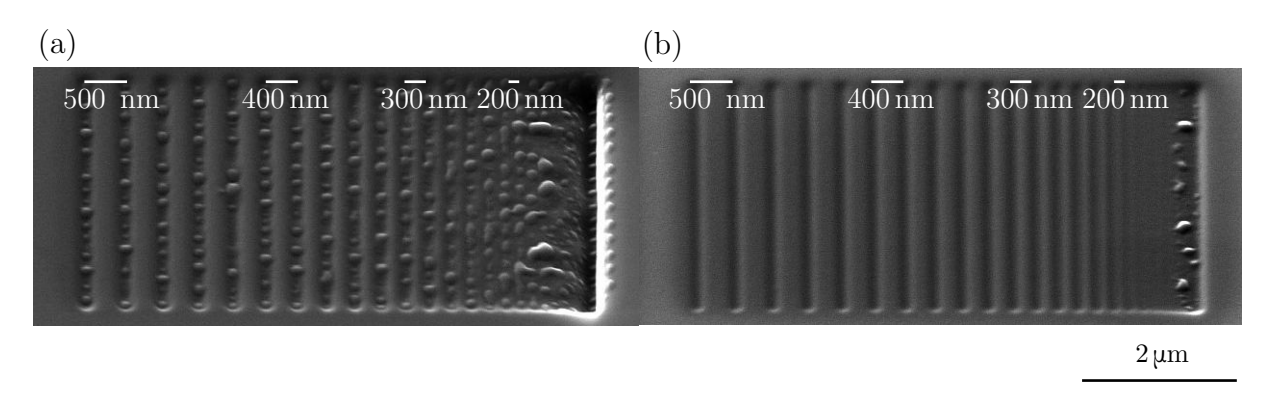


Figure 4.2: The resolution test to check what is the lowest periodicity that can be prepared using the focused ion beam milling. The milled pattern consists of 25 lines with the pitch changing from 500 nm to 40 nm by 20 nm. Each line was written with 2000 scans. The Ga ion beam energy used here is 30 keV and a beam currents of (a) 600 pA and (b) 60 pA. Nanodots, mainly visible in (a), are Ga-rich droplets formed due to the Ga FIB milling.

Figure 4.3 shows micrograph from scanning electron microscope (SEM) and 3D image from atomic force microscope (AFM, see sec. 3.1).

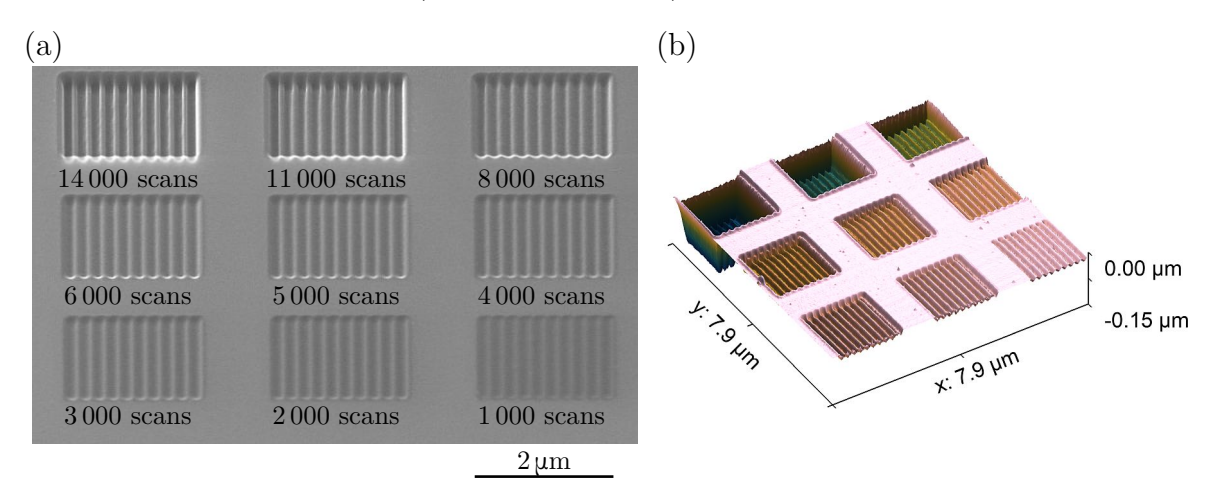


Figure 4.3: The modification of the peak-to-peak height, so-called amplitude of modulation.

(a) Tilted (55°) SEM micrograph of sinusoidal modulations fabricated using the Ga FIB milling at 30 keV on GaAs substrate using a beam current of 60 pA for a series of ion beam's number of scans per each line (written bellow each structure).

(b) AFM image of the same structure providing additional depth information.

However, due to the overlapping of the beam's tails and the Gaussian beam shape, the peak-to-peak height is constant and independent of the number of scans. At the lowest number of scans of 1000, only the substrate surface is modified. For the higher number of scans, the peak-to-peak height is not affected, and the milled "pit" goes deeper. Figure 4.4 shows Ga FIB milling results with a range of the number of scans and the resulting milled "pits" measured by AFM. The AFM was measured under ambient conditions using Bruker Dimension Icon microscope with silicon ScanAsyst-Air cantilevers in ScanAsyst mode. Additionally, three significant corresponding line profiles are depicted. The higher ion beam's number of scans also leads to the milled material's redeposition on the structure's edge. The AFM shows the depth of the milled pits ranging from 10 nm to 120 nm and the peak-to-peak height of 10 nm for the lowest number of scans of 1000, and 17 nm for all the higher number of scans. The AFM was measured in the direction perpendicular to the corrugated substrate's parallel grooves, i.e., in the corrugation direction, as shown in the line profiles in the right part of Figure 4.4. Furthermore, each line was averaged over 5 pixels to suppress noise.

In conclusion, by utilizing the focused ion beam milling, it is possible to modify the surface of the substrate, but the control over the shape and dimension is not sufficient. The resolution test showed that it is impossible to prepare structures with periodicity lower than 200 nm. Also, changing the ion beam's number of scans does not affect the amplitude of modulation but only creates deeper pits. Finally, the sinusoidal shape of the modulation, prepared using this approach, is distorted due to the redeposition and overlapping of the FIB tails. Therefore, we did not test the deposition of the magnetic layer on the substrate modulated by FIB.

To overcome issues that arise due to the FIB process, we decided to use a different technique. Instead of milling the substrate away, the curvilinear structures are prepared on the substrate using the focused electron beam-induced deposition (FEBID). The details are provided in the following section.

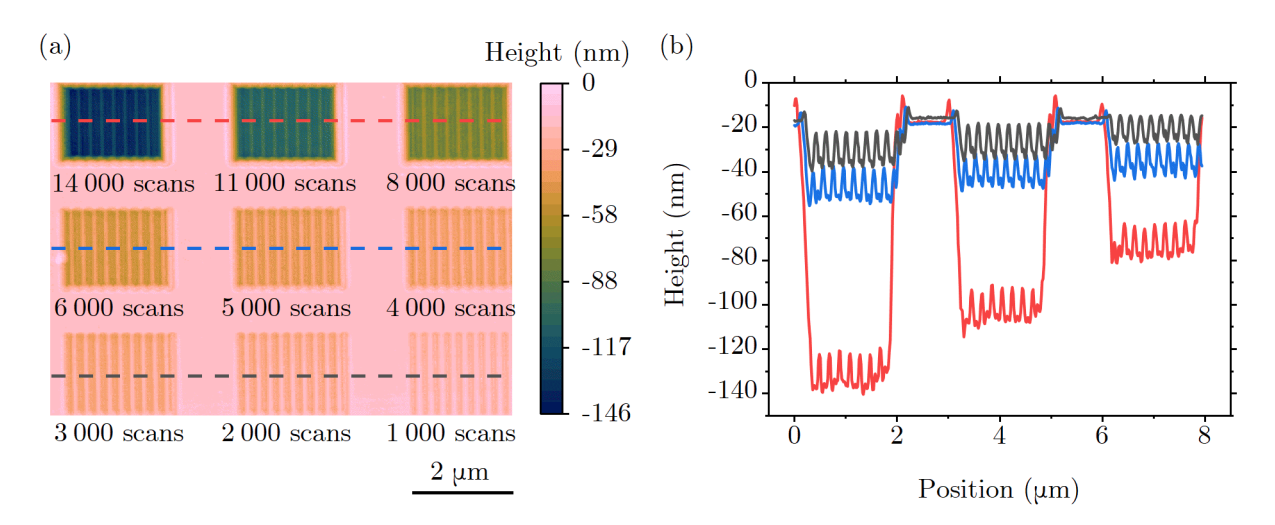


Figure 4.4: (a) Ga FIB milling with a range of the number of scans measured by atomic force microscopy. (b) The line profiles measured over color lines shown in (a). The line profiles are averaged over 5 pixels, i.e., five scan lines around the selected one are averaged. This approach helps with noise suppression. While measuring the AFM image, the tip was moving parallel to the corrugation direction.

4.1.2. Focused electron beam-induced deposition

We employed FEBID to control the uniaxial magnetic anisotropy locally. The physics behind this process is theoretically discussed in section 2.1. Recent advances in this technique allow us to prepare 3D structures, which cannot be prepared by standard lithography approaches. The move forward is mirrored mainly in the encouragement of the third dimension in magnonics [190, 191], as it offers a robust way to functionally integrate systems into smaller space, for the most part, made possible by a large number of vertical connections between layers. Also, the density of elements increases due to the third dimension allows for the fabrication of scalable and configurable magnonic networks [192].

To apply the FEBID method for creating the sinusoidal modulation of the substrate before the deposition of the magnetic layer, it is vital that the process runs as fast as possible to prevent any drift of the stage. Besides, the shape quality of created structures is also of the essence. The deposited structure properties depend on the precursor and equipment used and on the deposition parameters.

From the results of pioneering experiments, it was clear that it would be difficult to reach the exposure settings which would meet both requirements – the high speed of deposition and the high quality of the required shape and dimensions. Therefore, the created structures' quality in terms of geometry was chosen as the main criterion when selecting optimal exposure conditions, and the deposition rate was less important. The selection of the suitable deposition parameters follows theses by Šamořil [193] and Vyroubal [194].

In order to modify the substrate topography, we have decided to use PMCPS (2,4,6,8,10-pentamethylcyclopentasiloxane) precursor [195]. The final deposit is silicone dioxide. This precursor is liquid at room temperature with the boiling point at 54 °C. Therefore, the precursor reservoir does not require any heating to create a precursor gas. The precursor gas is introduced into the SEM vacuum chamber through the capillary, heated to the temperature of 70 °C. The nozzle, which is heated to the temperature of 75 °C, is positioned

ca. 100 µm above the substrate's surface. The gas injection system (GIS) geometry is on the LYRA microscope adapted for use with FIB and with the sample tilt of 55° – normal to the FIB column. In order to use the FEBID system with the highest possible resolution, the samples need to be tilted for the normal incidence of the electron beam. This results in a need to deviate the sample from the eucentric position by 0.4 mm. On the LYRA microscope, the eucentric point is at the working distance of 9 mm, and thus, for the successful approach of the GIS needle above the sample, the working distance should be 9.4 mm. Before the deposition, the GIS system must be outgassed.

Writing of small features is typically done at high beam energies (30 keV). We have performed a similar est as in Figure 4.2 where we have tested the patterning resolution of the method. In the SEM software, the beam current can be changed by choosing the beam intensity (BI) number. The beam intensity used in all depositions discussed in the thesis was BI 12. Correspondingly, the beam current measured in the Faraday cup for BI 12 was 542 pA and the spot size was 6.5 nm. This value was chosen as a compromise between the high deposition speed and the high geometrical quality of prepared structures. The theoretical smallest spot size of Lyra, calculated by *In-Flight Beam Tracing* technology, is 3.5 nm, and this is achieved for the working distance (WD) 9 mm and for the acceleration voltage 30 kV and BI 8.68.

Figure 4.5 depicts the resolution test. The resolution test consists of 25 lines where the distance between each adjacent line is varied from 500 nm to 40 nm by 20 nm step. The acceleration voltage was set to 30 kV, and the beam current measured in the Faraday cup was $542 \,\mathrm{pA}$. The base pressure in the chamber before introducing the PMCPS precursor was $1.8 \cdot 10^{-4} \,\mathrm{Pa}$. Each line was written with $N = 2\,000$ scans, dwell time 1 µs and spacing 1.709. The write field size was $100\,\mathrm{\mu m}$.



Figure 4.5: The resolution test prepared by focused electron beam-induced deposition using PMCPS precursor to test the lowest periodicity of the sinusoidal modulation that can be prepared using this technique. The pattern consists of 25 lines with different distances. The distance between the two lines is changing from 500 nm to 40 nm by 20 nm. The number of scans per line was $N=2\,000$ scans. The energy of electrons was 30 keV, and the beam current measured in the Faraday cup was 542 pA.

The potential of introducing harmonic modulation of the substrate is apparently much better for the FEBID method when compared to FIB milling. Even when the distance between two lines is 40 nm, the neighboring lines are still distinguishable. Furthermore, the final nanostructure is free from the Ga-rich droplets. The resolution can be further improved by choosing a smaller write field size using the digital-to-analog converter (DAC) resolution limits. It is recommended to use the exposure pitch that is higher than $4\times$ DAC resolution. The LYRA microscope is equipped with 16-bit DAC so that the DAC resolution when using write field size $100\,\mu\text{m}$ is $1.5\,\text{nm}$ and the exposure pitch is calculated as a multiplication of the spot size and the spacing.

¹The point where the sample's image does not move when the sample is tilted.

The control over the peak-to-peak height was tested by fixing the distance between neighboring lines and varying the electron beam's number of scans. We fabricated six $8 \times 8 \,\mu\text{m}^2$ squares that consisted of eighty one $8 \,\mu\text{m}$ long lines separated by the distance of 100 nm. The lines were parallel to the precursor gas flow direction. The exposition process was serial, i.e., each line was scanned the set number of times before the microscope started to scan the next line. The exposition parameters were the same as in the resolution test. In order to control the height of the modulation, we have varied the number of scans of each line from 9000 scans to 4000 scans by 1000 scans. Figure 4.6(a) shows SEM image of the as-prepared squares. The closer inspection reveals individual lines. The halo deposition around the primary deposits is typical for the FEBID process but does not possess any technological problem for the following steps. Figure 4.6(b) shows AFM line profiles over the colored lines shown in the SEM micrograph. The AFM was measured under ambient conditions using the AC240TS tip in Tapping Mode over the edge of deposited structures to check the shape and geometry and to exclude any tip-shape influence on the image. Each line scan is averaged over 128 pixels to omit any impurities and suppress noise. The AFM profiles clearly show the sinusoidal shape of the modulation. That is ensured by the gaussian shape of the e-beam and by the base-broadening discussed in section 2.1.

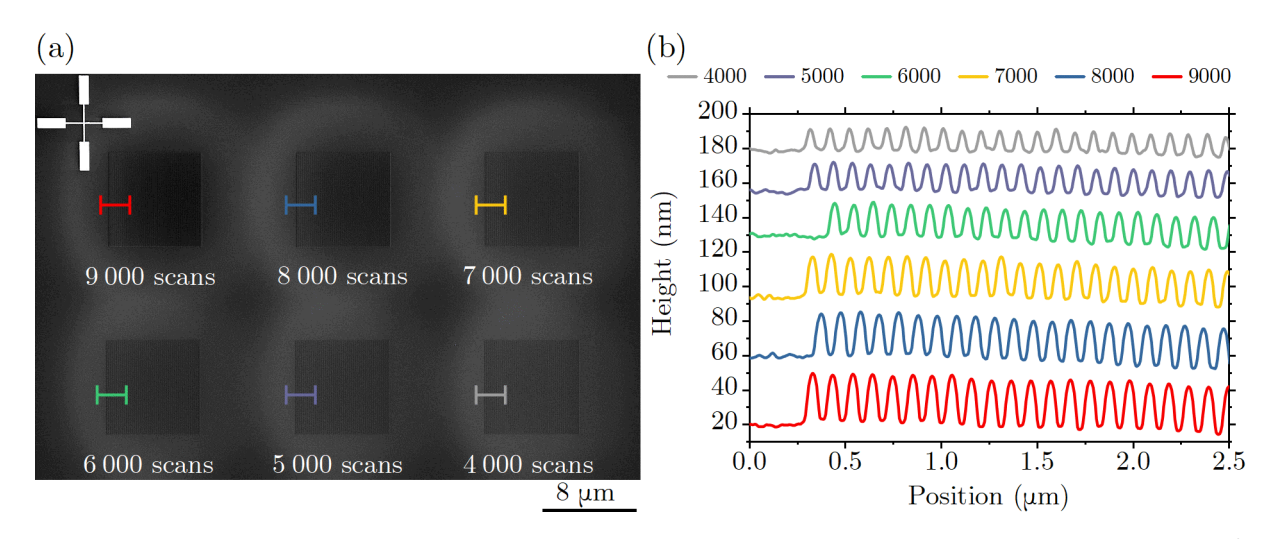


Figure 4.6: (a) SEM micrograph of prepared structures. The pattern consists of six 8×8 μm² squares. Each square is created by the deposition of eighty-one 8 μm long lines with the pitch of 100 nm. The number of scans per line was different for each square and is written below squares. The landing energy of electrons was 30 kV, the beam current was 542 pA, the dwell time 1 μs, and the spacing 1.709. (b) Corresponding AFM line profiles were measured over the colored lines of prepared structures. The line profiles are averaged over 128 pixels. For clarity, the line profiles are offset.

The AFM measurements reveal information about the topography more precisely. Therefore, it is possible to extract the dependence of the amplitude of modulation (peak-to-peak height) on the e-beam number of scans per line. For these reasons, we prepared structures with a minor step in the e-beam number of scans. However, as we mentioned above, the flow rate depends on the amount of precursor in the reservoir and influences the growth rate of prepared nanostructures. Therefore, it is advantageous to regularly check the amplitude of modulation (peak-to-peak high) of prepared structures.

To further understand the influence of the e-beam number of scans on the amplitude of modulation, we use the same analysis process for all our measurements. At the beginning of the AFM analysis process, we extract the line profile averaged over 128 pixels, see

Figure 4.7(a). Usually, the scanning window size is $3\,\mu\mathrm{m}$ with a resolution of 512 pixels. Therefore, one pixel represents 5.85 nm. We are interested in the 100 nm wide details; hence, this resolution is sufficient. We then analyze the line profile using the Peak Analyzer function in OriginLab. First, the baseline is created by looking for the peaks. The line interpolation creates the connection between neighboring peaks; see the red curve in Figure 4.7(b). The baseline is then subtracted from the measured AFM data. Then, the peaks in the negative direction are found and filtered by the threshold height. Together with the peak height, the peak center position is evaluated, and selected peaks are marked. In Figure 4.7(c), 25 peaks were found and evaluated. The amplitude of modulation is then calculated as the average value of measured peak heights. The error is calculated as a standard deviation. Using peak center values, we also verified that the periodicity of prepared modulation is $(100 \pm 10) \mathrm{nm}$.

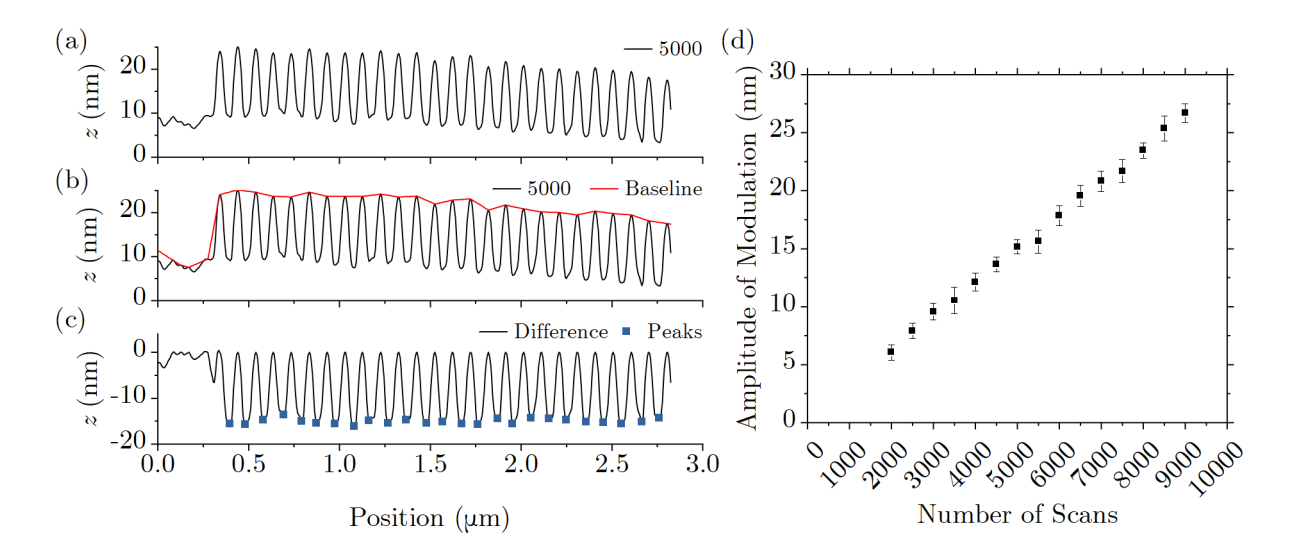


Figure 4.7: Processing of AFM data using the Peak Analyzer function in OriginLab (a) AFM line profile averaged over 128 pixels measured over the edge of structure created by 5 000 scans per line. The lines in the pattern are separated by 100 nm. (b) The baseline is created by finding the peaks in the AFM measurement. (c) The subtraction of the baseline from the AFM line profile determines the peak center position and peak height. (d) The dependence of the amplitude of modulation on the e-beam number of scans per line measured for fifteen structures.

Utilizing this method, we analyzed fifteen squares mentioned above. We varied the number of scans from 2000 to 9000 scans in 500 scan steps. The dependence of the amplitude of modulation on the number of scans of the electron beam per line is depicted in Figure 4.7(d). By increasing the number of scans per line, we see an increase in the peak-to-peak height of created modulation. Moreover, the dependence is apparently linear, which indicates a very low blurring of the lines. Unfortunately, due to the number of uncontrolled parameters on which the FEBID is dependent, we cannot convincingly use this linear dependence to predict the deposition rate and modulation amplitude. However, in the case of multiple depositions done in a single day, the amplitude of modulation is satisfyingly repetitive.

In conclusion, we have analyzed two techniques for creating the sinusoidal modulation of the substrate before the deposition of the magnetic layer. First, we have employed the focused ion beam milling technique, which showed promising results. However, the main drawback of this technique is limited critical dimension, i.e., it is impossible to prepare structures with low periodicity ($< 200\,\mathrm{nm}$), and the potential in the amplitude modulation is also low. Subsequently, we have shown that issues encountered in FIB can be overcome using the focused electron beam-induced deposition. We have also proven that modifying both the amplitude of modulation (peak-to-peak height) and periodicity is possible. Besides, we have found that the periodicity can be tuned down to $40\,\mathrm{nm}$. We demonstrated that the amplitude of modulation is linearly dependent on the number of scans per line.

Overall, the considerable adjustability of the FEBID technique opens many possibilities for the design of complex magnetic structures, e.g., the magnetic layer can be deposited on top of the modulated substrate. In the next section, we will show the changes in the static response of the magnetic system induced by the corrugation of the magnetic layer compared to the planar layer.

4.2. Magnetostatic study of corrugated structures

In the previous section, we have shown a procedure allowing highly deterministic and local control over the sinusoidal surface modulation of the substrate. This section is dedicated to the sample fabrication and subsequent magnetostatic characterization of magnetic structures prepared on such a modulated substrates. The method employed in the static characterization is Kerr microscopy, discussed in section 3.2.1.

4.2.1. Sample fabrication

For the fabrication of magnetic curvilinear structures, we combined the electron beam lithography technique with the FEBID. Before the FEBID process, we prepared the alignment marks for further lithographic processing. In the preparation of corrugated magnetic structures, we have followed the individual steps of the electron beam lithography depicted in Figure 2.3. The particular process was as follows:

1. Alignment marks

- The GaAs substrate was thoroughly cleaned in acetone and isopropyl alcohol (IPA) baths. To enhance the cleaning, we have used ultrasonic cleaning.
- A thin layer of positive e-beam resist AR-P 679.0 [poly(methyl methacrylate)] was spin-coated on top of substrate at $4\,000\,\mathrm{rpm}$ for $60\,\mathrm{s}$. Typically, for $5\times5\,\mathrm{mm}^2$ samples, we used $35\,\mu\mathrm{l}$ of resist. Post bake was done for $3\,\mathrm{min}$ on a hot plate heated to $150\,\mathrm{^{\circ}C}$. The thickness of the prepared layer was ca. $270\,\mathrm{nm}$.
- The e-beam patterning was done in an area exposure mode in the scanning electron microscope TESCAN MIRA3/RAITH LIS. The acceleration voltage was 20 kV, and the current measured in the Faraday cup was 260 pA. The structure layout was created in the KLayout software. The patterning was done at a working distance of 9 mm, and the write field size was 200 μm . The patterning dose was 220 $\mu C/cm^2$ with a step size of 10 nm.

- We put a sample into a beaker with the PMMA developer AR 600-56 for 3 min. The exposed resist areas were dissolved. The development was terminated by putting a sample in an isopropyl alcohol bath for 30s.
- The principal feature of alignment marks is a good contrast to the substrate in the scanning electron microscope. Thus, we deposited Ti $5\,\mathrm{nm/Cu}\ 100\,\mathrm{nm/Au}\ 10\,\mathrm{nm}$ multilayer using e-beam evaporation.
- The lift-off was accomplished by immersing the sample in an acetone bath for 2 hours followed by ultrasonic agitation. Lastly, the sample was washed with IPA and blowdried with nitrogen.

2. FEBID process

Following the preparation of alignment marks, we transferred the sample to LYRA microscope chamber and prepared the sinusoidal modulation, as described above, see section 4.1.2. The structures were fabricated in the near vicinity of the alignment marks to ease the subsequent EBL steps.

3. Magnetic layer

The second lithographic step follows the EBL procedure employed in step 1 with the only difference being the choice of the material. Here, we prepared a 10 nm thick layer of NiFe in the e-beam evaporator. The alignment marks were used to adjust the pattern on top of the structures prepared by FEBID.

A scheme of the corrugated magnetic structure prepared by following the above-discussed steps is presented in Figure 4.8(a). Furthermore, in Figure 4.8(b) we define the corrugation direction. It is a well-known term from a papermaking industry used in a corrugated fiberboard.

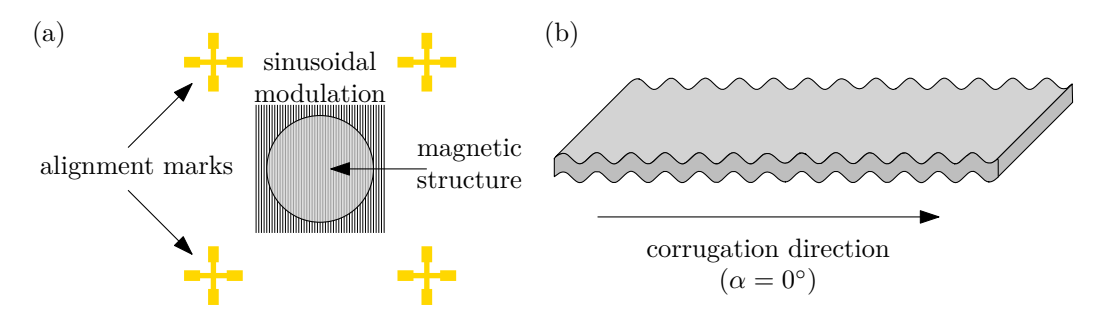


Figure 4.8: (a) Schematic illustration showing the design of the magnetic structure deposited on the sinusoidal modulation. The alignment marks are prepared in a first lithographic step to simplify the alignment of the FEBID and EBL techniques during later sample preparation. (b) Sketch with the definition of the corrugation direction.

The SEM micrograph of a sample ready for the magnetostatic characterization is depicted in Figure 4.9. It consists of an array of fifteen corrugated and one planar NiFe disks with diameter $D=7\,\mu\mathrm{m}$ fabricated on the GaAs (100) substrate. The period of the sinusoidal modulation is 100 nm. It was grown in a series of single lines separated by a 100 nm. We varied the number of scans for each pattern from 2 000 to 9 000, which resulted in the

modulation amplitudes ranging from 4 nm to 16 nm. The thickness of evaporated NiFe layer on top of the sinusoidal modulation is 10 nm. Visible vertical stripes are Moiré fringes are caused by the spatial frequency mismatch between the specimen grating and the raster scan lines [196]. The stripes can be fully eliminated by increasing the scanning resolution. Image of a single NiFe disc with the visible real modulation, captured with high resolution, is shown in Figure 4.9(b). The cross-section of a NiFe disc imaged by scanning transmission electron microscopy (STEM) in FEI Helios 660 microscope is presented in Figure 4.9(c). It shows another confirmation, besides AFM, that the silicon dioxide modulation prepared using FEBID grows in the desired sinusoidal shape directly on the substrate surface. Also, it demonstrates how the magnetic layer copies the surface topography of silicon dioxide modulation. The modulation amplitude (peak-to-peak height), measured directly from the STEM image, is 11 nm for this structure.

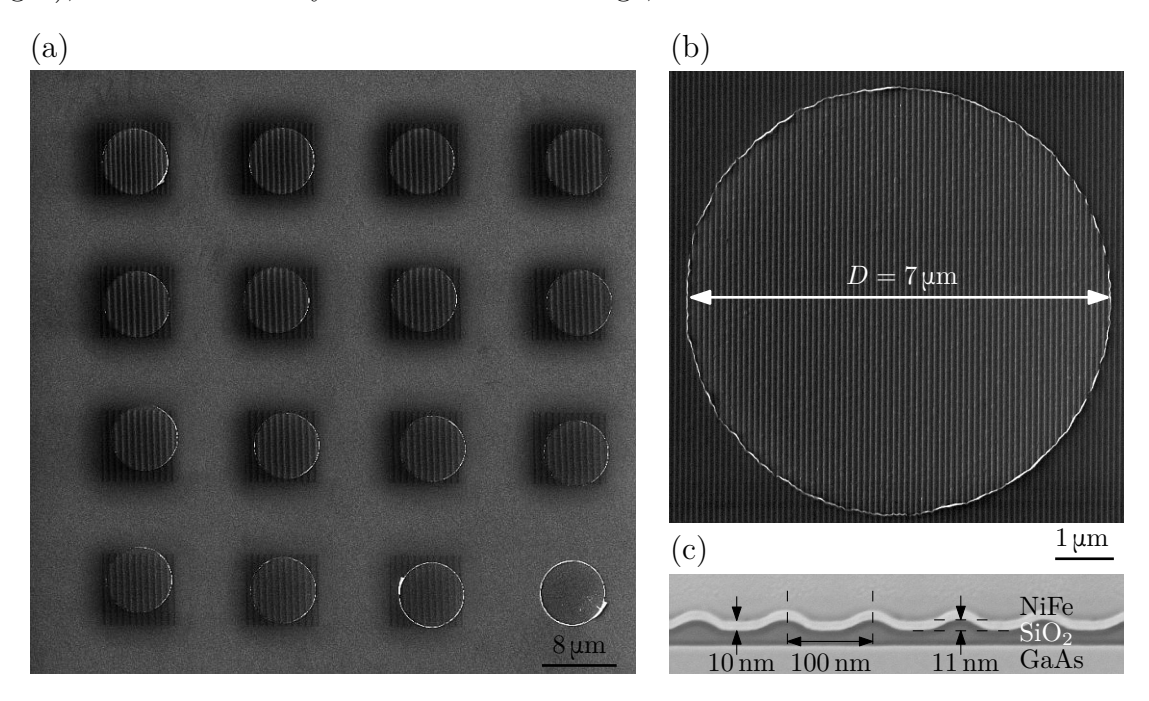


Figure 4.9: (a) SEM micrograph of an array of fifteen corrugated and one planar NiFe disks with diameter $D=7\,\mu\mathrm{m}$. The thickness of the NiFe layer is $t=10\,\mathrm{nm}$, and it is deposited on top of the modulated SiO₂ structure. The amplitude of modulation ranges from 4 nm to 16 nm. (b) The detail of a NiFe disc prepared on top of the sinusoidal modulation grown by FEBID. (c) STEM image of the magnetic structure. The period of modulation of the corrugation is 100 nm, and the amplitude of modulation (peak-to-peak) for this structure is 11 nm.

4.2.2. Kerr microscopy

The magnetization reversal processes and the quantification of the induced magnetic anisotropy in prepared corrugated structures depending on the corrugation parameters (modulation amplitude, periodicity) were measured using Kerr microscopy with an applied external in-plane magnetic field. We fabricated four sets of samples similar to the sample presented in Figure 4.9(a). Each sample consisted of fifteen corrugated NiFe discs with different modulation amplitude and one planar NiFe disc. The corrugated structures were grown using variations in the number of e-beam scans from 2000 to 9000 scans. The diameter of prepared discs was $7\,\mu m$. The only difference between these structures

was different modulation periodicity, which we have varied from 60 nm to 125 nm. The disc shape of structures studied in this experiment was chosen to suppress any unwanted contribution of the in-plane shape anisotropy into the measurement.

First, we have studied the influence of modulation periodicity on the magnetic anisotropy of prepared structures. We measured the angular magnetic field dependence of the magnetic response. The nomenclatures of interest were extracted from individual hysteresis loops measured for given angle of the external magnetic field. We have swept the in-plane magnetic field from -50mT to 50mT and acquired images using the Kerr microscopy. In the obtained images, the average gray contrast is proportional to the magnetization of the individual structures. We selected 16 structures with different modulation amplitudes and extracted 16 hysteresis loops, one for each disc. We did this measurement for all four periodicity values $-d_1 = 60$ nm, $d_2 = 75$ nm, $d_3 = 100$ nm, and $d_4 = 125$ nm every 10° from 0° to 180° . Overall, we obtained $16 \times 19 \times 4 = 1216$ hysteresis loops extracted from more than $15\,000$ images. The selection of the regions and subsequent analysis of hysteresis loops was made automatically using software developed by Dr. Lukáš Flajšman.

The hysteresis loops are normalized to the average value in the saturation level, i.e., the software found a certain number of points in the loop close to the maximum & minimum field and calculated a mean value. Additionally, the parasitic contributions to the signal (usually linear and quadratic field) were suppressed by subtracting the fitted linear and quadratic curve from the measured hysteresis loop using

$$I_{\text{norm}} = I_{0,\text{norm}} + fB + qB^2,$$
 (4.2)

where I_{norm} is the average gray intensity value devoid of the quadratic effect expressed by the coefficient q and Faraday's effect expressed by the coefficient f.

We selected a representative amplitude of modulation created by 3500 scans and compared hysteresis loops of the discs with a different periodicity of modulation for four angles between the corrugation direction and the external magnetic field, 0°, 30°, 60°, and 90°. The AFM measurement confirmed almost identical amplitude of modulation for all periodicites, i.e., $h_{60 \text{ nm}} = (7.7 \pm 0.6) \text{ nm}, h_{75 \text{ nm}} = (8.3 \pm 0.5) \text{ nm}, h_{100 \text{ nm}} = (6.9 \pm 0.3) \text{ nm},$ and $h_{125\,\mathrm{nm}} = (7.4 \pm 0.4)\,\mathrm{nm}$. Figure 4.10 reveals the comparison between experimental data and modeled curves for different periodicities of modulation. When we look at the hysteresis loops measured for the external magnetic field perpendicular to the corrugation direction ($\alpha = 90^{\circ}$), we see the square-shaped hysteresis loop, where M(H) is constant all the way from the saturation field to the remanence. At the coercive field we can clearly see sharp irreversible jump in which the magnetization reverses completely. Hence, this direction can be considered as a magnetic easy axis. The black curves correspond to the case where the external magnetic field is parallel to the corrugation direction, $\alpha = 0^{\circ}$. Here, hysteresis loops show almost linear and reversible behavior of the magnetization with a practically negligible remanence and coercive field. These features are typical for hard axis direction of uniaxial magnetic systems. For the magnetic fields oriented between the easy and hard axis, the shape of the loop continuously varies between easy and hard axis loops. Besides, from the shape of hysteresis loops for different periodicities, we see that by decreasing the periodicity, we effectively increase the coercive field. That allowed us to model loops using the Stoner-Wohlfarth model for a uniaxial anisotropy, see sec. 1.4. The modeled loops are presented in the bottom row of Figure 4.10. For each modulation periodicity, we estimated different uniaxial anisotropy constant $K_{60\,\mathrm{nm}} = 4.36\,\mathrm{kJ/m^3}$, $K_{75\,\mathrm{nm}} = 3\,\mathrm{kJ/m^3}, \; K_{100\,\mathrm{nm}} = 1.2\,\mathrm{kJ/m^3}, \; K_{125\,\mathrm{nm}} = 800\,\mathrm{J/m^3}.$ The saturation magnetization of the planar NiFe continuous layer was measured $M_{\rm s}=830\,{\rm kA/m}$ by the vibrating

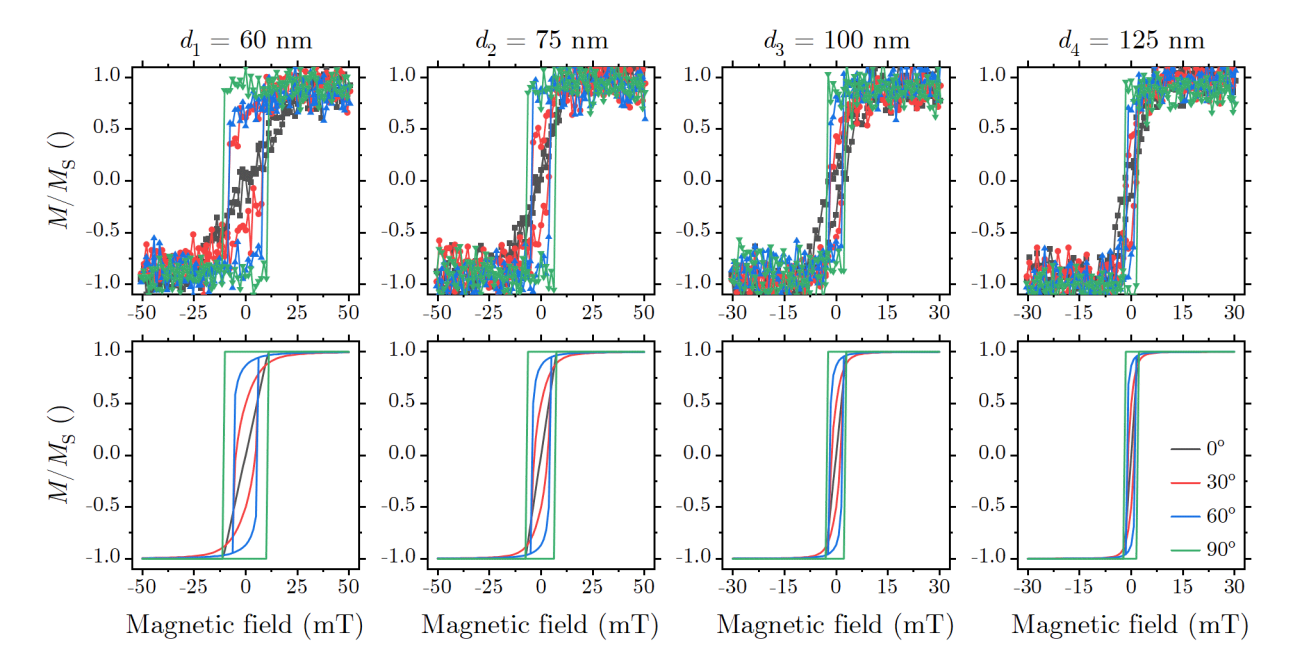


Figure 4.10: Comparison of the experimentally measured data with the Stoner-Wohlfarth model. The top row presents normalized hysteresis loops of a representative corrugated NiFe disc with a diameter of 7 μ m measured by Kerr microscopy. The amplitude of modulation was created by 3 500 scans. Each column corresponds to different periodicity of modulation – 60 nm, 75 nm, 100 nm, and 125 nm. Four different colors symbolize different angles between the corrugation direction and the external magnetic field. The bottom row shows the hysteresis loop modeled numerically using the Stoner-Wohlfarth model for a uniaxial anisotropy case. For each modulation periodicity, we considered different uniaxial anisotropy constant, $K_{60\,\mathrm{nm}} = 4.36\,\mathrm{kJ/m^3}$, $K_{75\,\mathrm{nm}} = 3\,\mathrm{kJ/m^3}$, $K_{100\,\mathrm{nm}} = 1.2\,\mathrm{kJ/m^3}$, $K_{125\,\mathrm{nm}} = 800\,\mathrm{J/m^3}$, and the saturation magnetization $M_\mathrm{s} = 830\,\mathrm{kA/m}$.

sample magnetometry (VSM). The measurement is presented in Figure A.1 in Appendix A. Using equation (1.22) we were able to calculate the coercive fields for different periodicities $\mu_0 H_{\rm c,60\,nm} = 10.5\,\rm mT$, $\mu_0 H_{\rm c,75\,nm} = 7.2\,\rm mT$, $\mu_0 H_{\rm c,100\,nm} = 2.9\,\rm mT$, $\mu_0 H_{\rm c,125\,nm} = 1.9\,\rm mT$. We consider this to be proof of the induced uniaxial anisotropy.

The corrugation-induced uniaxial magnetic anisotropy is caused by the interplay between exchange and dipolar energies. When the magnetization is aligned in the corrugation direction, the magnetic moments make small angles, causing both exchange and dipolar energies to increase. In contrast, in the direction perpendicular to the corrugation direction, they are aligned perfectly co-linear. From the energy perspective the latter case is preferred and thus defines the ground state of the system so that the magnetization is aligned perpendicular to the corrugation direction. When we decrease the modulation periodicity, the corrugation of the magnetic layer is increased. Hence, the induced uniaxial anisotropy is also increased. Micromagnetic simulations explaining the corrugation-induced anisotropy using the dipolar and exchange energy densities for different magnetization orientations were done by Václav Roučka and are well-explained in his master's thesis [197].

We performed another angular dependence characterization to further analyze the dependence of the corrugation-induced uniaxial magnetic anisotropy on the amplitude of modulation. This time we fixed the modulation periodicity to 100 nm. We used the automation software already discussed above and extracted the mean value from the positive and negative remanence. The errors are calculated as a standard deviation from the mean remanence value. We performed a series of measurements varying the angle between the external magnetic field and the corrugation direction by 10° from 0° to 360°. In the Figure 4.11 the mean remanence value $\frac{M_{\rm r}}{M_{\rm s}}$ as a function of the angle between the corrugation direction and the external magnetic field is presented for one planar disc and two corrugated discs with modulation amplitudes of (6.0 ± 0.5) nm and (8.2 ± 0.6) nm. This Figure, similar to Figure 1.7(b), shows a clear uniaxial anisotropy, which can be fitted from the squareness $\frac{M_{\rm r}}{M_{\rm s}}$ of the hysteresis loop using the equation[198]

$$\frac{M_{\rm r}}{M_{\rm s}} = \frac{M_{\rm r}^{\rm max}}{M_{\rm s}} \cdot |\cos(\alpha - \alpha_0)| + \frac{M_{\rm r}^{\rm off}}{M_{\rm s}}, \qquad (4.3)$$

where $M_{\rm r}^{\rm max}$ is the maximum measured remanence and $M_{\rm r}^{\rm off}$ is an angularly independent offset. The fit of the remanence data measured for the planar disc convincingly supported the absence of the in-plane shape anisotropy. Furthermore, the measurement of the corrugated discs revealed the formation of the easy axis perpendicular to the corrugation direction, i.e., at $\alpha=90^{\circ}$. The fit also confirmed that the amplitude of the corrugation-induced uniaxial magnetic anisotropy is increased when the corrugation amplitude is higher, i.e., when the modulation amplitude is higher.

As already mentioned above, the software used for the analysis of Kerr microscopy measurements allows for selecting multiple features in an obtained Kerr microscopy image. It extracts hysteresis loops for every selected structure. We decided to study more thoroughly the influence of the modulation amplitude on corrugation-induced uniaxial magnetic anisotropy. Figure 4.12 offers a comparison of a magnetostatic response of planar and corrugated NiFe discs. It shows 16 hysteresis loops measured for seven corrugated and one planar NiFe disc in two configurations of the external magnetic field with respect to the corrugation direction. The red curves represent the case where the external magnetic field is applied perpendicular to the corrugation direction, $\alpha = 90^{\circ}$. We see that the

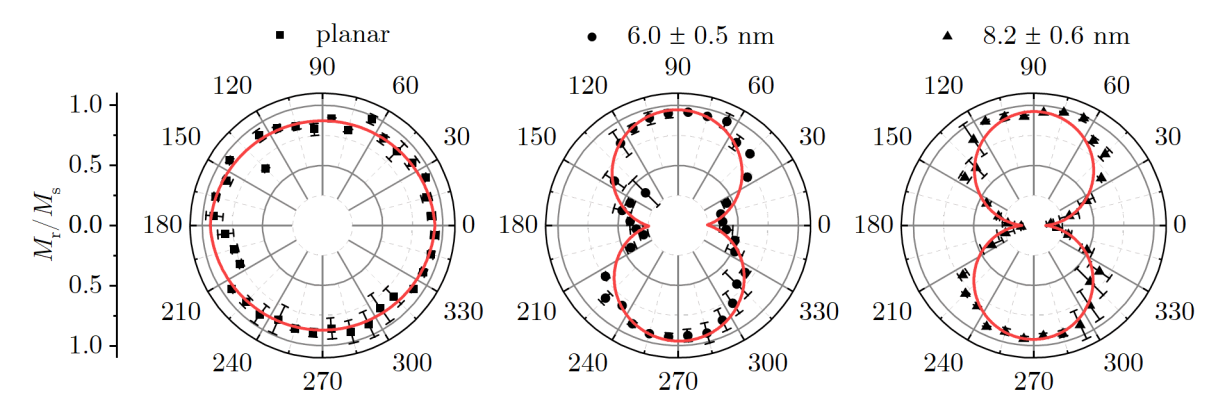


Figure 4.11: Angular dependence of the induced uniaxial magnetic anisotropy on the amplitude of modulation for one planar and two corrugated 10nm thick NiFe discs with amplitudes of modulation of (6.0 ± 0.5) nm and (8.2 ± 0.6) nm. Discs diameter is $7 \mu m$. The angle α is the angle between the corrugation direction and the external magnetic field. The mean remanence is extracted from hysteresis loops from the positive and negative remanence. The error bars are calculated as a standard deviation. The fit is calculated using equation (4.3).

hysteresis loops show typical easy axis loop behavior. On the other hand, hysteresis loops measured for the external magnetic field parallel to the corrugation direction ($\alpha=0^{\circ}$) clearly show hard axis features. Only for the case of a planar NiFe disc, the two curves coincide because there is no (in-plane) anisotropy in the planar disc.

The modulation amplitude of the corrugation was created using 2000 to 9000 scans. The corrugation periodicity was fixed to $d=100\,\mathrm{nm}$. The AFM measurements revealed that the amplitude of modulation ranges from 0 nm for the planar structure to $(14.3\pm1.5)\,\mathrm{nm}$ for the corrugated structure created by 9000 scans. From the shape of the hysteresis loops, we can see that the uniaxial magnetic anisotropy is becoming stronger with the increasing modulation amplitude. That is in agreement with the conclusions made after measuring the corrugation-induced uniaxial magnetic anisotropy dependent on the modulation periodicity and angular dependence of the corrugation-induced uniaxial magnetic anisotropy on the amplitude of modulation.

As we know from the equation (1.23), uniaxial anisotropy constant can be calculated from the anisotropy field $H_{\rm ani}$ and vice versa. Therefore, the anisotropy field value gives a good estimate about the quality of the corrugated structures. We decided to extract the values of the anisotropy field $H_{\rm ani}$ directly from the hard axis hysteresis loops measured in the direction perpendicular to the corrugation direction using piece-wise fit [199]

$$M/M_{\rm s} = \begin{cases} -1 & H_{\rm ext} \le -H_{\rm ani} \\ \frac{H_{\rm ext}}{H_{\rm ani}} & -H_{\rm ani} \le H_{\rm ext} \le H_{\rm ani} \\ 1 & H_{\rm ext} \ge H_{\rm ani} \end{cases}$$
(4.4)

To have the complete picture, we have extracted the anisotropy field values from structures where we varied both modulation amplitude h and periodicity d. The periodicity values were $d_1 = 60 \,\mathrm{nm}$, $d_2 = 75 \,\mathrm{nm}$, $d_3 = 100 \,\mathrm{nm}$ and $d_4 = 125 \,\mathrm{nm}$, and the modulation amplitude ranged from $4 \,\mathrm{nm}$ to $16 \,\mathrm{nm}$. Our study has also included planar discs where the anisotropy field is $0 \,\mathrm{mT}$ due to the absence of the in-plane shape anisotropy. This analysis yields the dependency of the corrugation-induced anisotropy field on the amplitude of

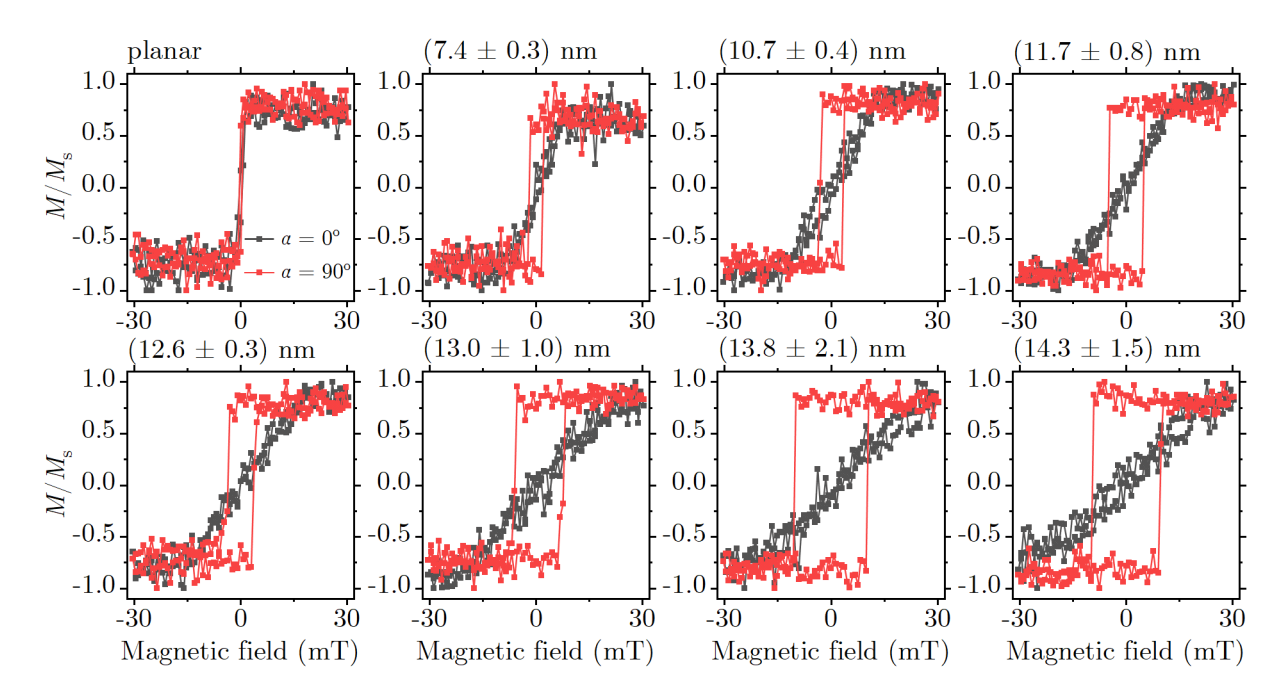


Figure 4.12: Normalized hysteresis loops of representative planar NiFe discs (reference) and corrugated NiFe discs with increasing modulation amplitude measured by Kerr microscopy. The red loops were measured in the external magnetic field aligned perpendicular to the corrugation direction, and black loops correspond to the measurement with the external magnetic field rotated by 90°. From the shape of the hysteresis curves, we can speak about the formation of easy and hard axes, respectively.

modulation. Furthermore, using equation (1.23), we calculated the uniaxial anisotropy constants.

Figure 4.13(a) shows an example of the extraction of the anisotropy field $H_{\rm ani}$ from the hard axis loops using the model discussed in (4.4) for two modulation periodicities $d_1 = 60 \,\mathrm{nm}$ and $d_2 = 75 \,\mathrm{nm}$ with similar amplitudes of modulation. Arrows indicate the anisotropy field values. Figure 4.13(b) then shows fitted anisotropy field values for all four fabricated corrugation periodicities dependent on the modulation amplitude in an ultimate comparison. The corrugation-induced uniaxial magnetic anisotropy shows a correlation of the magnitude of the anisotropy field with the total corrugation (corrugation periodicity & amplitude of modulation). In the periodicity of $d_1 = 60 \,\mathrm{nm}$, the anisotropy field shows a rapid increase up to 50 mT. However, the amplitude of modulation does not exceed 10 nm. That is caused by the gaussian shape of the e-beam and beam overlapping during the FEBID step of the sample fabrication process, discussed in section 4.1. Any higher number of e-beam scans during the FEBID process results in the same topography. Besides, error bars in the amplitude of the modulation axis and the anisotropy field axis are high. That is caused by the non-uniformity of the magnetic layer on top of the corrugation. In the case of the higher periodicities, the anisotropy field increase is not so abrupt as it is in the lower periodicities. We do not observe the saturation of the amplitude of modulation at some value as in the case of $d_1 = 60 \,\mathrm{nm}$. The corrugationinduced anisotropy shows a quadratic dependency on the amplitude of modulation. That is in agreement with the study by Chen et al. [14] who showed the quadratic dependency of the exchange and anisotropy energy densities on the modulation amplitude.

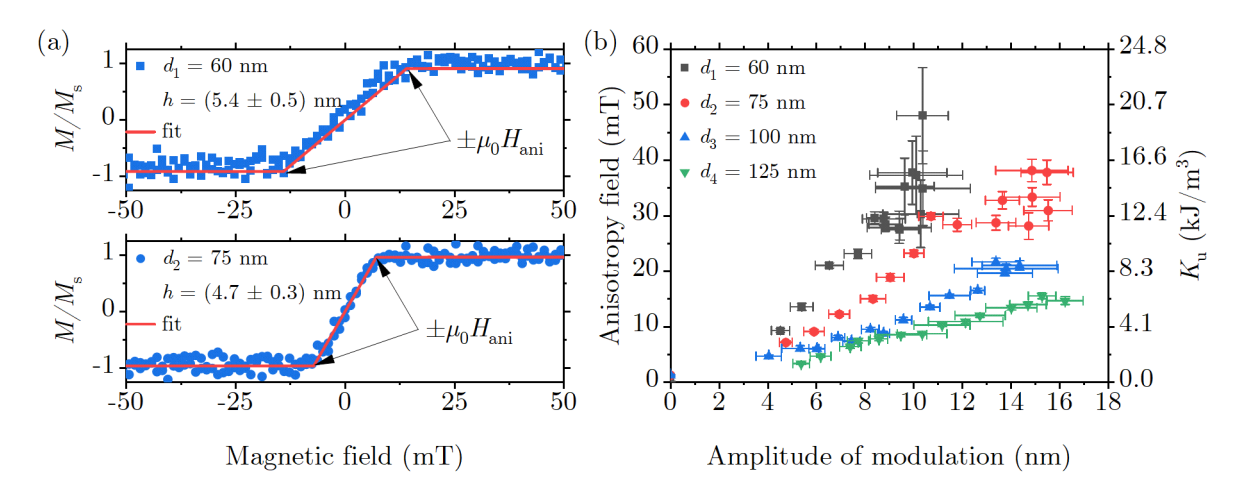


Figure 4.13: (a) The example of the hard axis loops measured for the structures with modulation periodicities of $d_1=60\,\mathrm{nm}$ and $d_2=75\,\mathrm{nm}$ with similar amplitudes of modulation. The red curve is the fitted function. The values of extracted anisotropy fields are indicated by arrows. (b) The dependence of the corrugation-induced anisotropy field on the amplitude of modulation for four periodicities – $d_1=60\,\mathrm{nm},\,d_2=75\,\mathrm{nm},\,d_3=100\,\mathrm{nm}$ and $d_4=125\,\mathrm{nm}$. The corrugation-induced uniaxial magnetic anisotropy constants are calculated using equation (1.23). The error bars in the amplitude of the modulation axis are obtained from the AFM measurement. The error bars in the anisotropy field axis are extracted from the fit.

4.3. Spin wave propagation in corrugated waveguides

In the previous section, we have summarized the magnetostatic properties of the structures with corrugation-induced uniaxial magnetic anisotropy. This section is devoted to studying the spin-wave propagation in magnonic waveguides with corrugation-induced uniaxial magnetic anisotropy. The main prospect is the propagation of spin waves in the Damon-Eshbach mode without the presence of an external magnetic field. Utilizing the above-described approach, we exploited the local control of the uniaxial magnetic anisotropy in magnetic waveguides. The source for the excitation of spin waves was a simple microstrip antenna. The magnetization dynamics was studied by the Brillouin light scattering microscopy, the technique introduced in section 3.4. The results, presented in this section, have been published in Applied Physics Letters [200].

Corrugated magnonic waveguides were fabricated using the same fabrication procedure as for the magnetic discs described in section 4.2.1. The SEM micrograph of the sample is shown in Figure 4.14. The dimensions of prepared magnonic waveguides were: width $w_{\rm w}=2\,\mu{\rm m}$, length $l_{\rm w}=20\,\mu{\rm m}$ and the amplitude of modulation ranging from 3 nm to 18 nm. The corrugation below magnonic waveguides was designed to have ca. $1\,\mu{\rm m}$ overlap on both sides to assure a safe fit of the waveguide on top of the corrugation. We have fabricated two sets of eleven corrugated waveguides and one planar (reference) magnonic waveguide. The periodicity of modulation was fixed at $d=100\,{\rm nm}$. The thickness of the NiFe layer deposited on top of the corrugation was $t=10\,{\rm nm}$. The excitation antenna was fabricated directly on top of magnonic waveguides. The width of the microstrip antenna was designed to $w_{\rm a}=1\,\mu{\rm m}$ in order to guarantee good excitation efficiency of the spin waves. The antenna is composed of a stack of layers prepared in an electron beam evaporator. The multilayer consists of Ti(5)/SiO₂(25)/Ti(5)/Cu(85)/Au(10) stack (the

order of the layers is listed from bottom to top – Ti is on the substrate and Au on air). The number in the bracket is the nominal thickness of the material in nanometers. The Ti layers are essential to enhance the adhesion between the magnonic waveguides and the excitation antenna so that it does not peel off during the ultrasonic agitation during the lift-off process. The SiO_2 layer prevents the shorting of the antenna. The Cu is the main conductor, and the Au layer prevents the oxidation of the Cu.

The design of the excitation antenna was inspired by the design presented in [58]. The antenna consists of a pad region, taper region, and excitation region. A wider pad region is designed in a bent shape which allows contacting the antenna by the microwave probe with a 50 µm pitch in 90° span. The connection between the microwave generator and the planar sample is ensured by the Model 50A high-frequency microwave probes of the brand Picoprobe by GGB industries [178]. The bent shape on the broader pad region of the excitation antenna is helpful for a spin-wave propagation study in an arbitrary orientation of the external magnetic field because, in the experimental setup, the orientation of the magnetic field is fixed. Thus, the change of the magnetic field orientation is only possible by rotating the sample.

The main parameter determining the properties of propagating spin waves in the magnonic waveguide is the local effective magnetic field. It defines the local direction of the magnetization, and thus, the local spin-wave dispersion. We discussed the total effective magnetic field in (1.13) using the micromagnetic theory. In our case, we need to add the corrugation-induced anisotropy contribution to have the complete picture. In section 1.3.3 we discussed the case of a rectangular-shaped polycrystalline NiFe structure with corrugation-induced uniaxial magnetic anisotropy perpendicular to the long axis of the rectangle. We concluded that in this case, the resulting easy axis is oriented in the stronger anisotropy direction, and the difference between the two anisotropy contributions gives the total anisotropy. The same applies for the local effective magnetic field, i.e., for

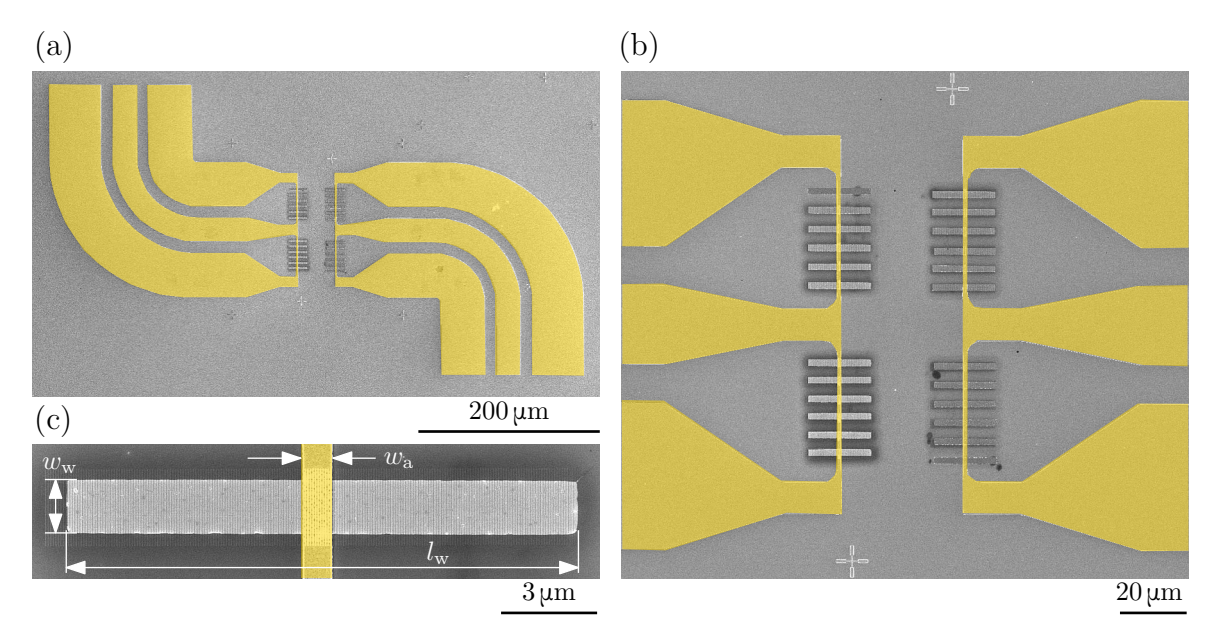


Figure 4.14: (a) SEM overview image of the magnonic waveguides with corrugation-induced uniaxial magnetic anisotropy with excitation antennas (highlighted by gold color).

(b) Enlarged image of two sets of eleven corrugated waveguides and one planar magnonic waveguide. (c) Detail of a corrugated magnonic waveguide with the excitation antenna.

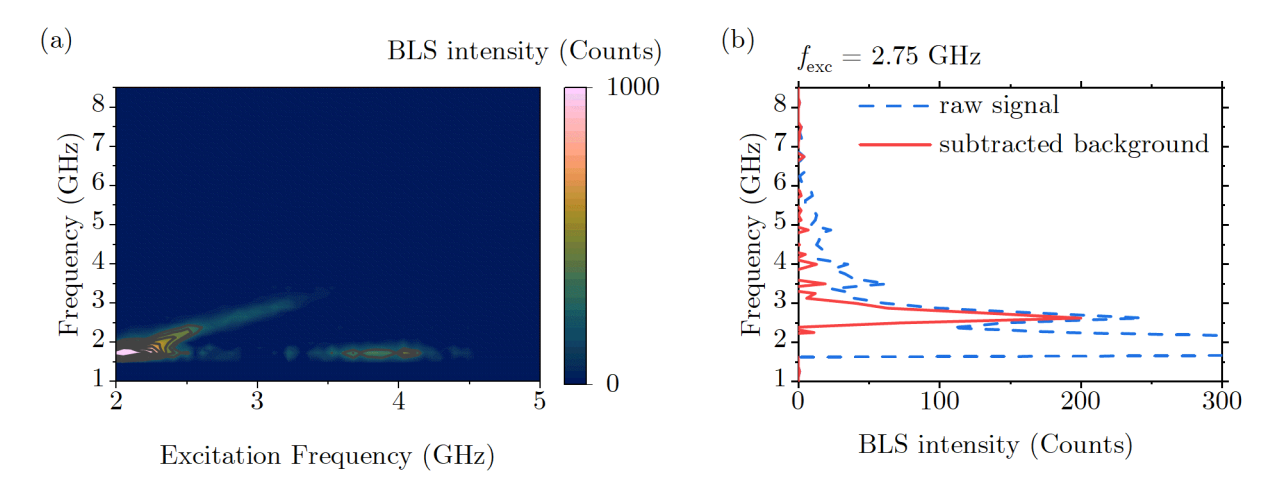


Figure 4.15: (a) 2D frequency map of measured BLS spectra for different excitation frequencies. The thermal spectrum was subtracted to suppress the background. The external magnetic field was zero. (b) Acquired BLS spectrum for the excitation frequency $f_{\rm exc} = 2.75\,{\rm GHz}$ (blue dashed line), and the same spectrum with subtracted background (red solid line). The peak at the frequency range of $1.6\,{\rm GHz} - 2.2\,{\rm GHz}$ represents a quasi-elastic scattering of the laser from the sample and additional peak at the frequency of $3.5\,{\rm GHz}$ corresponds to the additional laser mode elastically scattered from the sample.

the case of a corrugation-induced anisotropy being higher than the shape anisotropy, the local effective magnetic field is given by the difference between the corrugation-induced anisotropy contribution and the demagnetizing field contribution coming from the shape of the waveguide. Therefore, even at zero external magnetic field, the magnetization of the waveguide points perpendicular to the corrugation direction, i.e., perpendicular to the long axis of the waveguide.

Using Kerr microscopy, we have measured the magnetostatic response of a planar magnonic waveguide in the configuration, where the external magnetic field was aligned with the hard axis of the waveguide (perpendicular to the long axis of the rectangle). Applying (4.4) we fitted the demagnetizing field as 3 mT. In accordance with Figure 4.13(b), we have focused on the magnonic waveguide with the amplitude of modulation $h = (6.8 \pm 0.2) \,\mathrm{nm}$, where the corrugation-induced anisotropy field is 8 mT. The local effective magnetic field is then for this waveguide $\mu_0 H_{\mathrm{eff}} = 5 \,\mathrm{mT}$.

To find the RF excitation frequency at which the excited spin waves propagate with the maximum efficiency at zero external magnetic field, we have fixed the BLS laser spot at a distance of 5 µm from the excitation antenna, in the middle of the corrugated magnonic waveguide. The stable position of the laser spot was ensured by enabling image stabilization. We have swept the excitation frequency of the RF source from 2 GHz to 5 GHz. We have measured the BLS spectra for each excitation frequency, and the 2D frequency map is depicted in Figure 4.15(a).

When we looked at the spectra, we saw an additional peak independent of the excitation frequencies. The peak is observed at the frequency range of $1.6\,\mathrm{GHz}-2.2\,\mathrm{GHz}$. It is a quasi-elastic scattering of the laser from the sample [201]. Another peak is observed at the frequency of $3.5\,\mathrm{GHz}$. Even though we have used a single-frequency laser, it is an additional laser mode elastically scattered from the sample. Therefore, for the excitation of spin waves we selected the frequency of $2.75\,\mathrm{GHz}$ to be safely out of the frequency range of quasi-elastic scattering and the laser mode peak, see Figure 4.15(b). To suppress a non-

related background that is constant over the excitation frequencies, we subtracted the thermal BLS signal, i.e., the signal measured when the microwave generator was turned off.

At this point, we fixed the excitation frequency at $f_{\rm exc} = 2.75\,\rm GHz$ and acquired a two-dimensional spatial map of BLS intensity in the zero external magnetic field. We have scanned the part of the magnonic waveguide near the excitation antenna. We recorded the map over $3\times9\,\mu\rm m^2$ in 200 nm steps. We measured the BLS spectra at each spot and extracted the integral counts from the 2 GHz window around the excitation frequency.

We then extracted the propagation length by integrating the BLS intensity in the y-direction and fitted the exponential decay

$$I(x) = I_0 \cdot \exp\left(-\frac{2x}{\Lambda}\right) + b \tag{4.5}$$

where x is the distance from the antenna, Λ is the propagation length defined as the distance over which the spin-wave amplitude falls to the 1/e of its original amplitude, see (1.74), and b is an offset caused by the noise level of the measurement. The offset is extracted by fitting a constant function to the constant part of the exponential decay. The factor 2 in the exponent is to consider the BLS intensity being proportional to the square of the spin-wave amplitude [202].

However, for the fitting of the exponential decay we wanted to use a linear regression. Hence, we needed to transform the exponential function into a linear sum of functions. When we take the natural logarithm of both sides of the equation (4.5) we get

$$\log(I - b) = \log\left[I_0 \cdot \exp\left(-\frac{2x}{\Lambda}\right)\right]. \tag{4.6}$$

Substituting the left side with Y and the right side with A + Bx we obtain

$$\underbrace{\log(I-b)}_{Y} = \underbrace{\log I_0}_{A} \underbrace{-\frac{2}{\Lambda}}_{B} x, \qquad (4.7)$$

$$Y = A + Bx \to \Lambda = -\frac{2}{B}. \tag{4.8}$$

To get the 95% confidence interval of the propagation length, the uncertainty of the fit is recalculated using the propagation of error

$$\sigma_{\Lambda} = \sqrt{\left(\frac{\partial \Lambda}{\partial B}\right)^2 \cdot \sigma_B^2} = \frac{2\sigma_B}{B^2},$$
(4.9)

where σ_B is a standard deviation of B.

The two-dimensional spatial map of BLS intensity measured at the zero external magnetic field is depicted in Figure 4.16(a). The integrated spectra over the width of the magnonic waveguide and the fit used for the extraction of the propagation length are shown in Figure 4.16(b). The fitted propagation length with the 95% confidence interval was then $\Lambda_{\text{corrugated}} = (5.3 \pm 0.3) \,\mu\text{m}$.

To have a comparison between the zero external magnetic field propagation in the corrugated and planar magnonic waveguides, we repeated the same experiment using the planar magnonic waveguide of identical dimensions (width $w_{\rm w}=2\,\mu{\rm m}$, length $l_{\rm w}=20\,\mu{\rm m}$). The planar waveguide was directly prepared on the GaAs substrate without

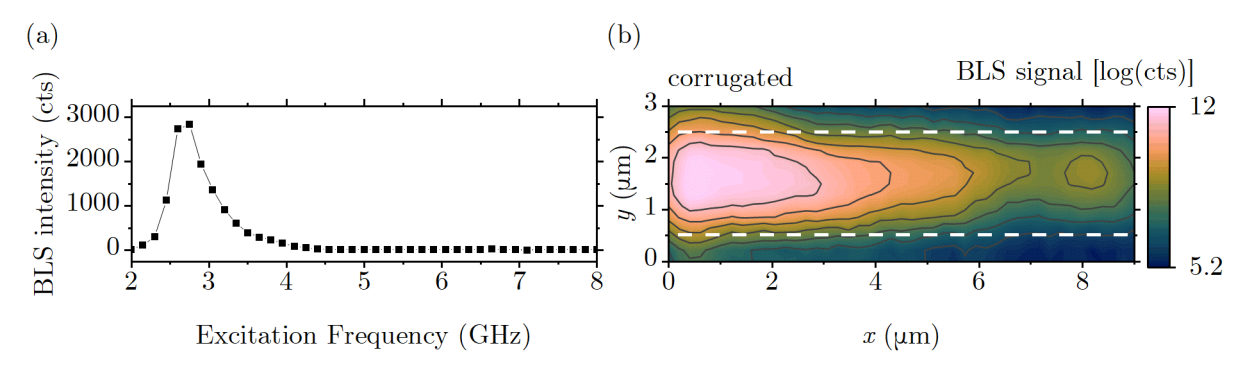


Figure 4.16: (a) The spin wave spectra measured using BLS 5 µm from the excitation antenna in the corrugated waveguide. The external magnetic field was zero. The peak corresponds to the optimum excitation frequency. (b) 2D map of the spin-wave intensity in the logarithmic scale measured on the corrugated waveguide in zero magnetic field with the excitation frequency $f=2.75\,\mathrm{GHz}$. Due to the corrugation of the magnonic waveguide, the magnetization vector lies perpendicular to the long axis of the waveguide. Therefore, spin waves propagate in the Damon-Eshbach geometry. The amplitude of modulation was $h=(6.8\pm0.2)\,\mathrm{nm}$ and the resulting effective field was $\mu_0 H_\mathrm{eff}=5\,\mathrm{mT}$. The map was recorded over $3\times9\,\mathrm{\mu m}^2$ by rastering the BLS laser spot with a 200 nm step. The white dashed lines indicate the edges of the waveguide. (b) The integrated spectra over the width of the magnonic waveguide (blue points). The solid red line is a linear fit of experimental data used to extract the propagation length.

any FEBID of the planar layer. In order to determine the optimum excitation frequency, we have swept the excitation frequency of the RF source from 1 GHz to 7 GHz at the power of 5 dBm and measured the BLS intensity 5 μ m from the excitation antenna. We have found the optimum excitation frequency at 1.8 GHz, see Figure 4.17(a). When compared to the corrugated waveguide, the optimum excitation frequency is lower. The shift to the lower frequencies in the excitation frequency is expected and is connected to the decrease of the local effective magnetic field. Also, in the planar magnonic waveguide, due to the shape anisotropy, the magnetization points parallel to the long axis of the rectangular waveguide. Therefore, the spin waves propagate in the backward volume geometry. The two-dimensional spatial spin-wave intensity map from this measurement is shown in Figure 4.17(b). Evidently, in this case, the propagation length is an order of magnitude smaller – approximately 0.6 μ m.

We wanted to compare the spin-wave propagation in flat and corrugated waveguides in comparable conditions. Therefore, we applied an external magnetic field of $\mu_0 H_{\rm ext} = 5\,\mathrm{mT}$ to "simulate" the contribution of corrugation induced anisotropy and repeated the two-dimensional spin-wave intensity mapping using the BLS at the excitation frequency of 2.75 GHz. We obtained similar result as for the corrugated waveguide measured at zero external magnetic field [see Figure 4.18(a) and compare with Figure 4.16(a)]. The propagation length was evaluated to: $\Lambda_{\rm planar} = (5.7 \pm 0.5)\,\mu{\rm m}$.

In the following step, we further analyzed how the modulation amplitude influences the spin-wave propagation length in corrugated magnonic waveguides with different amplitude of modulation. To have comparable conditions for all waveguides, we fixed the excitation frequency and varied the external magnetic field in order to have the constant spin-wave k-vector. We decided to perform this experiment in an effective field of $25\,\mathrm{mT}$ to be able to include and compare the waveguides even with the amplitudes of modulation

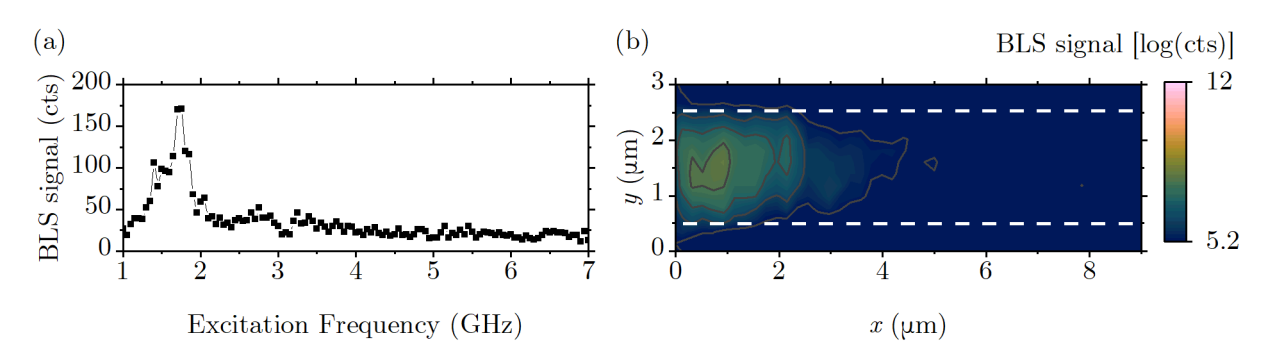


Figure 4.17: (a) The spin wave spectra measured at zero external magnetic field using BLS in the planar magnonic waveguide to determine the optimum spin-wave frequency. The BLS laser spot was fixed $5\,\mu\mathrm{m}$ from the excitation antenna. (b) BLS intensity map in the logarithmic scale measured in zero magnetic field on the planar magnonic waveguide. The excitation frequency was $f=1.8\,\mathrm{GHz}$. Due to the shape anisotropy of the waveguide, the magnetization is aligned parallel to the long axis. Hence, the spin waves propagate in the backward volume geometry.

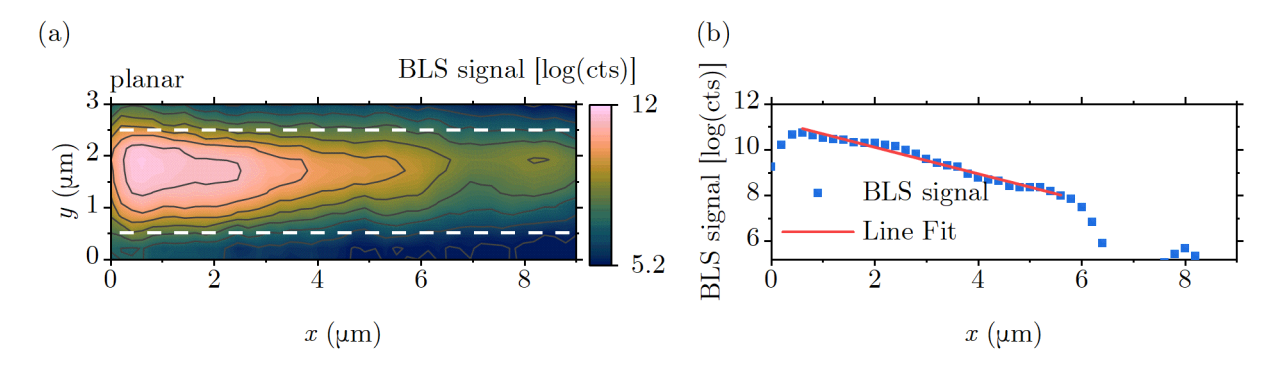


Figure 4.18: (a) BLS intensity map in the logarithmic scale measured in the external magnetic field of $\mu_0 H_{\rm ext} = 5\,\mathrm{mT}$ on the planar magnonic waveguide. The external magnetic field rotated the magnetization perpendicular to the long axis of the waveguide, and the spin-wave propagation geometry changed from backward volume to Damon-Eshbach geometry. (b) The BLS signal summed over the width of the magnonic waveguide with the linear fit to extract the propagation length.

above 14 nm. To find the optimal excitation frequency, we applied an external magnetic field of $\mu_0 H_{\text{ext}} = 25 \,\text{mT}$ to the planar magnonic waveguide and performed the sweep of the excitation frequency from 1 GHz to 7 GHz at the power of 5 dBm. The BLS laser spot was fixed at a distance of 1 µm from the excitation antenna. As can be seen from Figure 4.19(a), we have found the optimum excitation frequency at 6.3 GHz. To find the effective fields of each waveguide, we performed an external magnetic field sweep while having the excitation frequency fixed at 6.3 GHz at the power of 5 dBm 3 µm from the excitation antenna. The external magnetic field was applied perpendicular to the long axis of the rectangular magnonic waveguide to ensure the propagation of excited spin waves in the Damon-Eshbach geometry. Local effective magnetic fields $\mu_0 H_{\text{eff}}$ were calculated as a difference between the applied magnetic field corresponding to the highest BLS signal of the planar waveguide, and the matching applied magnetic field of the highest BLS signal of the corrugated waveguide. Figure 4.19(b) shows representative external magnetic field sweeps of the planar and corrugated waveguides. The calculation of the local effective magnetic field is schematically explained. It is not surprising that the local effective magnetic field depends on the modulation amplitude of the corrugated waveguide [see Figure 4.19(c) and compare with Figure 4.13(b)]. From the knowledge of each waveguide's local effective magnetic field, we were able to apply the appropriate magnitude of the external magnetic field to ensure the equal effective field of 25 mT for

Finding the excitation frequency and fixing it at f = 6.3 GHz, and varying the external magnetic field in such a way that the effective field is constant, $\mu_0 H_{\text{eff}} = 25 \,\text{mT}$ assured

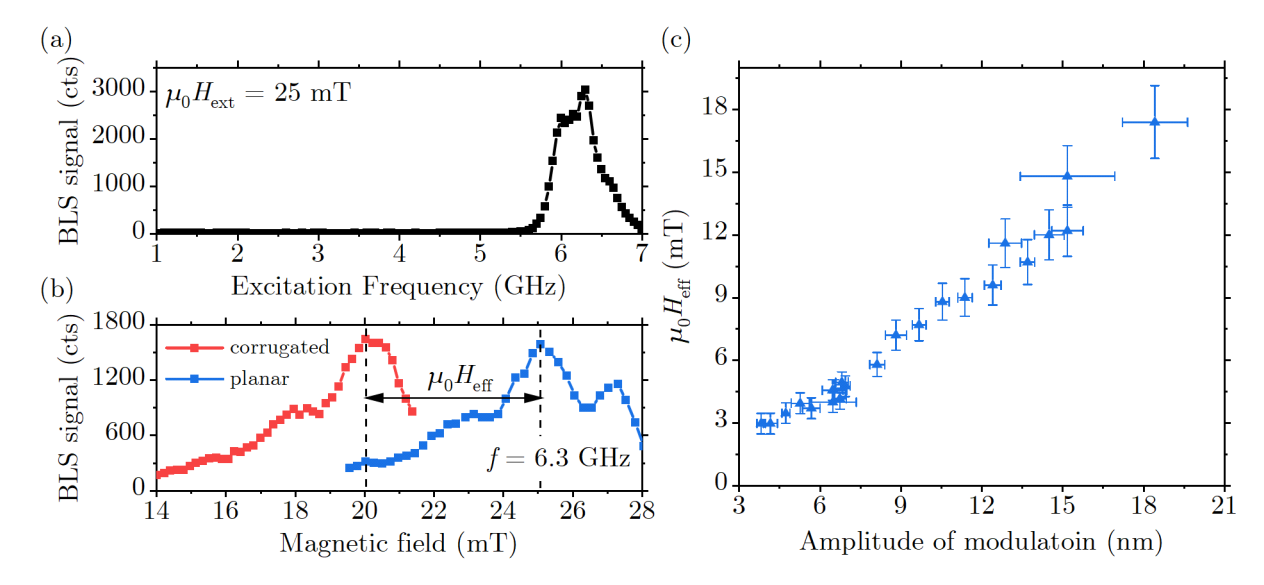


Figure 4.19: (a) Excitation frequency sweep with BLS laser spot fixed 1 μ m from the excitation antenna. The optimum excitation frequency $f=6.3\,\mathrm{GHz}$ will be used later in the experiment measuring the spin-wave propagation length in corrugated magnonic waveguides. (b) External magnetic field sweep to find the local effective magnetic fields of corrugated rectangular magnonic waveguides. The excitation frequency was fixed at $f=6.3\,\mathrm{GHz}$. The external magnetic field was applied perpendicular to the long edge of the rectangle. (c) The local effective magnetic field depending on the amplitude of modulation was calculated from the external magnetic field sweeps. The error bars in the local effective magnetic field are set to 10% of the measured value to compensate for the error of the measurement of the magnetic field [91].

comparable conditions for all waveguides. The fact that the k-vector does not change for each measurement of the spin-wave propagation length was checked before each measurement by measuring BLS interference line scans [203]. The representative phase-resolved BLS line scans measured for corrugated and planar waveguides at the same effective field are shown in Figure 4.20(a),(b). For the spin-wave wavelength extraction and the k-vector evaluation, we fitted the measured data with the model introduced in (3.15). The model quite nicely corresponds to the measured data. This approach ensured that we measured the propagation length always at the same point in the dispersion relation, and the contribution of the corrugation to the propagation length was isolated from the variations in the group velocity. In addition, Figure 4.20(c) shows a phase-resolved BLS line scan measured for corrugated waveguide at the zero external magnetic field. The conditions of this measurement correspond to the two-dimensional spatial map of BLS intensity depicted in Figure 4.16(a).

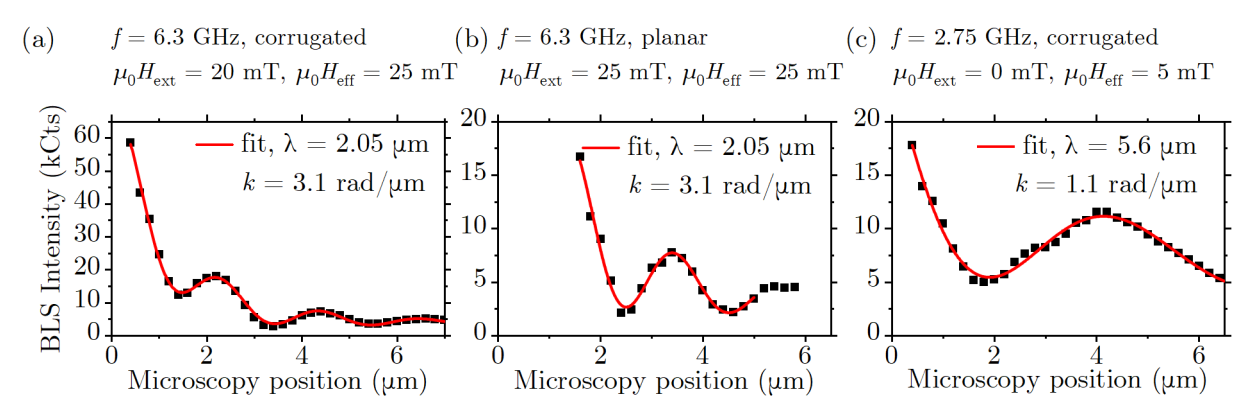


Figure 4.20: (a) Phase-resolved BLS line scan of a corrugated magnonic waveguide with the modulation amplitude of $h=(6.8\pm0.2)$ nm. The excitation frequency was fixed at $f=6.3\,\mathrm{GHz}$ and the applied external magnetic field was $\mu_0H_\mathrm{ext}=20\,\mathrm{mT}$ so that the local effective magnetic field is $\mu_0H_\mathrm{eff}=25\,\mathrm{mT}$. The red line represents the model which was used to fit the spin-wave wavelength ($\lambda=2.05\,\mathrm{\mu m}$) and evaluate the k-vector ($k=3.1\,\mathrm{rad/\mu m}$). (b) BLS interference line profile of a planar waveguide. The applied external magnetic field was $\mu_0H_\mathrm{ext}=25\,\mathrm{mT}$. The excitation frequency was fixed at $f=6.3\,\mathrm{GHz}$. The spin-wave wavelength was fitted as $\lambda=2.05\,\mathrm{\mu m}$ and the corresponding k-vector as $k=3.1\,\mathrm{rad/\mu m}$. (c) Phase-resolved BLS line profile of the same corrugated magnonic waveguide as in (a) measured in zero external magnetic field. The excitation frequency was fixed at $f=2.75\,\mathrm{GHz}$. Due to the corrugation of the waveguide, the local effective magnetic field was $\mu_0H_\mathrm{eff}=5\,\mathrm{mT}$. The spin-wave wavelength was $\lambda=5.6\,\mathrm{\mu m}$ and the k-vector $k=1.1\,\mathrm{rad/\mu m}$.

Finally, we measured the BLS line scans of magnonic waveguides with the different modulation amplitudes and extracted spin-wave propagation lengths using the linear regression fitting, see (4.6). Figure 4.21 shows the spin-wave propagation length dependence on the amplitude of modulation. From the results, it is apparent that the spin-wave propagation length significantly decreases for the amplitudes of modulation above approx. 8 nm (Figure 4.21, black points). The modulation of ca. 18 nm results in the decrease of the propagation length by a factor of three. This decrease can be caused by the inhomogeneities of the corrugated magnetic layer or by the corrugation-induced inhomogeneities of the internal effective magnetic field. Above mentioned inhomogeneities can give rise to

the spin-wave scattering and can also lead to the increase of the effective damping. The discussed effect negatively influences the spin-wave propagation length.

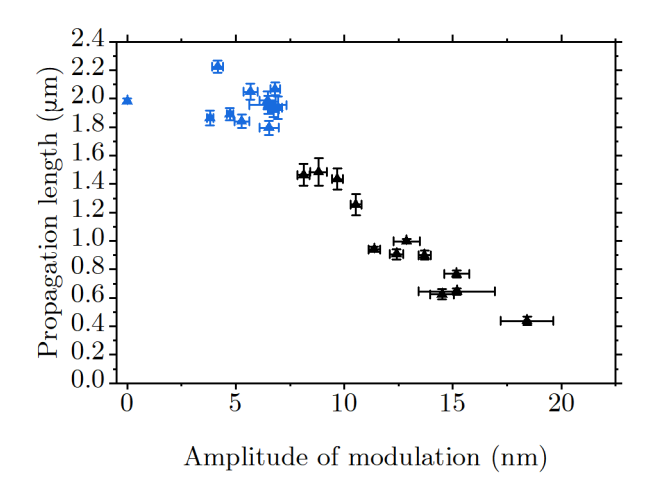


Figure 4.21: Dependence of the spin-wave propagation length on the amplitude of modulation of magnonic waveguides. The excitation frequency was $f=6.3\,\mathrm{GHz}$. To keep the k-vector at $3.1\,\mathrm{rad/\mu m}$ the external magnetic field was changed for every waveguide with the different amplitude of modulation so that the effective field remains constant, $\mu_0 H_{\mathrm{eff}} = 25\,\mathrm{mT}$.

The negligible decrease of the spin-wave propagation length is very convincingly visible for low modulation amplitudes, see Figure 4.21, blue points. For the magnonic waveguides with amplitudes of modulation below 8 nm (including the planar waveguide), we measured the propagation lengths in the range of 1.8 to 2.2 µm which corresponds to the propagation lengths of planar NiFe waveguides reported in other studies [202, 204, 205].

It is important to note that spin-wave propagation lengths are significantly lower than the propagation length extracted from Figure 4.16(a). The reason is that these experiments were performed at different k-vector (see Figure 4.20). When we look at the analytical calculation of the dispersion relation and propagation length for the first waveguide mode of a transversally magnetized planar NiFe waveguide plot in Figure 1.16 and Figure 1.18(b), we see that the spin-wave propagation length decreases with increasing k-vector. Also, the propagation length decreases with increasing the local effective magnetic field. Therefore, the applied conditions when measuring the spin-wave propagation length lead to a different point on the dispersion relation, hence, the different propagation length.

In conclusion, we have studied the spin-wave propagation in corrugated magnonic waveguides grown on a modulated surface prepared by the combination of FEBID and EBL. We have shown that waveguides can be oriented in any direction and placed anywhere on the sample while still allowing spin-wave propagation in highly efficient DE mode. Additionally, the spin waves in the corrugated waveguides without the presence of external magnetic fields propagate over a distance $10 \times$ larger than in the planar waveguide. Besides, when the applied external magnetic field to the planar waveguide matches the local effective magnetic field of the corrugated waveguide, the spin-wave propagation length is comparable. Furthermore, we have analyzed the influence of the modulation amplitude on the spin-wave propagation and concluded that for the modulation amplitudes below 8 nm, the propagation length is not affected. For larger modulations, the propagation length decreases linearly with increasing modulation amplitude. By using

phase-resolved BLS microscopy, we confirmed that the k-vector has not changed for each measurement. Our approach of shaping magnonic waveguide in the third dimension and exploiting the curvature-induced effects supports the possibility to locally control uniaxial magnetic anisotropy and propagate spin waves in the Damon-Eshbach mode without the need for external magnetic fields. The 3D nanofabrication approach is universal and can be scaled up via, e.g., nanoimprint lithography [206]. Moreover, any magnetic material can be used. Finally, it opens the way to new possibilities of local control of the internal magnetic field or magnetization direction in any magnetic system.

4.4. Ferromagnetic resonance of corrugated structures

We have already discussed the sample fabrication and magnetostatic characterization of magnetic structures with corrugation-induced anisotropy in the previous sections. Besides, we have provided a study of the spin-wave propagation in corrugated magnonic waveguides and showed that the spin waves propagate in the Damon-Eshbach geometry without the presence of an external magnetic field. This section aims to study the dependence of the damping constant α on the modulation amplitude h. The data provided in this chapter are measured by a two-port vector network analyzer ferromagnetic resonance (VNA-FMR). The essential introduction to this technique is given in section 3.5.

For the pioneering experiments with the data processing of the broadband VNA-FMR, we have used a $600 \times 600 \,\mu\text{m}^2$ NiFe pad with thickness $t=10 \,\mathrm{nm}$. The coplanar waveguide (CPW) was lithographically placed on top of this pad. The CPW is used for both exciting and detecting the FMR signal. The width of the signal line was $w_a=20 \,\mu\text{m}$, the width of the gap $w_g=14 \,\mu\text{m}$, and the width of ground lines was $w_{\rm gnd}=44 \,\mu\text{m}$. The length of the CPW was $l_a=170 \,\mu\text{m}$, and it was placed in the middle of the NiFe pad. The antenna is again composed of layers' stack as it was in the case of excitation antenna fabricated to study spin-wave propagation in corrugated waveguides. Nevertheless, here the multilayer consists of $\mathrm{Ti}(5)/\mathrm{SiO}_2(25)/\mathrm{Ti}(5)/\mathrm{Au}(100)$ stack because the gold is softer than copper, and the antenna can be used for the tilt correction of microwave probes. This is necessary because in VNA experiment, a perfect contact of the probe is required in order to get good results.

The response of the magnetization on a small oscillating magnetic field is described by the dynamic susceptibility, which has been theoretically calculated in sections 1.5.1 and 1.5.2. The great advantage of using the dynamic susceptibility in data analysis is that it can fit not only the resonance frequency $f_{\rm res}$ but also the resonance linewidth Δf from which the Gilbert damping parameter α can be extracted. However, to use the dynamic susceptibility, one has to measure all four S-parameters twice – first time for the measurement itself and the second time for the reference measurement making the acquisition time much higher. It has been previously studied by Bilzer et al.[207] and also in our group by Roučka[180] that this approach is often unnecessary.

In our study, we have used the CPW as a transmission line and measured both the real and imaginary value of the transmission S_{21} parameter. We have swept the frequency on the VNA from 1 GHz to 20 GHz with 40 MHz step. The external magnetic field was swept from 0 mT to 270 mT with 1 mT step. The magnetic field direction was aligned parallel to the transmission line. We calculated the magnitude (absolute value) of the signal abs (S_{21}) and depicted the two-dimensional frequency-field map of the abs (S_{21}) in Figure 4.22(a). However, due to other sources of frequency-dependent signal, the FMR peak is hidden in the background. To suppress the non-related non-magnetic background,

we used the simplest method of dividing the measured transmission by a known reference. As a reference, we have used the median value of the measured signal for every single frequency for all magnetic fields. The processing of the transmission signal successfully uncovered the FMR peak [see Figure 4.22(b)] from the background. Nevertheless, it also uncovered line artifacts.

The line artifacts were removed using a polynomial correction, i.e., each measured line (frequency sweep) is fitted by a first-degree polynomial and subtracted from the line. To ensure that we fit only the non-magnetic background, we apply the mask, removing the data points from the $\pm 1\,\mathrm{GHz}$ window around the FMR resonance peak. The processed data with clearly visible FMR resonance peak is shown in Figure 4.22(c).

Further in the text, we will use ΔS_{21} to denote data processed using the above-described data processing. The division by the reference moves the background to the value of 1, and the polynomial subtraction moves it to zero. The strength of the FMR signal is then denoted by the amplitude of the ΔS_{21} . Even though the signal acquisition time is much shorter, using the ΔS_{21} has no physical meaning. However, since we are interested only in the peak position, and the linewidth, this method is sufficient.

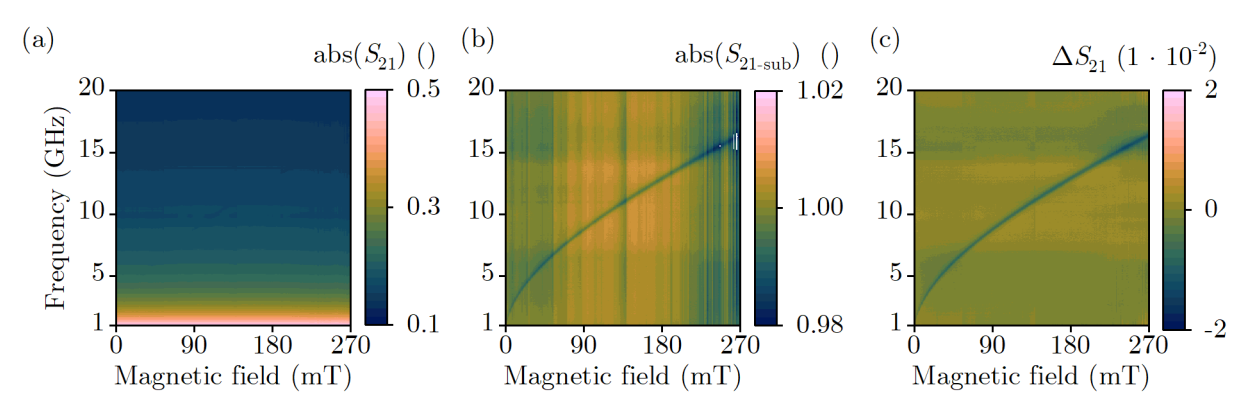


Figure 4.22: Data processing of VNA-FMR experiment. (a) The raw measured magnitude of the transmission parameter $abs(S_{21})$ acquired from 10 nm thick $600 \times 600 \,\mu\text{m}^2$ NiFe pad with lithographically prepared CPW. The excitation frequency was swept from 1 GHz to 20 GHz and external magnetic fields from 0 mT to 270 mT. (b) The result of the simplest data processing method by dividing the median value for every single frequency for all magnetic fields. (c) The line artifacts were removed using a polynomial correction.

The VNA-FMR allows for the characterization of magnetization dynamics and the extraction of the basic material parameters such as saturation magnetization $M_{\rm s}$, gyromagnetic ratio γ or the Gilbert damping α . To extract the saturation magnetization $M_{\rm s}$ and gyromagnetic ratio γ , the peaks corresponding to the FMR were fitted using the Kittel formula

$$f_{\rm FMR} = \frac{\gamma \mu_0}{2\pi} \sqrt{(H_{\rm ext} + H_{\rm ani})(H_{\rm ext} + H_{\rm ani} + M_{\rm s})}$$
 (4.10)

The Kittel formula has been already presented in (1.51) discussed in section 1.5.2. Figure 4.23 shows the extraction of the saturation magnetization $M_{\rm s}$ and gyromagnetic ratio γ from the processed VNA-FMR data from Figure 4.22(c) using Kittel formula (4.10). It is evident from Figure 4.23(c) that the fit is agreeable with the experimental data quite nicely. However, two material constants that are fitted, $M_{\rm s}$ and γ , are highly dependent on each other. When we fixed the saturation magnetization to the value previously measured using VSM (see Figure A.1 in Appendix A), $M_{\rm s} = 830\,{\rm kA/m}$ which is $\mu_0 M_{\rm s} =$

= 1.04 T, the fitted gyromagnetic ratio with the 95% confidence interval was $\gamma/(2\pi)$ = $(28.00 \pm 0.04)\,\mathrm{GHz/T}$. When, on the other hand, we fixed the gyromagnetic ratio on the theoretical value for NiFe $[\gamma/(2\pi) = 29.3\,\mathrm{GHz/T}]$, the fitted saturation magnetization was $M_\mathrm{s} = (724 \pm 2)\,\mathrm{kA/m}$ which is $\mu_0 M_\mathrm{s} = (0.910 \pm 0.003)\,\mathrm{T}$. NiFe used in our study is a metallic ferromagnet, and in metals the g-factor of conduction electrons considerably differs from the free electron value of g = 2 [28, page 314]. Gubbiotti et al. measured for the continuous NiFe films the g-factor (2.14 ± 0.02) [208], which confirms the theoretically predicted higher g-factor for metals. Thus, also the gyromagnetic ratio γ differs from the free electron value of $\gamma/(2\pi) = 28\,\mathrm{GHz/T}$. This value is valid only for magnetic insulators, such as YIG. The anisotropy field H_ani was in both cases fitted as $\mu_0 H_\mathrm{ani} = 1.1\,\mathrm{mT}$ and the fit reproduced the experimental data very well.

The mismatch in the saturation magnetization measurement by VSM and VNA-FMR might be caused by the uncertainty of the thickness of the layer measured by the VSM. In addition, the deposition of samples for the VSM and VNA-FMR occurred at different times. Thus, the quality of the material might be different.

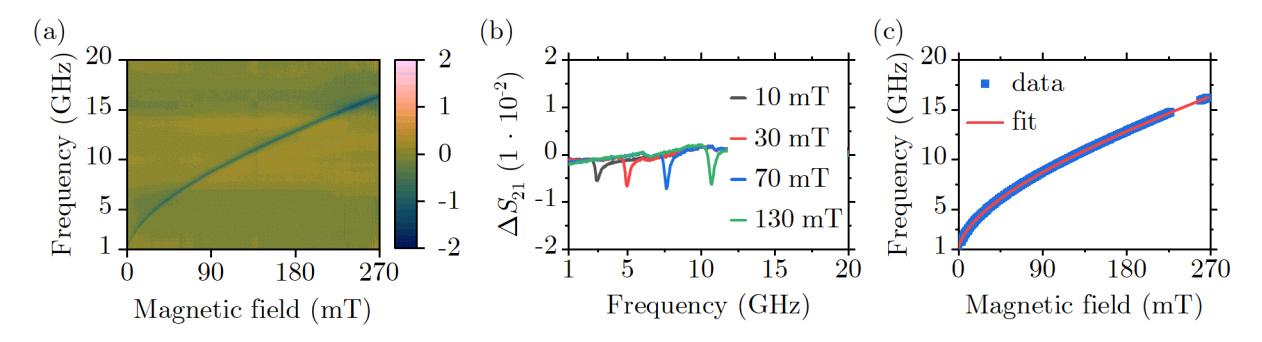


Figure 4.23: (a) VNA-FMR processed data ΔS_{21} of the ferromagnetic resonance for different magnetic fields and different frequencies. The thickness of the NiFe layer was $t = 10 \,\mathrm{nm}$. (b) Representative line scans for magnetic fields $10 \,\mathrm{mT}$, $30 \,\mathrm{mT}$, $70 \,\mathrm{mT}$, and $130 \,\mathrm{mT}$. (c) Resonance frequency peaks for various magnetic fields fitted with Kittel forumula (4.10).

The ferromagnetic resonance linewidth is a measure of the microwave loss properties of the ferromagnetic sample. The Gilbert damping α can be evaluated either from the fitting of the linewidth Δf of the Lorentzian peak which is used to approximate the imaginary part of the dynamic susceptibility, see equation (1.45), or from fitting the broadening of the FMR peak. As we mentioned above, the use of the dynamic susceptibility is time-consuming. Therefore, we used the processed transmission scattering parameter ΔS_{21} versus external magnetic field and fitted the measured curves by the the asymmetric Lorentzian function [209]:

$$\Delta S_{21} = C_{\text{sym}} \frac{\left(\frac{\Delta H}{2}\right)^2}{(H - H_r)^2 + \left(\frac{\Delta H}{2}\right)^2} + C_{\text{asym}} \frac{\left(\frac{\Delta H}{2}\right)(H - H_r)}{(H - H_r)^2 + \left(\frac{\Delta H}{2}\right)^2} + C_0 \tag{4.11}$$

where C_{sym} and C_{asym} are the weighs of the symmetric and asymmetric terms, respectively, and C_0 is the spectrum background. H_r is the resonance magnetic field and ΔH is the full width at half maximum (FWHM). Figure 4.24(a) shows an example Lorentzian fit for the frequency $f = 8.52 \,\text{GHz}$. In section 1.5.2 we have already introduced the extraction of the

Gilbert damping α by fitting the FMR peak broadening. Let us remind ourselves, that the damping parameter is then derived using equation combining the Landau Lifshitz or Gilbert damping model and the inohomogeneous broadening [56]

$$\mu_0 \Delta H = \frac{4\pi \alpha f_{\rm r}}{\gamma} + \mu_0 \Delta H_0 \,, \tag{4.12}$$

where ΔH_0 is aforementioned inhomogeneous broadening representing the extrinsic contributions to the damping. When we plot the fitted linewidth ΔH versus the frequency f, we can derive the Gilbert damping α using the linear fit, see the FMR peak broadening in Figure 4.24(b). The extracted Gilbert damping $\alpha = (8.9 \pm 0.2) \cdot 10^{-3}$ which is well comparable with the values in the literature [6, 56, 210]. The linear fit also yielded a value for the inhomogneous broadening $\mu_0 \Delta H_0 = (0.63 \pm 0.15)$ mT. At this place, it is important to note, that the extracted damping from the VNA-FMR experiment is the total damping α_{total} , which consists of all contributions given in section 1.6.

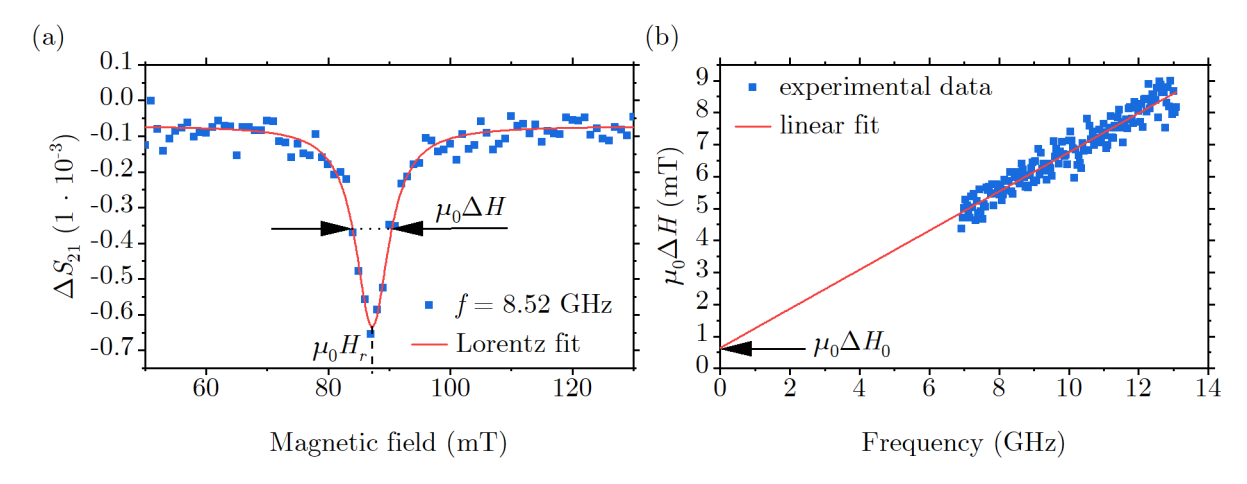


Figure 4.24: (a) The fit of the experimental data using asymmetric Lorentzian function, see equation (4.11). The excitation frequency was $f=8.52\,\mathrm{GHz}$. We extracted the linewidth ΔH and the resonance field H_r . (b) FMR linewidth as a function of frequency for the 10 nm NiFe film. Experimental data points are shown as squares and the solid line is a linear fit using equation (4.12). The extracted Gilbert damping $\alpha=(8.9\pm0.2)\cdot10^{-3}$ and inhomogeneous broadening $\mu_0\Delta H_0=(0.63\pm0.15)\,\mathrm{mT}$.

The ultimate goal of this section is to compare the total damping values extracted from the planar reference magnetic layer and corrugated magnetic layers with different amplitudes of modulation. However, due to the time-consumption of the FEBID process of preparing corrugation, we needed to experimentally check the lowest volume of the magnetic film that can be detected and analyzed using VNA-FMR so that we can limit the time spent during the FEBID process. For that, we fabricated set of 36 pads bellow the excitation antenna ($w_a = 20 \,\mu\text{m}$). We fixed the thickness of the NiFe film to $t = 10 \,\text{nm}$ and varied the width and length of these pads. from $(1 \times 10) \,\mu\text{m}^2$ to $(20 \times 35) \,\mu\text{m}^2$. Figure 4.25 shows measured data for different pad dimensions – (a) $(1 \times 35) \,\mu\text{m}^2$, (b) $(3 \times 35) \,\mu\text{m}^2$, (c) $(10 \times 35) \,\mu\text{m}^2$, (d) $(20 \times 35) \,\mu\text{m}^2$. It is clearly visible that the higher the volume of the magnetic pad, the higher the FMR peak we detect. Therefore, for the fabrication of corrugated pads, we decided on the highest tested magnetic volume in order to have the highest signal.

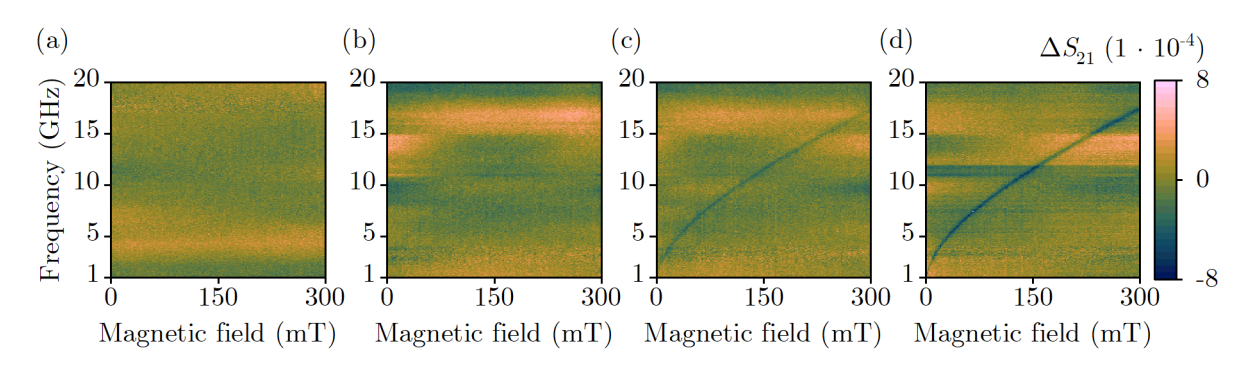


Figure 4.25: The comparison of the signal strength depending on the dimensions of the NiFe pad. The thickness of the NiFe layer was $t=10\,\mathrm{nm}$. The dimensions of the magnetic pads were (a) $(1\times35)\,\mathrm{\mu m^2}$, (b) $(3\times35)\,\mathrm{\mu m^2}$, (c) $(10\times35)\,\mathrm{\mu m^2}$, (d) $(20\times35)\,\mathrm{\mu m^2}$. The data were processed using above described algorithm.

To compare the total damping in planar and corrugated structures, we fabricated a set of 10 corrugated pads and one planar pad below the transmission line of the CPW. In order to detect the FMR peak, the dimensions of the pads were $(30 \times 30) \,\mu\text{m}^2$. The amplitude of modulation ranged from ca. 7 nm to 19 nm and the thickness of the NiFe film was fixed to $t=10\,\text{nm}$. The corrugation direction was parallel to the direction of the transmission line, and the magnetic field was applied perpendicular to the excitation field (parallel to the transmission line) to have the right conditions for the excitation of the FMR. We studied the broadening of the FMR peak using the technique discussed above. However, since the volume of the magnetic material is almost $1000\times$ lower than in the experiment with the $(600\times600)\,\mu\text{m}^2$ NiFe pad, also the detected magnitude of the FMR signal is lower, which makes the data processing and extraction of the linewidth even trickier.

Figure 4.26(a) shows fitted linewidths for one planar and three representative corrugated pads with modulation amplitudes $h_1 = (7.6 \pm 0.7) \,\mathrm{nm}$, $h_2 = (12.3 \pm 1.1) \,\mathrm{nm}$, and $h_3 = (16.6 \pm 0.9) \,\mathrm{nm}$. Due to the low volume of the magnetic material, the signal-to-noise ratio is quite low. We tried to utilize the same script that was used to extract the broadening of the FMR peak in Figure 4.24(b), but it was to no avail. Therefore, we selected some frequencies where we were able to manually fit the broadening of the FMR peak using equation (4.11). The error bars in the linewidth are extracted from 95% confidence intervals of Lorentzian fits. The dashed lines matching the color of the data points are linear fits employing equation (4.12) to extract the total damping α and the inhomogeneous broadening $\mu_0 \Delta H_0$.

When we consult the resonance-frequency dependence of linewidth $\mu_0 \Delta H$ for planar and corrugated pads, we see the difference in slopes and intersections of linear fits with y-axis. The difference in the FMR broadening between the planar (blue circles) and corrugated pad with the lowest modulation amplitude, $h_1 = (7.6 \pm 0.7) \,\text{nm}$ (red squares), is insignificant. The two linear fits almost coincide. The extracted total damping for the planar pad is $\alpha_{\text{planar}} = (10.3 \pm 1.2) \cdot 10^{-3}$ and for the pad with the lowest modulation amplitude $\alpha_1 = (10.6 \pm 2.4) \cdot 10^{-3}$. When we compare it with the damping extracted from Figure 4.24(b), we see that again, the error bars are considerably higher. That is mainly due to the low signal-to-noise ratio caused by the low volume of the magnetic material. The inhomogeneous broadening taken form the intersections with the y-axis is in both cases positive, $\mu_0 \Delta H_{0,\text{planar}} = (0.7 \pm 0.6) \,\text{mT}$, $\mu_0 \Delta H_{0,1} = (0.6 \pm 0.5) \,\text{mT}$. Although the

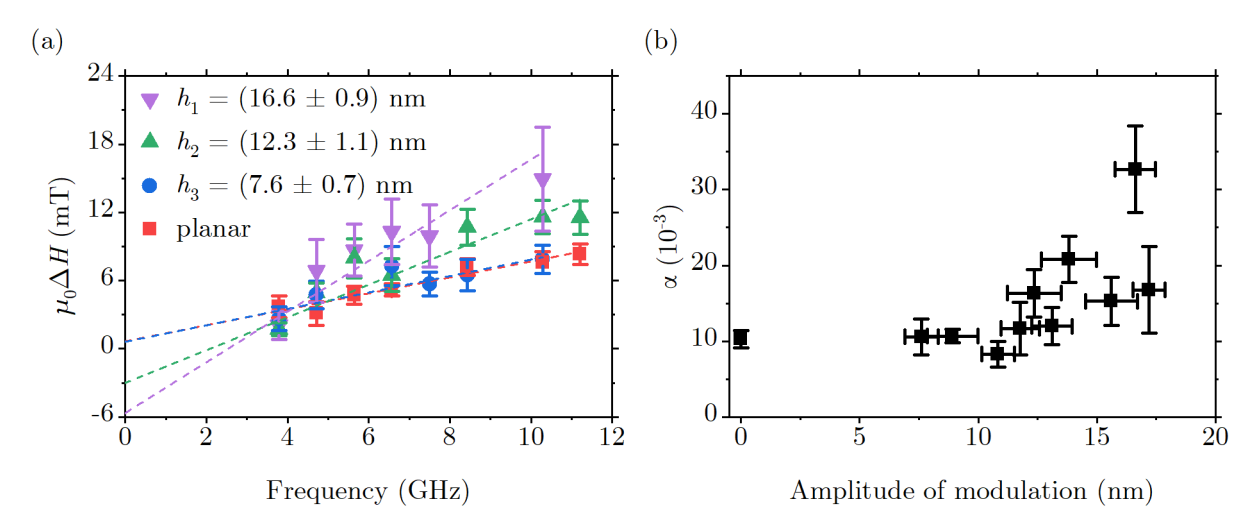


Figure 4.26: (a) Resonance-frequency dependence of the linewidth $\mu_0\Delta H$ for planar and three representative corrugated pads with the modulation amplitudes $h_1=(7.6\pm0.7)\,\mathrm{nm},\ h_2=(12.3\pm1.1)\,\mathrm{nm},\ \mathrm{and}\ h_3=(16.6\pm0.9)\,\mathrm{nm}.$ The datapoints were extracted using the assymetric Lorentzian function (4.11). The dashed lines are linear fits used to extract the total damping α and the inhomogeneous broadening $\mu_0\Delta H_0$. The error bars represent the 95% confidence interval from the fit. The extracted values are: $\alpha_{\mathrm{planar}}=(10.3\pm1.2)\cdot10^{-3},\ \mu_0\Delta H_{0,\mathrm{planar}}=(0.7\pm0.6)\,\mathrm{mT},\ \alpha_1=(10.6\pm2.4)\cdot10^{-3},\ \mu_0\Delta H_{0,1}=(0.6\pm0.5)\,\mathrm{mT},\ \alpha_2=(21\pm3)\cdot10^{-3},\ \mu_0\Delta H_{0,2}=(-3.0\pm1.2)\,\mathrm{mT},\ \mathrm{and}\ \alpha_3=(33\pm6)\cdot10^{-3},\ \mu_0\Delta H_{0,3}=(-6.0\pm2)\,\mathrm{mT}.$ (b) The dependence of the total damping on the amplitude of modulation for one planar and 10 corrugated $30\times30\,\mu\mathrm{m}^2$ pads.

error bars are huge, it suggests that other contributions to the damping (see section 1.6) are for these two pads of little importance.

However, with the increasing modulation amplitude, the difference between the planar and corrugated pads becomes substantial. The extracted total damping from the FMR broadening for the corrugated pad with the modulation amplitude of $h_2 = (12.3 \pm 1.1)$ nm (green triangles pointing up) is $\alpha_2 = (21 \pm 3) \cdot 10^{-3}$ and for the corrugated pad with modulation amplitude $h_3 = (16.6 \pm 0.9)$ nm (purple triangles pointing down), $\alpha_3 = (33 \pm 6) \cdot 10^{-3}$. When we look at the intersections with the y-axis, we see that with increasing modulation amplitude, the inhomogeneous broadening is more negative. For the corrugated pad with the modulation amplitude h_2 we found the intersection at $\mu_0 \Delta H_{0,2} = (-3.0 \pm 1.2)$ mT, and for the corrugated pad with the highest modulation amplitude h_3 , we extracted the inhomogeneous broadening as $\mu_0 \Delta H_{0,3} = (-6.0 \pm 2)$ mT.

If we would consider only intrinsic damping, the inhomogeneous broadening should always be positive. The negativity of the inhomogeneous broadening indicates that there are other extrinsic contributors to the total damping, mainly the two magnon scattering connected with the structure defects, surface roughness, and in our case, for the most part, with the corrugation. However, our experimental setup is not equipped with an out-of-plane magnetic field. Hence, we could not eliminate the two magnon scattering contribution.

When we look at Figure 4.26(b), we see the dependence of the total damping on the modulation amplitude. It shows results for one planar and ten corrugated pads. Even though the error bars are high, the trend is quite clear. With increasing modulation amplitude, the total damping extracted from the VNA-FMR experiment is also increasing.

Overall, the method of extracting the total damping from VNA-FMR data is not ideal for our samples. Due to the low magnetic volume, the signal-to-noise ratio is also low, and the data processing and fitting get cunninger than when processing large pads. The human error brought to the data processing is non-negligible, and the fitting must be handled cautiously. Nevertheless, when we compare the results measured by BLS and VNA-FMR, we see a similar trend.

Let us remind ourselves of the connection between the damping and the spin-wave propagation length. From equations (1.73),(1.74) we concluded, that propagation length $\Lambda \propto \alpha^{-1}$. The propagation length Λ also depends on the group velocity $v_{\rm g}$. Václav Roučka did a micromagnetic simulation study of the FMR and spin-wave propagation in flat and corrugated magnetic structures in his master's thesis [197]. He concluded that for the higher wave vectors, the dispersion relations of a corrugated structure are slightly different from a flat reference dispersion relation (see Fig. 4.6 on page 53 in [197]). However, with both BLS and VNA, the experimentally accessible range is minimal, and the group velocity of spin waves in a corrugated waveguide and a flat reference waveguide would not change.

Therefore, our focus is mainly on comparing the spin-wave propagation length depending on the modulation amplitude of corrugated waveguides measured by the BLS and the total damping depending on the modulation amplitude of corrugated structures measured by VNA. When we plot these two dependencies next to each other, see Figure 4.27, we can see a similar trend. Figure 4.27(a) shows the spin-wave propagation length already depicted in Figure 4.21. We can observe that for the corrugated structures with the modulation amplitude below 8 nm, the propagation length is in the range of 1.8 to 2.2 µm which is similar to the spin-wave propagation length in planar structures. Furthermore, when we look at Figure 4.27(b), we see the dependence of α^{-1} on the modulation amplitude. Here we notice that for modulation amplitudes below 8 nm the damping $\alpha \approx 10^{-2}$ which is also similar to the damping in planar structures. With increasing modulation amplitude, the propagation length Λ is decreasing, and similarly, the total damping α is increasing (α^{-1} is decreasing). When we compare it with the analytical calculation of the spin-wave propagation length in the Damon-Eshbach geometry dependent on the damping parameter α [see Figure 1.17(b)], we see a comparable result. With increasing damping parameter α , the spin-wave propagation length is decreasing.

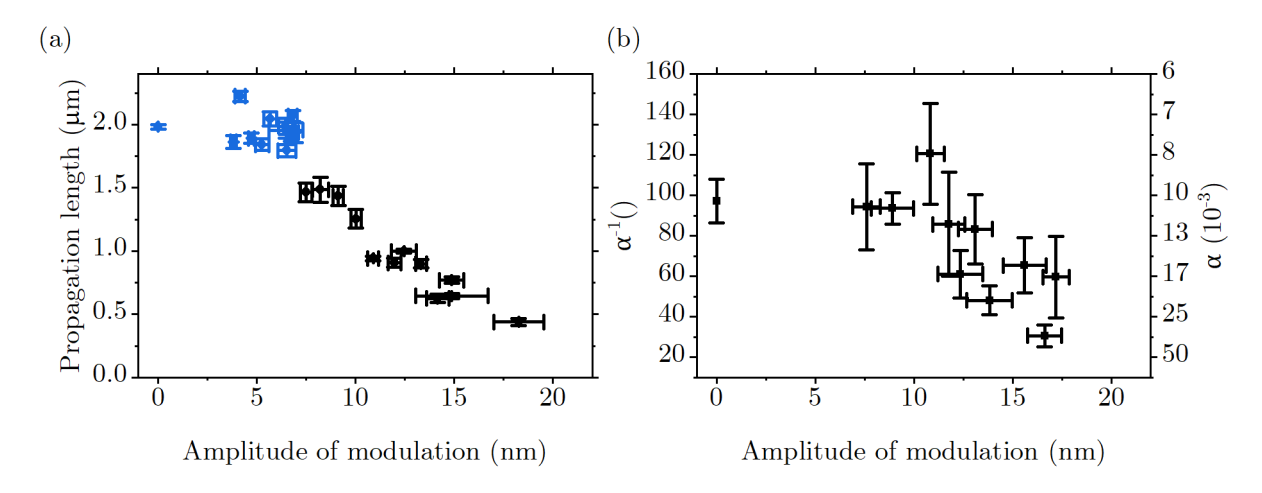


Figure 4.27: The comparison of (a) the BLS measurement of the spin-wave propagation length in corrugated waveguides and (b) the VNA-FMR measurement extracting the total damping from corrugated pads.

4.4. FERROMAGNETIC RESONANCE OF CORRUGATED STRUCTURES

In conclusion, we have used the VNA-FMR method to study the dependence of total damping on the modulation amplitude of corrugated magnetic structures. First, we discussed the necessity of data processing to remove the non-magnetic background. Besides, we have analyzed the signal strength depending on the area of the magnetic layer below the transmission line. We used that knowledge to effectively prepare a set of 10 corrugated pads to study the broadening of the FMR peak and extract the total damping parameter α . We compared it to the planar reference and concluded that the total damping also increases with increasing modulation amplitude. Furthermore, we noted a similar trend in the BLS measurement of the spin-wave propagation length in corrugated waveguides. We compared it with the corresponding analytical calculations and found the same trend. Therefore, the increase of the total damping parameter α due to the higher modulation amplitude (higher than 8 nm) of corrugated structures leads to the decrease of the propagation length measured in magnonic waveguides by BLS.

Conclusion

This thesis aimed to study magnetism in curved geometries. In the first part, we focused on the fabrication of curved geometries. We addressed the modulation of the substrate's surface before the deposition of the magnetic material. Such modification imprints the topography to the magnetic material deposited on top of it. We started with the focused ion beam milling and used it for modifying the substrate's surface. However, the mechanism of changing the ion dose per area was not sufficient to precisely control the parameters of the modulation, i.e., the amplitude and period of modulation. Hence, we focused on the different technique and modified the substrate's topography using the focused electron beam-induced deposition. We have proven that control over the modulation parameters is much better using FEBID. By pushing the scanning electron microscope to its limits, we have found that the modulation period can be tuned down to 40 nm while preserving the sinusoidal shape of the modulation. Using atomic force microscopy, we analyzed the relation of the modulation amplitude and the number of e-beam scans per line and shown that it is linearly dependent. Ultimately, we concluded that the FEBID technique offers many possibilities for the design of complex magnetic structures by modulating the substrate before the deposition of the magnetic material.

After successfully finished with the preparation of magnetic structures with curved geometries, we have experimentally tested the magnetization reversal processes and quantified the induced magnetic anisotropy depending on the corrugation parameters (modulation amplitude & period) using the experimental method of Kerr microscopy. Through a series of experiments, we have found that depending on the orientation of the external magnetic field with respect to the corrugation direction, the hysteresis loop shape changes. When we measured hysteresis loops for the external field parallel to the corrugation direction, we saw that this direction could be considered an easy magnetic axis. Correspondingly, when the external magnetic field was parallel to the corrugation direction, measured hysteresis loops showed features typical for the hard axis direction. Besides, we have quantitatively correlated the corrugation-induced uniaxial magnetic anisotropy with the corrugation parameters. With increasing modulation amplitude, the corrugationinduced anisotropy strength is also increasing. On the other hand, the increase of the corrugation periodicity is reflected in the decrease of corrugation-induced anisotropy. The main missing point of the presented work is the lack of the micromagnetic simulations that would convincingly support our experimental findings. However, the micromagnetic simulations explaining the origin of the corrugation-induced anisotropy using the dipolar and exchange energy densities for different magnetization orientations are very well summarized in the master's thesis of Václav Roučka [197].

Furthermore, we designed and experimentally tested a system for the study of spinwave propagation in corrugated magnonic waveguides. They were grown on modulated surfaces prepared by focused electron beam-induced deposition and electron beam lithography. We have proven that the magnonic waveguides with the corrugation-induced

uniaxial magnetic anisotropy can be locally placed anywhere on the sample. Additionally, we fabricated magnonic waveguides with an aspect ratio of 1:10 and utilized corrugationinduced anisotropy to overcome the shape anisotropy. The resulting effective, easy axis was, contradictory to the shape anisotropy, perpendicular to the long edge of a rectangular waveguide. The fabrication of an excitation antenna on the prepared magnonic waveguides helped us to study the spin-wave propagation. The corrugation-induced uniaxial magnetic anisotropy has been shown to be useful in the study of propagating spin waves without the presence of external magnetic fields. As the spin-wave propagation strongly depends on the angle between k-vector and magnetization, without the external magnetic field, spin waves propagate over a distance $10 \times$ larger in corrugated magnonic waveguides than in planar waveguides. Also, when the external magnetic field is applied to the planar magnonic waveguide to match the local effective magnetic field of the corrugated waveguide provided by the corrugation-induced anisotropy, the spin waves propagate with the same efficiency and the propagation length is comparable. We studied and analyzed the influence of the modulation amplitude on the spin-wave propagation and were able to conclude that for moderate modulation amplitudes (below 8 nm), the spin-wave propagation length is not affected. However, for larger modulation amplitudes, the propagation length decreases linearly with increasing amplitude of modulation. Using the phase-resolved BLS microscopy we confirmed that the spin-wave propagation length measured for magnonic waveguides with different modulation amplitude is evaluated for the same k-vector.

In the final part of the thesis, we used the VNA-FMR method to compare the total damping in the planar and corrugated magnetic structures. We struggled with the data processing to remove non-magnetic background due to the low volume of magnetic structures, but we managed to analyze dependence of the signal strength on the area of the magnetic layer below the transmission line. Gaining from that knowledge, we studied the broadening of the FMR peak and extracted to total damping parameter α . We correlated the measurement of the planar reference with the corrugated structures and confirmed previous allegations that the total damping increases with increasing modulation amplitude. Ultimately, we compared the BLS measurement of the spin-wave propagation length in the corrugated waveguides with the total damping measurements and with corresponding analytical calculations. All three dependencies showed the same trend. Therefore, the decrease of the propagation length measured by BLS for the waveguides with larger modulation amplitude is associated to the increase of the total damping parameter α measured by VNA-FMR.

Our pioneering experiments with the local control of the magnetization direction without applying external magnetic field are a big step forward toward the realization of complex magnonic circuits. Mainly due to the possibility of the zero external magnetic field propagation of spin waves in magnonic waveguides Damon-Eshbach mode. Until now, this has been possible only by expoliting structural phase transformation [182], or a direct current flowing through a gold wire underneath the magnonic waveguide [211]. In the future, this approach of modifying substrate's topography before the deposition of any magnetic material can be scaled up via, e.g. nanoimprint lithography [206]. The results of the thesis can serve as a starting point for more detailed study of the corrugation-induced effects on the spin-wave properties.

References

- 1. Lojek, B. *History of Semiconductor Engineering* 387. ISBN: 9783540342588. doi:10.1007/978-3-540-34258-8 (Springer Berlin Heidelberg, 2007) (cit. on p. 1).
- 2. Waldrop, M. M. The chips are down for Moore's law. *Nat. News* **530**, 144. doi:10 .1038/530144a (2016) (cit. on p. 1).
- 3. Mamaluy, D. & Gao, X. The fundamental downscaling limit of field effect transistors. *Appl. Phys. Lett.* **106**, 193503. doi:10.1063/1.4919871 (2015) (cit. on p. 1).
- 4. IEEE. International roadmap for devices and systems [online]. [Accessed on 2021-07-26]. https://irds.ieee.org (2020) (cit. on p. 1).
- 5. Kruglyak, V. V., Demokritov, S. O. & Grundler, D. Magnonics. *J. Phys. D: Appl. Phys.* **43**, 264001. doi:10.1088/0022-3727/43/26/264001 (2010) (cit. on p. 1).
- Chumak, A. V., Serga, A. A. & Hillebrands, B. Magnonic crystals for data processing. J. Phys. D: Appl. Phys. 50, 244001. doi:10.1088/1361-6463/aa6a65 (2017) (cit. on pp. 1, 26, 27, 90).
- 7. Chumak, A. V., Vasyuchka, V. I., Serga, A. A. & Hillebrands, B. Magnon spintronics. *Nat. Phys.* **11**, 453–461. doi:10.1038/nphys3347 (2015) (cit. on p. 1).
- 8. Sander, D., Valenzuela, S. O., Makarov, D., Marrows, C. H., Fullerton, E. E., Fischer, P., McCord, J., Vavassori, P., Mangin, S., Pirro, P., Hillebrands, B., Kent, A. D., Jungwirth, T., Gutfleisch, O., Kim, C. G. & Berger, A. The 2017 Magnetism Roadmap. J. Phys. D: Appl. Phys. 50, 363001. doi:10.1088/1361-6463/aa81a1 (2017) (cit. on p. 1).
- 9. Csaba, G., Papp, Å. & Porod, W. Perspectives of using spin waves for computing and signal processing. *Phys. Lett. A* **381**, 1471–1476. doi:10.1016/j.physleta.2017.02.042 (2017) (cit. on p. 1).
- 10. Wang, Q., Kewenig, M., Schneider, M., Verba, R., Kohl, F., Heinz, B., Geilen, M., Mohseni, M., Lägel, B., Ciubotaru, F., et al. A magnonic directional coupler for integrated magnonic half-adders. *Nat. Electron.* 3, 765–774 (2020) (cit. on p. 1).
- 11. Chumak, A. V., Serga, A. A. & Hillebrands, B. Magnon transistor for all-magnon data processing. *Nat. Commun* 5, 1–8. doi:10.1038/ncomms5700 (2014) (cit. on p. 1).
- 12. Topp, J., Heitmann, D., Kostylev, M. P. & Grundler, D. Making a Reconfigurable Artificial Crystal by Ordering Bistable Magnetic Nanowires. *Phys. Rev. Lett.* **104**, 207205. doi:10.1103/PhysRevLett.104.207205 (2010) (cit. on p. 1).

- 13. Fischer, T., Kewenig, M., Bozhko, D. A., Serga, A. A., Syvorotka, I. I., Ciubotaru, F., Adelmann, C., Hillebrands, B. & Chumak, A. V. Experimental prototype of a spin-wave majority gate. *Appl. Phys. Lett.* **110**, 152401. doi:10.1063/1.4979840 (2017) (cit. on p. 1).
- 14. Chen, K., Frömter, R., Rössler, S., Mikuszeit, N. & Oepen, H. P. Uniaxial magnetic anisotropy of cobalt films deposited on sputtered MgO(001) substrates. *Phys. Rev. B* 86, 064432. doi:10.1103/PhysRevB.86.064432 (2012) (cit. on pp. 1, 2, 62, 77).
- 15. Streubel, R., Fischer, P., Kronast, F., Kravchuk, V. P., Sheka, D. D., Gaididei, Y., Schmidt, O. G. & Makarov, D. Magnetism in curved geometries. *J. Phys. D: Appl. Phys.* 49, 363001. doi:10.1088/0022-3727/49/36/363001 (2016) (cit. on pp. 1, 10, 62).
- Tretiakov, O. A., Morini, M., Vasylkevych, S. & Slastikov, V. Engineering Curvature-Induced Anisotropy in Thin Ferromagnetic Films. *Phys. Rev. Lett.* 119, 077203. doi:10.1103/PhysRevLett.119.077203 (2017) (cit. on pp. 2, 11, 62).
- 17. Körner, M., Lenz, K., Gallardo, R. A., Fritzsche, M., Mücklich, A., Facsko, S., Lindner, J., Landeros, P. & Fassbender, J. Two-magnon scattering in permalloy thin films due to rippled substrates. *Phys. Rev. B* 88, 054405. doi:10.1103/Phys RevB.88.054405 (2013) (cit. on pp. 2, 21, 62).
- 18. Feng, W., Jiang, N.-Y., Huang, S.-D., Chen, H.-M., Cheng, C.-W., Chern, G. & Yu, C.-C. External forces are indispensable for the occurrence of exchange bias? *J. Appl. Phys.* **111**, 033904. doi:10.1063/1.3681174 (2012) (cit. on pp. 2, 62).
- 19. Ki, S. & Dho, J. Strong uniaxial magnetic anisotropy in triangular wave-like ferromagnetic NiFe thin films. *Appl. Phys. Lett.* **106**, 212404. doi:10.1063/1.4921784 (2015) (cit. on pp. 2, 62).
- 20. Kim, S. N., Nam, Y. J., Kim, Y. D., Choi, J. W., Lee, H. & Lim, S. H. Formation of Magnetic Anisotropy by Lithography. *Sci. Rep* 6, 1–6. doi:10.1038/srep26709 (2016) (cit. on pp. 2, 62).
- 21. Chikazumi, S. Study of Magnetic Annealing on Ni₃Fe Single Crystal. *J. Phys. Soc. Jpn.* **11**, 551. doi:10.1143/JPSJ.11.551 (1956) (cit. on pp. 2, 62).
- 22. Takahashi, M. Induced magnetic anisotropy of evaporated films formed in a magnetic field. J. Appl. Phys. 33, 1101. doi:10.1063/1.1728618 (1962) (cit. on pp. 2, 62).
- 23. Fernández-Pacheco, A., Skoric, L., De Teresa, J. M., Pablo-Navarro, J., Huth, M. & Dobrovolskiy, O. V. Writing 3D Nanomagnets Using Focused Electron Beams. *Mater.* 13, 3774. doi:10.3390/ma13173774 (2020) (cit. on pp. 2, 33).
- 24. Al Mamoori, M. K. I., Keller, L., Pieper, J., Barth, S., Winkler, R., Plank, H., Müller, J. & Huth, M. Magnetic characterization of direct-write free-form building blocks for artificial magnetic 3D lattices. *Mater.* 11, 289. doi:10.3390/ma11020289 (2018) (cit. on pp. 2, 33).
- 25. Vaz, C. A. F., Steinmuller, S. J. & Bland, J. A. C. Roughness-induced variation of magnetic anisotropy in ultrathin epitaxial films: The undulating limit. *Phys. Rev. B* **75**, 132402. doi:10.1103/PhysRevB.75.132402 (2007) (cit. on p. 2).

- 26. Skoric, L., Sanz-Hernández, D., Meng, F., Donnelly, C., Merino-Aceituno, S. & Fernández-Pacheco, A. Layer-by-Layer Growth of Complex-Shaped Three-Dimensional Nanostructures with Focused Electron Beams. *Nano Lett.* **20**, 184–191. doi:10.1021/acs.nanolett.9b03565 (2020) (cit. on p. 2).
- 27. Magén, C., Pablo-Navarro, J. & De Teresa, J. M. Focused-Electron-Beam Engineering of 3D Magnetic Nanowires. *Nanomaterials* **11.** doi:10.3390/nano1102040 **2** (2021) (cit. on p. 2).
- 28. Coey, J. M. D. Magnetism and Magnetic Materials 614. ISBN: 978-0-511-67743-4 (Cambridge University Press, Cambridge, 2010) (cit. on pp. 4, 7, 14, 89).
- 29. Krishnan, K. Fundamentals and Applications of Magnetic Materials ISBN: 978–0–19–957044–7. doi:10.1093/acprof:oso/9780199570447.001.0001 (Oxford University Press, Oxford, 2016) (cit. on pp. 4, 7, 12).
- 30. Kittel, C. Introduction to solid state physics 8th ed., 688. ISBN: 978-0471415268 (Wiley, Hoboken, NJ, 2005) (cit. on p. 4).
- 31. Aharoni, A. Introduction to the Theory of Ferromagnetism 2nd ed., 303. ISBN: 978-0-19-850809-0. doi:10.1063/1.881916 (Oxford University Press, Oxford, 2007) (cit. on p. 4).
- 32. Blundell, S. Magnetism in Condensed Matter 256. ISBN: 9780198505914 (Oxford University Press, Oxford, 2001) (cit. on p. 4).
- 33. Stöhr, J. & Siegmann, H. C. *Magnetism: From fundamentals to nanoscale dynamics* 822. ISBN: 978-3-540-30283-4. doi:10.1007/978-3-540-30283-4 (Springer, Berlin, 2006) (cit. on pp. 4, 14).
- 34. Hillebrands, B. & Ounadjela, K. Spin Dynamics in Confined Magnetic Structures I 340. ISBN: 978-3-540-41191-8. doi:10.1007/3-540-40907-6 (Springer, New York, 2001) (cit. on p. 4).
- 35. Stancil, D. B. & Prabhakar, A. Spin Waves: Theory and Applications 348. ISBN: 9780387778648. doi:10.1007/978-0-387-77865-5 (Springer, New York, 2009) (cit. on pp. 4, 23, 26, 27).
- 36. Demokritov, S. O. & Slavin, A. N. Magnonics (eds Demokritov, S. O. & Slavin, A. N.) ISBN: 978-3-642-30246-6. doi:10 . 1007 / 978 3 642 30247 3 (Springer, Berlin, Heidelberg, 2013) (cit. on p. 4).
- 37. Hubert, A. & Schäfer, R. *Magnetic Domains: The Analysis of Magnetic Microstructures* 696. ISBN: 978-3-540-64108-7. doi:10.1007/978-3-540-85054-0 (Springer, New York, 2009) (cit. on p. 5).
- 38. Goldfarb, R. B. The permeability of vacuum and the revised International System of Units. *IEEE Magn. Lett* 8, 1110003. doi:10.1109/LMAG.2017.2777782 (2017) (cit. on p. 6).
- 39. Landau, L. & Lifshitz, E. in *Perspectives in Theoretical Physics* (ed Pitaevski, L.) 51–65 (Pergamon, Amsterdam, 1992). ISBN: 978-0-08-036364-6. doi:10.1016/B978 -0-08-036364-6.50008-9 (cit. on p. 7).
- 40. Aharoni, A. Demagnetizing factors for rectangular ferromagnetic prisms. *J. Appl. Phys.* **83**, 3432–3434. doi:10.1063/1.367113 (1998) (cit. on p. 9).

- 41. Sheka, D. D., Kravchuk, V. P., Yershov, K. V. & Gaididei, Y. Torsion-induced effects in magnetic nanowires. *Phys. Rev. B* **92**, 054417. doi:10.1103/PhysRevB.9 2.054417 (2015) (cit. on p. 10).
- 42. Pylypovskyi, O. V., Sheka, D. D., Kravchuk, V. P., Yershov, K. V., Makarov, D. & Gaididei, Y. Rashba torque driven domain wall motion in magnetic helices. *Sci. Rep* **6**, 23316. doi:10.1038/srep23316 (2016) (cit. on p. 10).
- 43. Bruno, P. Dipolar magnetic surface anisotropy in ferromagnetic thin films with interfacial roughness. *J. Appl. Phys.* **64**, 3153–3156. doi:10.1063/1.341530 (1988) (cit. on p. 10).
- 44. Arias, R. & Mills, D. L. Theory of roughness-induced anisotropy in ferromagnetic films: The dipolar mechanism. *Phys. Rev. B* **59**, 11871–11881. doi:10.1103/Phys RevB.59.11871 (1999) (cit. on p. 10).
- 45. Gaididei, Y., Kravchuk, V. P. & Sheka, D. D. Curvature Effects in Thin Magnetic Shells. *Phys. Rev. Lett.* **112**, 257203. doi:10.1103/PhysRevLett.112.257203 (2014) (cit. on p. 10).
- 46. Gaididei, Y., Goussev, A., Kravchuk, V. P., Pylypovskyi, O. V., Robbins, J. M., Sheka, D. D., Slastikov, V. & Vasylkevych, S. Magnetization in narrow ribbons: curvature effects. *J. Phys. A Math. Theor.* **50**, 385401. doi:10.1088/1751-8121/a a8179 (2017) (cit. on p. 10).
- 47. Bisio, F., Moroni, R., Buatier de Mongeot, F., Canepa, M. & Mattera, L. Isolating the Step Contribution to the Uniaxial Magnetic Anisotropy in Nanostructured Fe/Ag(001) Films. *Phys. Rev. Lett.* **96**, 057204. doi:10.1103/PhysRevLett.96.057204 (2006) (cit. on p. 10).
- 48. Liedke, M. O., Körner, M., Lenz, K., Grossmann, F., Facsko, S. & Fassbender, J. Magnetic anisotropy engineering: Single-crystalline Fe films on ion eroded ripple surfaces. *Appl. Phys. Lett.* **100**, 242405. doi:10.1063/1.4729151 (2012) (cit. on p. 11).
- 49. Vayalil, S. K., Koorikkat, A., Gopi, A. K., Roth, S. V. & Kumar, P. S. A. Tailoring of uniaxial magnetic anisotropy in Permalloy thin films using nanorippled Si substrates. *J. Phys.: Condens. Matter* **32**, 185804. doi:10.1088/1361-648X/ab6d0d (2020) (cit. on p. 11).
- 50. Stoner, E. C. & Wohlfarth, E. P. A mechanism of magnetic hysteresis in heterogeneous alloys. *Philos. Trans. Royal Soc. A* **240**, 599–642. doi:10.1098/rsta.1948.0007 (1948) (cit. on p. 13).
- 51. Tannous, C. & Gieraltowski, J. The Stoner-Wohlfarth model of ferromagnetism. *Eur. J. Phys.* **29**, 475. doi:10.1088/0143-0807/29/3/008 (2008) (cit. on p. 13).
- 52. Skomski, R. *Simple Models of Magnetism* ISBN: 9780198570752. doi:10.1093/acpr of:oso/9780198570752.001.0001 (OUP Oxford, 2008) (cit. on p. 13).
- 53. Landau, L. D. & Lifshitz, E. M. On the theory of the Dispersion of Magnetic Permeability in Ferromagnetic Bodies. *Phys. Z. Sowjetunion* 8, 101–114. doi:10.1016/B978-0-08-036364-6.50008-9 (1935) (cit. on p. 14).
- 54. Gilbert, T. A phenomenological theory of damping in ferromagnetic materials. *IEEE Trans. Magn.* **40**, 3443–3449. doi:10.1109/TMAG.2004.836740 (2004) (cit. on p. 15).

- 55. Polder, D. On the Quantum Theory of Ferromagnetic Resonance. *Phys. Rev.* **73**, 1116–1116. doi:10.1103/PhysRev.73.1116 (1948) (cit. on p. 16).
- Kalarickal, S. S., Krivosik, P., Wu, M., Patton, C. E., Schneider, M. L., Kabos, P., Silva, T. J. & Nibarger, J. P. Ferromagnetic resonance linewidth in metallic thin films: Comparison of measurement methods. *J. Appl. Phys.* 99, 093909. doi:10.1063/1.2197087 (2006) (cit. on pp. 18, 28, 90).
- 57. Gurevich, A. G. & Melkov, G. A. Magnetization Oscillations and Waves ISBN: 9780849394607 (Taylor & Francis, 1996) (cit. on pp. 19, 20).
- 58. Flajšman, L. Magneto-optical study of the dynamic properties of magnetic nanostructures and nanostructured metamaterials Supervised by Michal Urbánek. PhD thesis (Brno University of Technology, Brno, 2019), 152 (cit. on pp. 19, 29, 48, 51, 79).
- 59. Stancil, D. Theory of Magnetostatic Waves ISBN: 9780387979694 (Springer-Verlag, 1993) (cit. on p. 20).
- 60. Azzawi, S., Hindmarch, A. T. & Atkinson, D. Magnetic damping phenomena in ferromagnetic thin-films and multilayers. *J. Phys. D: Appl. Phys.* **50**, 473001. doi:10.1088/1361-6463/aa8dad (2017) (cit. on p. 20).
- 61. Prange, R. E. & Korenman, V. Line width of ferromagnetic resonance in metals. J. Magn. Reson. (1969) 6, 274–280. doi:10.1016/0022-2364(72)90100-X (1972) (cit. on p. 21).
- 62. McMichael, R. D. & Krivosik, P. Classical model of extrinsic ferromagnetic resonance linewidth in ultrathin films. *IEEE Trans. Magn.* **40**, 2–11. doi:10.1109/TMAG.2003.821564 (2004) (cit. on p. 21).
- 63. Hickey, M. C. & Moodera, J. S. Origin of Intrinsic Gilbert Damping. *Phys. Rev. Lett.* **102**, 137601. doi:10.1103/PhysRevLett.102.137601 (2009) (cit. on p. 21).
- 64. Kamberský, V. On ferromagnetic resonance damping in metals. *Czech. J. Phys. B* **26**, 1366–1383. doi:10.1007/BF01587621 (1976) (cit. on p. 21).
- 65. Kuneš, J. & Kamberský, V. First-principles investigation of the damping of fast magnetization precession in ferromagnetic 3d metals. *Phys. Rev. B* **65**, 212411. doi:10.1103/PhysRevB.65.212411 (2002) (cit. on p. 21).
- 66. Kamberský, V. Spin-orbital Gilbert damping in common magnetic metals. *Phys. Rev. B* **76**, 134416. doi:10.1103/PhysRevB.76.134416 (2007) (cit. on p. 21).
- 67. Safonov, V. L. & Bertram, H. N. Impurity relaxation mechanism for dynamic magnetization reversal in a single domain grain. *Phys. Rev. B* **61**, R14893–R14896. doi:10.1103/PhysRevB.61.R14893 (2000) (cit. on p. 21).
- 68. Silberglitt, R. Effect of Spin Waves on the Phonon Energy Spectrum of a Heisenberg Ferromagnet. *Phys. Rev.* **188**, 786–792. doi:10.1103/PhysRev.188.786 (1969) (cit. on p. 21).
- 69. Berger, L. Effect of interfaces on Gilbert damping and ferromagnetic resonance linewidth in magnetic multilayers. *J. Appl. Phys.* **90**, 4632–4638. doi:10.1063/1.1 405824 (2001) (cit. on p. 21).
- 70. Berger, L. Emission of spin waves by a magnetic multilayer traversed by a current. *Phys. Rev. B* **54**, 9353–9358. doi:10.1103/PhysRevB.54.9353 (1996) (cit. on p. 21).

- 71. Barsukov, I., Landeros, P., Meckenstock, R., Lindner, J., Spoddig, D., Li, Z.-A., Krumme, B., Wende, H., Mills, D. L. & Farle, M. Tuning magnetic relaxation by oblique deposition. *Phys. Rev. B* 85, 014420. doi:10.1103/PhysRevB.85.014420 (2012) (cit. on p. 21).
- 72. Kalarickal, S. S., Krivosik, P., Das, J., Kim, K. S. & Patton, C. E. Microwave damping in polycrystalline Fe-Ti-N films: Physical mechanisms and correlations with composition and structure. *Phys. Rev. B* 77, 054427. doi:10.1103/PhysRev B.77.054427 (2008) (cit. on p. 21).
- 73. Mo, N., Hohlfeld, J., ul Islam, M., Brown, C. S., Girt, E., Krivosik, P., Tong, W., Rebei, A. & Patton, C. E. Origins of the damping in perpendicular media: Three component ferromagnetic resonance linewidth in Co–Cr–Pt alloy films. *Appl. Phys. Lett.* **92**, 022506. doi:10.1063/1.2834835 (2008) (cit. on p. 21).
- 74. Liu, X., Zhang, W., Carter, M. J. & Xiao, G. Ferromagnetic resonance and damping properties of CoFeB thin films as free layers in MgO-based magnetic tunnel junctions. *J. Appl. Phys.* **110**, 033910. doi:10.1063/1.3615961 (2011) (cit. on pp. 21, 22, 28).
- 75. Lindner, J., Barsukov, I., Raeder, C., Hassel, C., Posth, O., Meckenstock, R., Landeros, P. & Mills, D. L. Two-magnon damping in thin films in case of canted magnetization: Theory versus experiment. *Phys. Rev. B* **80**, 224421. doi:10.1103/PhysRevB.80.224421 (2009) (cit. on p. 21).
- 76. Kurebayashi, H., Skinner, T. D., Khazen, K., Olejník, K., Fang, D., Ciccarelli, C., Campion, R. P., Gallagher, B. L., Fleet, L., Hirohata, A. & Ferguson, A. J. Uniaxial anisotropy of two-magnon scattering in an ultrathin epitaxial Fe layer on GaAs. *Appl. Phys. Lett.* **102**, 062415. doi:10.1063/1.4792269 (2013) (cit. on p. 21).
- 77. Lock, J. M. Eddy current damping in thin metallic ferromagnetic films. *Br. J. Appl. Phys.* 17, 1645–1647. doi:10.1088/0508-3443/17/12/415 (1966) (cit. on p. 21).
- 78. Pincus, P. Excitation of Spin Waves in Ferromagnets: Eddy Current and Boundary Condition Effects. *Phys. Rev.* **118**, 658–664. doi:10.1103/PhysRev.118.658 (1960) (cit. on p. 21).
- 79. Bilzer, C. Microwave susceptibility of thin ferromagnetic films: metrology and insight into magnetization dynamics PhD thesis (Université Paris Sud Paris XI, Paris, 2007) (cit. on pp. 21, 55, 58).
- 80. Schoen, M. A. W., Shaw, J. M., Nembach, H. T., Weiler, M. & Silva, T. J. Radiative damping in waveguide-based ferromagnetic resonance measured via analysis of perpendicular standing spin waves in sputtered permalloy films. *Phys. Rev. B* **92**, 184417. doi:10.1103/PhysRevB.92.184417 (2015) (cit. on p. 22).
- 81. Li, Y. & Bailey, W. E. Wave-Number-Dependent Gilbert Damping in Metallic Ferromagnets. *Phys. Rev. Lett.* **116**, 117602. doi:10.1103/PhysRevLett.116.117602 (2016) (cit. on p. 22).
- 82. Schoen, M. A. W., Thonig, D., Schneider, M. L., Silva, T. J., Nembach, H. T., Eriksson, O., Karis, O. & Shaw, J. M. Ultra-low magnetic damping of a metallic ferromagnet. *Nat. Phys.* 12, 839–842. doi:10.1038/nphys3770 (2016) (cit. on pp. 22, 28).

- 83. Tserkovnyak, Y., Brataas, A. & Bauer, G. E. W. Enhanced Gilbert Damping in Thin Ferromagnetic Films. *Phys. Rev. Lett.* **88**, 117601. doi:10.1103/PhysRevLet t.88.117601 (2002) (cit. on p. 22).
- 84. Kumar, A., Pan, F., Husain, S., Akansel, S., Brucas, R., Bergqvist, L., Chaudhary, S. & Svedlindh, P. Temperature-dependent Gilbert damping of Co₂FeAl thin films with different degree of atomic order. *Phys. Rev. B* **96**, 224425. doi:10.1103/Phys RevB.96.224425 (2017) (cit. on p. 22).
- 85. Karenowska, A. D., Chumak, A. V., Serga, A. A. & Hillebrands, B. in *Handbook of Spintronics* (eds Xu, Y., Awschalom, D. & Nitta, J.) 1505–1549 (Springer Netherlands, 2016). ISBN: 9789400768932. doi:10.1007/978-94-007-6892-5_53 (cit. on p. 22).
- 86. Walker, L. R. Magnetostatic modes in ferromagnetic resonance. *Phys. Rev* **105**, 390. doi:10.1103/PhysRev.105.390 (1957) (cit. on pp. 22, 28).
- 87. Damon, R. W. & Eshbach, J. R. Magnetostatic modes of a ferromagnetic slab. *J. Appl. Phys.* **31**, S104–S105. doi:10.1063/1.1984622 (1960) (cit. on pp. 23, 31).
- 88. Walker, L. R. Resonant modes of ferromagnetic spheroids. *J. Appl. Phys.* **29**, 318–323. doi:10.1063/1.1723117 (1958) (cit. on p. 23).
- 89. Herring, C. & Kittel, C. On the theory of spin waves in ferromagnetic media. *Phys. Rev.* **81**, 869–880. doi:10.1103/PhysRev.81.869 (1951) (cit. on p. 24).
- 90. Kalinikos, B. A. & Slavin, A. N. Theory of dipole-exchange spin wave spectrum for ferromagnetic films with mixed exchange boundary conditions. *J. Phys. C: Solid State Phys.* **19**, 7013. doi:10.1088/0022-3719/19/35/014 (1986) (cit. on pp. 24, 25).
- 91. Wojewoda, O. *Phase-resolved Brillouin light scattering: development and applications* Supervised by Michal Urbánek. Master's thesis (Faculty of Mechanical Engineering Brno University of Technology, Brno, 2020), 66 (cit. on pp. 25, 28, 48, 51, 52, 54, 84).
- 92. Vaňatka, M. Static and dynamic properties of nanostructured magnetic materials Supervised by Michal Urbánek. PhD thesis (CEITEC Brno University of Technology, Brno, 2020), 113 (cit. on pp. 25, 47, 58, 59).
- 93. Vaňatka, M., Szulc, K., Wojewoda, O., Dubs, C., Chumak, A. V., Krawczyk, M., Dobrovolskiy, O. V., Kłos, J. W. & Urbánek, M. Spin-Wave Dispersion Measurement by Variable-Gap Propagating Spin-Wave Spectroscopy. *Phys. Rev. Applied* 16, 054033. doi:10.1103/PhysRevApplied.16.054033 (5 2021) (cit. on p. 25).
- 94. Chumak, A. V. in *Spintronics Handbook: Spin Transport and Magnetism, Second Edition* (eds Tsymbal, E. Y. & Žutić, I.) 247–302 (CRC Press, 2019). ISBN: 9781498769525. doi:10.1201/9780429423079-6 (cit. on pp. 27, 28).
- 95. Conca, A., Greser, J., Sebastian, T., Klingler, S., Obry, B., Leven, B. & Hillebrands, B. Low spin-wave damping in amorphous Co₄₀Fe₄₀B₂₀ thin films. *J. Appl. Phys.* **113**, 213909. doi:10.1063/1.4808462 (2013) (cit. on pp. 27, 28).
- 96. Mahmoud, A., Ciubotaru, F., Vanderveken, F., Chumak, A. V., Hamdioui, S., Adelmann, C. & Cotofana, S. Introduction to spin wave computing. *J. Appl. Phys.* **128**, 161101. doi:10.1063/5.0019328 (2020) (cit. on p. 28).

- 97. Aus, M. J., Cheung, C., Szpunar, B., Erb, U. & Szpunar, J. Saturation magnetization of porosity-free nanocrystalline cobalt. *J. Mater. Sci. Lett.* 17, 1949–1952. doi:10.1023/A:1006620812602 (1998) (cit. on p. 28).
- 98. Vernon, S. P., Lindsay, S. M. & Stearns, M. B. Brillouin scattering from thermal magnons in a thin Co film. *Phys. Rev. B* **29**, 4439. doi:10.1103/PhysRevB.29.4439 (1984) (cit. on p. 28).
- 99. Michels, A., Weissmüller, J., Wiedenmann, A., Pedersen, J. S. & Barker, J. G. Measuring the exchange-stiffness constant of nanocrystalline solids by elastic small-angle neutron scattering. *Philos. Mag. Lett.* **80**, 785–792. doi:10.1080/095008300 1000180S (2000) (cit. on p. 28).
- 100. Heinrich, B., Cochran, J. F., Kowalewski, M., Kirschner, J., Celinski, Z., Arrott, A. S. & Myrtle, K. Magnetic anisotropies and exchange coupling in ultrathin fcc Co(001) structures. *Phys. Rev. B* 44, 9348. doi:10.1103/PhysRevB.44.9348 (1991) (cit. on p. 28).
- 101. Brunsch, A. Magnetic properties and corrosion resistance of $(CoFeB)_{100-x}Cr_x$ thin films. J. Appl. Phys. **50**, 7603–7605. doi:10.1063/1.326858 (1979) (cit. on p. 28).
- 102. Danan, H., Herr, A. & Meyer, A. J. P. New determinations of the saturation magnetization of nickel and iron. *J. Appl. Phys.* **39**, 669–670. doi:10.1063/1.2163571 (1968) (cit. on p. 28).
- 103. Kim, Y. K. & Oliveria, M. Magnetic properties of sputtered Fe thin films: Processing and thickness dependence. J. Appl. Phys. 74, 1233–1241. doi:10.1063/1.354926 (1993) (cit. on p. 28).
- 104. Kin, M., Kura, H., Tanaka, M., Hayashi, Y., Hasaegawa, J. & Ogawa, T. Improvement of saturation magnetization of Fe nanoparticles by post-annealing in a hydrogen gas atmosphere. *J. Appl. Phys.* **117**, 17E714. doi:10.1063/1.4919050 (2015) (cit. on p. 28).
- 105. Vavassori, P., Bisero, D., Carace, F., di Bona, A., Gazzadi, G. C., Liberati, M. & Valeri, S. Interplay between magnetocrystalline and configurational anisotropies in Fe(001) square nanostructures. *Phys. Rev. B* 72, 054405. doi:10.1103/PhysRevB.72.054405 (2005) (cit. on p. 28).
- 106. Bishop, J. The shape, energy, eddy current loss, and relaxation damping of magnetic domain walls in glassy iron wire. *IEEE Trans. Magn.* **13**, 1638–1645. doi:10.1109/TMAG.1977.1059649 (1977) (cit. on p. 28).
- 107. Demidov, V. E. & Demokritov, S. O. Magnonic waveguides studied by microfocus Brillouin light scattering. *IEEE Trans. Magn.* **51**, 1–15. doi:10.1109/TMAG.2014.2388196 (2015) (cit. on p. 28).
- 108. Sebastian, T., Schultheiss, K., Obry, B., Hillebrands, B. & Schultheiss, H. Microfocused Brillouin light scattering: imaging spin waves at the nanoscale. *Front. Phys.* 3, 35. doi:10.3389/fphy.2015.00035 (2015) (cit. on pp. 28, 48, 51).
- 109. Serga, A. A., Chumak, A. V. & Hillebrands, B. YIG magnonics. *J. Phys. D: Appl. Phys.* **43**, 264002. doi:10.1088/0022-3727/43/26/264002 (2010) (cit. on p. 28).
- 110. Cherepanov, V., Kolokolov, I. & L'vov, V. The saga of YIG: spectra, thermodynamics, interaction and relaxation of magnons in a complex magnet. *Phys. Rep.* **229**, 81–144. doi:10.1016/0370-1573(93)90107-0 (1993) (cit. on p. 28).

- 111. Glass, H. L. Ferrite films for microwave and millimeter-wave devices. *Proc. IEEE* **76**, 151–158. doi:10.1109/5.4391 (1988) (cit. on p. 28).
- 112. Wadsley, A. D. Crystal chemistry of non-stoichiometric pentavalent vandadium oxides: crystal structure of Li1+ xV3O8. *Acta Crystallogr.* **10**, 261–267. doi:10.11 07/S0365110X57000729 (1957) (cit. on p. 28).
- 113. Klingler, S., Chumak, A. V., Mewes, T., Khodadadi, B., Mewes, C., Dubs, C., Surzhenko, O., Hillebrands, B. & Conca, A. Measurements of the exchange stiffness of YIG films using broadband ferromagnetic resonance techniques. *J. Phys. D: Appl. Phys.* 48, 015001. doi:10.1088/0022-3727/48/1/015001 (2014) (cit. on p. 28).
- 114. Pirro, P., Brächer, T., Chumak, A. V., Lägel, B., Dubs, C., Surzhenko, O., Görnert, P., Leven, B. & Hillebrands, B. Spin-wave excitation and propagation in microstructured waveguides of yttrium iron garnet/Pt bilayers. *Appl. Phys. Lett.* **104**, 012402. doi:10.1063/1.4861343 (2014) (cit. on p. 28).
- 115. Hahn, C., Naletov, V. V., De Loubens, G., Klein, O., d'Allivy Kelly, O., Anane, A., Bernard, R., Jacquet, E., Bortolotti, P., Cros, V., Prieto, J. L. & Muñoz, M. Measurement of the intrinsic damping constant in individual nanodisks of Y₃Fe₅O₁₂ and Y₃Fe₅O₁₂|Pt. Appl. Phys. Lett. **104**, 152410. doi:10.1063/1.4871516 (2014) (cit. on p. 28).
- 116. Dubs, C., Surzhenko, O., Linke, R., Danilewsky, A., Brückner, U. & Dellith, J. Sub-micrometer yttrium iron garnet LPE films with low ferromagnetic resonance losses. J. Phys. D: Appl. Phys. 50, 204005. doi:10.1088/1361-6463/aa6b1c (2017) (cit. on p. 28).
- 117. Sun, Y., Song, Y.-Y., Chang, H., Kabatek, M., Jantz, M., Schneider, W., Wu, M., Schultheiss, H. & Hoffmann, A. Growth and ferromagnetic resonance properties of nanometer-thick yttrium iron garnet films. *Appl. Phys. Lett.* **101**, 152405. doi:10.1063/1.4759039 (2012) (cit. on p. 28).
- 118. Yu, H., d'Allivy Kelly, O., Cros, V., Bernard, R., Bortolotti, P., Anane, A., Brandl, F., Huber, R., Stasinopoulos, I. & Grundler, D. Magnetic thin-film insulator with ultra-low spin wave damping for coherent nanomagnonics. *Sci. Rep* 4, 1–5. doi:10.1038/srep06848 (2014) (cit. on p. 28).
- 119. Onbasli, M. C., Kehlberger, A., Kim, D. H., Jakob, G., Kläui, M., Chumak, A. V., Hillebrands, B. & Ross, C. A. Pulsed laser deposition of epitaxial yttrium iron garnet films with low Gilbert damping and bulk-like magnetization. *APL Mater.* 2, 106102. doi:10.1063/1.4896936 (2014) (cit. on p. 28).
- 120. Liu, T., Chang, H., Vlaminck, V., Sun, Y., Kabatek, M., Hoffmann, A., Deng, L. & Wu, M. Ferromagnetic resonance of sputtered yttrium iron garnet nanometer films. J. Appl. Phys. 115, 17A501. doi:10.1063/1.4852135 (2014) (cit. on p. 28).
- 121. Glass, H. & Elliot, M. Attainment of the intrinsic FMR linewidth in yttrium iron garnet films grown by liquid phase epitaxy. *J. Crys. Growth* **34**, 285–288. doi:10.1 016/0022-0248(76)90141-X (1976) (cit. on p. 28).
- 122. Schmidt, G., Hauser, C., Trempler, P., Paleschke, M. & Papaioannou, E. T. Ultra Thin Films of Yttrium Iron Garnet with Very Low Damping: A Review. *Phys. Status Solidi B* **257**, 1900644. doi:10.1002/pssb.201900644 (2020) (cit. on p. 28).
- 123. Joseph, R. I. & Schlömann, E. Demagnetizing field in nonellipsoidal bodies. *J. Appl. Phys.* **36**, 1579–1593. doi:10.1063/1.1703091 (1965) (cit. on p. 28).

- 124. Kittel, C. On the theory of ferromagnetic resonance absorption. *Phys. Rev* **73**, 155–161. doi:10.1103/PhysRev.73.155 (1948) (cit. on p. 28).
- 125. Jorzick, J., Demokritov, S. O., Hillebrands, B., Bailleul, M., Fermon, C., Guslienko, K. Y., Slavin, A. N., Berkov, D. V. & Gorn, N. L. Spin wave wells in nonellipsoidal micrometer size magnetic elements. *Phys. Rev. Lett.* 88, 047204. doi:10.1103/PhysRevLett.88.047204 (2002) (cit. on p. 28).
- 126. Guslienko, K. Y., Demokritov, S., Hillebrands, B. & Slavin, A. Effective dipolar boundary conditions for dynamic magnetization in thin magnetic stripes. *Phys. Rev. B* **66**, 132402. doi:10.1103/PhysRevB.66.132402 (2002) (cit. on pp. 28, 31).
- 127. Guslienko, K. Y., Chantrell, R. W. & Slavin, A. N. Dipolar localization of quantized spin-wave modes in thin rectangular magnetic elements. *Phys. Rev. B* **68**, 024422. doi:10.1103/PhysRevB.68.024422 (2003) (cit. on p. 29).
- 128. Arias, R. E. Spin-wave modes of ferromagnetic films. *Phys. Rev. B* **94**, 134408. doi:10.1103/PhysRevB.94.134408 (2016) (cit. on p. 31).
- 129. Guslienko, K. Y. & Slavin, A. N. Boundary conditions for magnetization in magnetic nanoelements. *Phys. Rev. B* **72**, 014463. doi:10.1103/PhysRevB.72.014463 (2005) (cit. on p. 31).
- 130. Wang, Q., Heinz, B., Verba, R., Kewenig, M., Pirro, P., Schneider, M., Meyer, T., Lägel, B., Dubs, C., Brächer, T. & Chumak, A. V. Spin Pinning and Spin-Wave Dispersion in Nanoscopic Ferromagnetic Waveguides. *Phys. Rev. Lett.* **122**, 247202 doi:10.1103/PhysRevLett.122.247202 (2019) (cit. on p. 31).
- 131. Randolph, S. J., Fowlkes, J. D. & Rack, P. D. Focused, Nanoscale Electron-Beam-Induced Deposition and Etching. *Crit. Rev. Solid State Mater. Sci.* **31**, 55–89. doi:10.1080/10408430600930438 (2006) (cit. on pp. 33, 34).
- 132. Utke, I., Hoffmann, P. & Melngailis, J. Gas-assisted focused electron beam and ion beam processing and fabrication. *J. Vac. Sci. Technol. B* **26**, 1197–1276. doi:10.1 116/1.2955728 (2008) (cit. on p. 33).
- 133. Fernandez-Pacheco, A., Streubel, R., Fruchart, O., Hertel, R., Fischer, P. & Cowburn, R. P. Three-dimensional nanomagnetism. *Nat. Commun* 8, 15756. doi:10.1038/ncomms15756 (2017) (cit. on p. 33).
- 134. Huth, M., Porrati, F., Schwalb, C., Winhold, M., Sachser, R., Dukic, M., Adams, J. & Fantner, G. Focused electron beam induced deposition: A perspective. *Beilstein J. Nanotechnol.* 3, 597–619. doi:10.3762/bjnano.3.70 (2012) (cit. on p. 33).
- 135. Stewart, R. L. Insulating Films Formed Under Electron and Ion Bombardment. *Phys. Rev.* 45, 488–490. doi:10.1103/PhysRev.45.488 (1934) (cit. on p. 33).
- 136. Christy, R. W. Formation of thin polymer films by electron bombardment. *J. Appl. Phys.* **31**, 1680–1683. doi:10.1063/1.1735915 (1960) (cit. on p. 34).
- 137. Baker, A. G. & Morris, W. C. Deposition of metallic films by electron impact decomposition of organometallic vapors. *Rev. Sci. Instrum.* **32**, 458–458. doi:10.1 063/1.1717408 (1961) (cit. on p. 34).
- 138. Van Dorp, W. F. & Hagen, C. W. A critical literature review of focused electron beam induced deposition. *J. Appl. Phys.* **104**, 10. doi:10.1063/1.2977587 (2008) (cit. on p. 34).

- 139. Nanofabrication Using Focused Ion and Electron Beams: Principles and Applications (eds Utke, I., Moshkalev, S. & Russell, P.) 410–435. ISBN: 9780199734214 (Oxford University Press, New York, 2012) (cit. on pp. 35, 37).
- 140. Reimer, L. Scanning Electron Microscopy: Physics of Image Formation and Microanalysis ISBN: 9783540639763. doi:10.1007/978-3-540-3896 (Springer-Verlag Berlin Heidelberg, 1998) (cit. on p. 35).
- 141. Fowlkes, J. D., Randolph, S. J. & Rack, P. D. Growth and simulation of high-aspect ratio nanopillars by primary and secondary electron-induced deposition. *J. Vac. Sci. Technol. B* 23, 2825–2832. doi:10.1116/1.2101732 (2005) (cit. on p. 36).
- 142. Crozier, P. A., Tolle, J., Kouvetakis, J. & Ritter, C. Synthesis of uniform GaN quantum dot arrays via electron nanolithography of D₂GaN₃. Appl. Phys. Lett. 84, 3441–3443. doi:10.1063/1.1736314 (2004) (cit. on p. 36).
- 143. Silvis-Cividjian, N., Hagen, C. W., Kruit, P., v.d. Stam, M. A. J. & Groen, H. B. Direct fabrication of nanowires in an electron microscope. *Appl. Phys. Lett.* 82, 3514–3516. doi:10.1063/1.1575506 (2003) (cit. on p. 36).
- 144. Rauscher, H., Behrendt, F. & Behm, R. J. Fabrication of surface nanostructures by scanning tunneling microscope induced decomposition of SiH₄ and SiH₂Cl₂. J. Vac. Sci. Technol. B **15**, 1373–1377. doi:10.1116/1.589541 (1997) (cit. on p. 36).
- 145. Gatzen, H. H., Saile, V. & Leuthold, J. *Micro and Nano Fabrication* 1–32. ISBN: 978-3-662-44394-1. doi:10.1007/978-3-662-44395-8 (Springer Berlin Heidelberg, Berlin, Heidelberg, 2015) (cit. on p. 37).
- 146. Eaton, P. & West, P. *Atomic Force Microscopy* 256. ISBN: 9780191576676 (Oxford University Press, 2010) (cit. on p. 41).
- 147. Olympus. *OMCL-AC240TS* [online]. [Accessed on 2019-07-24]. http://probe.olympus-global.com/en/product/omcl_ac240ts_r3/ (2019) (cit. on p. 42).
- 148. Bruker. ScanAsyst Chip [online]. [Accessed on 2021-01-21]. https://www.brukerafmprobes.com/p-3726-scanasyst-air.aspx (2020) (cit. on p. 42).
- 149. Bruker. ScanAsyst Mode [online]. [Accesed on 2021-01-18]. https://www.bruker.com/products/surface-and-dimensional-analysis/atomic-force-microscopes/modes/modes/imaging-modes/peakforce-tapping/overview.html (2020) (cit. on p. 42).
- 150. Faraday, M. I. Experimental researches in electricity.—Nineteenth series. *Phil. Trans. R. Soc.* 1–20. doi:10.1098/rstl.1846.0001 (1846) (cit. on p. 43).
- 151. Weinberger, P. John Kerr and his effects found in 1877 and 1878. *Philos. Mag. Lett* **88**, 897–907. doi:10.1080/09500830802526604 (2008) (cit. on p. 43).
- 152. Voigt, W. in *Handbuch der Elektrizität und des Magnetismus* (ed Graetz, L.) 667–710 (A. Barth, 1920) (cit. on p. 43).
- 153. McCord, J. Progress in magnetic domain observation by advanced magneto-optical microscopy. *J. Phys. D: Appl. Phys.* **48**, 333001. doi:10.1088/0022-3727/48/33/33001 (2015) (cit. on pp. 43, 45).
- 154. Schäfer, R. in Handbook of Magnetism and Advanced Magnetic Materials (eds Kronmüller, H. & Parkin, S.) 1505–1549 (American Cancer Society, 2007). ISBN: 9780470022184. doi:10.1002/9780470022184.hmm310 (cit. on pp. 43, 46).

- 155. Protopopov, V. in *Practical Opto-Electronics* (ed Protopopov, V.) 231–252 (Springer Switzerland, 2014). ISBN: 9783319045139. doi:10.1007/978-3-319-04513-9_8 (cit. on p. 43).
- 156. Flajšman, L. Vectorial Kerr magnetometry Supervised by Michal Urbánek. Master's thesis (Faculty of Mechanical Engineering Brno University of Technology, 2015), 99 (cit. on p. 44).
- 157. Zak, J., Moog, E., Liu, C. & Bader, S. Universal approach to magneto-optics. *J. Magn. Magn. Mater.* **89**, 107–123. doi:10.1016/0304-8853(90)90713-Z (1990) (cit. on p. 44).
- 158. Jackson, J. D. *Classical Electrodynamics* 3rd ed., 832. ISBN: 9780471309321 (Wiley, Hoboken, NJ, 1998) (cit. on p. 45).
- 159. Vlaminck, V. & Bailleul, M. Spin-wave transduction at the submicrometer scale: Experiment and modeling. *Phys. Rev. B* 81, 014425. doi:10.1103/PhysRevB.81.0 14425 (2010) (cit. on p. 47).
- 160. Davídková, K. Excitation of exchange spin waves using microwave nano antennas Supervised by Michal Urbánek. Bachelor's thesis (Faculty of Mechanical Engineering Brno University of Technology, Brno, 2021) (cit. on p. 47).
- 161. Lucassen, J., Schippers, C. F., Rutten, L., Duine, R. A., Swagten, H. J. M., Koopmans, B. & Lavrijsen, R. Optimizing propagating spin wave spectroscopy. *Appl. Phys. Lett.* **115**, 012403. doi:10.1063/1.5090892 (2019) (cit. on p. 47).
- 162. Bang, W., Jungfleisch, M. B., Lim, J., Trossman, J., Tsai, C. C., Hoffmann, A. & Ketterson, J. B. Excitation of the three principal spin waves in yttrium iron garnet using a wavelength-specific multi-element antenna. *AIP Adv.* 8, 056015. doi:10.1063/1.5007101 (2018) (cit. on p. 47).
- 163. Schneider, T., Serga, A. A., Neumann, T., Hillebrands, B. & Kostylev, M. P. Phase reciprocity of spin-wave excitation by a microstrip antenna. *Phys. Rev. B* 77, 214411. doi:10.1103/PhysRevB.77.214411 (2008) (cit. on pp. 48, 53).
- 164. Sekiguchi, K., Yamada, K., Seo, S. M., Lee, K. J., Chiba, D., Kobayashi, K. & Ono, T. Nonreciprocal emission of spin-wave packet in FeNi film. Appl. Phys. Lett. 97, 022508. doi:10.1063/1.3464569 (2010) (cit. on p. 48).
- 165. Kostylev, M. P., Gubbiotti, G., Hu, J.-G., Carlotti, G., Ono, T. & Stamps, R. L. Dipole-exchange propagating spin-wave modes in metallic ferromagnetic stripes. *Phys. Rev. B* **76**, 054422. doi:10.1103/PhysRevB.76.054422 (2007) (cit. on p. 48).
- 166. Kostylev, M. Non-reciprocity of dipole-exchange spin waves in thin ferromagnetic films. J. Appl. Phys. 113, 053907. doi:10.1063/1.4789962 (2013) (cit. on p. 48).
- 167. Zhu, Y. Modern techniques for characterizing magnetic materials 1–600. ISBN: 1402080077. doi:10.1007/b101202 (2005) (cit. on p. 48).
- 168. Ibach, H. & Lüth, H. Solid-State Physics: An Introduction to Principles of Materials Science ISBN: 9783540938040. doi:10.1007/978-3-540-93804-0 (Springer Berlin Heidelberg, 2009) (cit. on p. 49).
- 169. Lindsay, S. M., Anderson, M. W. & Sandercock, J. R. Construction and alignment of a high performance multipass vernier tandem Fabry–Perot interferometer. *Rev. Sci. Instrum.* **52**, 1478–1486. doi:10.1063/1.1136479 (1981) (cit. on p. 50).

- 170. Sandercock, J. R. Brillouin scattering study of SbSI using a double-passed, stabilised scanning interferometer. *Opt. Commun.* 2, 73–76. doi:10.1016/0030-4018 (70)90047-7 (1970) (cit. on p. 50).
- 171. Hillebrands, B. Progress in multipass tandem Fabry-Perot interferometry: I. A fully automated, easy to use, self-aligning spectrometer with increased stability and flexibility. *Rev. Sci. Instrum.* **70**, 1589–1598. doi:10.1063/1.1149637 (1999) (cit. on p. 52).
- 172. Serga, A. A., Schneider, T., Hillebrands, B., Demokritov, S. O. & Kostylev, M. P. Phase-sensitive Brillouin light scattering spectroscopy from spin-wave packets. *Appl. Phys. Lett.* **89**, 063506. doi:10.1063/1.2335627 (2006) (cit. on p. 53).
- 173. Pozar, D. *Microwave Engineering* 4th ed. ISBN: 978-0-470-63155-3 (Wiley, Hoboken, NJ, 2011) (cit. on pp. 55–57).
- 174. Wilson, P. *The Circuit Designer's Companion* 3rd. ISBN: 978-0-08-097138-4. doi:1 0.1016/B978-0-08-097138-4.02002-4 (Newnes, USA, 2012) (cit. on p. 57).
- 175. Hiebel, M. Fundamentals of Vector Network Analysis ISBN: 9783939837060 (Rohde & Schwarz, 2016) (cit. on p. 57).
- 176. HUBER+SUHNER. RF Coaxial connectors [online]. [Accessed on 2021-03-03]. https://literature.hubersuhner.com/Technologies/Radiofrequency/RFConnectorsEN (2021) (cit. on p. 59).
- 177. Flajšman, L. Nanomagnetism and Spintronics Group [discussion]. [Happened on 2021-02-26]. https://www.aalto.fi/en/department-of-applied-physics/nanomagnetism-and-spintronics-nanospin (2021) (cit. on p. 58).
- 178. GGB Industries. *Picprobe microwave probe* [online]. [Accessed on 2021-02-26]. https://ggb.com/home/model-40a/ (2021) (cit. on pp. 59, 79).
- 179. MPI. MPI TS200 Probe Station [online]. [Accessed on 2021-03-07]. https://www.mpi-corporation.com/ast/engineering-probe-systems/mpi-manual-probe-systems/mpi-ts150-ts200-ts300/ (2021) (cit. on p. 60).
- 180. Roučka, V. Design of the device for magnetodynamic characterization of magnetic materials and nanostructures Supervised by Igor Turčan. Bachelor's thesis (Faculty of Mechanical Engineering Brno University of Technology, Brno, 2019), 50 (cit. on pp. 60, 87).
- 181. Urbánek, M., Flajšman, L., Křižáková, V., Gloss, J., Horký, M., Schmid, M. & Varga, P. Research Update: Focused ion beam direct writing of magnetic patterns with controlled structural and magnetic properties. *APL Mater.* **6**, 060701. doi:10.1063/1.5029367 (2018) (cit. on p. 62).
- 182. Flajšman, L., Wagner, K., Vaňatka, M., Gloss, J., Křižáková, V., Schmid, M., Schultheiss, H. & Urbánek, M. Zero-field propagation of spin waves in waveguides prepared by focused ion beam direct writing. *Phys. Rev. B* **101**, 014436. doi:10.1 103/PhysRevB.101.014436 (2020) (cit. on pp. 62, 96).
- 183. Nord, M., Semisalova, A., Kákay, A., Hlawacek, G., MacLaren, I., Liersch, V., Volkov, O. M., Makarov, D., Paterson, G. W., Potzger, K., et al. Strain anisotropy and magnetic domains in embedded nanomagnets. Small 15, 1904738. doi:10.100 2/smll.201904738 (2019) (cit. on p. 62).

- 184. Arranz, M. A., Colino, J. M. & Palomares, F. J. On the limits of uniaxial magnetic anisotropy tuning by a ripple surface pattern. *J. Appl. Phys.* **115.** doi:10.1063/1.4876232 (2014) (cit. on p. 63).
- 185. Mollick, S. A., Singh, R., Kumar, M., Bhattacharyya, S. & Som, T. Strong uniaxial magnetic anisotropy in Co films on highly ordered grating-like nanopatterned Ge surfaces. *Nanotechnology* **29**, 125302. doi:10.1088/1361-6528/aaaa74 (2018) (cit. on p. 63).
- 186. Xia, D., Jiang, Y.-B., Notte, J. & Runt, D. GaAs milling with neon focused ion beam: Comparison with gallium focused ion beam milling and subsurface damage analysis. *Appl. Surf. Sci.* **538**, 147922. doi:10.1016/j.apsusc.2020.147922 (2021) (cit. on p. 63).
- 187. Wei, Q., Lian, J., Lu, W. & Wang, L. Highly Ordered Ga Nanodroplets on a GaAs Surface Formed by a Focused Ion Beam. *Phys. Rev. Lett.* **100**, 076103. doi:10.110
 3/PhysRevLett.100.076103 (2008) (cit. on p. 63).
- 188. Grossklaus, K. A. & Millunchick, J. M. Mechanisms of nanodot formation under focused ion beam irradiation in compound semiconductors. *J. Appl. Phys.* **109**, 014319. doi:10.1063/1.3530839 (2011) (cit. on p. 63).
- 189. Kang, M. & Goldman, R. S. Ion irradiation of III–V semiconductor surfaces: From self-assembled nanostructures to plasmonic crystals. *Appl. Phys. Rev.* **6**, 041307. doi:10.1063/1.5079908 (2019) (cit. on p. 63).
- 190. Gubbioti, G. Three-Dimensional Magnonics: Layered, Micro-and Nanostructures ISBN: 9789814800730 (Jenny Stanford Publishing, 2019) (cit. on p. 66).
- 191. Sakharov, V. K., Beginin, E. N., Khivintsev, Y. V., Sadovnikov, A. V., Stognij, A. I., Filimonov, Y. A. & Nikitov, S. A. Spin waves in meander shaped YIG film: Toward 3D magnonics. *Appl. Phys. Lett.* 117, 022403. doi:10.1063/5.0013150 (2020) (cit. on p. 66).
- 192. Barman, A., Gubbiotti, G., Ladak, S., Adeyeye, A. O., Krawczyk, M., Gräfe, J., Adelmann, C., Cotofana, S., Naeemi, A., Vasyuchka, V. I., Hillebrands, B., Nikitov, S. A., Yu, H., Grundler, D., Sadovnikov, A. V., Grachev, A. A., Sheshukova, S. E., Duquesne, J.-Y., Marangolo, M., Csaba, G., Porod, W., Demidov, V. E., Urazhdin, S., Demokritov, S. O., Albisetti, E., Petti, D., Bertacco, R., Schultheiss, H., Kruglyak, V. V., Poimanov, V. D., Sahoo, S., Sinha, J., Yang, H., Münzenberg, M., Moriyama, T., Mizukami, S., Landeros, P., Gallardo, R. A., Carlotti, G., Kim, J.-V., Stamps, R. L., Camley, R. E., Rana, B., Otani, Y., Yu, W., Yu, T., Bauer, G. E. W., Back, C., Uhrig, G. S., Dobrovolskiy, O. V., Budinska, B., Qin, H., van Dijken, S., Chumak, A. V., Khitun, A., Nikonov, D. E., Young, I. A., Zingsem, B. W. & Winklhofer, M. The 2021 Magnonics Roadmap. J. Phys. Condens. Matter 33, 413001. doi:10.1088/1361-648x/abec1a (2021) (cit. on p. 66).
- 193. Šamořil, T. Application of the focused ion and electron beam in nanotechnologies Supervised by prof. Tomáš Šikola. PhD thesis (Brno University of Technology, Brno, 2015), 126 (cit. on p. 66).
- 194. Vyroubal, O. Deposition of magnetic nanostructures using ebid and optimalization of their chemical composition and morphology Supervised by Miroslav Kolíbal. Master's thesis (Vysoké učení technické v Brně, 2016), 54 (cit. on p. 66).

- 195. Sigma-Aldrich. 2,4,6,8,10-Pentamethylcyclopentasiloxane [online]. [Accessed on 2021-06-08]. https://www.sigmaaldrich.com/CZ/en/product/aldrich/517801 (2021) (cit. on p. 66).
- 196. Read, D. T. & Dally, J. W. Theory of electron beam moiré. *Journal of research of the National Institute of Standards and Technology* **101**, 47. doi:10.6028/jres.10 1.007 (1996) (cit. on p. 72).
- 197. Roučka, V. Spin wave propagation in structures with locally modified magnetic anisotropy Supervised by Michal Urbánek. Master's thesis (Faculty of Mechanical Engineering Brno University of Technology, Brno, 2021) (cit. on pp. 75, 93, 95).
- 198. Kuschel, T., Becker, T., Bruns, D., Suendorf, M., Bertram, F., Fumagalli, P. & Wollschläger, J. Uniaxial magnetic anisotropy for thin Co films on glass studied by magnetooptic Kerr effect. *J. Appl. Phys.* **109**, 093907. doi:10.1063/1.3576135 (2011) (cit. on p. 75).
- 199. Colino, J. M., Arranz, M. A., Barbero, A. J., Bollero, A. & Camarero, J. Surface magnetization and the role of pattern defects in various types of ripple patterned films. J. Phys. D: Appl. Phys. 49, 135002. doi:10.1088/0022-3727/49/13/135002 (2016) (cit. on p. 76).
- 200. Turčan, I., Flajšman, L., Wojewoda, O., Roučka, V., Man, O. & Urbánek, M. Spin wave propagation in corrugated waveguides. *Appl. Phys. Lett.* **118**, 092405. doi:10.1063/5.0041138 (2021) (cit. on p. 78).
- 201. Light Scattering in Solids VII Crystal-Fiel and Magnetic Excitations (eds Cardona, M., Güntherodt, G. & Merlin, R.) 303. ISBN: 978-3-540-48770-8. doi:10.1007/BFb 0103383 (Springer-Verlag Berlin Heidelberg, 2000) (cit. on p. 80).
- 202. Sebastian, T., Ohdaira, Y., Kubota, T., Pirro, P., Brächer, T., Vogt, K., Serga, A. A., Naganuma, H., Oogane, M., Ando, Y., et al. Low-damping spin-wave propagation in a micro-structured Co₂Mn_{0.6}Fe_{0.4}Si Heusler waveguide. Appl. Phys. Lett. 100, 112402. doi:10.1063/1.3693391 (2012) (cit. on pp. 81, 86).
- 203. Vogt, K., Schultheiss, H., Hermsdoerfer, S. J., Pirro, P., Serga, A. A. & Hillebrands, B. All-optical detection of phase fronts of propagating spin waves in a Ni₈₁Fe₁₉ microstripe. *Appl. Phys. Lett.* **95**, 182508. doi:10.1063/1.3262348 (2009) (cit. on p. 85).
- 204. Madami, M., Bonetti, S., Consolo, G., Tacchi, S., Carlotti, G., Gubbiotti, G., Mancoff, F. B., Yar, M. A. & Åkerman, J. Direct observation of a propagating spin wave induced by spin-transfer torque. *Nat. Nanotechnol.* **6**, 635. doi:10.1038/nnano.2011.140 (2011) (cit. on p. 86).
- 205. Demidov, V. E., Demokritov, S. O., Rott, K., Krzysteczko, P. & Reiss, G. Self-focusing of spin waves in Permalloy microstripes. *Appl. Phys. Lett.* **91**, 252504. doi:10.1063/1.2825421 (2007) (cit. on p. 86).
- 206. Konijn, M., Alkaisi, M. M. & Blaikie, R. Nanoimprint lithography of sub-100 nm 3D structures. *Microelectron. Eng.* **78**, 653–658. doi:10.1016/j.mee.2004.12.081 (2005) (cit. on pp. 87, 96).
- 207. Bilzer, C., Devolder, T., Crozat, P., Chappert, C., Cardoso, S. & Freitas, P. P. Vector network analyzer ferromagnetic resonance of thin films on coplanar waveguides: Comparison of different evaluation methods. *J. Appl. Phys.* **101**, 074505. doi:10.1063/1.2716995 (2007) (cit. on p. 87).

- 208. Gubbiotti, G., Kazakova, O., Carlotti, G., Hanson, M. & Vavassori, P. Spin-wave spectra in nanometric elliptical dots arrays. *IEEE Trans. Magn.* **39**, 2750–2752. doi:10.1109/TMAG.2003.815588 (2003) (cit. on p. 89).
- 209. Qin, Q., He, S., Song, W., Yang, P., Wu, Q., Feng, Y. P. & Chen, J. Ultra-low magnetic damping of perovskite La_{0.7}Sr_{0.3}MnO₃ thin films. *Appl. Phys. Lett.* **110**, 112401. doi:10.1063/1.4978431 (2017) (cit. on p. 89).
- 210. Gerrits, T., Hohlfeld, J., Gielkens, O., Veenstra, K. J., Bal, K., Rasing, T. & van den Berg, H. A. M. Magnetization dynamics in NiFe thin films induced by short inplane magnetic field pulses. *J. Appl. Phys.* 89, 7648–7650. doi:10.1063/1.1359462 (2001) (cit. on p. 90).
- 211. Vogt, K., Schultheiss, H., Jain, S., Pearson, J. E., Hoffmann, A., Bader, S. D. & Hillebrands, B. Spin waves turning a corner. *Appl. Phys. Lett.* **101**, 042410. doi:10.1063/1.4738887 (2012) (cit. on p. 96).
- 212. Nečas, D. & Klapetek, P. Gwyddion: an open-source software for SPM data analysis. *Open Physics* **10**, 181–188. doi:10.2478/s11534-011-0096-2 (2012).

List of abbreviations

AE Auger electrons

AFM Atomic force microscopy

ALD Atomic layer deposition

BLS Brillouin light scattering

BSE Backscattered electrons

BV Backward volume

CEITEC Central European Institute of Technology

CMOS Complementary metal-oxide-semiconductor

CPW Coplanar-waveguide

CVD Chemical vapor deposition

DAC Digital-to-analog converter

DE Damon-Eshbach

DI De-ionized

DUT Device under test

EBL Electron beam lithography

EOM Electro-opric modulator

FEBID Focused electron beam-induced deposition

FEMM Finite element method magnetics

FIB Focused ion beam

FIBID Focused ion beam-induced deposition

FMR Ferromagnetic resonance

FPI Fabry-Perot interferometer

FSR Free spectral range

FV Forward volume

FWHM Full width at half maximum

GIS Gas injection system

GSG Ground-signal-ground

IPA Isopropyl alcohol

LED Light-emitting diode

LLE Low-loss electrons

LLG Landau-Lifshitz-Gilbert

LMIS Liquid metal ion source

MIBK Methyl isbotutyl ketone

MO Magneto-optical

MOKE Magneto-optical Kerr effect

PE Primary electrons

PMCPS 2,4,6,8,10-Pentamethylcyclopentasiloxane

PMMA Poly(methyl methacrylate)

PSSW Perpendicular standing spin waves

PVD Physical vapor deposition

QPD Four quadrant photodiode

RF Radio-frequency

SE Secondary electrons

SEM Scanning electron microscopy

SOC Spin-orbit coupling

SOLT Short Open Load Through

SPM Scanning probe microscopy

STEM Scanning transmission electron microscopy

SW Spin waves

TFPI Tandem Fabry-Perot interferometer

TOSM Through Open Short Match

μBLS micro-focusd BLS

 ${\rm VNA} \qquad \qquad {\rm Vector\ network\ analyzer}$

VNA-FMR Vector network analyzer ferromagnetic resonance

VSM Vibrating sample magnetometry

WD Working distance

 $YIG \hspace{1cm} Yttrium \hspace{1cm} iron \hspace{1cm} garnet \hspace{1cm} Y_3Fe_5O_12$

Own publications

- 1. **Turčan, I.**, Flajšman, L., Wojewoda, O. Roučka, V., Man, O., and Urbánek, M. Spin wave propagation in corrugated waveguides. *Applied Physics Letters*, 092405, 2021. URL: https://doi.org/10.1063/5.0041138.
- Flajšman, L., Urbánek, M., Křižáková, V., Vaňatka, M., Turčan, I., and Šikola, T. High-resolution fully vectorial scanning Kerr magnetometer. Review of Scientific Instruments, 053704, 2016. URL: http://doi.org/10.1063/1.4948595.
- 3. Flajšman, L., Urbánek, M., Křižáková, V., Vaňatka, M., **Turčan, I.**, and Šikola, T. Vektorová Kerrova magnetometrie s vysokým prostorovým rozlišením. *Jemná mechanika optika*, 6. 2016.

Participation in conferences and summer schools

- Join European Magnetic Symposia (JEMS), Lisbon, Portugal (fully online due to the pandemic situation). Oral contribution: Spin wave propagation in corrugated waveguides. December 2020
- Join European Magnetic Symposia (JEMS), Uppsala, Sweden. Poster contribution: Magnetic anisotropy modulation in thin Permalloy films. August 2019
- Magnetics and Optics Research International Symposium, Prague, Czech Republic. Oral contribution: Uniaxial magnetic anisotropy modulation in thin Permalloy films. June 2019
- European School on Magnetism (ESM), Kraków, Poland. September 2018
- Join European Magnetic Symposia (JEMS), Mainz, Germany. Poster contribution: Modulation of uniaxial anisotropy in thin Permalloy films driven by artificial local corrugation of the substrate. August 2018
- Magnetism, Interactions and Complexity (MagIC), Poznań, Poland. Poster contribution: Detection of Spin-Wave Excitations via Nernst Effect. July 2017
- 16th IUVSTA International Summer School on Physics at Nanoscale, Devět Skal, Czech Republic. June 2017
- IEEE International Magnetics Conference (INTERMAG), Dublin, Ireland. Poster contribution: An instrument for measurement of spin-waves via thermoelectric detection. April 2017

Internship

The author did a one month long research internship in Augsburg in the group of prof. Manfred Albrecht at the University Augsburg. He learned how to prepare Yttrium Iron Garnet (YIG) layer using pulsed layer deposition (PLD) and characterized grown layer using Rutherford backscattering spectrometry, x-ray diffraction (XRD), atomic force microscopy (AFM) and superconducting quantum interference device (SQUID) magnetometry. Prepared layers will be used in the future collaboration within Czech-Bavarian project.

A. Vibrating sample magnetometry

In Figure A.1 we provide the vibrating sample magnetometry (VSM) measurement of the planar continuous NiFe layer. This measurement was used to extract the saturation magnetization.

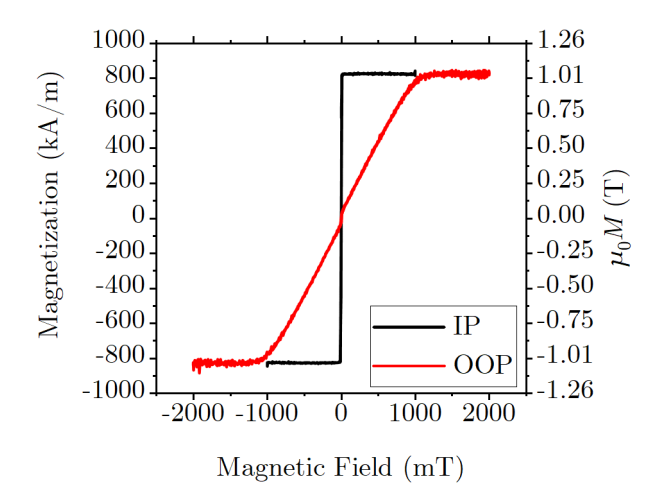


Figure A.1: Saturation magnetization of the planar NiFe continuous layer measured by vibrating sample magnetometry for the in-plane (IP) and out-of-plane (OOP) magnetic field

B. List of samples

Sample	Purpose	Figures
IGY #0.1	testing Si sample	Fig. 4.1
IGY $\#0.2$	testing GaAs sample	Fig. 4.2
IGY #6	FIB milling test	Fig. 4.3, 4.4
IGY #7	FEBID tests with alignment marks	Fig. 4.5, 4.6
IGY #8	FEBID tests with magnetic layer	Fig. $4.9(c)$
IGY #18	planar pads for VNA-FMR	Fig. 4.22, 4.23, 4.24, 4.25
IGY #21	smaller amplitudes of modulation	Fig. 4.15, 4.16, 4.17, 4.18, 4.19,
	for BLS	$4.20,\ 4.21,\ 4.27$
IGY $#23$	higher amplitudes of modulation for	Fig. 4.14, 4.19, 4.21, 4.27
	BLS	
IGY #24	corrugated pads for VNA-FMR	Fig. 4.26, 4.27
IGY #25	Discs with different amplitudes of the modulation and modulation periodicities for Kerr microscopy	Fig 4.9(a)-(b), 4.10, 4.11, 4.12, 4.13

- IGY #0.1 Clean Si substrate used for the pioneering experiments using FIB milling.
- IGY #0.2 Clean GaAs substrate used for the resolution test using FIB milling.
 - IGY #1 Clean Si substrate used for the pioneering experiments using FEBID.
 - IGY #2 Clean GaAs substrate used for the first experiments using FEBID.
 - IGY #3 Clean Si substrate used for the pioneering experiments using FIBID.
- IGY #4,#5 Clean GaAs substrates used for the growth rate experiments using FEBID.
 - IGY #6 Clean GaAs substrate used for the modification of the amplitude of modulation fabricated using FIB milling.
 - IGY #7 Sample with alignment marks used for the pioneering experiments using FEBID. The alignment marks were prepared using e-beam lithography. The process was as follows:
 - Sample-cleaning Aceton, IPA + Ultrasonic agitation.
 - Process of spin-coating: positive e-beam resist AR-P 679.04 spin-coated at $4\,000\,\mathrm{rpm}$ for $60\,\mathrm{s}$. Post bake for $3\,\mathrm{min}$ on a hot plate heated to $150\,\mathrm{^\circ C}$.
 - E-beam patterning using acceleration voltage of $20\,\mathrm{kV}$ and current $250\,\mathrm{pA}$. The write field size was $200\,\mu\mathrm{m}$ and the patterning dose was $220\,\mu\mathrm{C/cm^2}$ with a step size of $10\,\mathrm{nm}$.

- The development was done for 3 min using AR 600-56 developer.
- Ti 5 nm/Cu 100 nm/Au 10 nm multilayer deposited using e-beam evaporator.
- Lift off in acetone bath for 2 hours followed by ultrasonic agitation.

The substrate corrugation was prepared using FEBID.

- IGY #8 Sample with alignment marks and corrugated magnetic layer used for the preparation of STEM lamella. The alignment marks were prepared as described above (see IGY #7). The corrugation was prepared using FEBID. In the second lithographic step, 10 nm thick layer of Nife was prepared in the e-beam evaporator. The parameters of lithography were the same as for the alignment marks.
- IGY#9 #17 Samples with magnonic waveguides with corrugation-induced uniaxial magnetic anisotropy and excitation antennas used for the BLS experiments. For the process of fabrication see sample IGY #21. Samples were either corrupted, destroyed during the fabrication process or burned during the measurement process.
 - IGY #18 Sample with alignment marks, planar NiFe pads and coplanar waveguides on top of the pads used for the VNA-FMR experiments. The alignment marks were prepared as described above (see IGY #7). The NiFe pad was prepared in the second lithographic step using the same parameters as described in sample IGY #8. The coplanar waveguide was prepared using the same lithographic parameters as in the first and second lithographic steps, but the multilayer consisted of Ti 5 nm/SiO₂ 25 nm/Ti 5 nm/Au 100 nm.
- IGY #19, #20 Samples with alignment marks, corrugated and planar NiFe pads and coplanar waveguides for the VNA measurement used for the testing of the technique.
 - IGY #21 Sample with alignment marks, magnonic waveguides with corrugation-induced uniaxial magnetic anisotropy and excitation antennas used for the BLS experiments. The alignment marks were prepared as described above (see IGY #7). The corrugation below magnonic waveguides was prepared using FEBID. The magnetic layer was prepared using the same lithographic parameters as described in sample IGY #8. The excitation antenna consisted of Ti 5 nm/SiO_2 25 nm/Ti 5 nm/Cu 85 nm/Au 10 nm.
 - IGY #22 Sample with alignment marks for Kerr microscopy testing. Destroyed during lift-off.
 - IGY #23 Sample with alignment marks, magnonic waveguides with corrugation-induced uniaxial magnetic anisotropy and excitation antennas used for the BLS experiments. This sample differed from the sample IGY #21 only in higher amplitudes of modulation prepared during the FEBID step.
 - IGY #24 Sample with alignment marks, corrugated NiFe pads and coplanar waveguides on top of the pads used for the VNA-FMR experiments. The sample differed from the sample IGY #18 only in the corrugation bellow NiFe pads prepared during the FEBID step prior to the deposition of the magnetic layer.
 - IGY #25 Sample was prepared following the same procedure as for the sample IGY #8.

For the designs in gds and dbp of the most important samples visit https://ldrv.ms/u/s!AjRXxnpD0vtej0Z2Hf5as5aHBhMD7Q?e=nuLhHn. If the link is not working, or you have any additional questions, please contact the author of the thesis on igor.turcan@vutbr.cz.